FLOW IN CURVED DUCTS AND GUN SIMULATORS

MARK CHRISTOPHER SCHMIDT
B.Sc., M.Sc.

Thesis submitted for the degree of
Doctor of Philosophy
in the University of London
and for the
Diploma of Membership of the Imperial College

Department of Mechanical Engineering
Imperial College of Science, Technology and Medicine

January 1990

Dedicated to my parents

ABSTRACT

Three experimental investigations are described, concerned respectively with steady flows in curved ducts, unsteady flows in a straight pipe with velocities up to 40 m/s and unsteady flows in a straight pipe with velocities up to 450 m/s. The steady flows corresponded to water in out-of-plane double S-shaped ducts of relevance to the intake ducts of aircraft and the velocity characteristics and wall pressures are reported for laminar and turbulent Reynolds numbers. The two unsteady flows simulate the flows in gun barrels with the low-speed arrangement providing the experience and knowledge to guide the high-speed investigation. In both cases, the emphasis was on the measurement of variations of pressure, projectile and gas velocity and on the wall temperature and heat flux. The high-speed arrangement involved the design of the flow arrangement and of the instrumentation required to process the data in real time.

The steady flows corresponded to water flowing in S-ducts of rectangular and circular cross-sections. These arrangements were made up of constant cross-section ducts and diffusers previously investigated so that the measurements in the present out-of-plane combination could be related to those in single S-bends. The three cases investigated all showed that the flow in the first bend influenced that in the second so that the plane of the exit contained up to six cross-stream vortical motions. The maximum secondary-flow velocities in the exit plane for the laminar and turbulent flows were 0.18 and 0.11 m/s for the rectangular cross-section and the axial mean-velocity distributions had maxima off the centre and with no separated flow evident at the diffuser exit.

The low-speed gun simulator was used to measure the nature of the single-phase boundary layer, the effect of the addition of an inert second-phase with initial volume concentrations of 1.3 and 4 % and the variations of wall temperature and heat flux with position and time. The results show that the boundary layers were turbulent with characteristics similar to those of steady boundary layers. The higher concentration of 500 μm diameter Plexiglass beads indicated some non-uniformity of the discrete phase with higher concentrations around the edge of the boundary layer; there was also a tendency for the solid-phase velocity to lag the gas velocity initially and to lead later in the cycle. The thin-film sensor allowed measurements of wall temperature at several

locations and quantified the expected initial reduction in temperature after the projectile passed the measuring location. The temperature results were analysed, with consideration of the properties of the substrate of the film, to provide variations of heat flux and convective heat transfer coefficients which showed similar trends to those of developing turbulent boundary layers but with much higher initial values.

Gas-phase velocities, breech pressure, wall temperature and heat flux were measured in the high-speed gun simulator and required considerable effort to eliminate cyclic variations and prolong the projectile life. The pressure transducer, laser velocimeter, method for measuring projectile velocity and the thin-film were arranged to meet the higher frequency response implied by the much higher velocities. In addition, and perhaps even more demanding, the signal-processing arrangement was changed to allow the simultaneous processing of the signals with shot durations of less than 16 ms. It is of note that the resulting projectile-velocity variations were always within 4 %, at the largest initial pressure of 60 bar, of those predicted with the assumption of one-dimensional, isentropic expansion even though the flow was clearly two-dimensional with finite wall heat transfer. As with the low-speed simulator, the near wall flow exhibited characteristics similar to those of a steady two-dimensional turbulent boundary layers and the wall heat fluxes exhibited related trends with values very much higher immediately after the passage of the projectile.

ACKNOWLEDGEMENTS

I wish to thank my supervisor Professor J. H. Whitelaw for his sound guidance, continuous criticism, and suggestions during the course of my work; but most of all for having given me the opportunity to come to Imperial College and to use his research facilities and fulfill my ambitions.

I would like to express my gratitude to Dr. Yianneskis and Dr. Khezzar for support early in my research and especially to Dr. Bicen, who provided a great deal of patience and valuable experience.

My thanks also, go to Mr. Laker, Mr. Trowell, Mr. Vis, and Mr. Crew for their technical assistance.

Mrs. Caroline Hopkins, Mrs. Sue Pritchett and Mr. George Tindall have been most helpful to me during the course of my studies here and I am very grateful to them. I would also like to thank my friends Denise Smith, Mike Jordan and Philip Wigley for their continual support.

Financial support has been provided by NASA Lewis and the US Army European Research Office, and is gratefully acknowledged.

This thesis was composed on an Apple Macintosh Plus computer with WriteNow™, Cricket Graph, MS Fortran and MacDraft software.

I finally wish to thank my parents to whom this thesis is dedicated, for their loving and motivating support.

TABLE OF CONTENTS

		page
ABSTRACT		3
ACKNOWLEDGEMENTS		4
TABLE OF CONTENTS		6
LIST OF TABLES		8
LIST OF FIGURES		9
NOMENCLATURE		13
CHAPTER 1	INTRODUCTION TO THESIS	17
1.1	Flows Considered	17
1.2	Review of Curved Duct Flow Research	20
1.3	Review of Gun Simulator Research	24
1.4	Present Contribution	30
1.5	Thesis Outline	30
CHAPTER 2	EXPERIMENTAL TECHNIQUES	32
2.1	Introduction	32
2.2	Steady Curved Duct Experiments	32
	2.2.1 Pressure Measurements	32
	2.2.2 Laser Doppler Anemometer	33
2.3	Unsteady Low-Speed Gun Simulator Experiments	42
	2.3.1 Transient Pressure Measurements	42
	2.3.2 Laser Doppler Anemometer	43
	2.3.3 Heat Flux Measurements	49
2.4	Unsteady High-Speed Gun Simulator Experiments	53
	2.4.1 Transient Pressure Measurements	53
	2.4.2 Laser Doppler Anemometer	54
	2.4.3 Heat Flux Measurements	59
CHAPTER 3	CURVED DUCT FLOWS	69
3.1	Introduction	69
3.2	Flow Configuration	69

3.3	Duct Flow Results	74
	3.3.1 Rectangular Cross-section Duct - Laminar flow	74
	3.3.2 Rectangular Cross-section Duct - Turbulent flow	77
	3.3.3 Circular Cross-section Duct - Turbulent flow	81
3.4	Concluding Remarks	85
CHAPTER 4	LOW-SPEED GUN SIMULATOR	105
4.1	Introduction	105
4.2	Flow Configuration	105
4.3	Low-Speed Simulator Results	109
	4.3.1 Projectile Dynamics and Breech Pressure	109
	4.3.2 Single-Phase Flow	111
	4.3.3 Two-Phase Flow	112
	4.3.4 Heat Transfer	117
4.4	Concluding Remarks	120
Appendix 4.1	Projectile Velocity Program Listing	123
CHAPTER 5	HIGH-SPEED GUN SIMULATOR	148
5.1	Introduction	148
5.2	Flow Configuration	148
5.3	High-Speed Simulator Results	150
	5.3.1 Projectile Dynamics	150
	5.3.2 Single-Phase Flow	157
	5.3.3 Heat Transfer	161
5.4	Concluding Remarks	166
CHAPTER 6	CLOSURE	198
6.1	Conclusions	198
	6.1.1 Experimental Techniques	198
	6.1.2 Curved Duct Flow	198
	6.1.2 Low-Speed Gun Simulator	199
	6.1.3 High-Speed Gun Simulator	200
6.2	Recommendations For Further Work	200
REFERENCES		203

LIST OF TABLES

2.1 Characteristics of duct optical arrangement.
2.2 Summary of estimated S-Duct measurement uncertainty.
2.3 Characteristics of low-speed simulator optical arrangement.
2.4 Summary of estimated low-speed simulator measurement uncertainty.
2.5 Physical properties of Kapton Foil substrate and low-speed thin-film sensor.
2.6 Characteristics of high-speed simulator optical arrangements.
2.7 Summary of estimated high-speed simulator measurement uncertainty.
2.8 Physical properties of Pyrex 7740 substrate and high-speed thin-film sensor.
3.1 Parameters in the duct flow configuration.

LIST OF FIGURES

2.1 Measuring volume of laser-Doppler anemometer.
2.2 Laser-Doppler anemometer signal.
2.3 Optical configuration of laser-Doppler anemometer.
2.4 Low-speed gun simulator and related instrumentation.
2.5 Thin-film circuit for low-speed gun simulator.
2.6 High-speed gun simulator and related instrumentation.
2.7 Data acquisition program flow chart.
2.8 Thin-film circuit for high-speed gun simulator.
3.1(a) Rectangular duct: flow configuration and coordinate system.
3.1(b) Rectangular duct: coordinate notation in duct and diffuser exit.
3.2 Circular duct: flow configuration and coordinate system.
3.3 Rectangular diffuser: Laminar flow, centreline variation of U velocity.
3.4 Rectangular diffuser: Laminar flow, centreline variation of V velocity.
3.5 Rectangular diffuser: Laminar flow, contours of U/V_B at the exit plane.
3.6 Rectangular diffuser: Laminar flow, contours of V/V_B at the exit plane.
3.7 Rectangular diffuser: Laminar flow, profiles of U/V_B at X*=12.375 and 16.735.
3.8 Rectangular diffuser: Laminar flow, profiles of V/V_B at X*=12.375 and 16.735.
3.9 Rectangular duct: Turbulent flow, C_{p^*} variation along duct.
3.10 Rectangular diffuser: Turbulent flow, centreline variation of U velocity.
3.11 Rectangular diffuser: Turbulent flow, centreline variation of V velocity.
3.12 Rectangular diffuser: Turbulent flow, centreline variation of $\tilde{u}$ velocity.
3.13 Rectangular diffuser: Turbulent flow, centreline variation of $\tilde{v}$ velocity.
3.14 Rectangular diffuser: Turbulent flow, centreline variation of $\tilde{u}\tilde{v}/V_B^2$.
3.15 Rectangular diffuser: Turbulent flow, contours of U/V_B at the exit plane.
3.16 Rectangular diffuser: Turbulent flow, cross-flow vectors of V & W at the exit plane.
3.17 Rectangular diffuser: Turbulent flow, contours of $\tilde{u}/V_B$ at the exit plane.
3.18 Rectangular diffuser: Turbulent flow, contours of $\overline{uv}/V_B^2$ at the exit plane.
3.19 Rectangular diffuser: Turbulent flow, profiles of U/V_B at X*=12.375 and 16.735.
3.20 Rectangular diffuser: Turbulent flow, profiles of V/V_B at X*=12.375 and 16.735.
3.21 Circular duct: Turbulent flow, C_{p^*} variation along duct.
3.22 Circular diffuser: Turbulent flow, centreline variation of U velocity.
3.23 Circular diffuser: Turbulent flow, centreline variation of V velocity.
3.24 Rectangular diffuser: Turbulent flow, centreline variation of $\tilde{u}$ velocity.

3.25 Rectangular diffuser: Turbulent flow, centreline variation of $\tilde{v}$ velocity.

3.26 Circular diffuser: Turbulent flow, contours of U/V_B at the exit plane.

3.27 Circular diffuser: Turbulent flow, contours of $\tilde{u}/V_B$ at the exit plane.

4.1 Geometry of low-speed gun simulator with constant-diameter and chamfered initial volume.

4.2 Particle injector mechanism for chamfered initial volume.

4.3 Photograph of low-speed gun simulator and instrumentation with constant-diameter initial volume.

4.4 Photograph of low-speed gun simulator and instrumentation with chamfered initial volume.

4.5 Photograph of chamfered initial volume with injection mechanism.

4.6 Calculated and measured projectile travel distance with time.

4.7 Calculated and measured projectile velocity with travel distance.

4.8 Calculated and measured projectile velocity with time.

4.9 Temporal variation of measured breech pressure.

4.10 Temporal variation of measured and calculated centreline mean velocity; single-phase flow in constant-diameter geometry.

4.11 Temporal variation of measured and calculated centreline mean velocity; single-phase flow in chamfered geometry.

4.12 Radial variation of single-phase streamwise mean velocity in chamfered geometry.

4.13 Radial variation of single-phase streamwise turbulence intensity in chamfered geometry.

4.14 Variation of velocity profiles inside the boundary layer.

4.15 Clauser chart for the deduction of C_f.

4.16 Velocity distribution displayed in standard Wall coordinates Y^+ and U^+.

4.17 Centreline mean velocity time records at x=4.96d; single- and two-phase flows with 1.3% and 4% particle loading.

4.18 Radial profiles of mean and rms velocity at various axial locations for a time of around 24 ms in the shot; single- and two-phase flow with 1.3% particle loading.

4.19 Radial profiles of mean velocity at x = 4.96d for various times in the shot; single- and two-phase flow with 1.3% and 4% particle loading.

4.20 Radial profiles of rms velocity at x = 4.96d for various times in the shot; two-phase flow with 4% particle loading.

4.21 Diagram illustrating the two orientations of the injection plate.

4.22 Temporal variation of two-phase data as a function of injection plate orientation; 0.09 r/R from wall.

4.23 Temporal variation of two-phase data as a function of injection plate orientation; 0.12 r/R from wall.

4.24 Effect of radial positioning of sensor on sensor temperature at x=2.88d; single-phase flow in constant-diameter geometry.
4.25 Sensor temperature variation at x=2.88d over five shots.
4.26 Sensor temperature time records at various axial locations relative to free-stream temperature; single-phase flow in constant-diameter geometry.
4.27 Sensor temperature time records at various axial locations; single-phase flow in constant-diameter geometry.
4.28 Curve-fit approximations to sensor temperature data.
4.29 Heat flux at various axial locations; single-phase flow in constant-diameter geometry.
4.30 Convection coefficients at various axial locations; single-phase flow in constant-diameter geometry.
4.31 Evaluated convection coefficients at various axial locations.
4.32 Wall heat flux at various axial locations; single-phase flow in constant-diameter and chamfered geometries.
4.33 Wall heat flux at various axial locations; single-phase and two-phase flows in chamfered geometry.
5.1 Geometry of high-speed gun simulator.
5.2 Photograph of the entire high-speed gun simulator.
5.3 Photograph of the high-speed initial volume, test section and instrumentation.
5.4 Calculated projectile travel distance with time; 13 g projectile.
5.5 Calculated and measured projectile velocity with travel distance; 13 g projectile.
5.6 Measured breech pressure with a worn projectile.
5.7 Centreline single-phase velocity at 5, 10 and 15 bar initial pressures with new and used projectiles.
5.8 Centreline single-phase rms velocity fluctuations at 5, 10 and 15 bar initial pressures with new and used projectiles.
5.9 Geometry of old and new projectile designs.
5.10 Photograph of old and new design of projectile.
5.11 Cyclic variation of centreline single-phase velocity; 13.1 g projectile.
5.12 Cyclic variation of centreline single-phase velocity; 10.5 g projectile.
5.13 Calculated projectile velocity with travel distance for 10.5 & 13.1 g projectiles.
5.14 Calculated and measured projectile travel distance with time; 10.5 g projectile.
5.15 Calculated and measured projectile velocity with travel distance; 10.5 g projectile.
5.16 Calculated and measured projectile velocity with time; 10.5 g projectile.
5.17 Measured breech pressure for under 8.0 bar initial pressure.
5.18 Measured breech pressure for 10, 15, 20, 25 &.30 bar initial pressure.
5.19 Typical velocity traces at windows #1 & #5 for an initial pressure of 10 bar.

5.20 Measured and calculated centreline mean velocity for an initial pressure of 10 bar.
5.21 Measured and calculated centreline rms velocity fluctuations for an initial pressure of 10 bar.
5.22(a) Measured mean and rms velocity versus time; Window #1, X=60.81 d.
5.22(b) Measured mean and rms velocity versus time; Window #2, X=70.72 d.
5.22(c) Measured mean and rms velocity versus time; Window #3, X=80.63 d.
5.22(d) Measured mean and rms velocity versus time; Window #4, X=90.54 d.
5.22(e) Measured mean and rms velocity versus time; Window #5, X=110.36 d.
5.23(a) Radial profiles of mean and rms velocity; Window #1, X=60.81 d.
5.23(b) Radial profiles of mean and rms velocity; Window #2, X=70.72 d.
5.23(c) Radial profiles of mean and rms velocity; Window #3, X=80.63 d.
5.23(d) Radial profiles of mean and rms velocity; Window #4, X=90.54 d.
5.23(e) Radial profiles of mean and rms velocity; Window #5, X=110.36 d.
5.24 Measured and calculated boundary layer thickness variation versus time.
5.25 Axial variation of calculated and measured boundary layer thickness.
5.26(a) Boundary layer profiles; Window #2, X=70.72 d.
5.26(b) Boundary layer profiles; Window #3, X=80.63 d.
5.26(c) Boundary layer profiles; Window #4, X=90.54 d.
5.26(d) Boundary layer profiles; Window #5, X=110.36 d.
5.27(a) Clauser chart for the deduction of C_f; Window #2, X=70.72 d.
5.27(b) Clauser chart for the deduction of C_f; Window #3, X=80.63 d.
5.27(c) Clauser chart for the deduction of C_f; Window #4, X=90.54 d.
5.27(d) Clauser chart for the deduction of C_f; Window #5, X=110.36 d.
5.28 Velocity distribution displayed in standard Wall coordinates Y^+ and U^+.
5.29 Photograph of high-speed thin-film sensor and mounting window.
5.30 Sensor temperature record at windows #1, #3, #5 & #6 for an initial pressure of 10 bar.
5.31 Sensor temperature records relative to free-stream temperature.
5.32 Wall heat flux at windows #1, #3, #5 & #6 for an initial pressure of 10 bar.
5.33 Convection coefficients at various axial locations for an initial pressure of 10 bar.
5.34 Calculated convection coefficients at various axial locations by Equation 4.3.
5.35 Calculated convection coefficients at various axial locations by Equation 5.2.
5.36 Calculated convection coefficients at various axial locations by Equation 5.3.

NOMENCLATURE

Roman characters

A	Cross-sectional area of the projectile base.
a_0	Speed of sound in the initial volume at the initial pressure.
C_f	Mean local skin friction coefficient.
C_{p*}	Static pressure coefficient for duct surfaces.
C_s	Specific heat of substrate upon which the thin-film is deposited.
d	Diameter of the gun simulator.
De	Dean number = Re $(1/2\ D_h/R_c)^{1/2}$.
$D_{e^{-2}}$	Laser beam diameter at output of laser (to e^{-2} intensity points).
$d_{e^{-2}}$	Waist of the focussed laser beam diameter in air (to e^{-2} intensity points).
D_h	Hydraulic diameter of the inlet of the duct.
D_m	Height of the measuring volume in fluid medium.
G	Gain of thin-film bridge circuit amplifier.
h	Convection heat transfer coefficient.
k_f	Thermal conductivity of fluid.
k_s	Thermal conductivity of substrate upon which the thin-film is deposited.
L_1	Focal length of laser focusing lens.
L_2	Focal length of collimating lens.
L_3	Focal length of imaging lens.
L_4	Focal length of collecting lens.
L_m	Length of the measuring volume in fluid medium.
l_m	Length of the measuring volume in the direction of the velocity gradient (y).
M	Mass of the projectile.
N	Statistical sample size.
N_m	Number of fringes in the measuring volume in fluid medium.
Nu_x	Nusselt number = $h\ x/k_f$.

Nu_d Nusselt number = $h\ d/k_f$.

P Laser output power.

p Static surface pressure.

p_o Initial pressure of the initial volume.

Pr Prandtl number = ν/α.

p_{ref} Static surface reference pressure.

$\dot{q}$ Heat flux from the surface.

$q'_{(t)}$ Heat flux from the surface at time t.

$q_n'_{(t)}$ Calculated heat flux from the surface at time t with n time divisions.

St Stanton number = $Nu_d/(Re_d\ Pr)$.

R_1 Resistance of Wheatstone bridge component.

R_2 Resistance of Wheatstone bridge component.

R_3 Resistance of Wheatstone bridge component.

R_c Radius of curvature of curved duct/diffuser centreline.

Re Reynolds number = $V_B\ D_h/\nu$.

Re_d Reynolds number =$U_\infty\ d/\nu$.

Re_x Reynolds number =$U_\infty\ X/\nu$.

R_I Resistance of constant current circuit component.

r_i Inner radius of the curved duct/diffuser.

r_o Outer radius of the curved duct/diffuser.

R_s Resistance of thin-film sensor.

r^* Normalized radial distance.

t Time from the start of the event.

T_∞ Isentropic free-stream temperature.

t_c Transient time (rms) of the particle crossing the measuring volume.

Ts Sensor temperature.

$T_{(t)}$ Surface temperature in degrees Kelvin at time t.

U Mean velocity in the streamwise direction.

$\langle U \rangle$ Measured mean velocity in the streamwise direction.

U_∞ Free-stream velocity.

$\tilde{u}$ Rms fluctuations of velocity in the streamwise direction.

$\langle \tilde{u} \rangle$ Measured Rms fluctuations of velocity in the streamwise direction.

U_{error} Statistical error of ensemble mean velocity.

$\tilde{u}_{error}$ Statistical error of ensemble Rms fluctuations of velocity.

$\widetilde{uv}$ Cross correlations in the streamwise plane U and cross-stream plane V.

$\widetilde{uw}$ Cross correlations in the streamwise plane U and cross-stream plane W.

U_{x° Mean velocity at x° angle to the streamwise direction.

V Mean velocity in a cross-stream direction.

$\vec{V}$ Vector of cross-stream mean velocity component V.

$\tilde{v}$ Rms fluctuations of velocity in a cross-stream direction.

V_B Bulk velocity at the inlet of the duct.

V_b Thin-film bridge voltage.

V_{ex} Thin-film circuit excitation voltage.

V_I Voltage of constant current circuit component.

V_m Volume of the measuring volume in fluid medium.

V_{off} Voltage offset of thin-film bridge circuitry.

V_{out} Voltage output of thin-film bridge circuitry.

V_{sc} Voltage across the signal conditioner in the low-speed thin-film circuit.

W Mean velocity in a cross-stream direction.

$\vec{W}$ Vector of cross-stream mean velocity component W.

$\tilde{w}$ Rms fluctuations of velocity in a cross-stream direction.

X Streamwise distance along centreline from the S-duct inlet, in hydraulic diameters.

X Distance from the breech in diameter in the simulators.

x Distance from the breech.

X* Streamwise distance along centreline from the S-diffuser inlet, expressed in hydraulic diameters.

x_0 Initial chamber length.

$x_{p\,1st}$ Projectile travel distance when the first reflected wave reaches it.

y Direction of the velocity gradient being evaluated.

y* Normalized gapwise distance.

z* Normalized spanwise distance.

Z_c Statistical confidence criterion constant.

Greek characters

α Thermal diffusivity of substrate of thin-film ($\alpha=k_s/(\rho_s C_s)$.

α_s Thin-film temperature coefficient of resistance.

$\Delta R_{s(t)}$ Resistance change of thin-film sensor at time t.

Δt Time difference for calculated heat flux from the surface.

ΔT Temperature difference between the wall and free-stream in degrees Kelvin.

$\Delta T_{(t)}$ Surface temperature change of thin-film sensor in degrees Kelvin at time t.

δ_f Fringe spacing.

η Index of refraction of the fluid medium (η = 1 for air and η = 1.33 for water).

θ Diffusing bend turning angle.

λ Wave length of laser illumination (λ = 632.8 ηm for Helium - Neon).

μ Viscosity of the fluid at the free-stream temperature.

μ_s Viscosity of the fluid at the surface temperature.

ν Kinematic viscosity of fluid.

π Constant (3.14156295).

ρ_∞ Density of fluid assuming an isentropic expansion.

ρ_f Density of fluid, ie water in the duct experiments.

ρ_s Density of substrate upon which the thin-film is deposited.

τ Variable of integration.

φ Measured half angle between anemometer beams.

CHAPTER 1 INTRODUCTION TO THESIS

1.1 Flows Considered

This thesis focuses on the experimental investigation of two different types of internal flow; steady incompressible water flow in curved ducts and unsteady compressible inert multiphase flow in gun simulators. This introduction discusses the flow in curved ducts and gun simulators and reviews the relevant literature. The chapter ends with a description of the present contribution and an outline of the thesis.

Curved ducts and diffusers are used in a broad range of engineering situations and many investigations have been motivated by the requirements of aircraft intake ducts with dorsal or wing-root intakes, such as those used in commercial airplanes (Lockheed L-1011, Boeing 727) and numerous military fighter aircraft (Mirage, F-4, F-14, F-15, Tornado, MiG-25). The pressure driven secondary flows which are known to occur in curved ducts result in distortion of the flow profiles at the duct outlet with possible consequences for compressor and engine performance. The arrangement of an intake duct to provide a uniform velocity distribution to the engine face, over a wide range of angles of attack and yaw and constrained by the location, shape and size of the propulsion turbine and the fuselage, can lead to improved reliability and efficiency of the propulsion system.

Intake ducts can take the form of S-bends, where the flow channel is turned in a plane at a radius to one side and then turned in the opposite direction to result in a parallel entry and exit and a particular centreline displacement, which depends upon the radius of curvature and turning angle. If the cross-section area, perpendicular to the centreline, remains constant, the duct is called a S-bend duct. Alternately, if the cross-section area increases along the centreline, the arrangement is referred to as a S-bend diffuser. Practical aircraft intake duct geometries commonly comprise S-bend ducts and S-bend diffusers in series. If the planes which contain the centreline of the S-bends, ie. the plane of symmetry, are not identical, the bends are denoted as out-of-plane. Most real intake ducts employ an out-of-plane double S-bend duct and diffuser where the planes of symmetry have been rotated normal to each other, ie. 90°. Depending on the orientation

of the two duct and diffuser centreline planes, the right- and left-hand-side intakes of an aircraft will be distinct.

Left- and right-hand-side out-of-plane double S-bend intake geometries are mirror images of each other about a vertical plane which contains the aircraft axis. The symmetry plane of the S-duct, oriented horizontally, displaces the flow to the left-side, as viewed from the front, in a left-hand side intake and to the right for the right-hand intake, and the symmetric plane of the S-diffuser lies vertically, resulting in a displacement of the flow upward in both right- and left-hand side intakes. The pressure driven secondary flows at the exit of the first S-bend on the right hand side will be identical but rotated 180° in relation to the corresponding plane on the left side duct. The pressure characteristics, resulting from the geometry, are responsible for generating the secondary flows in the S-diffuser and are identical for the right and left intakes ducts since the symmetric planes are parallel and both displace the flow in the same direction, upward. In the present analysis left-hand-side intakes were investigated, but extrapolation to right-hand-side intakes can be made.

The investigation of the flow in a gun simulator, similar to the study in curved ducts, provides insight into a wide range of practical engineering problems and was motivated by the interior-ballistic needs of the armed forces. As the name suggests, gun simulators principally model the gun or ballistic cycle and the results help the understanding of flows in high-speed engines and other enclosed transient multiphase cycles with heat transfer. Two chapters of this thesis detail the experimental investigations in two gun simulators, referred to as the low-speed and high-speed gun simulators because of the relative projectile and fluid velocities. In both simulators, the flow was inert, unsteady, compressible, with heat transfer and multiphase flow in the first case. The focus of the experimental investigation was on the interior ballistic portion of the cycle from the initial movement of the projectile to its exit from the muzzle. The main purpose of the gun simulator research was to aid understanding of the single- and two-phase flow and heat transfer characteristics and to provide experimental results with which to validate modeling codes. The research will therefore assist the proficiency of numerical techniques, which will subsequently be used to improve the performance characteristics and reduce barrel erosion in real guns. As a result, the gun simulator research has relevance to other transient multiphase flows with heat transfer, which are

common in many engineering situations.

A real gun cycle can be characterized by a rapid expansion of a dense reacting mixture of gas and solid particles and/or liquid droplets in the increasing volume of a barrel between a breech and a moving projectile. The exothermic reaction of the charge can lead to local temperatures up to about 3000° K, *Farrar & Lemming (1983)*, and the velocity of the expanding multiphase mixture approaches that of the projectile which may exceed 12,000 m/s, *Seigel (1979)*, in experimental guns. A single-stage gun system consists of a single chamber containing a propellant charge, a primer used to ignite the propellant and a projectile which is propelled by the increasing chamber pressure from the reacting propellant. In all guns, the boundary layer formed on the inside wall of the barrel is transient and gives rise to a region of high heat transfer behind the projectile and erosion of the walls of the barrel. The salient features of the interior ballistic cycle are described in much greater detail in the discussions in *Farrar & Lemming (1983)* and *Krier & Adams (1979)*, where particular attention is given to the effects of different types of propellants and ignition methods.

The desire to understand and be able to predict the characteristics of the real interior ballistic cycle has led to the development of many sophisticated computer codes. The object of these codes is to enable the performance of a gun system to be optimized and reduce or eliminate erosion of the barrel to increase the operational life. The numerical approximation of the characteristics of the complex ballistics cycle comprises several areas which require the modeling of the chemical reaction of the propellant and the second-phase (particles or liquid droplets) interaction with the surrounding flow. As has been recognized by many, for example *Klingenberg et al (1985,1986)* and *Krier & Summerfield (1979)*, the benchmark validation of codes with experimental results from gun simulators is vital to the development of a thorough understanding of the interior ballistic cycle since the experimental analyses of real guns has been limited over the years primarily to pressure, temperature and projectile travel records. The many complexities of the real interior ballistics cycle and the limitations of measuring equipment and techniques has made it necessary to model the actual gun cycle with simplified models in order to facilitate the appraisal of the complicated flow and heat transfer phenomenon.

The real gun is modeled in simulators by the inert expansion of a compressed

gas, with particles in the two-phase experiments, behind a projectile in a cylindrical barrel by assuming that the propellant has reacted completely before the projectile is allowed to move. The preburned propellant gun, PP gun or Lagrange gun as it is often referred to, simplifies the real gun cycle and allows the fluid and particle dynamics and heat transfer characteristics to be evaluated in laboratory conditions and at a relatively low cost. In order to simplify the modeled gun cycle even further, the gas or propellant can be assumed to be an ideal (or perfect) gas. The PPIG (preburned propellant ideal-gas) gun forms the foundation upon which many gun simulators have been developed and is discussed at length by *Seigel (1965,1979)*. In standard single-stage guns, the initial chamber, in which the charge is assumed to reach the initial and peak pressure, is either of constant-diameter, when the initial chamber is the same diameter as the barrel, or chamfered, when the chamber diameter is greater than the diameter of the barrel. By reducing the complex interior ballistic cycle prevalent in real guns to a modeled preburned propellant ideal-gas gun and emulating typical initial chamber geometries, two gun simulators were investigated here to provide insight into the interior ballistic cycle and provide experimental results for comparison with modeling codes.

1.2 Review of Curved Duct Flow Research

This section presents a synopsis of previous work in curved and diffusing bends to provide a foundation for the discussion of the experimental results in chapter 3. A brief review of the theoretical and numerical methods employed for the solution of the transport equations in bends and diffusing bends is followed by a summary of previous experimental investigations which have provided understanding of the physics of the flow and the implications important for the interpretation of theoretical and numerical solutions.

A thorough biography of theoretical and experimental investigations of flows in bends, diffusing straight and curved bends can be found in *Rojas-Menendez (1986)* and the implications of the experimental work at Imperial College, *Melling & Whitelaw (1976), Humphrey et al (1977, 1981), Taylor et al (1980, 1981a,b, 1982, 1984), Rojas et al (1983a,b,c, 1984), Schmidt et al (1986,1987)* and *Yu (1989)* will be addressed in detail below.

The broad analysis of fluid motion in a bend, *Schlichting (1979)* and *Ward-Smith (1980)*, provides a general illustration of the cause of the secondary flow. When a fluid moves along an initially straight pipe of constant cross-section and encounters a bend changing the direction of the flow, the fluid near the axis of the duct, having the highest velocity, is subjected to a larger centrifugal force than the slower-moving fluid near the duct walls. The resulting secondary flow consists of a pair of helical vortices and causes the the flow in the centre region to move away from the centre of curvature and the fluid near the duct walls to move towards the centre of curvature. In long bends, the axial and secondary velocity distributions eventually become independent of the distance along the axis of the pipe and are called fully-developed. In practice, the fully-developed case is rarely attained and up-stream and down-stream geometries influence the resulting flow characteristics in the bend. Early analyses of flows in curved ducts were typically of two types, involving solution of equations for viscous, fully developed laminar flow and inviscid flow.

Dean (1927, 1928) solved the continuity and momentum equations for fully developed laminar flow in pipe bends and found a pair of counter-rotating helical vortices which resulted from an imbalance between induced radial pressure gradients and centrifugal forces near the walls. Dean proposed that the flow be characterized by the ratio of the product of the inertia and centrifugal forces to the viscous forces, known as the Dean number ($De = Re\ (1/2\ D_h/R_c)^{1/2}$) where Re, D_h and R_c are the Reynolds number, hydraulic diameter and radius of curvature of the bend respectively. Subsequent to Dean's laminar viscous flow solution, investigations of flows at a wide range of Dean numbers have ensued and are reviewed by *Berger et al (1983)*. They have limited application to practical aircraft intake ducts since the turning ratios, D_h/R_c, are usually small, the fully developed condition is rarely met and real flows are turbulent.

The incompressible inviscid equations were solved by *Squire & Winter (1951)* and *Hawthorne (1951)* in the form of a simplified form of the vorticity equation. Non-uniformities in the inlet velocities generated secondary flows and *Hawthorne (1951)* showed that the cross-flow developed in an oscillatory manner with downstream distance. *Rowe (1970)* compared the inviscid solutions for flows in a circular 180°

bend and in S-ducts with measurements and found agreement up to 75° of the single-bend and in the 30°/30°S-bend. *Rowe* attributed the break down of the computational technique to the absence of any mechanism for vortex dissipation and the practical difficulties of refining the numerical calculations to cope with regions having large local variations in secondary flow. The driving mechanism for the secondary flows was the local total pressure gradient which produced the streamwise vorticity. In the S-bend, the secondary flow caused a complete interchange of the slow moving wall fluid and the faster central core. The inviscid assumption can be used to predict the secondary flow patterns and the pressure distribution for developing flow in short bends but, since viscous effects are not considered, the theory cannot predict the effects of turbulence and near-wall flow characteristics.

Numerous experimental investigations of flow in single S-bend ducts and diffusers have been undertaken over the years and the measurements in out-of-plane double S-bend were designed to augment previous studies and increase the understanding of the complex practical intake duct geometries. The constant cross-section S-bend was identical to that investigated by *Taylor et al (1981b)*, with the square cross-section, and similar to that of *Taylor et al (1984)* for the circular duct. The diffusing S-duct sections in both the rectangular and circular cross-sections were identical to those investigated by *Rojas et al (1983a,c)*. From the many studies of single S-shaped ducts, it is known that the curvature of the second half of the S-bend does not cancel the secondary flow generated in the first bend and that a pair of vortices rotating in the same sense as in the first bend, is formed at the outside wall of the second bend. *Bansod & Bradshaw (1972)* attribute the production of vortices, in S-bends with small radius of curvatures, to the production of streamwise vorticity in the first bend and vortex stretching towards the end of the second bend. In S-bends with developing flow, mild curvature and thin inlet boundary layers, *Taylor et al (1981b,1984)*, the production of vortical structures was due to the change of the local sign of radial vorticity along the second bend. The studies of developing flow in S-diffusers, *Rojas et al (1983a,c)*, and constant diameter ducts of the same curvature produced similar results with larger cross-stream flows in the former case.

Numerical solutions of equations for laminar and turbulent flows in S-ducts have been reported by *Humphrey et al (1977, 1981)*, *Levy et al (1980,1983)*, *Towne*

and Anderson (1981) and *Towne (1984)* employing three-dimensional viscous analyses with various turbulence models for the turbulent cases. The results predicted the trends of the primary and secondary flow reasonably well and discrepancies were attributed to the turbulence models and limited grid mesh refinement. The studies of fully developed laminar flow showed that the primary secondary flow patterns consisted of two counter-rotating vortices with the maximum streamwise velocity shifted towards the outer side of the bend as Dean number increased. For Dean numbers greater than 100, *Joseph et al (1975)* suggest that laminar flows in a square cross-section ducts should give rise to four, rather than two, vortices so that the duct cross-section has a large influence on the secondary flow. In the absence of large regions of flow separation, finite-difference forms of the Navier-Stokes equations were solved by forward-marching procedures with savings in computational storage and time and show good qualitative (*Towne and Anderson (1981)*) and quantitative (*Levy et al (1980,1983)* and *Towne (1984)*) comparisons with experimental results. The dependence of the numerical solutions on the particular turbulence model was relatively small for all regions except next to the wall because the duct flows are predominately pressure controlled with turbulence contributed only to the local mixing characteristics, which allowed simple mixing length models to be used, as by *Levy* and *Towne*, with success.

All investigations of single S-ducts and diffusers show that the exit flow depends on the particular geometry and inlet conditions which have usually been assumed symmetric. The symmetric condition is of limited use in the understanding of practical intake ducts because the inlet to the first S-duct would usually be asymmetric as a result of varying angles of attack and fuselage boundary layers and the upstream S-duct will produce asymmetric inlet conditions into the second S-bend diffuser. The effects of the distorted inlet conditions in the ducts, such as those discussed by *Yu (1989)*, have relative minor consequences for the flow at the exit from an out-of-plane double S-bend, compared to those from the secondary flows of the first S-bend as quantified by the results of chapter 3.

1.3 Review of Gun Simulator Research

This portion of the chapter provides a review of the literature available on the theoretical and experimental investigations of gun simulators to which the discussions of the experimental results in the low-speed and high-speed simulators, chapter 4 and 5, will be related.

A general review of the progress of internal ballistics since the turn of the century and a thorough biography of available publications can be found in the collection of articles, edited by *Krier and Summerfield (1979).* The present review will be concerned primarily with the theory of flow in modeled guns, *Seigel (1965,1979), Gough (1979), Krier & Adams (1979)* and *Klingenberg et al (1985)* and previous experimental investigations in gun simulators, *Bicen et al (1986a,b,c) and Khezzar (1987).*

As mentioned briefly in section, 1.1, the analysis of the complex flow in real guns involves the modeling of the cycle through the use of simplifying assumptions such as those of the preburned propellant ideal-gas or Lagrange gun. The classical problem, studied by *Lagrange (1832),* occurs when a projectile, initially at rest, is propelled by a preburned propellant in a constant-diameter initial chamber. If the expansion of the gas is considered to be one-dimensional, frictionless, adiabatic and the density of the gas assumed to be spatially constant throughout the cycle but changing with time, the velocity of the gas at any instant increases linearly with distance along the bore from zero at the breech to the projectile velocity at its base. The Riemann theory of characteristic waves has been employed by many models and *Seigel (1965)* applied the method of characteristics to the Lagrange problem numerically. The constant-diameter PPIG gun is the simplest model, *Seigel (1965,1979),* because the expansion is assumed to be one-dimensional, adiabatic and reversible (isentropic) and the gas to be ideal. This approach does not account for the effects of friction and the viscosity of the fluid and, therefore is not adequate for practical calculations of heat transfer to the walls of the barrel.

The equations describing the adiabatic, one-dimensional expansion show that the characteristic disturbances waves, caused by the movement of the projectile, are

transmitted to the breech and eventually reflected back towards the projectile base. When the projectile motion begins, a rarefaction disturbance is sent back at the speed of sound into the gas behind it. If the reflection of the first characteristic wave on the breech does not reach the projectile as it accelerates down the barrel, the ballistic cycle is said to be in the simple-wave region. In practice, only guns with long initial chamber lengths or large initial pressures and small projectile mass produce simple-wave cycles because the projectile base pressure is unaffected by the presence of the breech and the reflected characteristic waves. In the present case, an effectively infinite chamber length can be assumed and permits a relatively simple solution to the interior ballistic problem. In most constant-diameter arrangements, the chambers is not infinite and disturbances originating at the projectile reflect from the breech of the chamber and subsequently reach the projectile. Before these disturbances reach the projectile, the motion of the entire gas is described by the simple-wave equations. After the characteristic reflections off the breech reach the projectile, the expansion is no longer a simple-wave expansion since the characteristic waves reduce the effective projectile base pressure and affect the subsequent projectile dynamics.

The difficulties caused by a finite chamber length are compounded by a chamfered initial volume geometry which is common in guns. In the development of the modern gun, the comparison between chamfered initial geometries and the constant-diameter initial chamber of the same volume has demonstrated that an increase in the projectile base pressure, and hence the projectile velocity, occurs with chamfered initial geometries. The higher velocities were attributed to the two-dimensional unsteady flow in the transitional section between the chamber diameter and the barrel diameter. In the simplest constant-diameter case, the chamber length would be infinite and *Seigel (1965)* showed that, by assuming an infinite chamber diameter, an increase in the projectile velocity can occur up to half the speed of sound, due to the chamberage relative to a constant-diameter geometry. Large chamberage diameters with a practical gun geometry are uncommon and only relatively small increases in projectile velocity with a chamfered initial volume have been recorded.

During the 1970's, there were two main numerical methods used to calculate the behavior of the projectile. The first was the method of characteristics and this was applied to the PPIG guns of various chamberage ratios, finite initial chamber lengths and

loading by *Seigel (1965)*. The second method was a Lagrangian scheme in which the gas was broken into small layers to each of which was applied Newton's law. The movement of the sides of each layer determined the new volume for each layer and therefore the new pressure for each layer at each stage of the cycle for the newly calculated pressures. Before the advent of digital computers, the solution of models for ballistic cycle were limited to the single-phase, one dimensional inviscid Lagrange problem. The Lagrangian approach, by far the simpler of the two methods, once modified to take into account shocks, has been utilized with success at many of the national laboratories, notably Lawrence Livermore, Sandia and Los Alamos, to calculate PP gun performance.

In the numerical analysis of PPIG guns, the simplifying assumption require discussion. Many calculation methods ignore the influence of gas in the barrel in front of the projectile, between the projectile and the muzzle, and this assumption is justifiable only when the projectile is fired into a vacuum. *Seigel (1961,1965,1979)* has provided an approximate general equation for the reduction in projectile velocity due to the counter-pressure exerted by the column of gas in front of the projectile. As mentioned before, the applicability of the isentropic theory to guns requires neglect of the effects of friction and heat transfer and this can only be justified if the process is infinitesimally slow and the gradients are infinitesimally small. The expansion process in a gun barrel is very rapid and large temperature, velocity and pressure gradients exist. The extent to which the rapid expansion is non-isentropic has been investigated at many laboratories, General Motors, NASA Ames Research Center, Ballistic Research (BRL), Naval Research (NRL) and Naval Ordnance Laboratories (NOL) by using heated propellants and all the data indicates that the isentropic theory gives good agreement, with in 2 %, with experimental results at velocities less than 4000 m/s.

An analytical analysis of the modeled interior ballistic cycle shows that there are at least two reasons for the deviations from isentropic theory; neglect of friction and heat transfer. The projectile-barrel friction as the projectile moves toward the muzzle, even in the smooth-bore gun simulators, can never be eliminated from the gun cycle and constitutes a small loss of energy from the cycle. As the inert gas of a simulator expands behind the projectile, the free-stream temperature drops and a thermal boundary layer develops on the barrel wall with heat flux from the wall into the fluid. In the simulator,

the heat flux to the flow from the barrel increases the energy of the cycle slightly but this has not been quantified. The heat transfer to the expanding gas tends to counteract the losses due to the boundary layer and the friction between the projectile and the barrel. Previous experiments in well-machined precision simulators, summarized by *Seigel (1979)*, demonstrated an approximately 2 % velocity difference between isentropic theory and experiments, of which about 1 % was attributed to the projectile-barrel friction and the other 1 % to the boundary layer, but it is unclear if heat flux to the gas was considered.

Extensive numerical efforts have been undertaken by a host of authors; *Gibeling et al (1980,1983), Celmins & Schmitt (1984a,b), Gibeling & McDonald (1984), Schmitt (1985), Gütlin et al (1987), Heiser (1987,1988), Garloff & Heiser (1988), Heiser & Hensel (1988)*, to apply finite-difference solutions of forms of the Navier Stokes equations for turbulent multiphase combusting flows. The computational efforts have produced promising results but the difficulties with the ignition of the combustion and the need for sufficient experimental results for comparison, particularly with the multiphase models, are demonstrated.

Preburned propellant ideal-gas gun simulators, frequently referred to in some literature as a Lagrange gun, have been built to model the real gun with an inert or simple combustion unsteady flow. The nature of the Lagrange gun is similar to that of a shock tube, which has been investigated by *Seiler (1983)* and *Modarress (1986)* in square and circular cross-sections. Seiler investigated the effect of the chamberage and the projectile base, boat-tails, on the turbulence and boundary layer thickness in a square cross-sections shock-tube. Modarress studied the boundary layer induced by a shock over a dust bed in both square and circular shock tubes and found that the boundary layer height, defined by the presence of dust particles, was larger than that defined by the gradient of the streamwise velocity.

Experimental gun systems have provided a variety of measurements with which the numerical efforts can be compared. Velocity and temperature measurements were made in multi-stage (multiple initial chambers) light (low atomic weight) gas guns by *Mach & Hensel (1986)*. In single-stage real gun experiments, extensive measurements of the initial chamber and barrel temperatures with resulting heat transfer have been

conducted by *Klingenberg (1985a,b)* and recent efforts to reduce the heat flux to the barrel with additives to the propellant have been evaluated by *Lawton (1988)*. In real gun conditions, *Klingenberg and Mach (1978)* have measured the radial temperature profiles and axial variation of the gas velocity and found that the particle and gas velocities did not vary linearly between the breech and the projectile base. This contrasts with the assumption of a one-dimensional expansion and was attributed to the velocity lag between gas and particle flow. The experiments in real guns have shown that the characteristics of the propellant play an important role in the interior ballistic cycle and this has subsequently led to research into propellants and two-phase flow interactions. The difficulties associated with measuring in the harsh combusting environment with in a real gun barrel and the limitations of the experimental techniques are the main reasons for the experimental investigation of preburned propellant ideal-gas gun simulators.

Seigel (1952) quantified the expansion of compressed gases behind a piston in an 'ERMA' (expansion rate measuring apparatus) which measured the velocity and position of the projectile/piston as it was driven by the expanding gas. Experiments in simulators based on the PPIG or Lagrangian gun, similar to that studied by Seigel, were begun at Imperial College in 1985 by *Bicen, Kliafas & Whitelaw (1986b)*. The first simulator utilized a gear and rack mechanism to determine the expansion of the gas and the velocity of the piston/projectile while the pressure and gas velocities were measured with a transducer and a dual-beam laser Doppler anemometry. The boundary layers formed in the wake of the piston/projectile were found to be thin, of the order of less than 1 % of the 76.5 mm barrel diameter and the rack mechanism was shown to cause cycle-to-cycle variations. The test rig was limited to velocities less than 20 m/s, but provided experience in the design, construction and operation of gun simulators. This experience led to solutions to the limiting difficulties of the mechanical design and to improvement of the measuring instrumentation.

The second generation gun simulator at Imperial College, sometimes referred to as the Mark II or subsonic gun simulator, is described by *Khezzar (1987)* and *Bicen et al (1986a,c)* and benefitted from experience of the first rig. It was operated with both a constant-diameter, 76.5 mm diameter, and a chambered initial volume charged up to a maximum initial pressure of 8 bar gauge, and had a muzzle velocity of approximately 40

m/s. Projectile velocity and breech pressure were recorded with a pulse timer and a pressure transducer interfaced with an analog-to-digital converter to a microcomputer with both initial geometries. The single- and two-phase velocities were measured with a dual-beam laser Doppler anemometer and stored in a buffer memory of the data acquisition microcomputer for statistical processing. The measured projectile dynamics were compared to those determined by a one-dimensional, unsteady form of the continuity and Euler equations, where the muzzle velocity was 0.7 % larger, confirming that the friction force between the projectile and the wall of the barrel as well as the other losses in heat transfer are negligible at this range of projectile velocities. The boundary layer thickness was shown to be turbulent and to occupy less than 20 % of the internal radius behind the projectile and less than 1 % in the constant-diameter initial chamber. The effect of the initial geometry on the flow was found to be insignificant for the range of velocities considered. The velocity of a second-phase injected into the cycle with an initial concentration of 1.3 % by volume in the chamfered initial geometry was measured. The particle phase velocity was shown to lag behind the gas-phase, measured in the absence of particles, in regions close to the projectile and lead by as much as 20 % of the velocity as the projectile exits the test section.

The gun simulator used by *Khezzar (1987)* and *Bicen et al (1986a,c)*, yielded understanding of the low-speed simulator cycle and suggest that more work should be done to provide detailed measurements in the transient turbulent boundary layers and two-phase flow of a larger concentration, in addition to the evaluation of heat flux during the simulated cycle. The limitations of the low-speed simulator and its instrumentation, projectile velocities less than 40 m/s, necessitated the development of a new simulator which would approach real gun velocities and this required the development of high-speed transient pressure, velocity and heat flux measuring techniques.

1.4 Present Contribution

The contributions of the present work on flows in curved ducts and gun simulators presented can be divided into four main parts which are discussed in the following four chapters. In chapter 3, measurement of the velocity and static pressure characteristics in a complex out-of-plane double S-bend are reported and demonstrate the importance of the inlet conditions and of the interaction of the cross-flows in sufficient detail to assist the development of numerical methods. In the low-speed simulator of chapter 4, the detailed analysis of the single-phase boundary layer, two-phase flow and heat transfer characteristics are presented and are shown to contribute to the understanding of the complex simulation of the interior ballistics cycle. The high-speed simulator of chapter 5 was designed, built and tested to provide projectile and gas velocities similar to those of practical gun systems and characterized the gas-phase velocity and surface heat transfer. Chapter 2 describes the experimental techniques used to obtain the results. Those used in the high speed simulator are new and this development and evaluation represents an important contribution of this thesis.

1.5 Thesis Outline

The thesis is separated into five chapters as described below.

The following chapter discusses the experimental techniques in the steady curved duct experiments and in the unsteady low- and high-speed gun simulators. The new instrumentation and signal processing methods are described in detail and uncertainties associated with the duct static pressure measurement, laser Doppler anemometry in all test rigs and transient pressure and heat flux measurement in the gun simulators are examined and quantified.

Chapter 3 presents and discusses the measurements in out-of-plane double S-bend ducts flows with laminar flow, in a rectangular cross-section, and turbulent flow in a rectangular and circular cross-section. The results are compared to those from a single S-bend and conclusions on the effects of the inlet conditions into the second S-bend on

the streamwise and secondary flow for both cases are demonstrated.

Chapter 4 focuses on the measurements in the unsteady low-speed gun simulator. Detailed descriptions of the single-phase boundary layer and general two-phase flow characteristics with two initial concentrations are provided in addition to the breech pressure and heat flux measurements at several axial measuring positions.

Chapter 5 presents and discusses the experimental results from the unsteady high-speed gun simulator and how they compare to a simple one-dimensional model. The breech pressure record and description of the projectile dynamics at a spectrum of initial conditions are detailed and the analysis of the momentum boundary layer and heat transfer during the cycle at several axial measuring positions are presented.

The final chapter, chapter 6, concludes the thesis by restating the conclusions and contribution of the research and by recommending future work.

CHAPTER 2 EXPERIMENTAL TECHNIQUES

2.1 Introduction

This chapter describes the experimental equipment and associated techniques employed in the analysis of flow in curved ducts and gun simulators. The first section discusses the static pressure-measurement and laser Doppler anemometry techniques employed in the steady curved duct experiments and the following sections address the experimental equipment and techniques utilized in the unsteady low- and high-speed gun simulators. The description of the techniques used with the gun simulator has been subdivided to consider separately transient pressure, laser Doppler anemometry and thin-film heat flux measurement methods. Laser-Doppler anemometry was used in all three flows, but in different forms. Thus, the essential principles are stated in section 2.2 and the particulars of each arrangement described in the three subsections.

2.2 Steady Curved Duct Experiments

2.2.1 Pressure Measurements

Wall static pressure measurements were obtained in the duct experiments to provide quantitative understanding of the magnitude and manner in which kinetic energy was converted to pressure energy as previously reported by *Taylor et al (1980, 1981a,b, 1982, 1984), Rojas et al (1983a,b,c, 1984)* and *Schmidt et al (1986).* The static pressure coefficient (C_{p^*}), defined in Equation 2.1, was measured along all duct configurations in the turbulent flow cases. No static pressure measurements were made in the laminar flow cases since the instrumentation could not provide results of useful accuracy with the small pressure differences.

$$C_{p^*} = \frac{p - p_{ref}}{\frac{1}{2}\rho_f V_B^2} \qquad 2.1$$

The static pressure measurement along the duct were facilitated by 0.5 mm diameter

sharp-edged holes opening normal to the wall and flush to the smooth inner surface. The pressure tap holes were machined on three of the four sides of the double S-bend ducts and diffusers. One of the duct and diffuser surfaces did not contain pressure taps because of the plane of symmetry in the single S-bends. The pressure taps were situated along the centreline of each surface (r*=1.0, z*=-1.0, z*=1.0, r*=0.0) with approximately 1.1 hydraulic diameter spacing in the axial (X) direction. The radial static pressure distribution was not measured due to the limited number of pressure taps in the radial direction in each duct. The duct surfaces were carefully polished to remove any burrs at the inner surface resulting from the machining and frequent cleaning of the holes was performed to reduce errors associated with the measuring technique. The influence of the hole length, approximately 3 mm, the internal counter-bore diameter of the tap connector, 1 mm, and the hole diameter on the static pressure measurements, as discussed by *Shaw (1960)*, was less than 0.5% of the velocity head.

The static pressure measurements were obtained with a differential micro-manometer containing a dense fluid, Fluro-Carbon (1888 kg/m^3), immiscible with water. The two sides of the manometer were connected via a small transparent plastic tube (1.5 mm inner diameter and ≈ 0.5 m long) to the pressure reference position, one diameter upstream (X= -1, r* = 0.5, z* = -1.0) of the duct inlet, and to the measuring position pressure tap. Special care was taken to remove air bubbles, which could have caused erroneous pressure results. The systematic and random uncertainty in the manometer fluid height were about 0.5 mm and ±0.5 mm which corresponded to 0.75 % and 1.5 % uncertainty in C_{p^*} respectively.

2.2.2 Laser Doppler Anemometer

Laser Doppler anemometry was used for velocity measurements in the duct experiments because it allowed the precise non-intrusive determination of mean and turbulence quantities required to enhance understanding of the influence of the upstream S-bends on the subsequent developing flow in the diffuser. Many references describe the laser Doppler technique in detail, including *Durst et al (1981), Goldstein and Adrian (1971)* and technical publications by manufactures such as TSI and DISA, so that only a brief account of the single-component dual beam technique will be presented here.

The concept of the laser Doppler anemometry is derived from the Doppler scattering of coherent laser light by particles in motion in the flow. In the case of dual beam anemometry, the intersection of two laser beams, of equal intensity at their focussed waists, forms an ellipsoidal volume consisting of light and dark fringes due to the constructive and destructive interference of the coherent laser light. As depicted in Figure 2.1, the direction in which the flow can be measured is perpendicular to the mean angle of the beams, the major axis of the measuring volume.

Laser Doppler anemometry requires particles, such as those produced by small amounts of milk in water and silicon oil droplets in air, in order to measure the velocity characteristics of a flow field. A small particle crossing the measuring volume, as indicated in Figure 2.1, will scatter the fringe illumination, primarily in the forward direction. The scattered light from a single particle passing through the measuring volume is called a Doppler burst of which Figure 2.2 is typical. The mass and size of the particle determine the extent to which it can follow velocity fluctuations so that solid particles of the order of 5 μm in diameter were adequate for the relatively low velocity steady water duct flows where the turbulence does not exist beyond around 900 Hz. The particles naturally occurring in the water flow were able to capture the flow characteristics, because of the small difference in their density from that of water, and the comparatively low turbulence frequencies.

The optical configuration employed in the velocity measurements is shown in Figure 2.3. A laser beam was focused onto a radial diffraction grating housed in the main optical unit to split the source beam into two equal intensity beams. Where necessary, the diffraction grating was rotated at a constant angular velocity to provide frequency shift up to 5.5 MHz, positive or negative, enabling directional discrimination and ensuring that the Doppler signal was in the optimum frequency range of the tracker signal processing instrumentation.

The light scattered along the forward axis by a particle crossing the measuring volume, Figure 2.1, was collected and focussed by the collecting lens on the pinhole aperture of a photomultiplier tube as illustrated in Figure 2.3. Due to the refraction and reflection of the laser beams at the inner and outer duct surfaces as they traverse the test

section, the collecting lens was masked to eliminate spurious illumination. Signal noise is inherent in the photodetection process and was abated by maintaining optically clean flat surfaces with corresponding reductions in reflection, flare at interfaces and image distortion. A fast (50 ns total time response) 52 mm diameter 12 stage photomultiplier (Thorn EMI model 9817B) was used to provide a gain of about 3×10^6 to the collected Doppler signal.

The frequency of a Doppler signal produced by a particle passing through the measuring volume depends on the characteristics of the optical arrangement, with correction for a frequency shift, if employed. The half-angle of the beam intersection (φ) was measured each time the optical components were moved or adjusted because of the misalignment of the geometric and optical centers relative to the collimated beams. The fringe spacing (δ_f) can be derived from Equation 2.2.

$$\delta_f = \lambda / 2 \sin \varphi \qquad 2.2$$

The distance between fringes facilitates the conversion of the Doppler frequency directly to fluid velocity, ie. $\delta_f = 1.95$ μm means that a frequency of 1 MHz corresponds to a velocity of 1.95 m/s with no frequency shift.

The dimensions of the measuring volume, Figure 2.1, (waist, height, and length) to the e^{-2} intensity points can be calculated if all the lens focal lengths and source laser beam characteristics for the optical arrangement are known. The waist diameter of the focussed beams ($d_{e^{-2}}$) can be obtained from Equation 2.3 assuming a Gaussian beam distribution and the height (D_m) and length (L_m) of the elliptical measuring volume, at the e^{-2} intensity points, evaluated by Equations 2.4 and 2.5. The dimensions of the measuring volume depend upon the index of refraction (η) of the fluid medium and Equation 2.5, represents this for the duct flow where the fluid medium was water.

$$d_{e^{-2}} = \frac{4 \lambda L_3 L_1}{\pi L_2 D_{e^{-2}}} \qquad 2.3$$

$$D_m = \frac{d_{e^{-2}}}{\cos \varphi} \qquad 2.4$$

$$L_m = \frac{\eta\, d_e^{-2}}{\sin \varphi} \qquad 2.5$$

The probe volume (V_m) and the number of fringes (N_m) across the minor axis, (D_m) can be evaluated from Equations 2.6 and 2.7, respectively.

$$V_m = \frac{\pi}{6} D_m L_m d_e^{-2} \qquad 2.6$$

$$N_m = \frac{D_m}{\delta_f} \qquad 2.7$$

A helium-neon laser, with a wavelength (λ) of 632.8 nm, and a nominal power of 5 mW was used to provide the incident light. The optical characteristics are summarized in Table 2.1.

Table 2.1 Characteristics of duct optical arrangement.

Laser power output (P)	5 mW
Laser e^{-2} intensity diameter (D_e^{-2})	0.65 mm
Focal length of focusing lens (L_1)	200 mm
Focal length of collimating lens (L_2)	300 mm
Focal length of imaging lens (L_3)	200 mm
Index of refraction of fluid medium (η)	1.33
Measured half angle of beams (φ)	9.35° †
Fringe spacing (δ_f)	1.95 μm †
Focussed e^{-2} intensity diameter (d_e^{-2})	0.165 mm †
Measuring volume diameter in fluid (D_m)	0.167 mm †
Measuring volume length in fluid (L_m)	1.351 mm †
Volume of the measuring volume (V_m)	0.0195 mm^3 †
Number of fringes in measuring volume (N_m)	86 †

† Not appropriate for cross-stream V and W velocity measurements in circular duct case.

All surfaces through which the light beams passed, except in the circular duct case, were constructed of flat polished plexiglass. With the circular cross-section, the curved inner interface between the water and perspex duct make measurements more

difficult and ray tracing techniques were necessary to resolve the position and dimensions of the probe volume, as described for examples by *Bicen (1981), Rojas et al (1983c)* and *Taylor et al (1984).*

The resolution of the velocity components in three orthogonal directions involved the rotation of the single-component optical head and consequential equations. The streamwise (U, $\tilde{u}$) and the cross stream (V, W, $\tilde{v}$, $\tilde{w}$,) mean, rms velocities and cross-correlations ($\widetilde{uv}$, $\widetilde{uw}$) were resolved in the duct flows from measurements at 0.0°, +45° and -45° angles to the streamwise direction in the U & V or U & W planes. Equations 2.8 to 2.12, modified from *Melling & Whitelaw (1976)*, were used for this purpose.

$$U = U_{0^\circ} = \frac{U_{-45^\circ} + U_{+45^\circ}}{\sqrt{2}} \qquad 2.8$$

$$V = \frac{U_{-45^\circ} - U_{+45^\circ}}{\sqrt{2}} \qquad 2.9$$

$$\tilde{u} = \sqrt{\overline{\tilde{u}_{0^\circ}^{\,2}}} \qquad 2.10$$

$$\tilde{v} = \sqrt{\overline{\tilde{u}_{+45^\circ}^{\,2}} + \overline{\tilde{u}_{-45^\circ}^{\,2}} - \overline{\tilde{u}_{0^\circ}^{\,2}}} \qquad 2.11$$

$$\widetilde{uv} = \frac{\overline{\tilde{u}_{+45^\circ}^{\,2}} - \overline{\tilde{u}_{-45^\circ}^{\,2}}}{2} \qquad 2.12$$

The equations for the second cross-stream component result from substitution of W and $\tilde{w}$ for V and $\tilde{v}$ in equations 2.9, 2.11 and 2.12.

A frequency tracker (Cambridge Consultants Model CC01) was used in the duct experiments to convert the Doppler frequency into a voltage which, in turn, was linearly related to velocity. *Durst et al (1981), Drain (1980)* and others discuss the characteristics and limitations of tracker systems which consists of a voltage oscillator controlled by a feedback loop, filter and discriminator. The oscillator is tuned to the input Doppler frequency by the direct frequency discriminator. The tracker based signal processing system requires careful operation with special consideration of signal drop-out, dynamic response limitation, transient broadening, tracking range and noise.

The term drop-out refers to the time when the tracker was not locked on the frequency of a Doppler signal and during these periods, it maintained the frequency of the previous signal. When long drop-out times occurred, signal noise could be tracked if there were low particle concentrations and/or a substantial difference between the Doppler frequencies of two successive particles. The natural high particle concentration in water caused drop-out times, of less than 0.5 ms, which did not have an effect on the measurements. The dynamic response, the ability of the tracker to deal with a range of Doppler frequencies, was limited by the intermediate frequency filter and integrator loop of the tracker which followed the maximum frequency present in the water flow with out difficulty and similarly able to follow amplitude changes associated with the maximum intensity levels of 15 %. Transient-time broadening could arise due to the finite duration of the Doppler signal as a particle crosses the measuring volume and occurs with all frequency-domain instruments. The magnitude of the relative uncertainty is related to the number of fringes, *George & Lumley (1973)*, so that an error of just over 1 % could occur with 86 fringes but with frequency shift became negligible. The transient time was approximately 0.17 ms and did not effect the measurements because of the relatively low turbulence intensity and use of shift. The tracking range sets the limits of the smallest and largest velocity variations which can be tracked. If the instantaneous frequency was outside the frequency range, the probability density function of the Doppler signal will be skewed usually toward the lower end of the frequency range, *Durst et al (1981).* The tracker was always operated in the 0.1 - 1.0 MHz range which contained the entire signal spectrum between 0.25 - 0.75 MHz, corresponding to a 15 % maximum turbulence intensity, with the assistance of the frequency shift. The Doppler signals were subject to noise associated with imperfect optical components, signals observed from outside the measuring volume, the photomultiplier and electrical components. The noise signals were rejected by the tracking filter provided care was taken to locate the Doppler signal, with the help of the imposed frequency shift, in the upper part (>0.3 of full scale) of the frequency range band where the noise generated by the tracker itself was small.

By increasing the particle seeding with the addition of a small amount of milk, using frequency shift to ensure the optimum tracker range containing the entire Doppler signal spectrum, lowering the threshold amplitude level to validate an input signal and

the reduction of signal noise, the limitations and uncertainties associated with the use of the frequency tracker were eliminated and qualified respectively. The tracker based signal processing system was used in the steady duct water flows to measure the mean and rms of fluctuations of the Doppler frequency to accuracy less than 1 % of the full scale deflection (systematic error), as quoted by the instrument manufacture.

The analog output of the frequency tracker signal processor provided a voltage proportional to the Doppler frequency, and this was digitized by a 12 bit analog-to-digital converter which was sampled by an Apple II microcomputer at a rate of 4 KHz in the turbulent flow duct tests and at 1 KHz in the laminar duct measurements. Each point measurement was made up of signals from at least 6000 particles and was repeated three times to ensure reliability and increased accuracy. Many measurements were repeated in the regions of large velocity gradients near the walls and variations of less than 1 % of the bulk velocity were recorded.

The laser Doppler anemometry technique involved two main sources of possible uncertainty due to positional ambiguities and Doppler broadening.

The positional ambiguities occurred in the measurement of the beam angle, which affected the fringe spacing and frequency to velocity conversion, and in the positioning of the measuring volume inside the test section. The radial and spanwise resolution of approximately ±0.2 mm represents an uncertainty of less than 1.0% of the hydraulic diameter of the duct. The uncertainty in the measured beam angle gives rise to an uncertainty of the fringe spacing (δf) and therefore in velocity of less than ±0.25 % in all directions. The bulk flow was provided by a valve controlled constant-head tank system and measured by calibrated precision-bore flow-meters with in an accuracy of ± 1 %.

Velocity gradient broadening occurs when the measuring volume of finite size is positioned in a region of mean velocity gradients. The time averaged measured velocity can be affected if the gradient is ignored on either side of the centre of the volume. It is common to minimize velocity broadening by orientating the elliptical measuring volume with the smallest dimension in the direction of the highest velocity gradients. The subject of gradient broadening has been discussed extensively, as for example by *Durst*

et al (1981), Adrian (1983), Drain (1980) and *Melling (1975).* The consequences of a velocity gradient across the measuring volume affects the probability density function so that if the velocity gradient is linear or zero, the mean average is unaffected and the mean square deviation of the fluctuations in the fluid velocity is proportional to the magnitude of the velocity gradient. If the velocity gradient varies non-linearly across the measuring volume, as is usually the case, the probability density function will be skewed and the mean velocity will also be incorrectly measured. The magnitude of the gradient broadening was evaluated for measurements where velocity gradients were large, like those in the wall boundary layers.

Correction of the mean and rms velocity quantities for the effect of gradient broadening, *Melling (1975)*, requires approximation of the higher partial derivatives. The correction formula for point measurements are:

$$\langle U \rangle - U \approx \frac{l_m^{\,2}}{2}\left(\frac{\partial^2 U}{\partial y^2}\right) + \frac{l_m^{\,4}}{8}\left(\frac{\partial^4 U}{\partial y^4}\right) + \ldots \qquad 2.13$$

$$\left\langle [U - \langle U \rangle]^2 \right\rangle \approx l_m^{\,2}\left(\frac{\partial U}{\partial y}\right)^2 + \frac{l_m^{\,4}}{2}\left(\frac{\partial^2 U}{\partial y^2}\right)^2 + \ldots \qquad 2.14$$

where Equation 2.13 quantifies the displacement of mean velocity and Equation 2.14 evaluates the approximate variance associated with velocity gradient broadening. The magnitude of the effect was dependent on the second-order derivative in the case of mean velocity, and first- and second-order derivatives in the evaluation of the rms quantities. The first and second partial derivatives of the velocity relative to the direction (y) of the measuring volume dimension, l_m, can be approximated by second-order polynomials with three or more points. The gradient broadening correction was dependent upon the number of local points used in the curve fitting process which therefore makes it sensitive to the small experimental uncertainties. The maximum effects determined in this way corresponded to an uncertainty of less than 1 % of the mean and 3 % of the rms and only occurred close to the duct wall. No correction of the presented results for gradient broadening in the duct measurements were made because of the relatively low magnitude.

A summary of the overall estimated systematic and random uncertainties in the S-duct are presented in Table 2.2. By adding the square root of the sum of the squares of the uncertainties, an overall random uncertainty for the mean and fluctuating velocities can be derived.

Table 2.2 Summary of estimated S-Duct measurement uncertainty.

	Systematic Uncertainty	Random Uncertainty
Streamwise distance along axis (X)	0.25 mm	±0.02 mm
Radial, and spanwise distances (r*, z*, y*)	0.2 mm	±0.02 mm
Diffusing bend turning angle , duct flow (θ)	1.5°	±0.4°
Measured half angle of beams (φ)	0.03°	nil
Fringe spacing (δ_f)	0.015 μm	nil
Bulk velocity (V_B) (laminar)	1.0 %	±1.0 %
Bulk velocity (V_B) (turbulent)	nil	±0.75 %
Mean velocity in X direction (U)	nil	2.0 %
Mean velocity in z* direction (V)	nil	3.0 %
Mean velocity in r* direction (W)	nil	3.0 %
Rms fluctuations of velocity in X ($\widetilde{u}$)	nil	up to 4.5 %
Rms fluctuations of velocity in z* ($\widetilde{v}$)	nil	up to 6.0 %
Rms fluctuations of velocity in r* ($\widetilde{w}$)	nil	up to 6.0 %
Cross correlations ($\widetilde{uv}$, $\widetilde{uw}$)	nil	up to 8.5 %
Frequency shift	less than 0.01 V_B	±0.005
Static pressure (C_{p*})	0.0004	±0.003

The total uncertainty for all the mean duct velocity measurements was approximately 2 % of the bulk velocity in the streamwise and 3 % in the cross-stream directions and 4.5 % and 6 % for velocity fluctuations respectively. The frequency tracker was however limited to steady, well seeded flows with turbulence intensities below 20 %, and Doppler frequencies below 10 MHz. The steady water duct tests were perfectly suited to the tracker based signal processing technique since speed was not vital, with Doppler frequencies of the order of 0.5 MHz and intensities less than 15 %.

2.3 Unsteady Low-Speed Gun Simulator Experiments

2.3.1 Transient Pressure Measurements

The transient gas pressure in the low-speed gun simulator was measured with a piezoelectric pressure transducer which was mounted flush to the inner wall of the breech. The transducer had no effect on the flow or heat transfer during a cycle and responded to the local pressure changes which occurred at the breech. The miniature quartz pressure transducer (KISTLER type 6121) was connected to a charge amplifier (KISTLER type 5007) and enabled the transient pressure to be measured by a custom built analog-to-digital converter interfaced with an ITT 2020 microcomputer. The charge amplifier was set with a long time constant ($>10^3$ seconds) to allow the absolute pressure during the charging of the initial volume to be monitored prior to the release of the projectile and a transient record subsequent to the start of the measuring sequence.

A diagram of the low-speed gun simulator instrumentation, Figure 2.4, shows the pressure transducer and charge amplifier connected to the initial volume. The initiation of the measuring sequence was facilitated by a laser beam focussed through the test section, near the projectile front-end in the initial position, onto a photo-diode which was connected to a timer module interfaced with the ITT 2020 microcomputer (the original Apple II model) running a 6502 machine language code. The initial movement of the projectile disrupts the laser beam to the diode which in turn triggers the main computer program to initiate sampling of the pressure information. The time between the start of the cycle and the triggering of the instrumentation was around 2 mm of projectile travel (0.2% of total travel length) and has not been compensated for in the presented results since it is less than 1 % of the total cycle time. This laser-diode-timer arrangement allowed time encoding of the recorded breech pressure cycle, as well as the velocity and surface temperature data.

The frequency response of the quartz pressure transducer was quoted by the manufacture as 6 kHz with a transient drift of less than 0.02 bar. The charge amplifier has a frequency range up to 180 kHz, a time constant of 10^3 - 10^5 seconds and a drift of approximately ± 0.05 bar over a typical test. In order to reduce as much as possible the

transient drift error associated with the pressure transducer and the charge amplifier, the amplifier was reset immediately before each test cycle and the offset pressure charge, before and after a test cycle, was averaged. The consequence of the response and drift characteristics of the pressure signal processing system was an uncertainty of less than 1 % of the initial pressure.

The analog output (0 - 10 volts) of the charge amplifier, proportional to the pressure, was digitized by a custom built analog-to-digital converter, interface directly with the memory of an ITT 2020 microcomputer controlled by a 6502 machine language code. In the low-speed gun simulator, a sample rate of approximately 30 kHz with a 12 bit analog-to-digital conversion was sufficient to characterize the breech pressure change over the cycle duration which was typically 34 ms.

2.3.2 Laser Doppler Anemometer

The laser Doppler anemometer is shown in Figure 2.4, and was used to obtain measurement of single- and two-phase velocity in the low-speed gun simulator. The characteristics of the optical arrangement, the frequency counter based signal processing system and the inherent uncertainties resulting from the bias and gradient broadening, similar to those addressed in the S-duct laser Doppler anemometer section 2.2.2, are discussed and evaluated. In addition to the previous Doppler anemometer description, the uncertainty due to non-turbulent broadening from the transient velocity gradient and the ensemble statistical technique employed in deriving the transient velocity characteristics of the unsteady flow are determined.

The axial component of velocity was measured by positioning the incident light beams in the plane and perpendicular to the axis of the barrel. Seeding for the single phase measurements was provided by a custom built air blast atomizer designed and built for pressures up to 3 bar gauge and using silicone oil. This resulted in droplets of 1 μm nominal diameter, as implied by the visibility and modulation of the Doppler signal, which will capture the transient flow characteristics of the low-speed simulator as indicated by the analyses of *Durst et al (1981)* and *Clift et al (1973)*. Seeding for the second phase flow was provided by 500 μm median diameter plexiglass or perspex (Diakon™) beads. The Doppler signals scattered from the second phase particles were

distinct from those of the smaller single phase particles because of the much greater amplitude and signal pedestal levels. The signals from the second phase particles could be isolated from those of the single phase by decreasing the collecting lens mask aperture, decreasing the photomultiplier voltage and/or increasing the amplitude validation levels on the signal processor.

As with the duct anemometer, the velocimeter was operated with forward scattered light and employed a fast (50 ns total time response) 52 mm diameter 12 stage photomultiplier (Thorn EMI model 9817B) which provided a gain of about 3×10^6 to the collected Doppler signal.

The optical arrangement in the low-speed gun simulator was very different from that employed in the duct measurements. A larger 35 mW laser was used to to provide the incident light and a smaller focal length lens, 150 mm, to allow the beams to enter the windows. The laser and focussing lens changes resulted in a greater fringe spacing, 3.0 μm, and a smaller number of fringes, 32, relative to the duct optical arrangement. Table 2.3 lists the characteristics of the optical arrangement.

Table 2.3 Characteristics of low-speed simulator optical arrangement.

Laser power output (P)	35 mW
Laser e^{-2} intensity diameter ($D_{e^{-2}}$)	1.25 mm
Focal length of focusing lens (L_1)	150 mm
Focal length of collimating lens (L_2)	300 mm
Focal length of imaging lens (L_3)	300 mm
Index of refraction of fluid medium (η)	1
Measured half angle of beams (φ)	6.05°
Fringe spacing (δ_f)	3.0 μm
Focussed e^{-2} intensity diameter ($d_{e^{-2}}$)	0.097 mm
Measuring volume diameter in fluid (D_m)	0.097 mm
Measuring volume length in fluid (L_m)	0.920 mm
Volume of the measuring volume (V_m)	0.0045 mm^3
Number of fringes in measuring volume (N_m)	32

The windows through which the illumination passed were made of flat polished

plexiglass machined to conform to the inside wall of the barrel except in the center where a small flat surface (9 mm wide) was milled to insure that the incoming laser beams and forward scatter optical path would not be affected by curvature. The length of the flat surface relative to the radius of curvature did not influence the momentum boundary layer formation and the influence on the thermal characteristics will be addressed in the pertinent heat flux result section. As in the duct, the outer and inner surfaces of the plexiglass windows were polished so as to minimize signal noise, which could be caused by scratches or dust in the optical paths.

The transient nature of the gun simulator flow made it necessary to process the Doppler signals with a frequency counter. *Durst et al (1981), Drain (1980)* and others discuss the characteristics and limitations of frequency counters which primarily consist of a high frequency clock and digital counting circuitry. A counter measures the frequency of a Doppler signal by counting the number of high frequency clock pulses for a specified number of cycles. The timing is performed with respect to the zero-crossings after a preset threshold has been surpassed. Each velocity measurement is interrogated to ensure that it exceeds a prescribed amplitude threshold for a sufficient number of cycles and further validation is achieved by a time comparison among the cycles in a Doppler burst. If the comparison times are within a preset tolerance level, the signal was accepted and the digital information, ie. frequency, was passed to the microcomputer where it is stored along with the necessary time information. The counter then waits for the next Doppler signal to reach the threshold level to begin counting and performing validation checks.

In the low-speed simulator, the frequency information of the Doppler signal was resolved with a custom built frequency counter, described by *Founti & Laker (1981)* (Model FS #1) and interfaced with an ITT 2020 microcomputer controlled by a machine code program. The signal from the photomultiplier was filtered to remove the low frequency component associated with particle arrival rate and the high frequency signal associated with noise, and the resulting signal amplified. Care was taken to ensure that the filter range accommodated the entire signal spectrum and thereby prevent biasing of the Doppler signal. A frequency shift of approximately -2.5 MHz was employed in the low-speed simulator to 'down shift' the Doppler frequencies away from the upper

frequency limit of the counter. The counter was limited to Doppler frequencies less than 15 MHz, with an accuracy of better than 0.5 % and an effective maximum sample rate of about 10 kHz. The counter interrogated the amplitude of each Doppler burst and compared the time for the first 8 and the first 16 cycles: the measured frequency was verified if the difference was less than 1 %. The real-time information for each frequency count, supplied by the trigger timer module, was accurate to within ± 2 μs.

The anemometer for the low-speed simulator gave rise to four main sources of uncertainty due to positional ambiguities and Doppler broadening, as in the duct, in addition to biasing and transient broadening effects associated with the ensemble averaging and statistical techniques.

As with the laser Doppler anemometer of section 2.2.2, uncertainties in position and the measured beam angle affected the accuracy of positioning inside the test section and the frequency to velocity conversion. The radial resolution of approximately ±0.2 mm represents an uncertainty of less than 1.0% of the radius of the barrel. The systematic error in the measured beam angle gives rise to an uncertainty of the fringe spacing (δf), and therefore in velocity, of less than ±0.33 %.

The effect of gradient broadening was evaluated using the method discussed in section 2.2.2. The partial derivatives in Equations 2.13 and 2.14 were approximated by second-order polynomials with three or more points and the influence of velocity gradient broadening was found to affect some results in the boundary layer. Corrections were therefore applied to measurements near the wall with maximum magnitudes of 4 % and 15 % for the mean and rms values respectively. No corrections were applied where the velocity gradient caused broadening of less than 1 % and 3 % in the mean and rms values respectively.

Biasing errors in a counter based signal processing system can occur as a result of the observation of more fast moving particles, from the integration characteristics of the photo-multiplier and from the filter characteristics of the high and low pass Doppler signal filters. *McLaughlin & Tiederman (1973)* discuss the velocity biasing at length and conclude that it was unimportant at turbulence intensities less than about 15 % which was the case in the low-speed gun simulator. Several references, *Durst et al (1981)* and

Durao & Whitelaw (1978), suggest that amplitude bias due to the photo-multiplier integration characteristics, can occur and counteracts the velocity bias but the present low intensities imply that the total bias of all the results present here would result in an uncertainty of less than 0.5 % of the mean velocity.

The unsteady nature of the flow in the gun simulator implies the need for the measurements of on-line velocity traces and ensemble averaging methods. The ensemble averaging technique makes it possible to describe the transient velocity characteristics during a cycle by the calculation of the mean and rms quantities in a particular time window over a series of test events, typically twenty. The ensemble method however gives rise to non-turbulent broadening and statistical uncertainties which are discussed below.

Non-turbulent broadening, similar to that discussed in section 2.2.2, results from the finite-time interval over which the mean and rms velocity quantities are evaluated. The complete equations quantifying the effect of transient sample broadening have been set down by *Morse (1977)* for the crank angle broadening of measurements within internal-combustion engines, and are represented in various reduced forms by *Morse et al (1979), Rask (1981)* and *Acroumanis et al (1984)*. The simplified equations primarily neglect the change of number of Doppler signals per unit time, $\partial N/\partial t$. A simplified form of the correction equations for the non-turbulent broadening caused by the finite ensemble time window has been derived and is presented in Equations 2.15 and 2.16 for the mean and turbulence quantities respectively, where N is the sample count, Δt the time interval width and $\partial U/\partial t$ the velocity gradient.

$$U - \langle U \rangle \approx \frac{\Delta t^2}{12\,N}\left(\frac{\partial U}{\partial t}\right)\left(\frac{\partial N}{\partial t}\right) \qquad 2.15$$

$$\frac{\widetilde{u}^2 - \langle \widetilde{u} \rangle^2}{U^2} \approx \frac{\Delta t^2}{12\,U^2}\left(\frac{\partial U}{\partial t}\right)^2 \qquad 2.16$$

In the low-speed simulator, overlapping ensemble time windows of 3.0 ms width (Δt) were used for the calculation of the mean and rms velocity quantities. With this small time window interval, relative to cycle duration, the mean velocity quantities were

unaffected where the velocity changes are approximately linear and the distribution of frequency counts was uniform. In regions where the change of velocity signals per unit time, $\partial N/\partial t$, varied a great deal, like immediately behind the projectile, the non-turbulent broadening correction could not be evaluated and the results were therefore not presented. The maximum velocity gradient ($\partial U/\partial t$), -0.7 (m/s)/ms, observed in the low-speed simulator resulted in an increase of less than 3 % of the rms intensities and were therefore not compensated for in the results.

The statistical uncertainty due to the finite number of velocity realizations can be evaluated in terms of a given confidence level (the normalized constant $Z_c = 2.0$ and 2.6 for 95 and 99% confidence limits respectively), standard deviation ($\tilde{u}$) and sample size (N). According to *Yanta (1973)*, equations 2.17 and 2.18 represent the uncertainty for the mean (U_{error}) and turbulence ($\tilde{u}_{error}$) velocity characteristics in terms of the normalized distribution sample size N, confidence criterion constant Z_c and measured velocity characteristics quantities <U> and $<\tilde{u}>$.

$$U_{error} = \frac{Z_c}{\sqrt{N}} \left(\frac{\langle \tilde{u} \rangle}{\langle U \rangle} \right) \qquad 2.17$$

$$\tilde{u}_{error} = \frac{Z_c}{\sqrt{2N}} \qquad 2.18$$

Thus, the uncertainty in the mean velocity, U_{error}, is dependent upon the local turbulence intensity which is the same as the standard deviation of the normalized distribution and the uncertainty in the rms of the velocity fluctuations, $\tilde{u}_{error}$, a function of the confidence limit and the sample size. The minimum sample of 200 points in each ensemble window required an average of 20 releases of the projectile and corresponding velocity traces. With a 95 % confidence limit, ie. the normalized constant $Z_c = 2.0$, the ensemble averages had a statistical uncertainty of less than 1 % for the mean and 10 % for the rms of velocity fluctuation. If the minimum sample size of 200 points in an ensemble window was not achieved because of insufficient Doppler seeding and the statistical criterion could not be met, the measurement was considered inadequate and not presented.

A summary of the overall estimated systematic and random uncertainties in the

low-speed simulator is presented in Table 2.4. As with the duct uncertainties, an overall random uncertainty for the mean and fluctuating velocities can be derived.

Table 2.4 Summary of estimated low-speed simulator measurement uncertainty.

	Systematic Uncertainty	Random Uncertainty
Streamwise distance along axis (X)	0.2 mm	±0.02 mm
Radial, and spanwise distances (r)	0.1 mm	±0.02 mm
Measured half angle of beams (φ)	0.02°	nil
Fringe spacing (δ_f)	0.01 μm	nil
Mean velocity in X direction (U)	nil	1.5 %
Rms fluctuations of velocity in X ($\tilde{u}$)	nil	11 %
Frequency shift	less than 1.0 %	±0.005

With the correction for the gradient broadening near the wall and sufficiently large samples, the anemometer for the low-speed gun simulator enabled the mean and rms of velocity fluctuations to be measured within 1.5 % and 11 % respectively.

2.3.3 Heat Flux Measurements

Wall temperature measurements were made at various axial locations along the barrel by employing fast response thin-film resistance thermometry. The heat flux from the thin-film sensor was derived from the surface temperature records by a procedure which assumes one-dimensional heat conduction and ignores the effect of the finite film and substrate thickness. The thin-film probes (Dantac 55R47) comprised a nickel film approximately 0.15 μm thick (±.05 μm), 0.9 mm (±0.1 mm), and 0.1 mm (±0.01 mm) deposited on a 50 μm thick insulator substrate of Kapton foil. The probes were mounted flat in recesses (0.1 mm) on the inter-changeable plexiglass windows used by the anemometer so that they would not be damaged when the measuring station was swept by the projectile. The plexiglass windows were machined to conform to the inside wall of the barrel except in the center where the sensor was recessed into a small flat surface (9 mm wide). As noted in the above anemometry section, the length of the flat surface

relative to the radius of curvature does not influence the momentum boundary layer formation but the different thermal properties, relative to the steel barrel, would have an effect on the measured thermal characteristics which will therefore be addressed in the pertinent result section. The physical properties of Kapton foil and the sensor at 25° C, required for the calculation of the sensor temperature and subsequent heat flux from the substrate, are listed below in Table 2.5.

Table 2.5 Physical properties of Kapton Foil substrate and low-speed thin-film sensor.

Density of the Kapton foil substrate (ρ_s)	1420 Kg/m^3
Specific heat of the Kapton foil substrate (C_s)	1092.8 J/(Kg K)
Thermal conductivity of the Kapton foil substrate (k_s)	0.1558 J/(m s K)
Thermal diffusivity of the Kapton foil substrate (α) ($\alpha=k_s/(\rho_s C_s)$	0.1 x 10^{-6} m^2/ s
Thin-film temperature coefficient of resistance (α_s)	0.045 Ω /° K

The electrical resistance of a thin-film changes with temperature and provided a measure of the surface temperature change and subsequent heat flux from the substrate on which the thin-film was deposited. The temperature change ($\Delta T_{(t)}$) of the sensor can be calculated as a function of time by Equation 2.19 where $\Delta R_{s(t)}$ is the change of thin-film sensor resistance and α_s the temperature coefficient of resistance of the thin-film at operating conditions with units of Ω /° K.

$$\Delta T_{(t)} = \Delta R_{s(t)} / \alpha_s \qquad 2.19$$

The change in resistance of the film was measured with a electrical circuit, the output voltage of which was proportional to the sensor resistance. The custom-built constant current circuit, Figure 2.5, is similar to that used in hot-wire anemometry. Since the voltage drop, V_{sc}, across the thin-film sensor was small during a typical test, typically 0-120 mV, a signal conditioner was necessary to provide a gain (G) of 200 and a variable offset voltage (V_{off}) as well as a scaled gain (G_a) of 10 as represented by Equation 2.20.

$$V_{out} = (V_{sc} G - V_{off}) G_a \qquad 2.20$$

The signal conditioner Equation, 2.20, made the measurement of small changes in the thin-film resistance possible and facilitated the calculation of the temperature change of the thin-film. The laser-diode-timer module described in section 2.3.1 was again used to trigger the instrumentation and the thin-film signal was sampled through an analog-to-digital converter and stored in the memory of the ITT microcomputer.

The thin-film sensors had a dynamic response of less than 1 μs for 63 % of a step input. The output of the temperature circuit amplifier was, however, limited to around 8 KHz at -3 dB and the microcomputer sampled the signal at a rate of about 10 KHz. The dynamic response of the system as a whole was fast relative to the time-resolved temperature variations, typically 6 degrees centigrade, during a shot lasting for 34 ms which means that the sample rate of 10 kHz was sufficient to resolve the transient temperature characteristics of the low-speed cycle. The overall noise level of the system was of the order of 25 mV peak-to-peak and corresponded to a temperature uncertainty of about ±0.3° C which represents about ± 5% of the maximum temperature change achieved during a shot.

The time-resolved heat flux from the sensor was evaluated from the measured surface temperatures by the procedure of *Schultz and Jones (1973)* which assumes one-dimensional heat conduction and ignores the effect of the finite film and substrate thickness. The heat flux (q') was related to the surface temperature on the substrate and the properties of the substrate material as demonstrated by Equation 2.21;

$$q'_{(t)} = \sqrt{\frac{\rho_s C_s k_s}{\pi}} \left[\frac{T_{(t)}}{\sqrt{t}} + \frac{1}{2} \int_0^t \frac{T_{(t)} - T_{(\tau)}}{(t-\tau)^{3/2}} d\tau \right] \qquad 2.21$$

where $T_{(t)}$ is the measured surface temperature change and ρ_s, C_s, & k_s are the density, specific heat and thermal conductivity of the substrate respectively. In this form, however, there is a singularity in the integral at $t = \tau$, and this can give rise to errors in the values of heat flux and these are larger for small times. If the heat transfer rate was constant, Equation 2.21 would simplify to Equation 2.22, and the surface temperature

change would be parabolic in form.

$$q'_{(t)} = \frac{\sqrt{\pi}}{2} T_{(t)} \sqrt{\frac{\rho_s C_s k_s}{t}} \qquad 2.22$$

The assumption of a local constant heat flux would simplify the calculation of the transient heat flux characteristics of the simulated ballistics cycle but this would be inappropriate at the onset of the measurement cycle. Numerical integration of the second part of the expression of Equation 2.21 enables the heat flux to be determined when the heat transfer rate is not constant, as long as the singularity is avoided. Equation 2.23 represents one such method by applying a trapezoidal rule to evaluate the integral over the first (n-1) time divisions and the contribution of the last interval was evaluated by assuming a linear relation between temperature and time and integrating directly, thereby avoiding the singularity at $t = \tau$.

$$q'_{(t)} = \sqrt{\frac{\rho_s C_s k_s}{\pi}} \left\{ \frac{T_{(t_n)}}{\sqrt{t_n}} + \sum_{i=1}^{n-1} \left[\frac{T_{(t_n)} - T_{(t_i)}}{\sqrt{t_n - t_i}} - \frac{T_{(t_n)} - T_{(t_{i-1})}}{\sqrt{t_n - t_{i-1}}} + \frac{2\left(T_{(t_i)} - T_{(t_{i-1})}\right)}{\sqrt{t_n - t_i} + \sqrt{t_n - t_{i-1}}} \right] + \frac{T_{(t_n)} - T_{(t_{n-1})}}{\sqrt{\Delta t}} \right\} \qquad 2.23$$

The only approximation involved in the use of Equation 2.23 was the local linearization of the surface temperature. Approaches of this type have been used, for example by *Cook & Felderman (1966), Schultz and Jones (1973), Tsou & Chen (1983)* and *Bicen et al (1987, 1988a,b)* to approximate the transient one-dimensional heat conduction equation, Equation 2.21.

The transient heat flux was difficult to resolve immediately after the projectile swept the measuring station because the surface temperature can be perturbed by friction heating and cooling by the small amount of 'blow-by', gases escaping past the projectile. A comprehensive discussion of the difficulties associated with heat flux measurements in the simulator will be addressed in the results section. The signal noise level of the system, about ±0.3° C or ± 5% of the maximum temperature change, made curve fitting of the surface temperature results necessary in order to calculate the heat flux from

Equation 2.23. The signal noise constituted the maximum uncertainty of the surface temperature and corresponded to an uncertainty in the heat flux from the surface of approximately ± 5 %, rising to ± 10 % immediately behind the projectile.

2.4 Unsteady High-Speed Gun Simulator Experiments

The characteristics of the high-speed gun simulator demanded the development of new techniques and equipment strategies to resolve breech pressure, gas velocity, surface temperature and heat flux during a cycle time of between 7 and 16 ms. The high-speed instrumentation is shown in Figure 2.6 with the three major peripheral instruments connected with the microcomputer. The trigger signal conditioner, frequency counter and pressure/temperature analog-to-digital converter and direct-memory-access interface are discussed in detail in the following sections. The way in which the entire high-speed data acquisition instrumentation was orchestrated is indicated in the flow chart of Figure 2.7.

2.4.1 Transient Pressure Measurements

The transient gas pressure in the high-speed gun simulator was measured with the same piezoelectric pressure transducer and charge amplifier used in the low-speed simulator, discussed in section 2.3.1. The transducer was mounted flush to the inner wall of the breech so that it would not interfere with the flow but respond to local pressure changes. As in the low-speed simulator, the charge amplifier was set with a long time constant (10^3 seconds) to allow the initial charge pressure to be monitored and provide an absolute pressure record during the cycle. The miniature quartz pressure transducer and charge amplifier enabled the transient pressure to be recorded at a maximum rate of 100 KHz by a commercially available multi-channel analog-to-digital converter (MetraByte Model DAS20) with an 8 bit direct-memory-access to a microcomputer (IBM-ATX) operating at 8 MHz. The high sampling rate of the transient breech pressure in the high-speed simulator was necessary to resolve the pressure characteristics in the brief cycle.

The trigger circuit for the high-speed simulator was similar to that used in the

low-speed simulator and was connected directly to the transient pressure analog-to-digital interface board, in addition to the velocity and temperature interfaces. The bulky projectile lock and release mechanism, described in detail in section 5.2, restricted the access of the trigger laser beam. The laser was positioned as close to the base of the projectile as possible, near to the O-ring sealing the initial volume, so that the projectile, in the initially locked position, disrupted the beam. After the first 6 mm of projectile travel, 0.2 % of the total travel length, the laser beam traversed the test section and along a fiber optic cable to the trigger signal conditioner, interfaced with the microcomputer, Figure 2.6. The laser illumination immediately registered and a signal passed to the measuring instrument interfaces in the microcomputer indicating the start of a test sequence. Once again, the small delay between the start of the cycle and the instrumentation triggering produced an offset time between the real and measured cycle which has not been compensated in the presented results. The trigger mechanism communicate when the projectile had departed from the initial position to the data acquisition program, which was written in complied Basic and Macro assembler. The channel of the analog-to-digital and direct-memory-access interface, through which the pressure signal was passed to the microcomputer memory, was initiated by the computer program subsequent to the trigger signal. The pressure signal direct-memory-access interface employed a controller relying on the microcomputer's input-output facilities for real time operation. By engaging the input-output for real time operation, no other interface or device could interact with the microcomputer and the implications of this will be addressed in the discussion on the counter interface, section 2.4.2.

The accuracy of the transducer arrangement was limited by the 8-bit resolution of the analog-to-digital conversion with direct-memory-access and the drift of the charge amplifier, approximately ± 0.5 % each. The total uncertainty of the pressure results in the high-speed gun simulator was about ±1.0 % of the initial pressure.

2.4.2 Laser Doppler Anemometer

The differences in the laser Doppler anemometer used in the high-speed simulator, Figure 2.6, from those of the low-speed simulator described in section 2.3.2, are presented below. The axial component of the velocity was measured by positioning the incident anemometer beams in the plane and perpendicular to the axis of the barrel

and, as indicated in Figure 2.6, the optical axis was turned 90° by a flat mirror ($\lambda/8$) at 45° to make the traversing mechanism stable and secure during measurements and yet easier to move between each window.

Seeding was again provided by a custom built air blast atomizer producing silicone oil droplets of 1 μm nominal diameter. An assessment, equating the acceleration/deceleration forces with the Stokes drag of the seeding particles, *Durst et al (1981) & Taylor (1988)*, indicates that the seeding should adequately capture the flow characteristics. Separately, from the analyses proposed by *Durst et al (1981)* and *Clift et al (1973)*, the silicone oil seeding particles were shown to capture the transient flow characteristics of the high-speed simulator with initial pressures up to approximately 40 bar gauge.

The anemometer was operated in forward scatter mode and employed a fast 12 stage photomultiplier (Thorn EMI model 9817B) which provided a gain to the collected Doppler signal. The only modification of the low-speed optical arrangement for the high-speed simulator was the use of a 100 mm focal length lens (L_1) which resulted in a slight difference in the beam angle, a smaller number of fringes, 21, and a marginally larger fringe spacing, 3.135 μm. Table 2.6, lists the optical characteristics of the arrangements used in the high-speed simulator velocity measurements.

Table 2.6 Characteristics of high-speed simulator optical arrangements.

Laser power output (P)	35 mW
Laser e^{-2} intensity diameter ($D_{e^{-2}}$)	1.25 mm
Focal length of focusing lens (L_1)	100 mm
Focal length of collimating lens (L_2)	300 mm
Focal length of imaging lens (L_3)	300 mm
Index of refraction of fluid medium (η)	1
Measured half angle of beams (φ)	5.79°
Fringe spacing (δ_f)	3.135 μm
Focussed e^{-2} intensity diameter ($d_{e^{-2}}$)	0.0645 mm
Measuring volume diameter in fluid (D_m)	0.0648 mm
Measuring volume length in fluid (L_m)	0.639 mm
Volume of the measuring volume (V_m)	0.0014 mm^3
Number of fringes in measuring vol. (N_m)	21

Since the high-speed simulator consisted of a barrel of 22 mm diameter, the length of the probe volume was approximately 3 % of the bore diameter. The plexiglass windows were machined and polished to conform to the inside wall of the barrel except in the center where a small flat surface (4 mm wide) was milled to insure that the incoming laser beams and forward scatter optical path would not be affected by curvature. The length of the flat surface relative to the radius of curvature again does not influence the momentum boundary layer formation and the influence on the thermal characteristics will be addressed in the pertinent heat flux result section.

The measurement of the gas velocity made use of a frequency counter interfaced through a purpose-built FIFO (first-in-first-out) buffer memory, to a microcomputer and activated by the trigger signal conditioner mentioned in the previous pressure section. The counter (TSI model 1990C) was digitally interfaced with the purpose-built interface card, which stored the validated 16 bit digital frequency signals with the 24 bit time information in the FIFO memory whenever a data ready signal was received from the counter. The bit accuracy of the validated frequency signals corresponded to an uncertainty of less than 1 % for velocities up to 300 m/s. The range of the counter system was 1 KHz to 150 MHz or about 10 times greater than the custom built counter employed in the low-speed instrumentation and made frequency shifting unnecessary. The counter interrogated the first 8 cycles (2^3) and compared measured frequencies over 5 and 8 cycles, accepting results with a difference of less than 3 %. The maximum rate at which the FIFO memory encoded and stored the doppler frequency was approximately 500 KHz or 50 times faster than in the low-speed instrumentation. The maximum number of velocity and time data during a test cycle was limited to 2000 per cycle over a 40 ms total cycle time by the FIFO interface board memory, 8K (8192) x 16-bit. Careful addressing of the direct-memory-access of the velocity and time data subsequent to the end of the cycle was necessary to insure that the data did not write over the memory occupied by the compiled program or previously direct-memory-accessed pressure-temperature data. By increasing the counter frequency range to 150 MHz and improving the rate of effective sampling to 500 KHz, the characterization of the high-speed gun simulator flow velocities was possible without demanding any time consuming interaction with the microcomputer except to prepare, initiate (start) and eventually signal the final direct-memory-access of the velocity data to the available microcomputer

memory.

The maximum design pressure of 60 bar implied projectile and gas velocities up to 450 m/s, corresponding to a 150 MHz Doppler frequency, and with a total cycle time of 7 ms. Even at the lowest initial pressure used here, 5 bar gauge, the fluid velocities correspond to frequencies which exceed those of the low-speed instrumentation. Thus a high speed microcomputer (IBM- ATX) was used and operated at 8 MHz to control the data acquisition sequence as in the flow chart of Figure 2.7. Once the pressure and temperature sampling sequence and counter board memory were primed, the program paused until the trigger signal was received from the trigger signal conditioner. After the trigger signal, the counter FIFO was enabled and the pressure/temperature analog-to-digital conversion with direct-memory-access was begun. Once the prescribed measuring time has passed, the pressure/temperature interface was automatically disabled and the velocity and time direct-memory-access was undertaken. With the breech pressure, surface temperature and velocity & time data in the main computer memory, the program could graphically display, list, print and store on disk any or all test information before preparing for another test sequence. The technique of temporarily storing velocity and time in FIFO board memory made simultaneous high-speed measurements possible.

Storage of the velocity data traces over at least 20 tests of the high-speed simulator made possible the post ensemble averaging and the subsequent evaluation of the statistical uncertainty at a particular position. Ensemble averages in particular time windows during the cycle were calculated and the probability density function displayed along with the statistical uncertainty by a stand-alone program. Filtering of the data sample was accomplished by eliminating noise evident in the probability density function with upper and lower limits for a particular axial window, radial position, initial pressure and cycle time window.

As in the low-speed simulator anemometer setup, section 2.3.2, the high-speed optical arrangement gave rise to uncertainty due to positional ambiguities, Doppler broadening, biasing and transient broadening effects resulting from the ensemble averaging and statistical techniques.

The radial and spanwise resolution of approximately ±0.1 mm represents an uncertainty of less than 1% of the diameter of the high-speed gun simulator. The systematic error in the measured beam angle gives rise to an uncertainty of the fringe spacing (δ_f) and therefore in velocity of less than ±0.3 %.

The effect of gradient broadening was again evaluated using second-order polynomials with three or more points. Unfortunately, the much small diameter in the high-speed simulator made velocity measurements close to the wall, relative to those in the low-speed simulator, impossible. The resulting uncertainties were less than 1 % and 3 % in the mean and rms and corrections were not applied.

Biasing uncertainties in the high-speed counter are unimportant as turbulence intensities were less than about 15 %, also the case in the low-speed simulator. Amplitude bias was also negligible and the overall uncertainty in the mean velocity was less than 0.5 %.

Ensemble averaging techniques were again used for the calculation of the mean and rms velocity quantities. Mean values of ensemble velocities were unaffected by the small overlapping time windows of 0.5 ms width since the velocity changes were approximately linear and the distribution of frequency counts was approximately uniform. The maximum velocity gradient ($\partial U/\partial t$) of -11.0 (m/s)/ms resulted in an increase of less than 1.5 % of the rms intensities and corrections were not applied. The minimum sample set size in each ensemble window, 200 points, required an average of 20 normal measurement tests. With a 95 % confidence limit, the ensemble averages had a statistical uncertainty of less than 1 % for the mean and 10 % for the rms of velocity fluctuation. A summary of the overall estimated systematic and random uncertainties in the high-speed simulator are presented in Table 2.7.

Table 2.7 Summary of estimated high-speed simulator measurement uncertainty.

	Systematic Uncertainty	Random Uncertainty
Streamwise distance along axis (X)	0.1 mm	±0.02 mm
Radial, and spanwise distances (r)	0.1 mm	±0.02 mm
Measured half angle of beams (φ)	0.02°	nil
Fringe spacing (δ_f)	0.01 μm	nil
Mean velocity in X direction (U)	nil	3.5 %
Rms fluctuations of velocity in X (u')	nil	11 %

The counter validation, 3 %, and digital accuracy, 1 %, constituted a majority of the combined uncertainty. The bit accuracy and validation criterion of the counter, positional, gradient broadening, biasing, transient broadening effects and statistical criterion contributed to the overall measurement uncertainty of approximately 3.5 % and 11 % in the ensemble mean and root mean square of velocity fluctuations in the high-speed simulator.

2.4.3 Heat Flux Measurements

The surface temperature was converted to a voltage across the thin-film gauge and sampled by the multi-channel analog-to-digital converter with direct-memory-access interface (MetraByte Model DAS20) mentioned in section 2.4.1. The maximum sampling rate of the temperature circuit was restricted by the analog-to-digital signal range of the interface, 0 -1.0 volts, to 40 KHz and was sufficient to resolve the characteristics of the high-speed cycle. The sampling process was initiated by the trigger signal conditioner, as with the high-speed pressure and velocity instrumentation so that temperature measurements were conducted in parallel with pressure measurements via a separate channel of the interface discussed in section 2.4.1.

The high-speed test rig required a fast thin-film sensor and associated circuitry in order to capture the rapidly changing surface temperature and a platinum thin-film gauge (Medtherm Corporation model PTF-100-20293) was used. The platinum film

was deposited on an insulator substrate of Pyrex 7740 and the physical properties of the sensor and Pyrex 7740 at 25° C, required for the calculation of the sensor temperature and subsequent heat flux from the substrate, are listed below in Table 2.8.

Table 2.8 Physical properties of Pyrex 7740 substrate and high-speed thin-film sensor.

Density of the Pyrex 7740 substrate (ρ_s)	2220 Kg/m^3
Specific heat of the Pyrex 7740 substrate (C_s)	775.0 J/(Kg K)
Thermal conductivity of the Pyrex 7740 substrate (k_s)	1.36 J/(m s K)
Thermal diffusivity of the Pyrex 7740 substrate (α) ($\alpha=k_s/(\rho_s C_s)$)	0.79 x 10^{-6} m^2/ s
Thin-film temperature coefficient of resistance (α_s)	0.275 Ω /° K

The resistance of the thin-film changes with temperature thereby providing a measure of the surface temperature change and heat flux from the substrate, Pyrex 7740 in this case. A fast response sensitive bridge circuit was constructed to enable accurate measurement of the change in resistance of the high-speed thin-film sensor, proportional to the film surface temperature and heat flux, as demonstrated in section 2.3.3. The high-speed thin-film circuitry consisted of a Wheatstone bridge, Figure 2.8, with one of the four resistance arms (R_s) occupied by the thin-film sensor. The bridge voltage (V_b) and subsequent amplifier equations are presented below in Equations 2.24 and 2.25.

$$V_b = \frac{\frac{R_1}{R_4} - \left(1 + \frac{R_s}{R_3}\right)}{\left(1 + \frac{R_1}{R_4}\right)\left(1 + \frac{R_s}{R_3}\right)} V_{ex} \qquad 2.22$$

$$V_{out} = V_b G - V_{off} \qquad 2.23$$

By adjusting the amplifier gain (G = 202) and voltage offset (V_{off}), small changes in the resistance of the thin-film sensor, corresponding to a surface temperature change, can be detected by the instrumentation system provided the output voltage (V_{out}) was always in the 0.0 to 1.0 volt range of the analog-to-digital converter. As with the pressure signal, the analog output from the circuit was digitally sampled by the analog-to-digital converter and stored directly in the memory of the microcomputer. Equation 2.24 was linearized

by fixing the value of R_s in the denominator to the approximate working temperature resistance for the sensor used, 95 ohms in this case. The linearization approximation gave rise to some uncertainty but this was less than the variation of the thin-film coefficient of resistance (α_s) of about 1 % over the observed temperature range. The overall noise level of the system was of the order of 2.5 mV peak-to-peak and corresponded to a temperature uncertainty of about ±0.05° C which represents less than ± 1 % of the maximum temperature change achieved during a typical test shot.

The sensor had a dynamic response of less than 0.1 μs for 63 % of a step input. The output of the amplifier was limited to around 20 KHz at -3 dB and the microcomputer sampled the signal at a rate of 40 KHz. The dynamic response of the high-speed thin-film instrumentation system was fast relative to the time-resolved temperature variations during a shot lasting for less than 16 ms. The high-speed thin-film instrumentation was an improvement over the low-speed thin-film instrumentation by a factor of approximately 10 in speed and 5 in sensitivity to temperature change with an overall uncertainty of ± 1 % of surface temperature.

The heat flux from the surface was computed using the method described in the low-speed thin-film section 2.3.3, from the stored temperature measurements, with a stand-alone program similar to that used in the analysis of velocity results. The high data rate and low signal noise reduced the need for curve fitting of the surface temperature record. The difficulties associated the heat flux calculation immediately behind the projectile were increased at the larger projectile velocities in the high-speed simulator and will be addressed in the results section. Since the signal noise of the system, 1 % or 0.06° C, was much better than that of the low-speed instrumentation, the heat flux program allowed the calculation of the transient heat transfer characteristics at each high-speed measurement window with an overall uncertainty of approximately ± 2 %, rising to ± 5 % immediately behind the projectile.

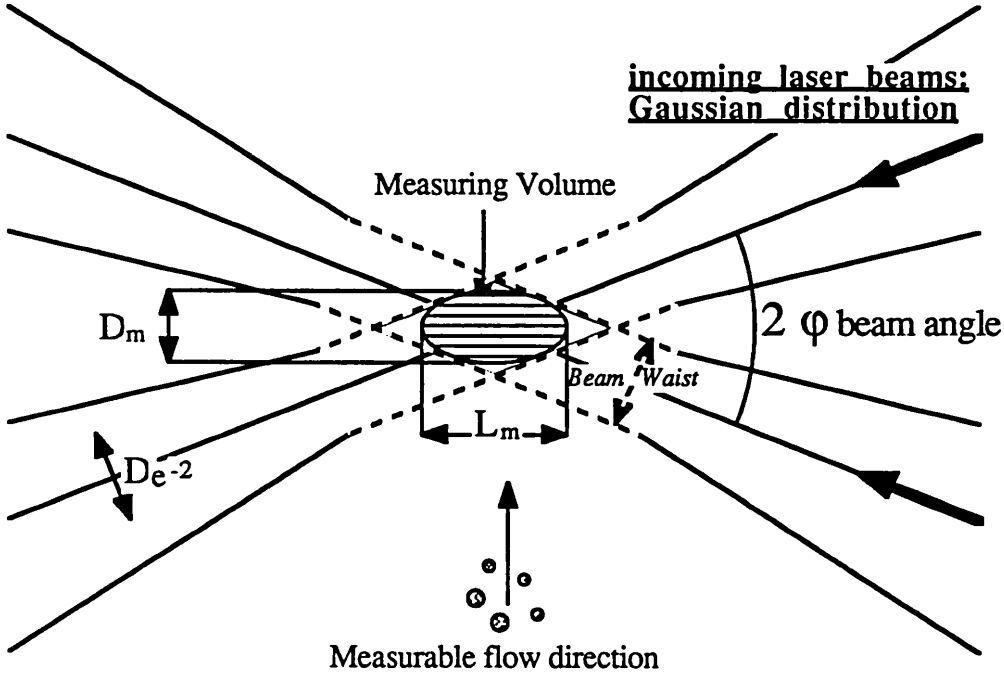


Figure 2.1 Measuring volume of laser-Doppler anemometer.

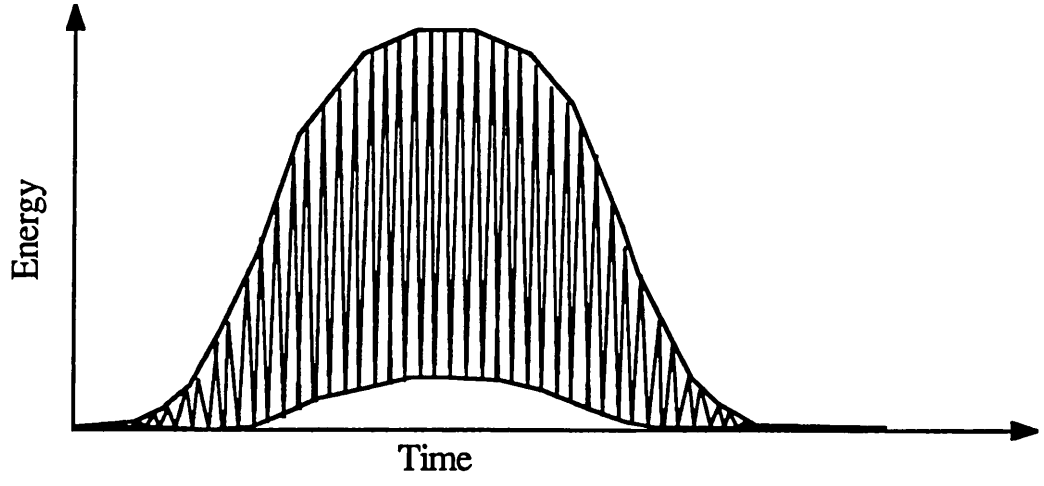


Figure 2.2 Laser Doppler Anemometer signal.

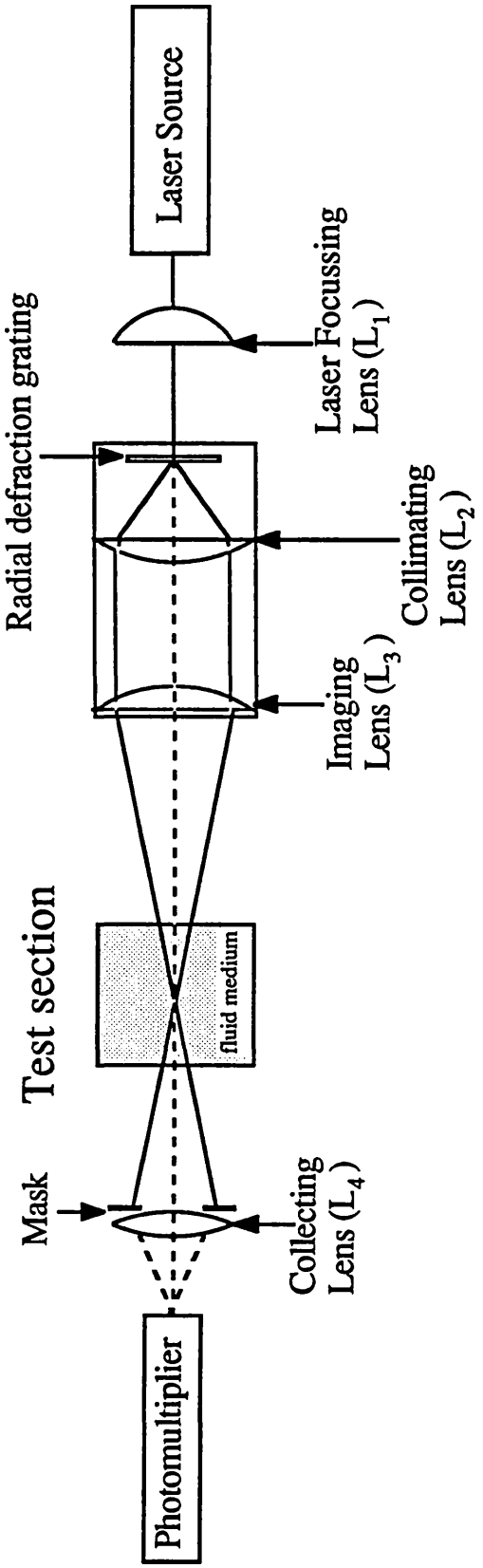


Figure 2.3 Optical configuration of laser-Dopp ler anemometer.

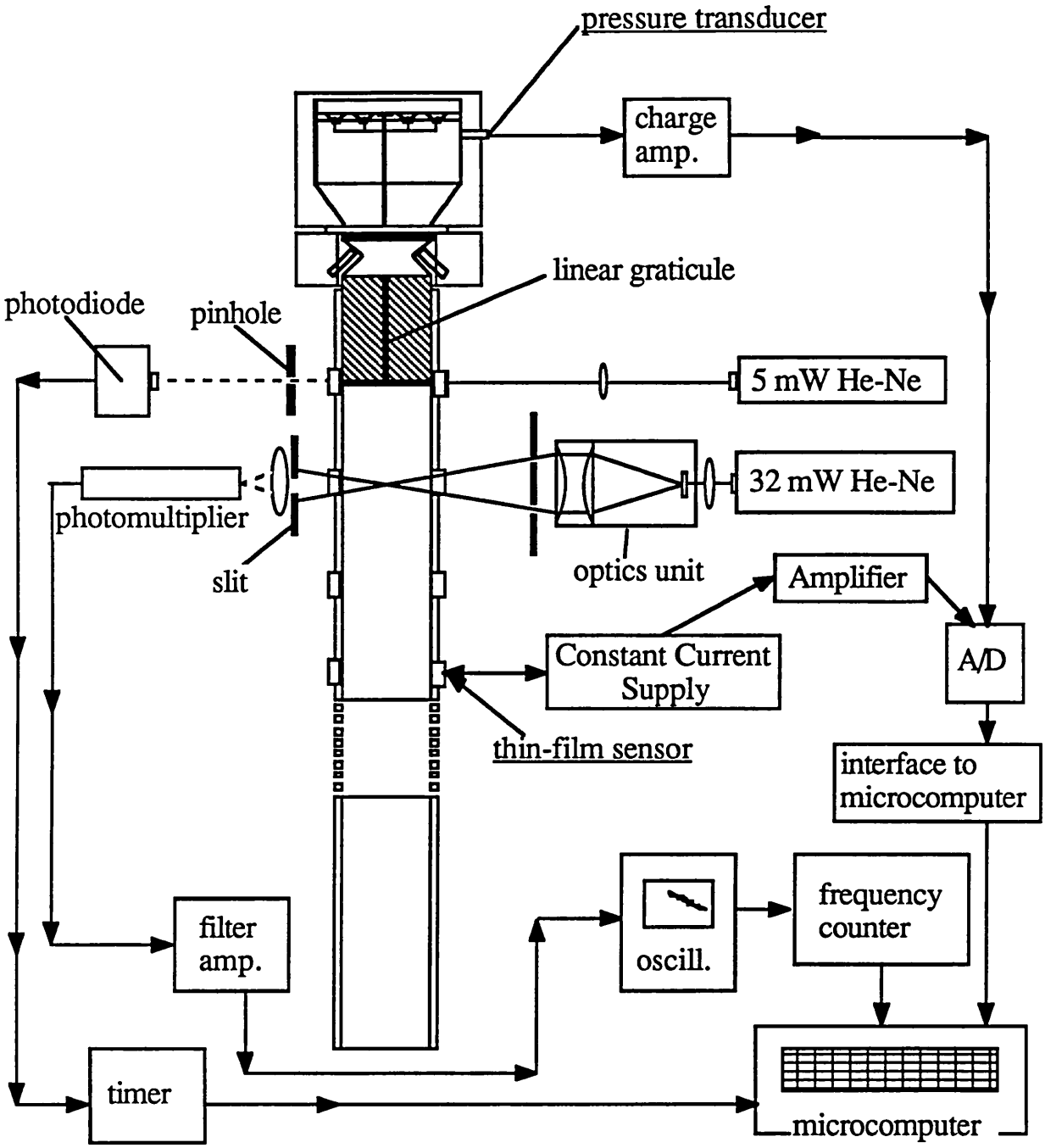


Figure 2.4 Low-speed gun simulator and related instrumentation.

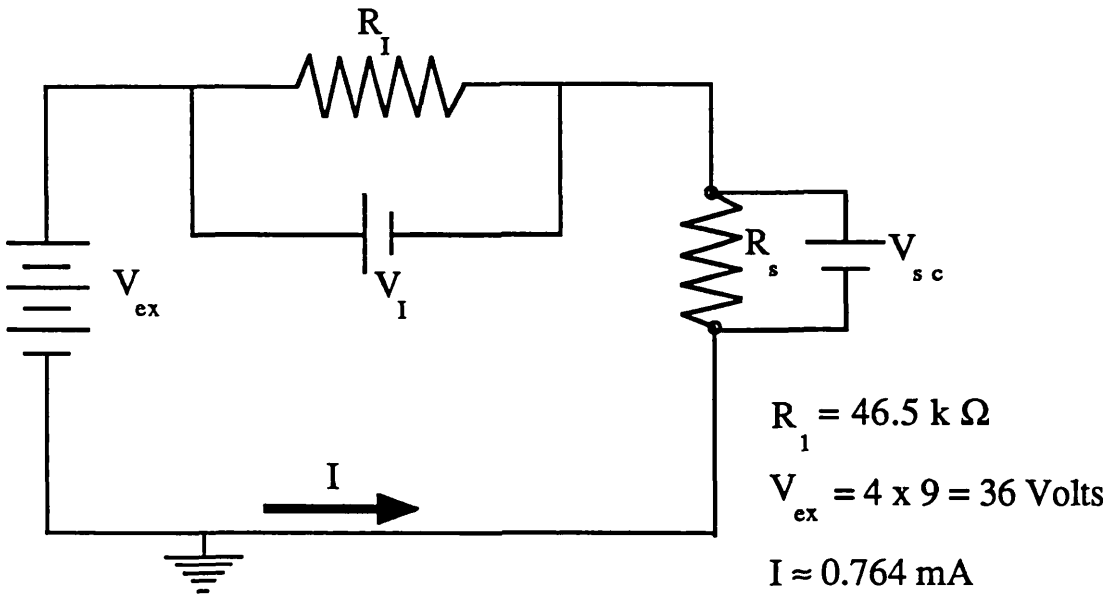


Figure 2.5 Thin-film circuit for low-speed gun simulator.

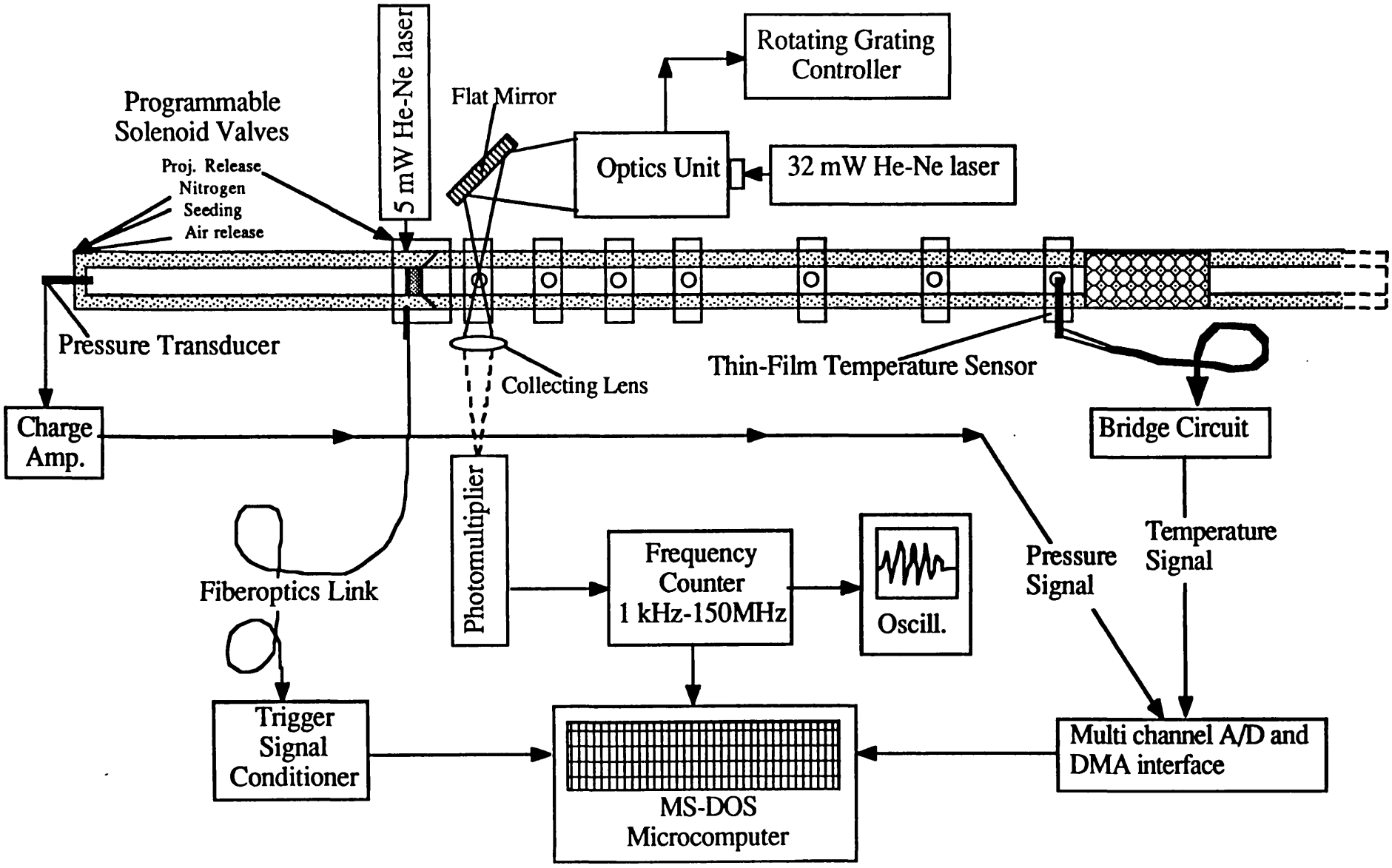


Figure 2.6 High-speed gun simulator and related instrumentation.

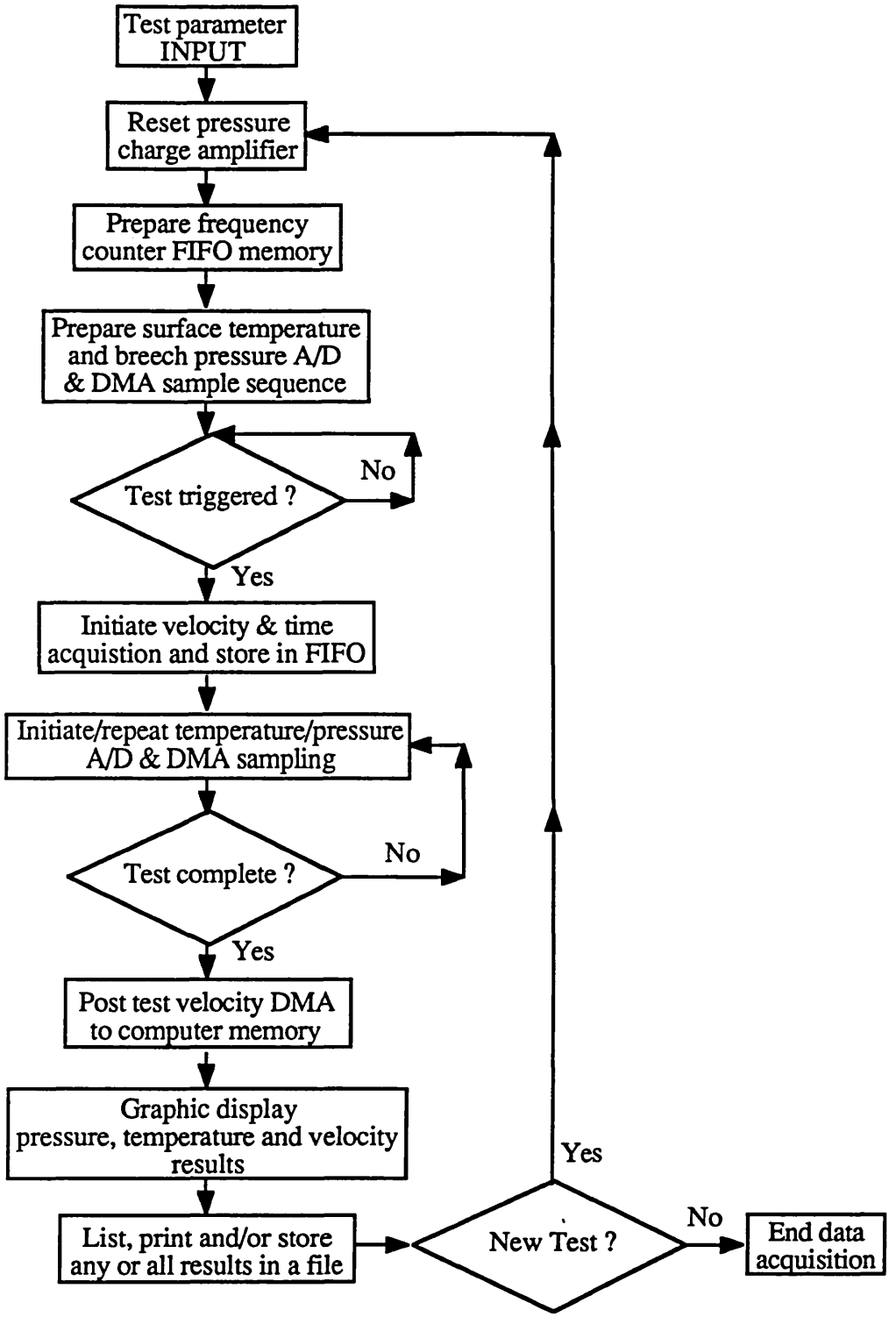


Figure 2.7 Data acquisition program flow chart.

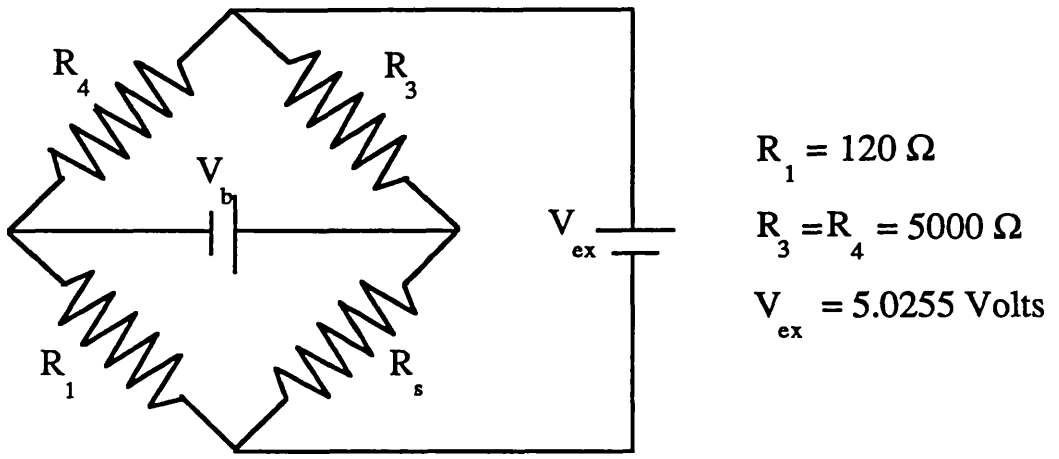


Figure 2.8 Thin-film circuit for high-speed gun simulator.

CHAPTER 3 CURVED DUCT FLOWS

3.1 Introduction

This chapter is concerned with the flows in the steady out-of-plane double S-bend duct. The first section describes the rectangular and circular cross-section flow configurations in which pressure and fluid velocity were measured and the second section presents and discusses the results. The measurements from the rectangular duct corresponded to developing laminar and turbulent flow and those in the circular cross-section duct to developing turbulent flow. The chapter ends with a discussion of the more important conclusions from the experimental investigation.

3.2 Flow Configuration

In practical aircraft wing-root intakes, where the efficient redirection of the flow, with some pressure recovery and uniform velocity profile at the duct exit (ie. at the turbine compressor face) are required, a combination of out-of-plane S-shaped bends is commonly used and is modeled by the experimental flow arrangement. The flow configurations for the rectangular and circular cross-section ducts and coordinate systems are shown in Figures 3.1 and 3.2 and each comprised a uniform cross-sectional area S-duct connected to an S-diffuser with an exit-to-inlet area ratio of 1.5. The inlet and exit planes were parallel in both configurations, and the centreline of the diffusing duct lay in a plane normal to that containing the centreline of the first duct. The orientation of the plane of symmetry of the S-bend and S-diffuser ducts in the arrangements of Figure 3.1(a) and 3.2 corresponds to a simulated left-hand-side intake duct typical of dorsal or wing-root intakes. The results in the left-hand out-of-plane double S-bend can be extrapolated to right-hand-side intakes because their geometries are mirror images of each other about a vertical plane which contains the aircraft axis.

Many experimental investigations of flows in ducts with large turning angles (>45°) and small radii of curvature (R_c/D_h<3.5) have been undertaken for laminar and turbulent flows including those of *Rowe (1970)*, *Bansod & Bradshaw (1972)* and

Agrawal et al (1978), and several at Imperial College for fully developed flow *Humphrey et al (1977, 1981)* and for developing flow, *Taylor et al (1980, 1981a)*, *Enayet et al (1982a)*. The results indicate that weaker secondary flows are present in the developing flow cases, mainly due to the thinner inlet boundary layers. In order to reduce the likelihood of flow separation at the walls of the ducts, small centreline displacements and relatively mild curvature ducts, *Enayet et al (1982b)* and *McMillian (1982)*, were investigated and found to produce cross-stream flows with magnitudes half those in the strongly curved duct of *Taylor et al (1980, 1981a)*. The mildly curved ducts were analogous to practical aircraft intake configurations because the pressure losses resulting from separated flow and unnecessary redirection of the flow are avoided in realistic aircraft intake geometries. The influence of the inlet conditions on the incipient separation in the flows in C-shaped 45° diffusers was examined at length by *Rojas et al (1984)* under a wide range of conditions and is not therefore, addressed here.

The square cross-section S-bend was identical to that investigated by *Taylor et al (1981b)* and the circular duct similar to that of *Taylor et al (1984)*. The diffusing S-duct sections in both the rectangular and circular cross-sections were identical to those investigated by *Rojas et al (1983a,c)*. The rectangular duct, Figure 3.1(a), consisted of a square cross-section (40 mm x 40 mm) 22.5°-22.5° S-bend upstream and a rectangular cross-section 22.5°-22.5° S-diffuser downstream. The circular duct, Figure 3.2, comprised a 45°-45° constant cross-section area S-duct of 48 mm diameter upstream with a 22.5°-22.5° S-diffuser downstream. The greater turning angle of the round duct is expected to produce stronger secondary motion. The ratio of the radius of curvature of the centreline (R_c= 280 mm for the rectangular duct, and 336 mm for the circular duct) to the hydraulic diameter at the duct inlet (D_h= 40 mm for the rectangular duct and 48 mm for the circular duct) was 7.0 for both ducts. The displacement of the duct centreline from the parallel inlets to the exits, a function of the radius of curvature and turning angle, was 42 mm in both the 22.5°-22.5° rectangular S-duct and diffuser and 196.8 and 25.6 mm in the 45°-45° circular cross-section S-duct and 22.5°-22.5° S-diffuser respectively. The length along the centreline from the inlet to the S-duct to the exit of the S-diffuser in the rectangular and circular cross-section double S-ducts was 15.5 and 16.5 diameters. Details of the two ducts and the flows are presented in Table 3.1.

Table 3.1 Parameters in the duct flow configurations

			Rectangular Cross-section Duct	Circular Cross-section Duct
Hydraulic diameter	Duct	(D_h)	40 mm	48 mm
	Diffuser inlet		40 mm	48 mm
	Diffuser exit		48 mm	58.8 mm
Radius of curvature (centreline)		(R_c)	280 mm	336 mm
Bulk velocity:	Laminar flow	(V_B)	19.75 mm/sec	-----
	Turbulent flow		1.0 m/s	1.0 m/s
Reynolds number:	Laminar flow	(Re)	790	-----
	Turbulent flow		40,000	48,000
Dean number:	Laminar flow	(De)	211	-----
	Turbulent flow		10,690	12,828
Radius of curvature	S - duct	(r_o)	300 mm	360 mm
		(r_i)	260 mm	312 mm
	S - diffuser inlet	(r_o)	300 mm	360 mm
		(r_i)	260 mm	312 mm
	S - diffuser exit	(r_o)	310 mm	365.4 mm
		(r_i)	250 mm	306.6 mm
Upstream tangent			300 mm	210 mm
Downstream tangent			2.0 m	1.82 m
Area ratio (S-diffuser)			1.5	1.5
Effective divergence angle (S-diffuser)			5.2°	2.35°

The increase in the cross-sectional area of both the diffusers was made in a linear fashion so that the area of any cross-section was proportional to its centreline distance from the beginning of the area expansion. The rectangular S-diffuser expanded in area to a rectangular outlet 40 mm x 60 mm so that only the radial dimension changed while the spanwise dimension was kept constant along the length of the duct. The total divergence angles for a straight diffuser equivalent to the present curved ones are 2.4° and 5.2° for the circular and rectangular diffusers respectively and are small enough to result in attached flow through the S-diffuser, although there was a large region of slow moving fluid near the outside wall, *Rojas et al (1983a,c, 1986)*, relative to the S-duct, *Taylor et al (1981b, 1984)*.

The flow was provided by a large plenum chamber supplied by an elevated constant head tank with overflow to a large sump tank at floor level. The upstream tangents were preceded by smooth area contractions (12:1) with multiple baffles and a honeycomb screen in the plenum chamber. A 0.5 mm boundary layer trip was located around the duct perimeter between the outlet of the contraction and the upstream tangent to insure symmetric developing turbulent boundary layers in the duct as in the previous single duct and diffuser investigations. The joints between the individual bends of the test section were aligned to within ± 0.1 mm so that no inner surface discontinuities were present to disrupt the developing flow. The flow facilities were similar to those described by *Humphrey et al (1977, 1981), Taylor et al (1980, 1981a,b, 1982, 1984), Enayet et al (1982a,b)* and *Rojas et al (1983a,b,c, 1984).* After the test section, the flow entered a downstream tangent prior to measurement by a precision-bore flow meter and drained into the sump tank feeding the pump to the overhead supply tank. The water temperature was maintained between 18° and 22° C by the addition of cold or hot water.

For consistency of presentation, the coordinate notation at the inlet was unaltered through the double S-bends so that there was no rotation of r^* and z^* directions upon entry to the second out-of-plane S-bend diffuser. As a result of this coordinate notation, the plane of curvature of the second bend was not the radial coordinate plane as normally defined in previous investigations. The coordinates, for the rectangular duct case, Figure 3.1(b), indicate the positive direction of the V and W velocity vectors and will help the interpretation of the results. The z^* direction lies always in a vertical plane and the r^* direction lies in a horizontal plane throughout the duct length. However, and in order to enable comparisons with previous investigations in single S-bends, the cross-stream velocity components in the second bend (in the z^* direction) are denoted by V and $\tilde{v}$ while the components in the spanwise (r^*) direction are denoted by W and $\tilde{w}$, in correspondence with the notation used in previous diffuser research work. The streamwise distances, X and X*, are measured in hydraulic diameters (D_h) along the centreline from the inlet to the first S-bend and from the inlet to the S-diffuser respectively.

Measurements were made at Reynolds numbers, based on the hydraulic diameter and bulk velocity at the upstream tangent, of 790 and 40,000 in the rectangular

duct and 48,000 in the circular duct. The bulk velocities (V_B) were 1.00 m/s for both turbulent flows and 19.75 mm/s for the laminar flow in the rectangular duct. The corresponding Dean numbers are 10,690, 12,828, and 212 respectively. Water was employed to obtain the same Reynolds number at a scale much smaller than that achieved in air to allow a high measurement accuracy. The rectangular and circular cross-section ducts were constructed of polished transparent plexiglass to allow optical access of the laser Doppler anemometer, discussed in detail in section 2.2.2, along the entire duct from upstream tangent to downstream tangent. The rectangular cross-section had flat parallel walls and the circular cross-section duct had a rectangular exterior. The effect of the curvature on the light beams, at the plexiglass/water interface in the circular duct cross-section, was compensated for by the use of ray tracing techniques, *Bicen (1981)*, as in *Rojas et al (1983c)* and *Taylor et al (1984)*.

As noted in section 2.2.1, the static pressures were measured in the turbulent flows relative to the reference position (X= -1, r* = 0.5, z* = -1.0), and were facilitated by pressure taps on the sides of the double S-bend ducts and diffusers and a differential micro-manometer. The pressure taps were machined flush with the duct walls and were situated along the centreline of each surface (r*=1.0, z*=-1.0, z*=1.0, r*=0.0) with approximately 1.1 hydraulic diameter spacing in the axial (X) direction; they were designed in accordance with the recommendations of *Shaw (1960)* and did not protrude into or disrupt the flow.

The laminar and turbulent flow results are suitable for the assessment of numerical methods and turbulence models used for the calculation of these flows, have been tabulated by *Schmidt et al (1986)* and are available on IBM compatible and Macintosh disks from the author.

The out-of-plane double S-bend duct velocity and pressure results are presented and discussed in the following sections beginning with the rectangular duct laminar and turbulent flows and followed by the circular cross-section turbulent flow results. The chapter ends with a summary of the more important conclusions.

3.3 Duct Flow Results

3.3.1 Rectangular Cross-section Duct - Laminar flow

The streamwise and cross-stream velocities in the constant area S-duct were measured at the inlet (X = 0.0) and exit (X = 5.5) to insure identical inlet conditions to those of *Taylor et al (1981b)*. The thickness of the inlet boundary layers, defined at 95 % of the maximum velocity, were approximately 25 % of the hydraulic diameter at the inlet for the laminar case and the results at the exit to the S-duct were symmetric with maximum velocities of 1.7 V_B at r*= 0.3 and maximum cross-flows of 15 % of the bulk velocity, V_B, as quantified by *Taylor et al (1981b)*. The flow from the S-duct exit passed through the spacer between the S-duct and S-diffuser and the maximum streamwise velocity migrated slightly toward the r*=1.0 wall with the cross-flow maximum sustained at approximately 0.15 V_B. The variation of the streamwise velocity component along the centreline of the S-diffuser, Figure 3.3, showed a rapid rise from 0.95 V_B in the first bend (X*=0.0 to 2.75) to around 1.5 V_B at 3.8 D_h downstream of the inlet and subsequently decreased to around 1.4 V_B at the diffuser exit. The centreline progression of the streamwise velocity was very different from that of *Rojas et al (1983a)* where the centreline velocity decreased from 1.7 V_B at the inlet to 0.8 V_B. In the single-diffuser, the core flow drifted towards the r* = 0.0 wall, whereas the perturbed inlet conditions due to the upstream S-duct caused the core to be redistributed by the strong cross-flow vortices, thus causing the streamwise velocity along the centreline to increase in the mid-section of the diffusing S-bend and decrease slightly towards the exit as a result of the area expansion.

The centreline variation of the radial component of velocity through the diffuser, Figure 3.4, exhibited two sign reversals from 0.03 V_B at the inlet to -0.16 V_B at around 2.8 D_h thereafter increasing sharply to 0.16 V_B at the diffuser exit. In the single S-diffuser, similar characteristics were observed but with a smaller magnitude at the inlet and a higher reversed flow of -0.35 V_B rising to 0.15 V_B at the exit plane. The differences in the cross-stream velocity at the inlet were caused by the secondary flow from the S-bend duct which resulted in a smaller negative flow near the middle of the diffuser.

Careful interpretation of the centreline variation of the streamwise and cross-stream velocity must be exercised because the results do not give a clear indication of the causes of the flow changes as it progresses along the diffuser. For this reason, the flow in the exit plane of the S-shaped diffuser was measured in detail and compared with the results obtained in the single S-diffuser. Contours of the streamwise velocity at the exit plane of the S-diffuser are shown in Figure 3.5, with the corresponding cross-stream contours in Figure 3.6. Those denoted by dashed lines were extrapolated between adjacent points. The uncertainty due to the spatial resolution of the exit plane velocity measurements was approximately ± 0.03 and ± 0.05 in the z* and r* coordinates respectively or at worst 5 % in the spanwise direction r*. The streamwise velocities show an asymmetric flow pattern with two maxima of 1.4 V_B to one side of the plane of symmetry (r* = 0.5). In the single S-diffuser, the flow was symmetric about the r*= 0.5 plane and the peak streamwise velocity was 1.55 V_B at z* = 0.4. The four $\partial U/\partial r$ gradients associated with the two peaks indicate the existence of several secondary flow cells, vortices, like those encountered at the exit of single symmetric S-bend ducts (see e.g. *Taylor et al (1981a)* and *Rojas et al (1983c)*) but of larger magnitude. The small peak near z*=-1.0, r*=0.7 suggests the existence of another smaller vortical cross-flow motion in that region. The perturbation of the inlet flow conditions to the diffuser, by the upstream duct has a dramatic effect on the streamwise contours at the exit plane as evident in the movement of the peak velocities toward the r* = 0.0 wall and the two smaller maximum as a result of at least two vortical secondary flows in the core region.

The cross-stream velocity profiles at the duct exit, Figure 3.6, confirm the complex cross-flow pattern particularly near the r* = 1.0 wall, corresponding to the inner wall of the first S-duct bend, and they and the contours show that a plane of symmetry does not exist. There are four predominate regions of negative radial cross-flow velocity directed towards the z*=1.0 wall, evidence of at least four vortices near the wall, two at r*=0.1 around z*=-0.6 and 0.9, and two at r*=0.9, around z*=0.1 and 0.8 which were also apparent in the corners of the single S-diffuser laminar results presented by *Rojas et al (1983c)*. The negative cross-stream velocity evident in the plane of symmetry (r* = 0.5) from the z* = -1.0 wall to z* = -0.2 in the *Rojas* investigation, is not observed here but a corresponding low velocity region extending over the same length was apparent at r* = 0.6. The maximum radial velocity measured at the exit in the

double S-bend arrangement was 0.18 V_B and larger than the 0.15 V_B measured in the single S-diffuser case.

In contrast to the four vortices observed by *Rojas*, Figures 3.5 and 3.6 suggest at least six cross-flow motions, one in each corner of the duct and two around z*=0.1, r*=0.9. Three of these vortices rotate in a counter-clockwise direction and three in a clockwise fashion (viewed from the exit plane as in Figure 3.1(b)). There is some evidence of an additional cross-flow vortex indicated by the results near the z* =1.0 wall at r*=0.7 by the local peak in cross-stream velocity but no local negative values of velocity were measured. Negative cross-flow velocities would be expected closer to the walls indicating the presence of additional and smaller near-wall vortices but such measurements were rarely possible due to limited optical access of the laser Doppler anemometer. The contours of the streamwise and cross-stream velocities provide evidence of at least six cross-flows of varying magnitudes and show that the loss of symmetry was due to the effect of the upstream S-duct on the resulting S-diffuser flow, thereby substantiating the detailed analysis of the exit plane in the laminar case.

Measurements were made in the downstream tangent to examine the recovery of the flow downstream of the double S-bend. Streamwise and cross-stream velocity profiles at r*=0.5, X*=12.375 and 16.735 (6.875 and 10.875 D_h downstream of the exit of the diffuser), Figures 3.7 and 3.8, show that the recovery of the flow was very slow and, at the furthest downstream station, the large gradients in the profile indicate the strong influence of the upstream S-bend duct in the form of the double peak. The radial velocity profiles, Figure 3.8, show that the cross-flow velocities had maxima of 0.105 and 0.07 V_B at the two stations. From the decrease in the secondary flow, Figure 3.8, the breakdown of the pressure generated vortices in the laminar case cannot be expected until far downstream in the tangent, resulting in a very slow recovery of the flow as one would expect for the laminar flow case.

3.3.2 Rectangular Cross-section Duct - Turbulent flow

The wall static pressure measurements for turbulent flow in the rectangular duct are presented in Figure 3.9 in terms of the pressure coefficient, as defined in section 2.2.1. Four variations of C_{p^*} with X are shown along the centreline of the four surfaces, corresponding to the wall at $r^* = 0.0$ and $z^* = 0.0$, $z^* = -1.0$ and $r^* = 0.5$, $r^* = 1.0$ and $z^* = 0.0$, and along the $z^* = 1.0$ wall at $r^* = 0.5$. The upstream and downstream influence of the geometry, approximately one hydraulic diameter, was evident as in all the previous investigations. The pressure gradients in each bend are characteristic of flow in single bends and have an obvious effect on each other at the middle of each of the S-bends and between the two S-ducts, making the radial pressure gradients appear to be distinct and separated. The static pressure coefficient differences across each of the four constituent bends have maxima of approximately 0.25, 0.26, 0.27 and 0.17 C_{p^*}, which were similar to those measured in the single S-duct investigations by *Taylor et al (1981b)* and *Rojas et al (1983a)* to within the accuracy of the manometer. The pressure drop through the S-duct was about 10 % of the velocity head ($\rho_f V_B^2$) and the pressure recovery through the S-diffuser was around 20 %, resulting in an overall pressure rise of about one tenth of the velocity head across the whole duct. The static wall pressure results give little indication of the perturbation of the inlet into the diffuser though close inspection of the diffuser pressure results along the $r^* = 1.0$ wall revealed a slightly skewed distribution relative to those measured at the outer and inner curved duct walls, a consequence of disturbed inlet flow conditions and associated secondary flow generated in the first S-duct and measurement accuracy.

Measurement of the streamwise and cross-stream velocities in the constant area S-duct were completed at the inlet (X = 0.0) and exit (X = 5.5) with turbulent flow to insure identical inlet conditions to those of *Taylor et al (1981b)*. The thickness of the inlet boundary layers, again defined at 95 % of the maximum velocity, for the S-duct were approximately 15 % of the hydraulic diameter. The exit plane results of the S-duct were very slightly asymmetric, suggesting a small up-stream influence of the second S-bend, with maximum velocities of 1.2 V_B at $r^* = 0.4$ and maximum cross-flows of 10 % of the bulk velocity near the lower and upper walls, $z^* = \pm 1.0$ walls, similar to those measured by *Taylor et al (1981b)*. The water from the S-duct exit flowed through the

spacer between the S-duct and S-diffuser and the maximum streamwise velocity migrated slightly toward the centreline, r*=0.5, as a result of the cross-flow.

The mean velocity component along the centreline of the S-diffuser, Figure 3.10, decreases linearly from a value of 1.2 V_B at the inlet to 0.93 V_B at the diffuser exit. The centreline progression of the streamwise velocity was similar to that measured by *Rojas et al (1983a)*, where the the centreline decreased linearly from 1.1 V_B at the inlet to 0.95 V_B at the exit, the only difference being that the centreline inlet velocity was larger as a result of the previous bend and migration of the maximum to the centreline through the spacer. The streamwise velocity progression along the duct does not reveal the effect of the perturbed inlet condition resulting from the upstream S-duct and the decrease in streamwise velocity resulted from the area expansion. The corresponding centreline variation of the radial cross-stream mean velocity component through the diffuser, Figure 3.11, has two changes in the sign and follows closely the trend observed in the laminar flow case. The magnitude of radial secondary flow decreases from 0.06 V_B at the inlet of the diffuser to -0.16 V_B around X*= 2.8 and rises again to a value of 0.06 V_B at the exit plane. The single S-diffuser turbulent results were similar but with a drop from 0.03 to - 0.12 and rise to 0.05 at the exit. The larger magnitudes of the cross flow in the inlet and middle of the bend are a result of the upstream bend and the pressure driven secondary flows that it generated, as also seen in the laminar results, but the exit values imply a smaller effect.

The centreline variations of two components of turbulence intensity $\tilde{u}/V_B$ and $\tilde{v}/V_B$ and of the cross-correlation are shown in Figures 3.12, 3.13 and 3.14 respectively. The intensity levels in the axial direction rise from 0.015 V_B at the diffuser inlet to 0.065 V_B at the exit, Figure 3.12, and those based on the cross-stream normal stress increased from 0.008 V_B at the inlet to 0.042 V_B at the exit, Figure 3.13. The centreline variation of the two components of turbulence intensity in the single S-diffuser, *Rojas et al (1983a)*, was constant in both at a level of approximately 0.01 V_B. The increase in the turbulence intensity along the centreline occurs because the secondary flow generated by the first S-duct caused the near-uniform velocity core to move off the centreline. The normalized cross-correlations of Figure 3.14 have the expected small values along the duct centreline up to X*= 4.0 and rise to a maximum value of 0.0008 in the vicinity of the diffuser exit where there were vortical structures in the cross-flow as the core moves

off the centreline. The scatter near X*= 3.0 in Figure 3.14 was due to the small magnitudes of the correlations, which are close to the experimental precision.

Streamwise mean velocity profiles were measured at r*=0.1, 0.3, 0.5, 0.7, and 0.9 at three axial stations and at r*=0.3 and 0.7 at one axial station in the duct. The intermediate station results are not presented here and can be found in *Schmidt et al (1986)* along with all the results in tabular form. Asymmetry was evident in the profiles along the second S-bend especially at the exit plane of the diffuser. Contours of the results at the diffuser exit are shown in Figure 3.15 and reveal that the near-potential core flow was located near r*=0.4 and z*=0.6. The contours show a movement towards the r*=0.0 wall, slow moving fluid toward the upper wall, z*=-1.0 and the core center approach the bottom wall, z* = 1.0. The maximum of streamwise mean velocity, 1.0 V_B, was slightly larger than that produced by the single S-diffuser due to the thicker boundary layers and larger core velocity at the inlet to the diffuser. The bulk of the streamwise flow has moved to the bottom half of the duct and toward the left hand side, r*=0.0, as a result of the effect of the diffuser pressure field on the upstream duct induced secondary flows. The streamwise velocity contours show qualitative similarities with the laminar results presented in Figure 3.5, with the regions of high velocity less pronounced in the turbulent flow case because of mixing and redistribution by the secondary flow and turbulence. A minor rise shown in the upper right hand quarter in Figure 3.15 corresponds to that evident in the same location in Figure 3.5 but of larger magnitude as expected in the turbulent case. The pressure driven secondary flows generated in the S-duct were caused by the pressure field of the diffuser and resulted in numerous vortices of different magnitudes and rotating direction, subsequently causing asymmetries at the exit plane.

The velocity vectors in the r*-z* plane at the diffuser exit (i.e. $\sqrt{\vec{V}^2+\vec{W}^2}$) are presented in Figure 3.16 with the spanwise component measured at a station 13 mm (0.325 D) downstream of the exit. The maximum radial cross-flow velocity was 0.11 V_B at r* = 0.7 and the cross-flow direction was towards the z* = -1.0 wall except for two small regions at the two corners of the duct near the z* = 1.0 wall, where negative radial velocities of up to 0.03 V_B were measured. The spanwise mean velocities imply at least four cross-flow vortices with maximum cross-flow velocity of around 0.05 V_B.

Consideration of all three velocity components suggests that there are six cross-stream vortices in the r* - z* plane at the duct exit, four located around r* = 0.7 and two around r* = 0.3, and are in contrast with the laminar flow results. The cross-stream velocities are smaller in turbulent flow as one would expect due to the influence of turbulent mixing. The very large vortex in the top left quarter was established in the top half of the S-duct, z* from -1.0 to 0.0, and sustained through the diffuser because of the expansion in area and tendency for the core to migrate to the outer wall of the first section of the duct, ie. toward the z* = 1.0 wall.

The streamwise turbulence level contours at the exit from the rectangular diffuser, Figure 3.17, are nearly uniform near the two side walls with magnitudes around 0.068 of V_B, and in the remainder of the cross-section vary from a maximum of 0.11 of V_B down to the minimum of 0.03 V_B corresponding to the maximum streamwise velocity peak. In the single S-diffuser experiments, the streamwise turbulence intensities were substantially lower varying from 7 to 1 % at the peak velocity. The overall increase in turbulence intensity to the values at the exit plane occurred because of the secondary flow generated by the S-duct and the subsequently higher levels present at the diffuser inlet. The radial turbulence levels exhibit similar distributions to the $\tilde{u}/V_B$ results but are of smaller magnitude, with maxima of around 0.06 V_B. The span wise turbulence intensities measured at 0.325 D downstream of the exit were similar to those of the radial component and did not exceed 0.06 V_B. Turbulent mixing aids the local redistribution of the streamwise velocity by the pressure driven vortices and causes the breakup of the vortices to increase turbulence intensities.

The $\overline{uv}$ cross-correlations of Figure 3.18 have a maximum value of around 0.0032 V_B^2 near the position of maximum turbulence intensity and the $\overline{uw}$ values were some 30% smaller. The maximum cross-correlation at the exit of the out-of-plane double S-bend was twice that produced by single S-diffusers, *Rojas et al (1983a)*, 0.0015 V_B^2, and comparable to those found in single square S-ducts, *Taylor et al (1981b)*, 0.003 V_B^2. The maximum near the z* =1.0 wall noticed previously by, *Rojas et al (1983b)*, was not evident but a minor peak was apparent near the r* = 1.0 wall at z* = 0.2. The large cross-correlation was a result of the large Reynolds stress associated with the large $\partial V/\partial z^*$ of Figure 3.16.

Measurements were made in the downstream tangent to examine the recovery of the flow and profiles of streamwise and radial mean velocity at r*=0.5, at 6.875 D_h and 10.875 D_h downstream of the diffuser exit, Figure 3.19 and 3.20, are more uniform than in laminar flow and the flow recovery was more rapid. The maximum streamwise velocity along the r*=0.5 plane at the exit of the diffuser decreased from 1.0 at the exit to 0.92 and 0.85 V_B and migrated from z* = 0.5 to 0.3 and 0.2, at the two downstream measuring tangents. The maximum radial velocity decreased from 0.047 to 0.042 V_B at the downstream location compared to the 0.08 V_B maximum at r*=0.5 at the diffuser exit. The secondary flow vortices were well established in the diffuser and persist to aid the redistribution of the mean streamwise velocity by the turbulence, as seen in Figure 3.19.

The influence of the second S-diffuser on the secondary flow vortices generated in the first S-duct, was to aid the breakup of the pressure generated vortices downstream along with the increased turbulence intensities of the multiple duct arrangement. The pressure driven secondary flows of the diffuser compliment and counteract the vortices established in the upstream duct which causes one vortex, in the upper left corner of the exit plane, rotating counter-clockwise, to appear to expand and others, like those produced in the corners, are suppressed and broken down by turbulent mixing. The enlarged vortex was not in the boundary layer which grows along the duct and resulted from the effects of the diffuser pressure gradient on the secondary flow established by the upstream duct.

3.3.3 Circular Cross-section Duct - Turbulent flow

The wall static pressure measurements for turbulent flow in the circular duct are presented in Figure 3.21 in terms of the pressure coefficient and are qualitatively similar to those measured in the rectangular duct. Four variations of C_{p*} with X were measured along the centreline of the four surfaces corresponding to the wall at r* = 0.0 and z* = 0.0, z* = -1.0 and r* = 0.5, r* = 1.0 and z* = 0.0, and along the z* = 1.0 wall at r* = 0.5. The upstream and downstream influence of the geometry, approximately one hydraulic diameter, are evident as in the previous tests, *Taylor et al (1981b,1984)* and *Rojas et al (1983a,c)*, with both cross-sections. The static pressure gradients in the

circular cross-section duct, as in the rectangular duct, are typical of flow in single bends and have an obvious influence on each other between the bends in the S-duct and between the two S-bends. Since no spacer separated the circular cross-section duct and diffuser, the pressure characteristics at X=10.5 and 12 have been interpolated by dotted lines. The static pressure coefficient differences across each of the bends in the first S-duct have maxima of approximately 0.26 C_{p^*}, which are similar to those in the corresponding rectangular S-duct investigated by *Taylor et al (1981b)* and *Rojas et al (1983a)*, with a pressure drop through the S-duct of about 14 % of the velocity head ($\rho_f V_B^2$). In the S-diffuser, the C_{p^*} variation was again similar to that in the rectangular diffuser with a pressure recovery of around 0.2 $\rho_f V_B^2$, causing an overall pressure rise of about 6 % of the velocity head across the entire duct length. The wall static pressure measurements re similar to those of *Taylor et al (1984)* and *Rojas et al (1983c)* to within the accuracy of the manometer. As observed in the rectangular S-diffuser, the circular cross-section static wall pressure results gave little indication of the perturbation of the inlet into the diffuser though close inspection of the diffuser pressure results along the $r^* = 1.0$ wall again revealed a slightly skewed distribution relative to those measured at the outer and inner curved duct walls, a consequence of disturbed inlet flow conditions and associated secondary flow generated in the first S-duct.

Mean streamwise and radial velocities were measured along the centreline of the diffuser and at the exit. To measure the radial component, the beams were oriented 90° to the streamwise direction and ray-tracing techniques were employed to resolve the position of the measuring volume and the beam angle, as described by *Bicen (1981), Rojas et al (1983c)* and *Taylor et al (1984)*. Figure 3.22, shows that the streamwise mean velocity decreases linearly as the cross-sectional area increases along the diffuser, from 0.96 V_B at the inlet to 0.82 V_B at the exit. The single S-diffuser displayed a identical decrease along the centreline but from a higher initial level of 1.05 to 0.91 V_B. The differences in the levels are due to the deflection of the uniform velocity core toward the $r^* = 0.0$ wall by the S-duct and the cross-section area expansion. The radial mean velocity, Figure 3.23, decreases from $0.02V_B$ at the inlet to $-0.05V_B$ at $X^*=2.9$ and subsequently increases to 0.015 V_B at the exit, as in the rectangular diffuser. The single S-diffuser turbulent results are similar but with a drop from 0.01 to - 0.9 and rise to 0.01 at the exit. The larger magnitudes of the cross-flow velocity in the inlet, middle and exit

of the bend are the result of the upstream bend and the pressure driven secondary flows that it generated. Unlike in the turbulent flow in the rectangular duct, the increase in the magnitude at the exit implies an increased effect of the upstream S-duct generated secondary low as it progresses downstream.

The centreline variation of the streamwise and radial components of turbulence intensity are shown in Figures 3.24 and 3.25. The axial intensities decrease from 0.053 to 0.043 V_B at the exit, Figure 3.24, and those based on the cross-section normal stress were constant through the diffuser at a magnitude of approximately 0.043 V_B, Figure 3.25. The relatively constant turbulence intensities are in contrast to the increase found in the rectangular cross-section double S-duct discussed in the previous section and results from the different migration of the near-potential core flow region through the ducts in the two geometries. The centreline variation of the two components of turbulence intensity in the single S-diffuser was constant in both cases at a level of approximately 0.015 V_B of the inlet bulk, which was slightly larger than the 0.01 V_B recorded in the single rectangular diffuser.

Contours of the streamwise mean velocity at the exit plane of the circular cross-section diffuser are shown in Figure 3.26 with dashed lines representing extrapolation between measurements spaced greater than 5 mm apart and the solid lines linear interpolated between measurements closer than 5 mm. The measured maximum and minimum streamwise velocities were 0.86 and 0.42 V_B respectively. Asymmetry about the r*= 0.5 plane is evident but less pronounced than in the rectangular duct exit contours. Unlike the rectangular cross-section, the upstream bend deflects the bulk streamwise flow toward the r*= 1.0 wall. In the single S-diffuser of circular cross-section, velocities from 0.9 to 0.3 V_B were measured at X* = 5.01. The narrow range in exit velocities in the double S-bend was a result of the redistribution of the mean streamwise flow by the substantial pressure driven secondary flow produced in the 45°/ 45° bend and turbulent mixing. The cross flow was sustained in the diffuser with the aid of the cross-section shape and resulted in the core maximum convecting toward the r* = 1.0 wall which was not evident in the rectangular case.

The streamwise turbulence level contours at the duct exit are shown in Figure 3.27 with a maximum of 0.097 V_B, located around z*=-0.4 and r*=0.6. As displayed in

the streamwise mean velocity contours, the breakdown of the plane of symmetry at r* = 0.5 is evident and results from the pressure driven secondary motion at the inlet to the diffuser. The turbulence intensities in the single S-diffuser varied between 0.08 and 0.02 V_B at the measuring station closest to the exit, X*=5.01 and those at the exit to the combined S-diffuser were generally higher, between 0.09 and 0.04 V_B, which can be attributed to perturbed inlet conditions prior to entry to the diffuser as in the rectangular cross-section. A notable feature was that the minimum turbulence intensity did not coincide with the maximum streamwise peak and again this was attributed to the strong cross-flow vortices established in the upstream duct and turbulent mixing.

The radial mean velocities along the z* = 0.0 axis at the exit plane have a maximum value of around 0.034 V_B at r* = 0.4 and a minimum of -0.27 at r* = 0.8. The secondary motion indicates a large vortex rotating around the near-core peak in the bottom right of the exit plane and a much smaller vortex rotating near the r*=0.0 wall.

The influence of the downstream S-diffuser, on the strong counter-rotating secondary flow vortices generated in the upstream S-duct, assists the breakup and turbulent mixing of the pressure generated vortices downstream along with the increased turbulence intensities of the multiple duct arrangement, but this was not sufficient to move the near-core flow significantly off the centreline in the circular cross-section duct as in the rectangular duct. The pressure driven secondary flows of the circular-cross section diffuser compliment and counteract the vortices established in the upstream duct which resulted in one vortex, in the lower right half of the exit plane, rotating clockwise, to appear to expand as the others are suppressed and broken down by turbulent mixing. As in the rectangular duct, the enlarged vortex was not in the boundary layer which naturally tend to grow with distance along the duct. This was in marked contrast to the result in the rectangular cross-section duct and a consequence of the effect of the diffuser pressure gradient on the large induced secondary flow from the upstream 45°/45° S-duct.

3.4 Concluding Remarks

Comparisons of the present measurements with those obtained in the single S-duct and S-diffuser configurations of *Taylor et al (1981b) 1984)* and *Rojas et al (1983a,c)* show that the effects of the non-uniform conditions at the inlet of the second S-bend diffuser on the flow at the exit of the out-of-plane double S-bend ducts has been quantified. The conclusions resulting from the experimental investigation of out-of-plane double S-bend ducts are summarized as follows:

1. The laminar flow in the exit plane of the rectangular cross-section diffuser has large asymmetries with at least six cross-flow vortices due to the perturbed inlet conditions, the recovery in the downstream tangent was very slow.

2. Pressure characteristics of the turbulent flows in the rectangular and circular cross-section ducts are similar to those measured in single bends but with a combined reduction in the pressure recovery at the exit of the diffuser because the constant cross-section duct causes a decrease in the pressure coefficient which was later recouped in the diffuser. The rectangular and circular diffusers both displayed some slight side-to-side (outer and inner surface of the bend) asymmetry caused by the perturbed inlet conditions and strong secondary flow.

3. The turbulent flow results show that the flow patterns at the exit of the rectangular duct were complex, with up to six cross-stream vortical motions in evidence. The flow patterns are strongly asymmetric with large variations and gradients of velocity throughout the duct cross-section. The superposition of the pressure-driven secondary flows generated in the rectangular S-ducts, displayed schematically in Figure 3.28, resulted in the large counter-clockwise rotating vortex in the upper left corner in a region of low streamwise velocity.

4. The flow in the diffuser duct of circular cross-section showed a migration of the core from the geometric plane of symmetry towards the outer wall of the bend due to the strong cross-flow generated by the S-duct upstream bend. The superposition of the cross-flows in the circular ducts resulted in a clockwise rotating

vortex in the bottom right corner, Figure 3.28, which dominated the secondary flow circulating around the maximum streamwise velocity. The axial velocity, however, did not show large variations in the bulk mean and was always positive.

5. The turbulence levels at the exits from the present configurations are higher than in single S-bends and there is no near-potential flow region. The absolute values of turbulence intensities are, however, still small enough to suggest that there are no new qualitative or gross effects of turbulence other than the mixing and gradual breakup of the vortices.

6. No regions of flow detachment were observed throughout the experiments and, although it is possible that small pockets of incipient separation may have existed, the geometry of the ducts was such that the high momentum fluid following an approximately straight-line path through the ducts will re-energize the flow and tend to suppress separation along the inner curved wall in the diffuser exit where separation was most likely to occur.

7. It is evident that the inlet conditions and geometry control the development of the secondary flows and that the flows are predominantly pressure-controlled. The pressure distribution caused by the duct geometry determines the direction and magnitude of the bulk flow while turbulence dictated the mixing characteristics in the near wall region. The dominant cross-flow vortex was caused by the pressure driven secondary motion generated in the S-duct prior to the diffuser therefore demonstrating the significance of the inlet conditions on subsequent out-of-plane double S-bend duct flow.

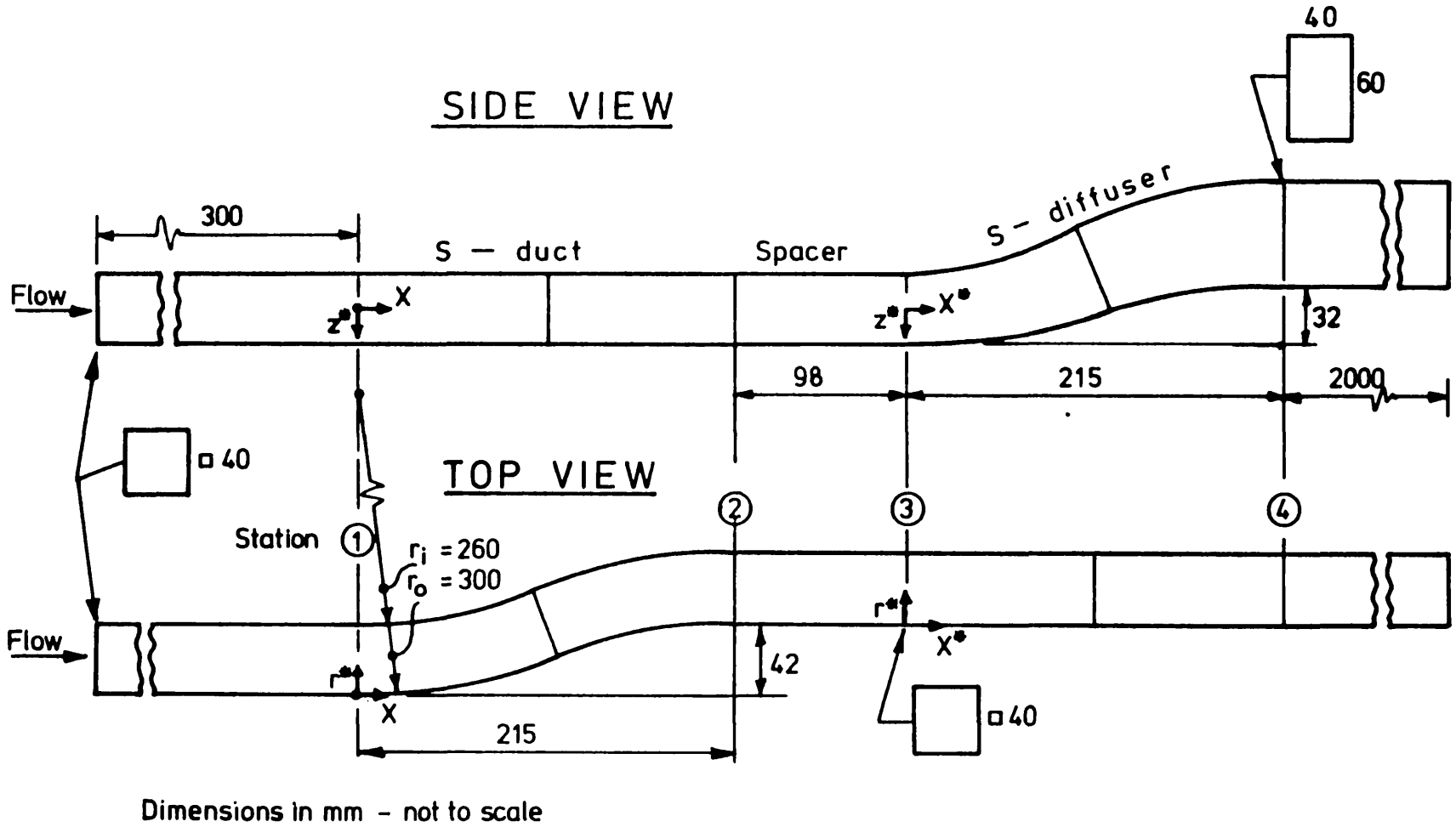


Figure 3.1(a) Rectangular duct: flow configuration and coordinate system.

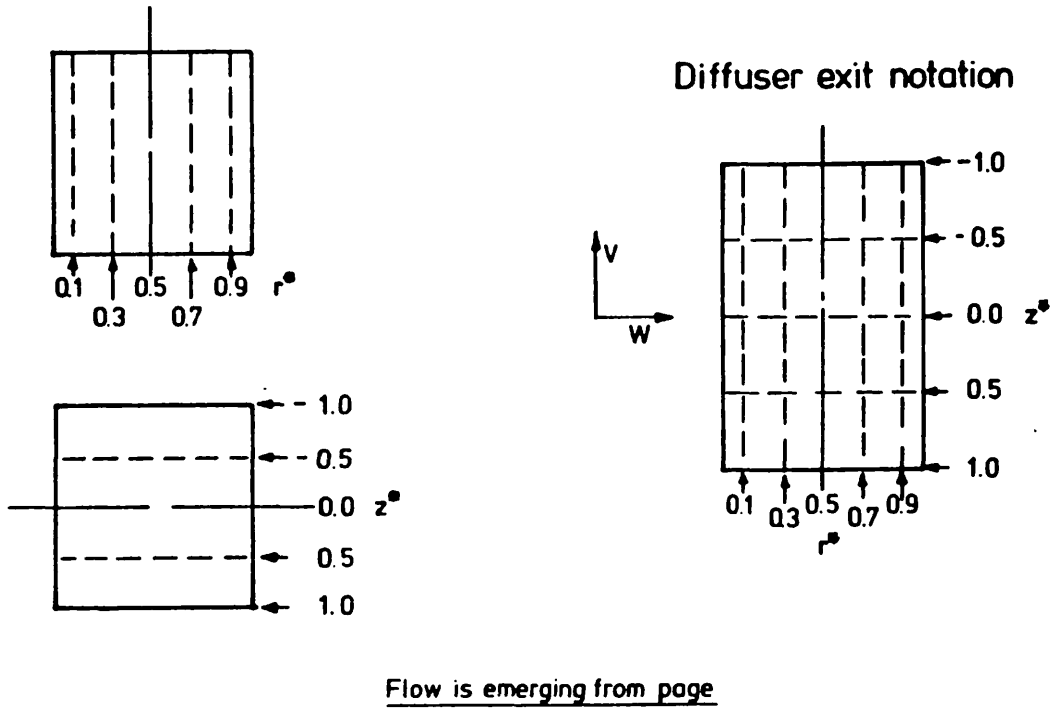


Figure 3.1(b) Rectangular duct: coordinate notation in duct and diffuser exit.

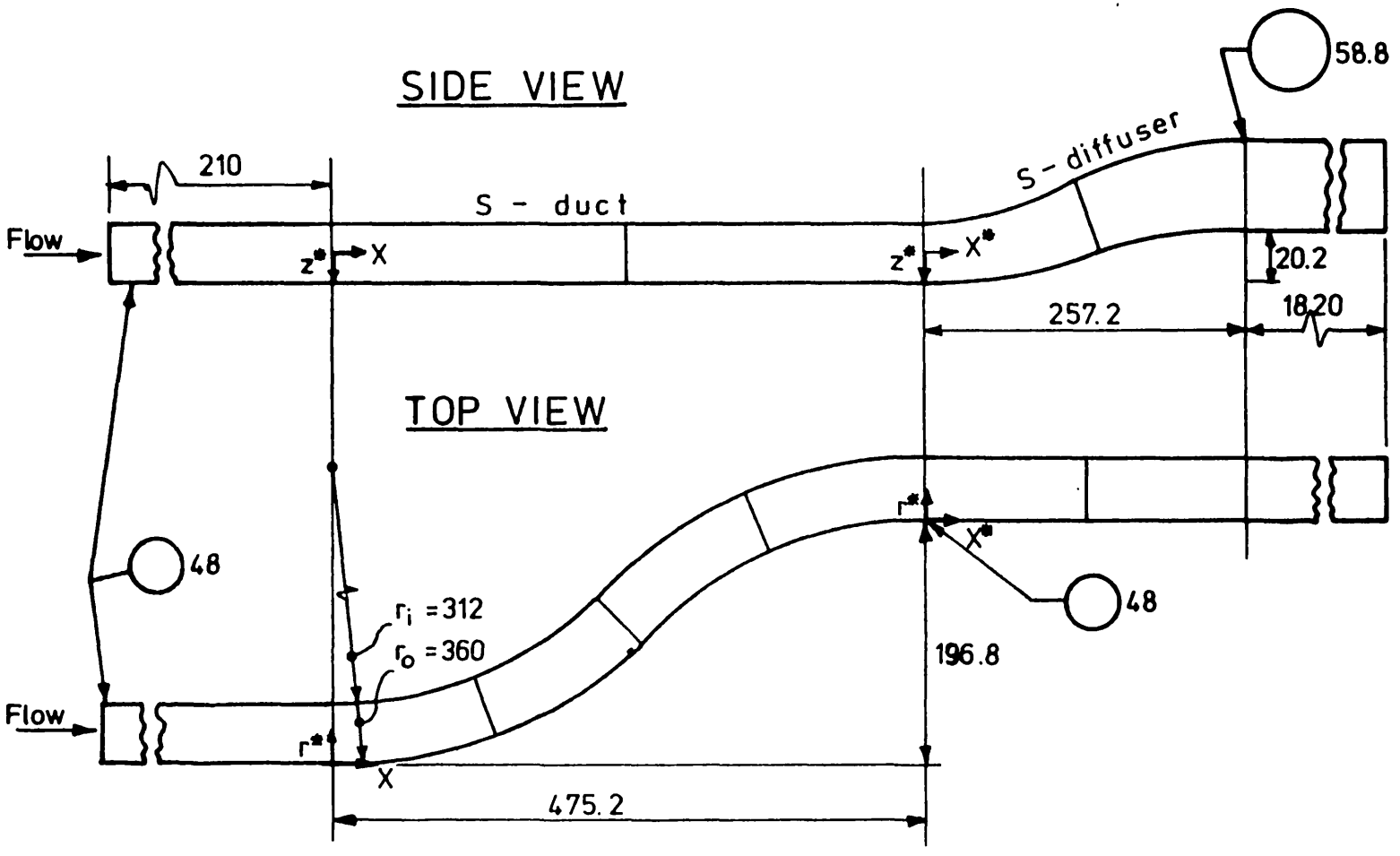


Figure 3.2 Circular duct: flow configuration and coordinate system.

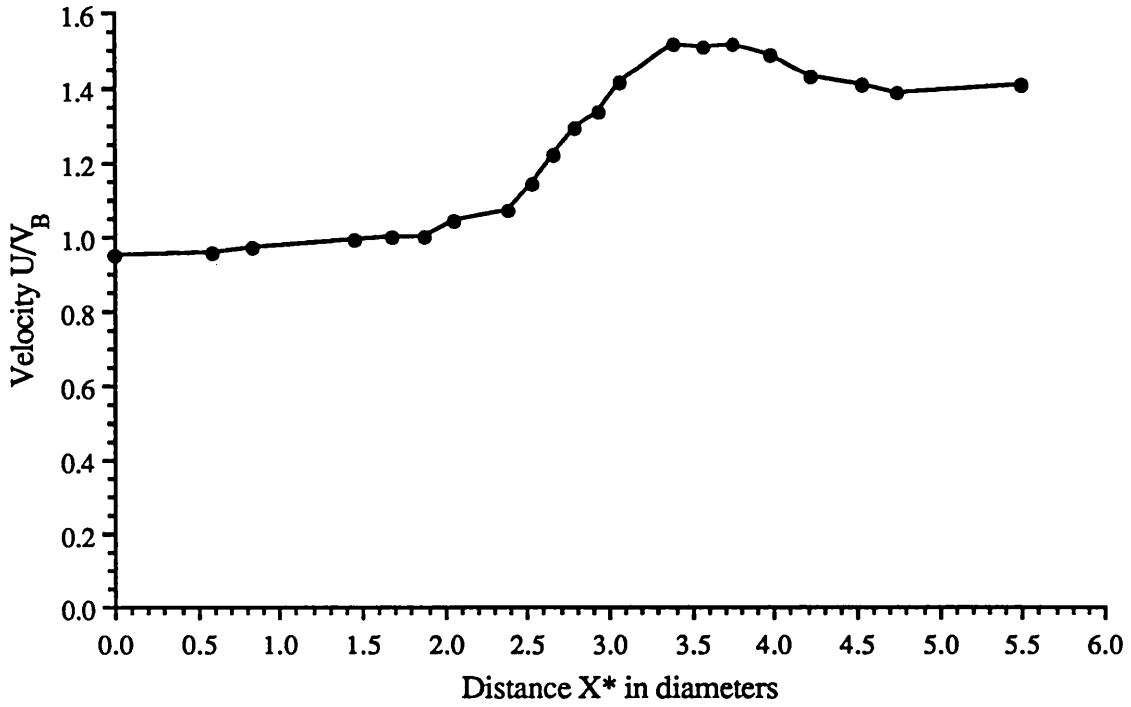


Figure 3.3 Rectangular diffuser: Laminar flow, centreline variation of U velocity.

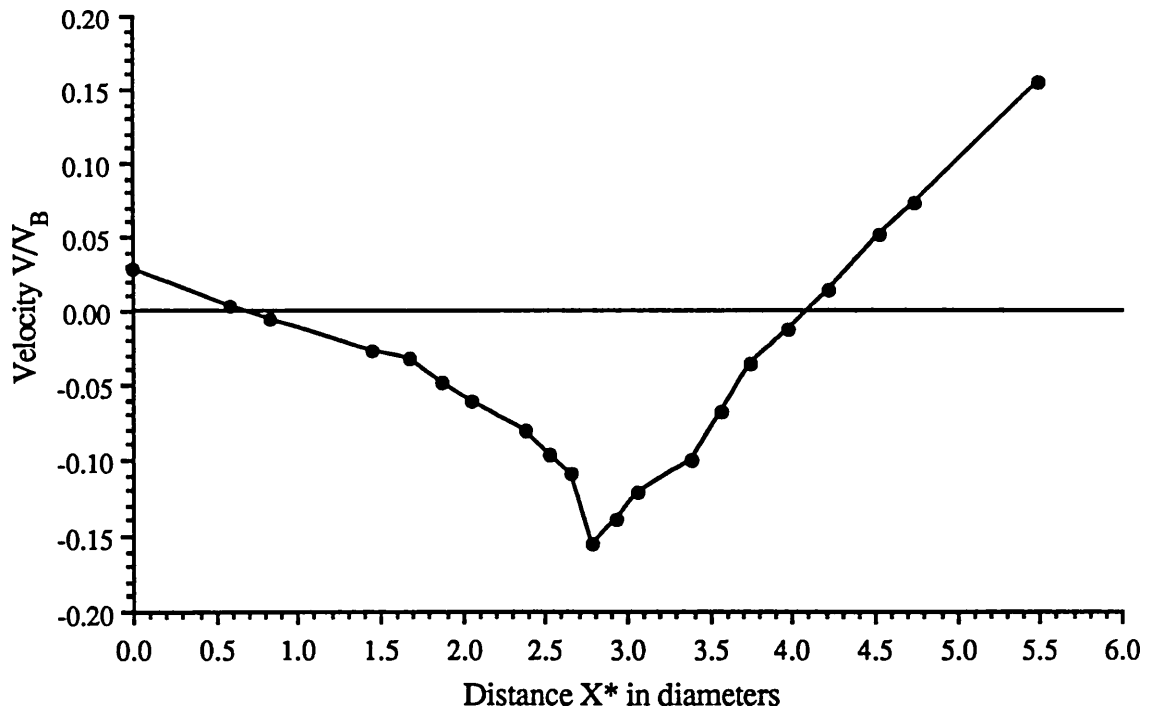


Figure 3.4 Rectangular diffuser: Laminar flow, centreline variation of V velocity.

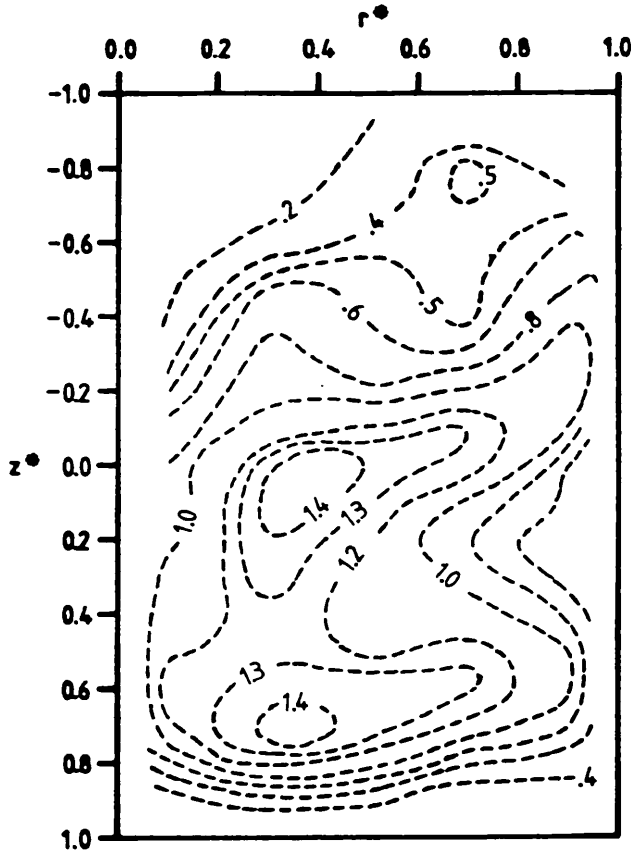


Figure 3.5 Rectangular diffuser: Laminar flow, contours of U/V_B at the exit plane.

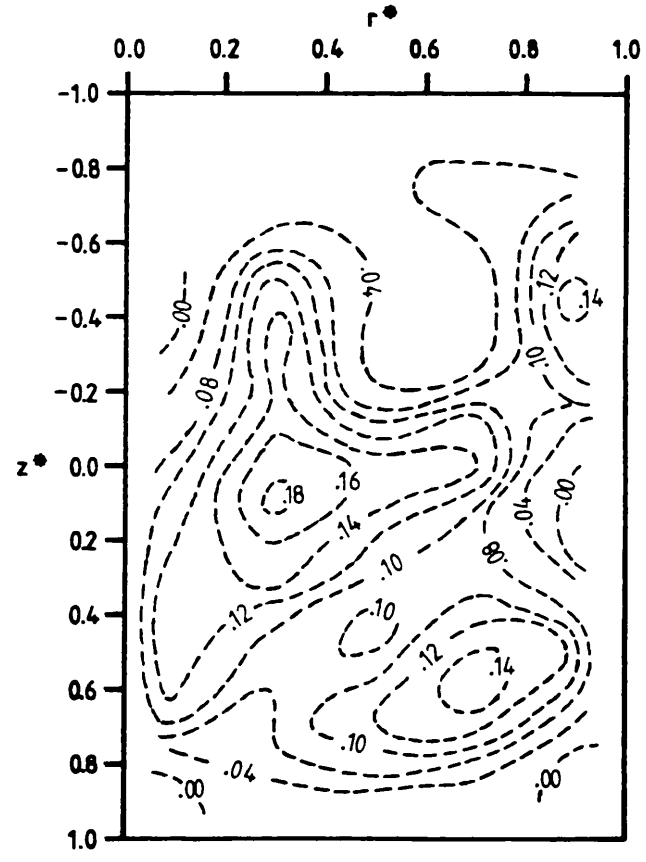


Figure 3.6 Rectangular diffuser: Laminar flow, contours of V/V_B at the exit plane.

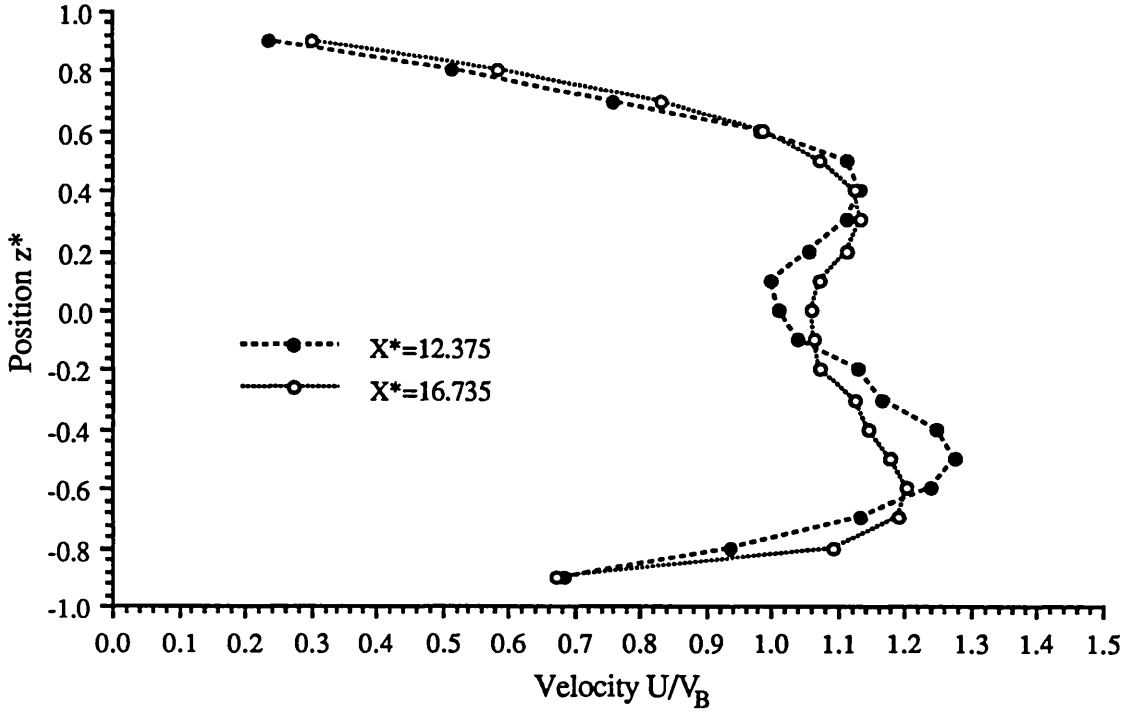


Figure 3.7 Rectangular diffuser: Laminar flow, profiles of U/V_B at X* = 12.375 and 16.735.

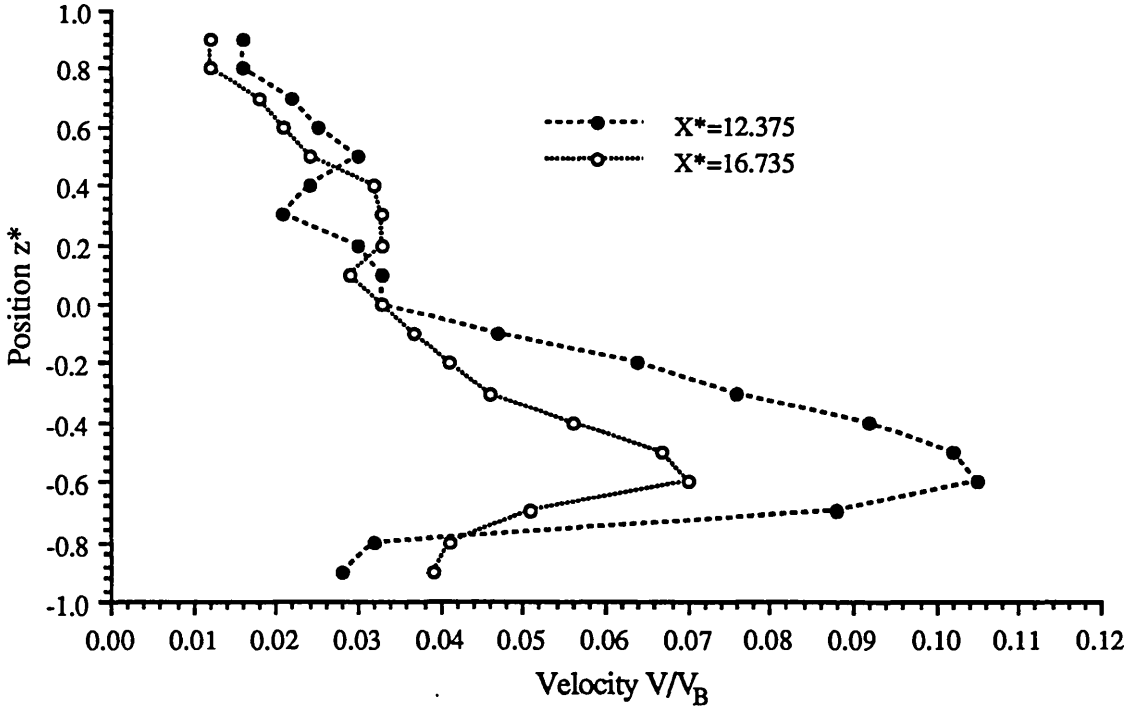


Figure 3.8 Rectangular diffuser: Laminar flow, profiles of V/V_B at X* = 12.375 and 16.735.

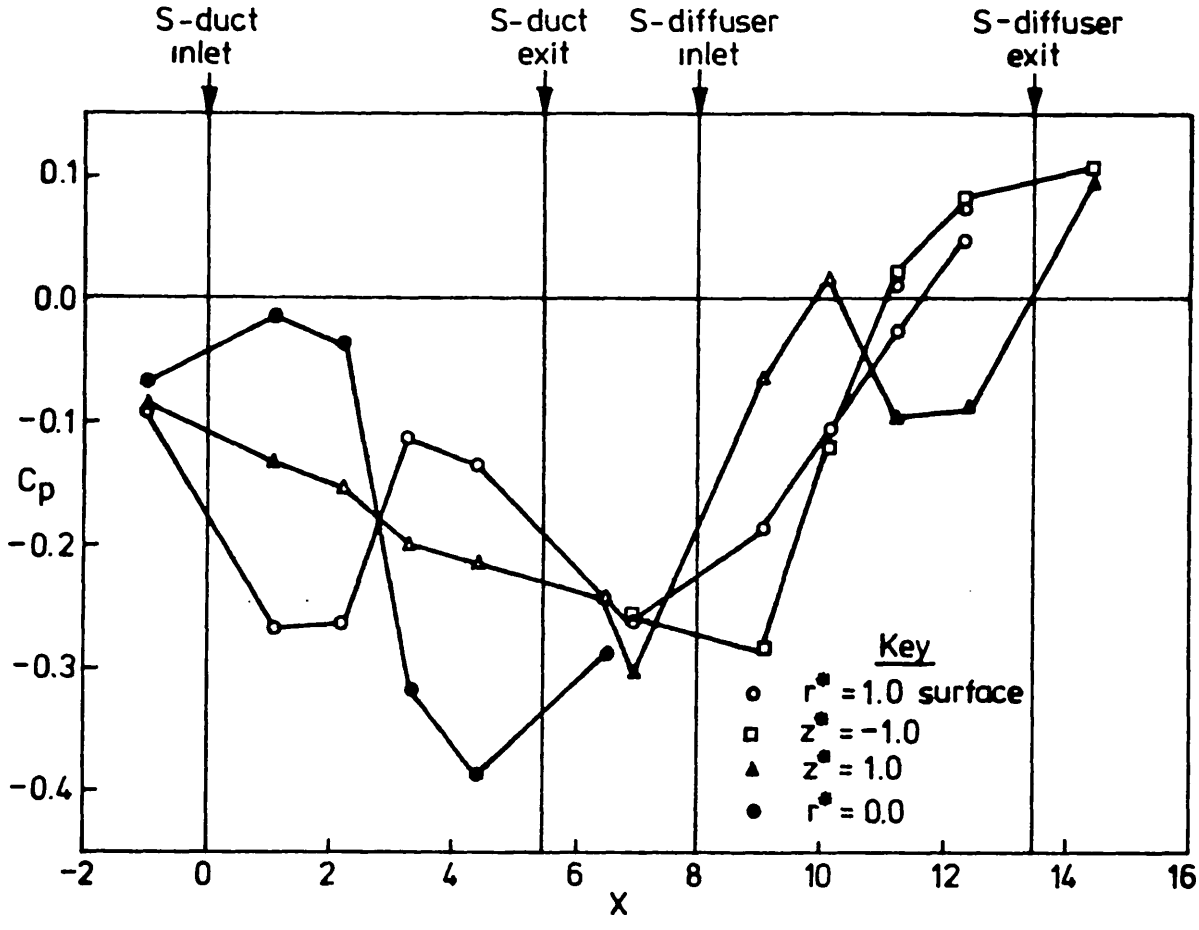


Figure 3.9 Rectangular duct: Turbulent flow, C_{p^*} variation along duct.

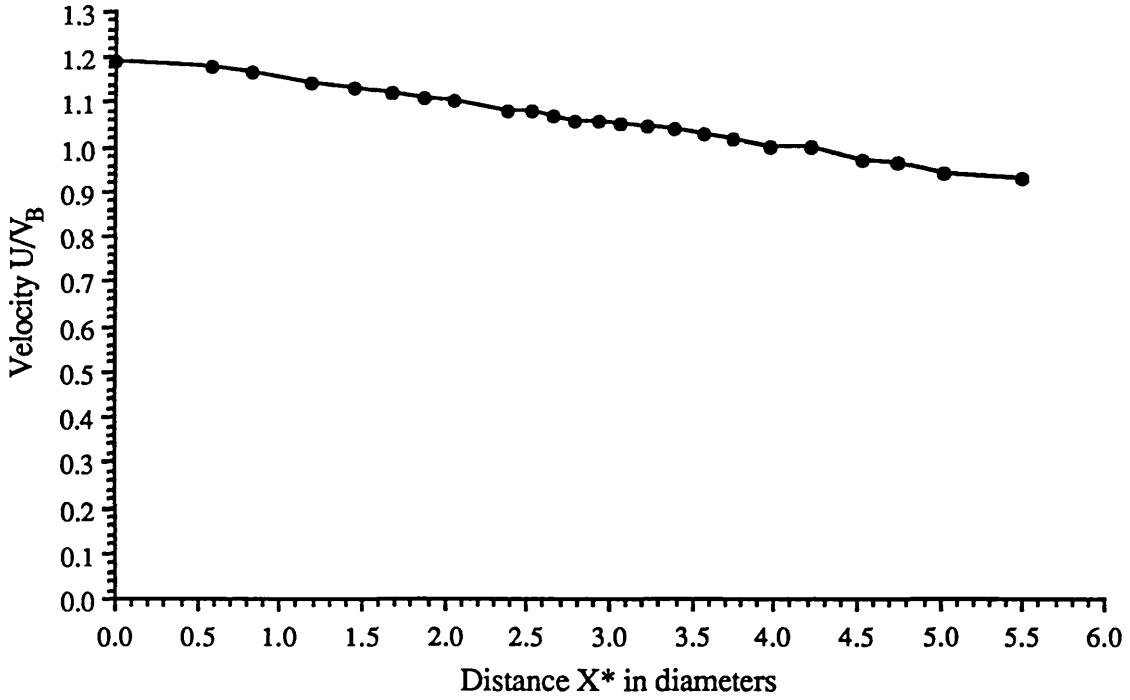


Figure 3.10 Rectangular diffuser: Turbulent flow, centreline variation of U velocity.

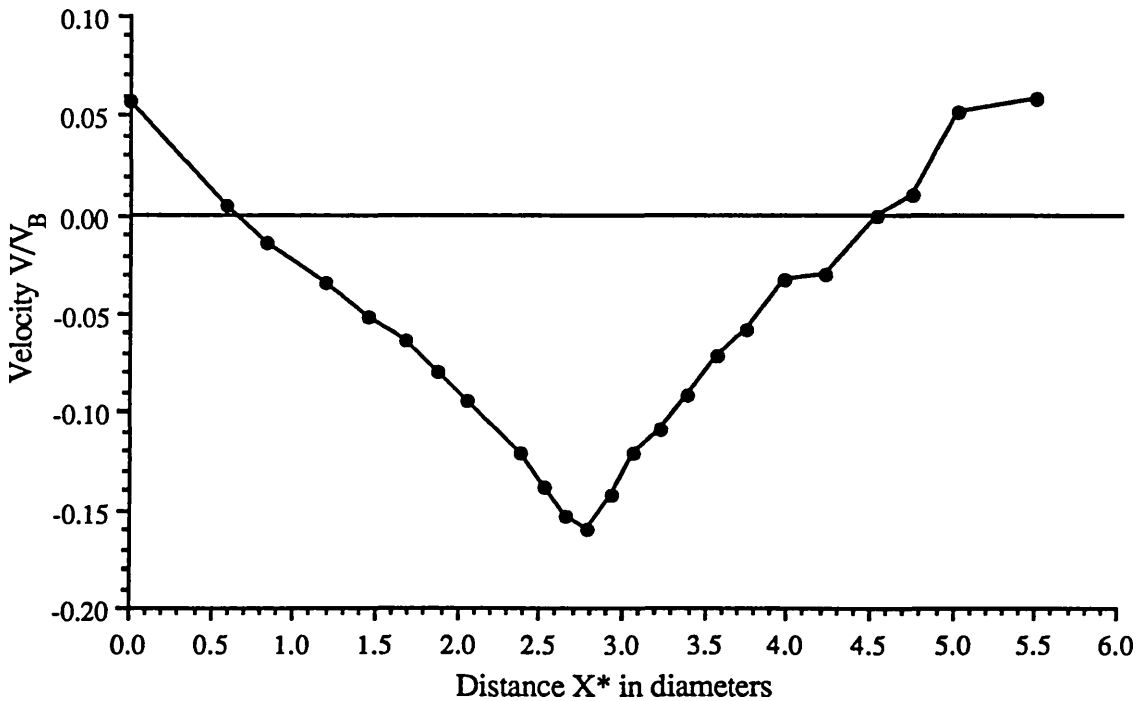


Figure 3.11 Rectangular diffuser: Turbulent flow, centreline variation of V velocity.

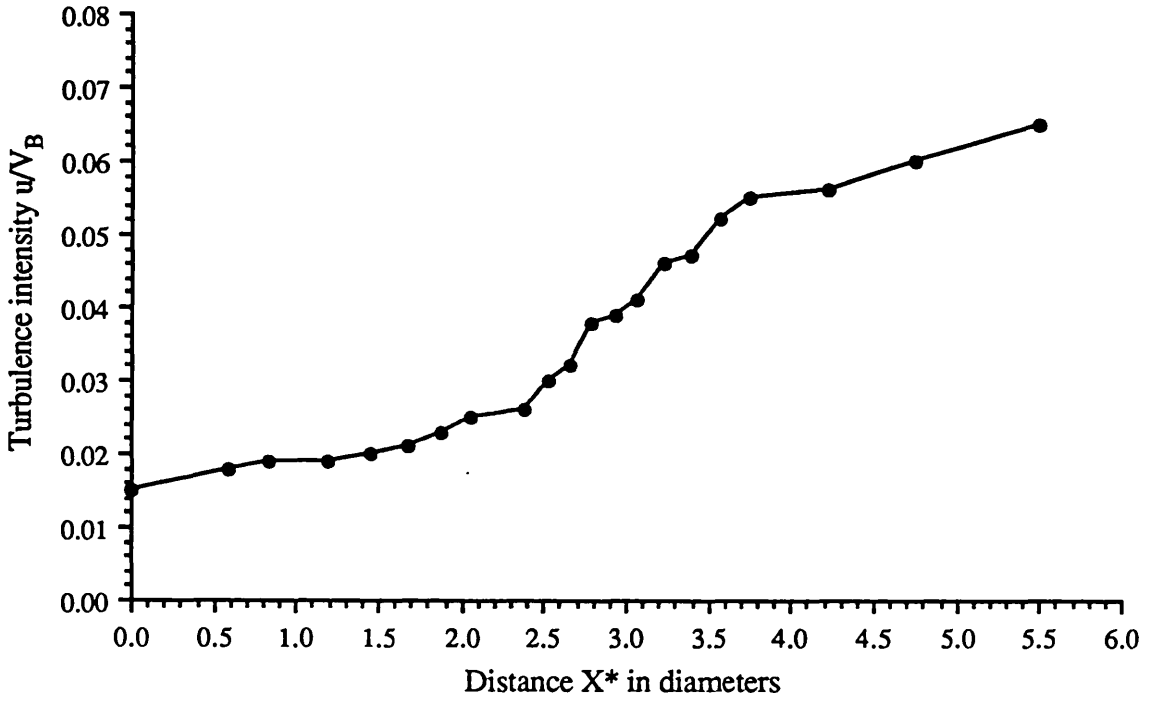


Figure 3.12 Rectangular diffuser: Turbulent flow, centreline variation of $\tilde{u}$ velocity.

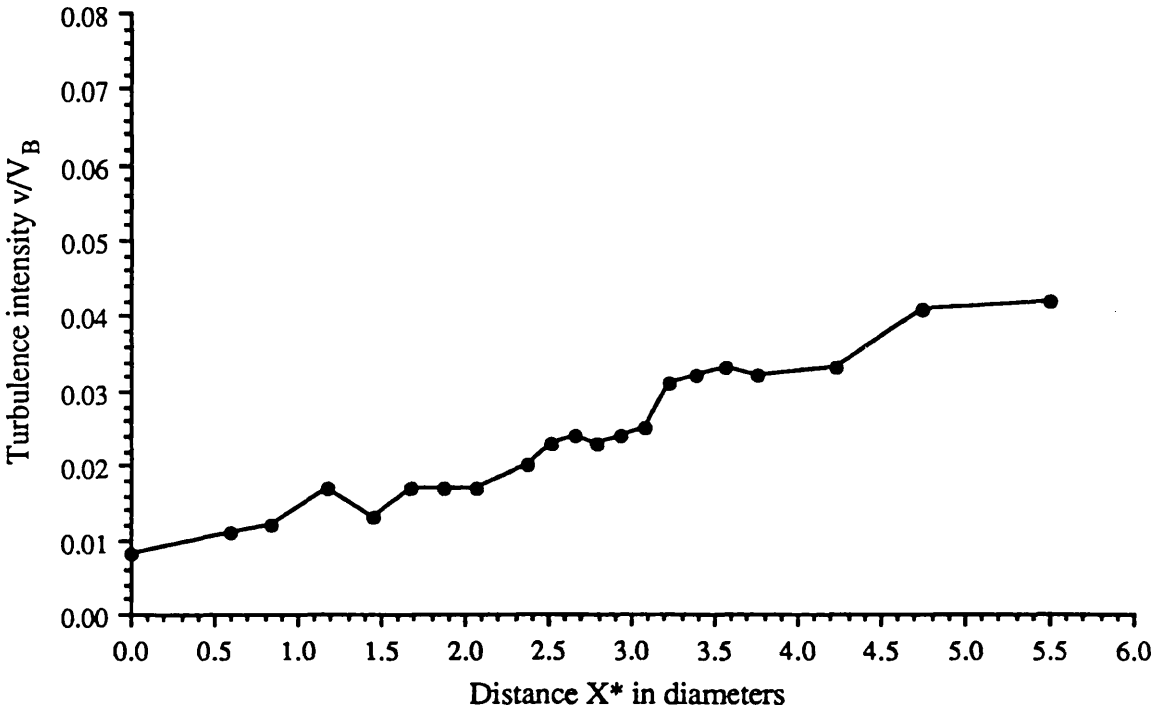


Figure 3.13 Rectangular diffuser: Turbulent flow, centreline variation of $\tilde{v}$ velocity.

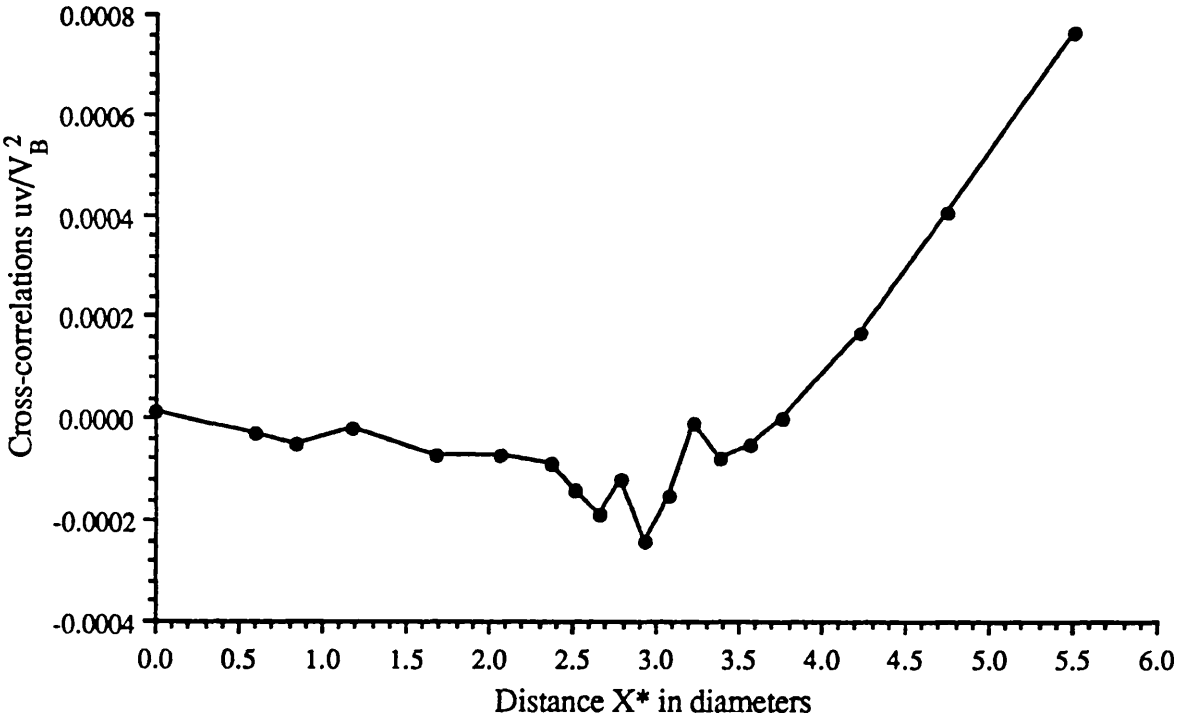


Figure 3.14 Rectangular diffuser: Turbulent flow, centreline variation of $\overline{uv}/V_B^2$.

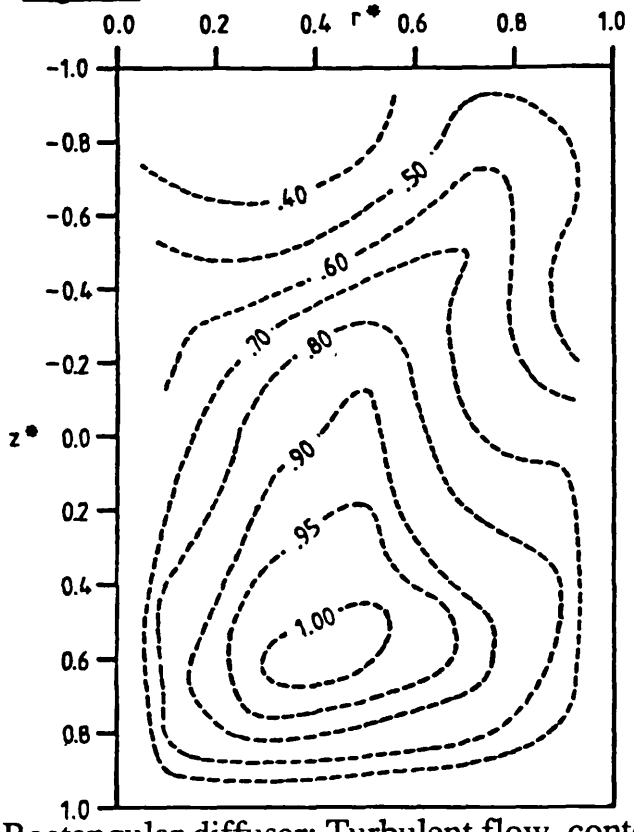


Figure 3.15 Rectangular diffuser: Turbulent flow, contours of U/V_B at the exit plane.

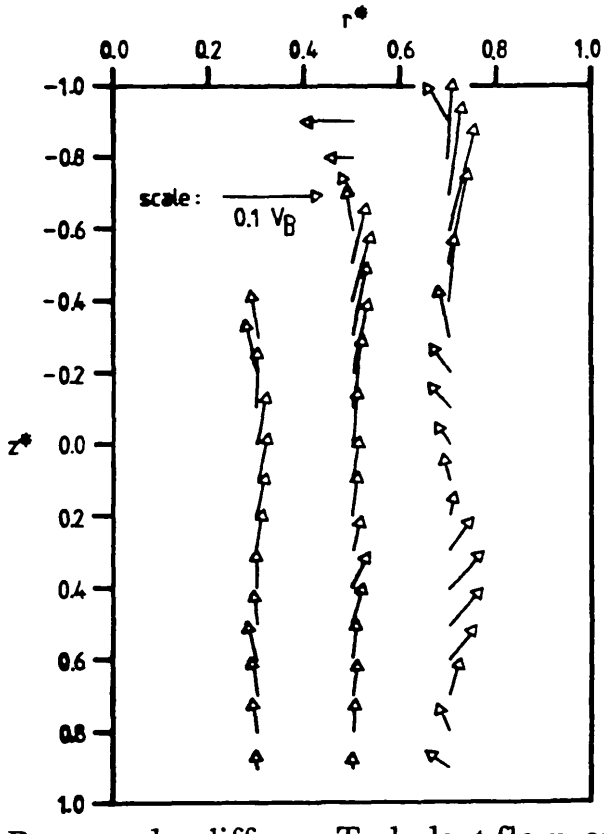


Figure 3.16 Rectangular diffuser: Turbulent flow, cross-flow vectors of V & W at the exit plane.

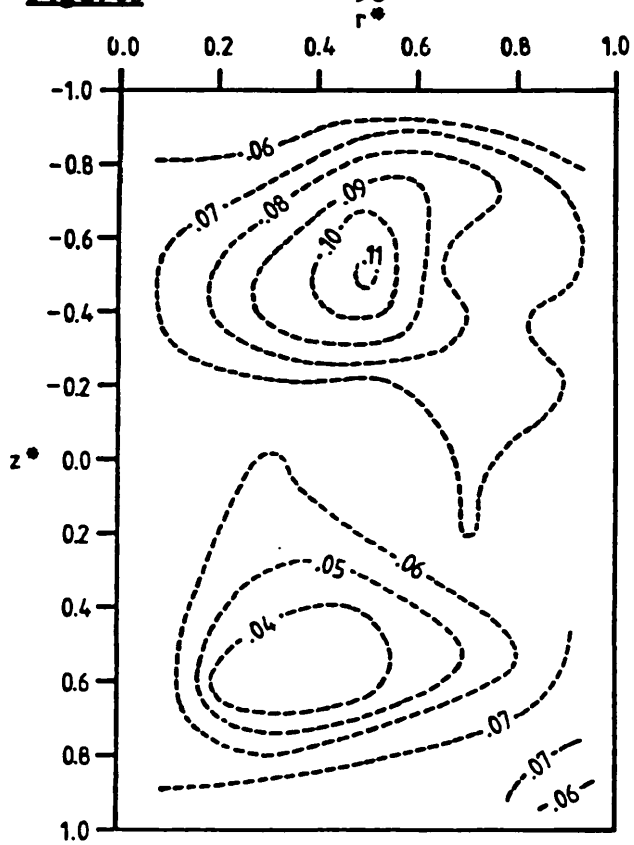


Figure 3.17 Rectangular diffuser: Turbulent flow, contours of $\tilde{u}/V_B$ at the exit plane.

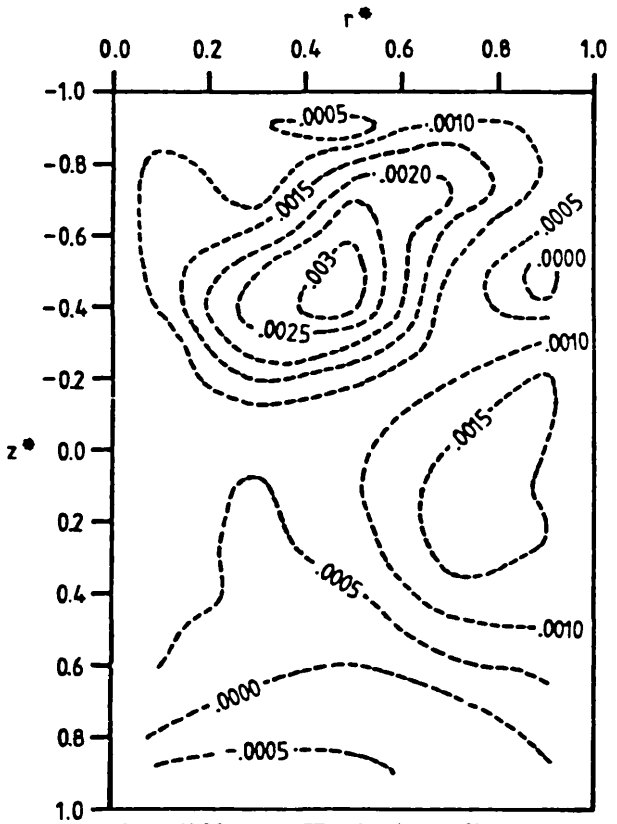


Figure 3.18 Rectangular diffuser: Turbulent flow, contours of $\overline{uv}/V_B^2$ at the exit plane.

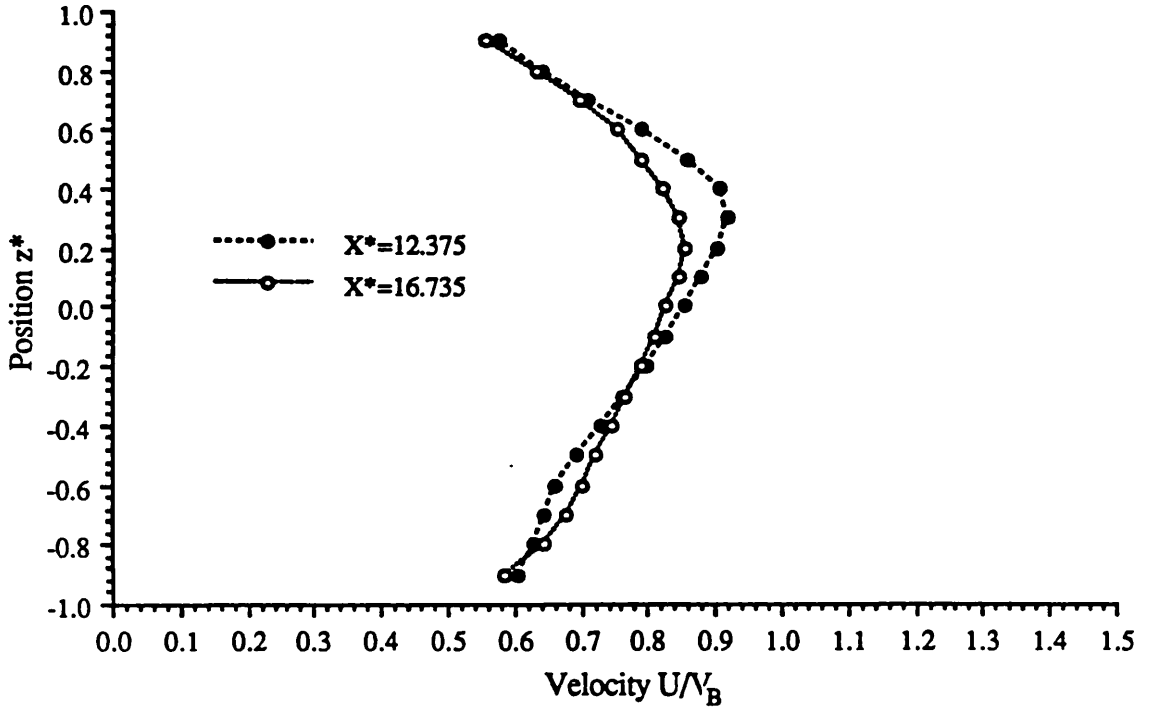


Figure 3.19 Rectangular diffuser: Turbulent flow, profiles of U/V_B at X* = 12.375 and 16.735.

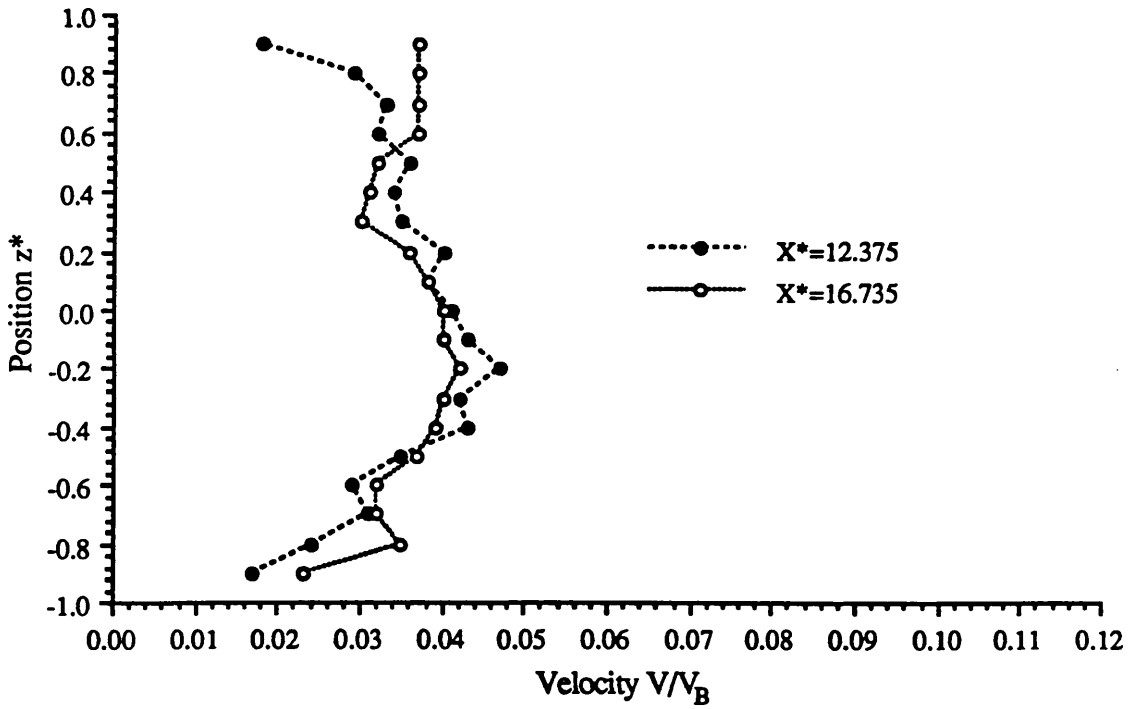


Figure 3.20 Rectangular diffuser: Turbulent flow, profiles of V/V_B at X* = 12.375 and 16.735.

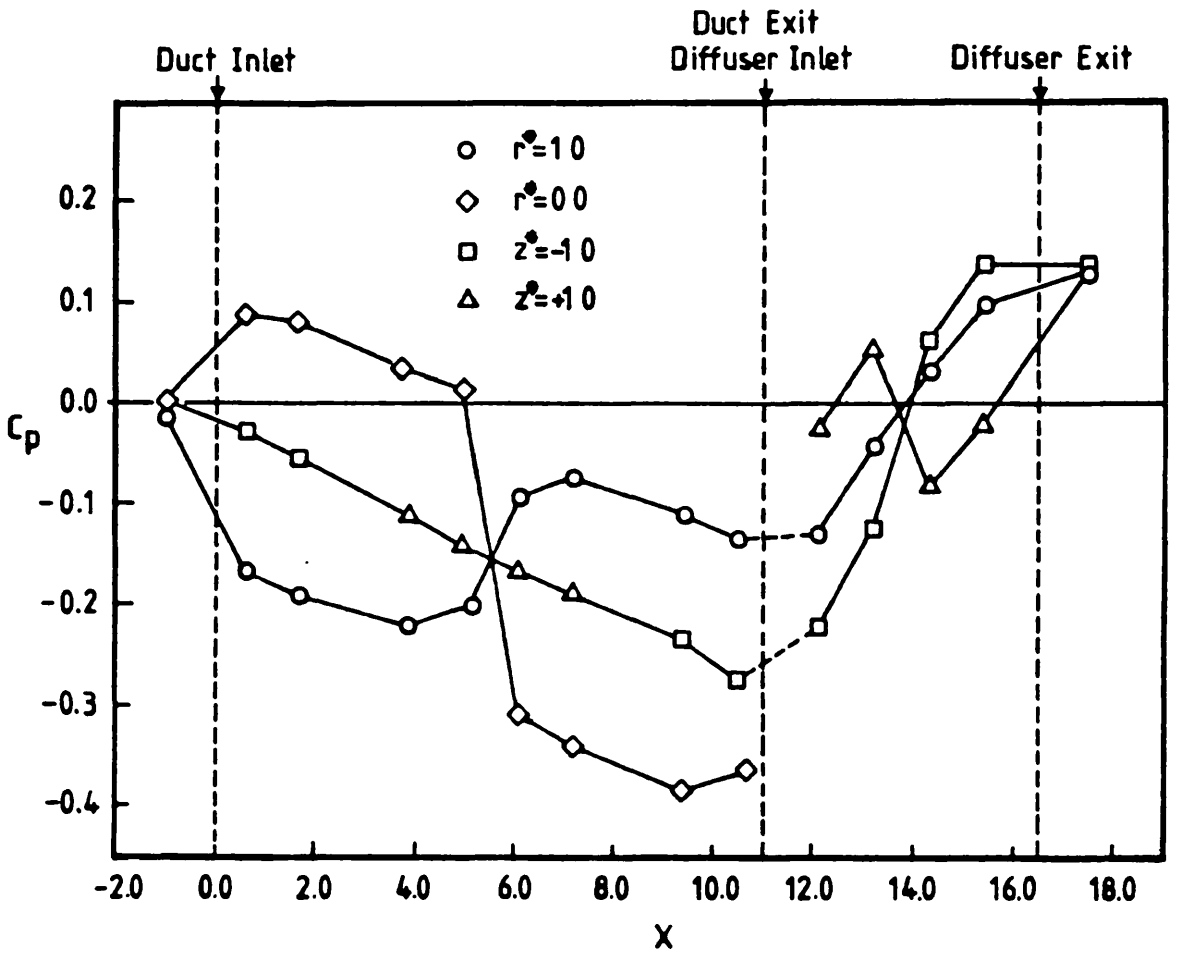


Figure 3.21 Circular duct: Turbulent flow, C_{p^*} variation along duct.

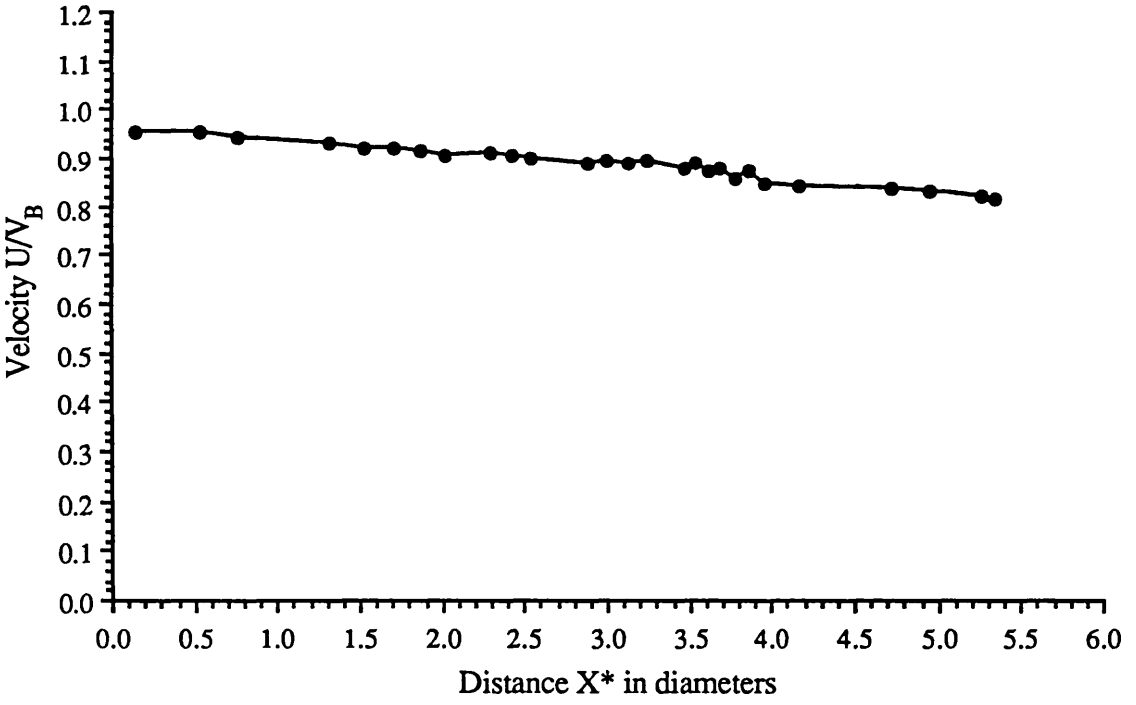


Figure 3.22 Circular diffuser: Turbulent flow, centreline variation of U velocity.

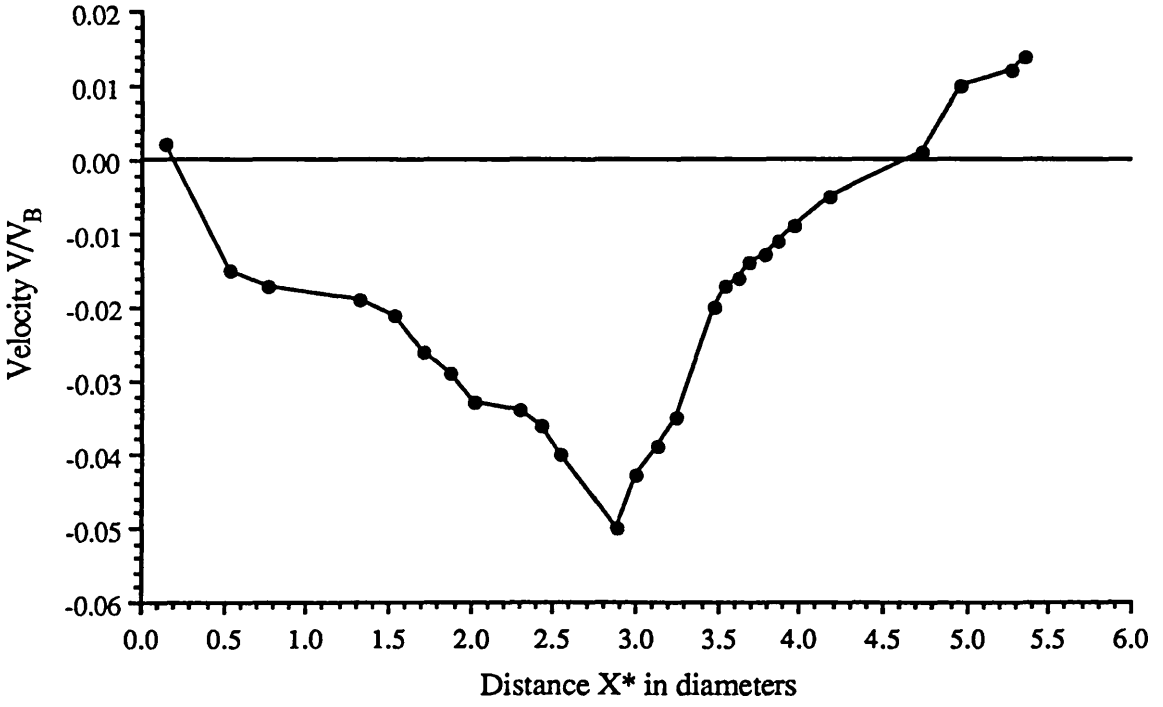


Figure 3.23 Circular diffuser: Turbulent flow, centreline variation of V velocity.

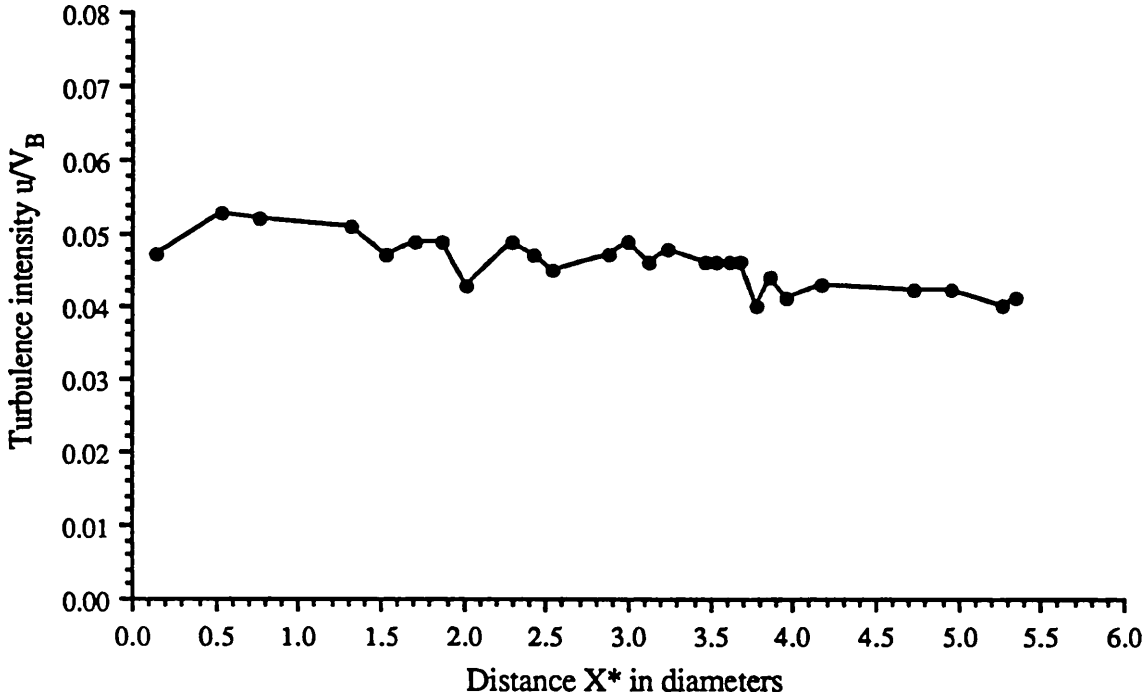


Figure 3.24 Circular diffuser: Turbulent flow, centreline variation of $\tilde{u}$ velocity.

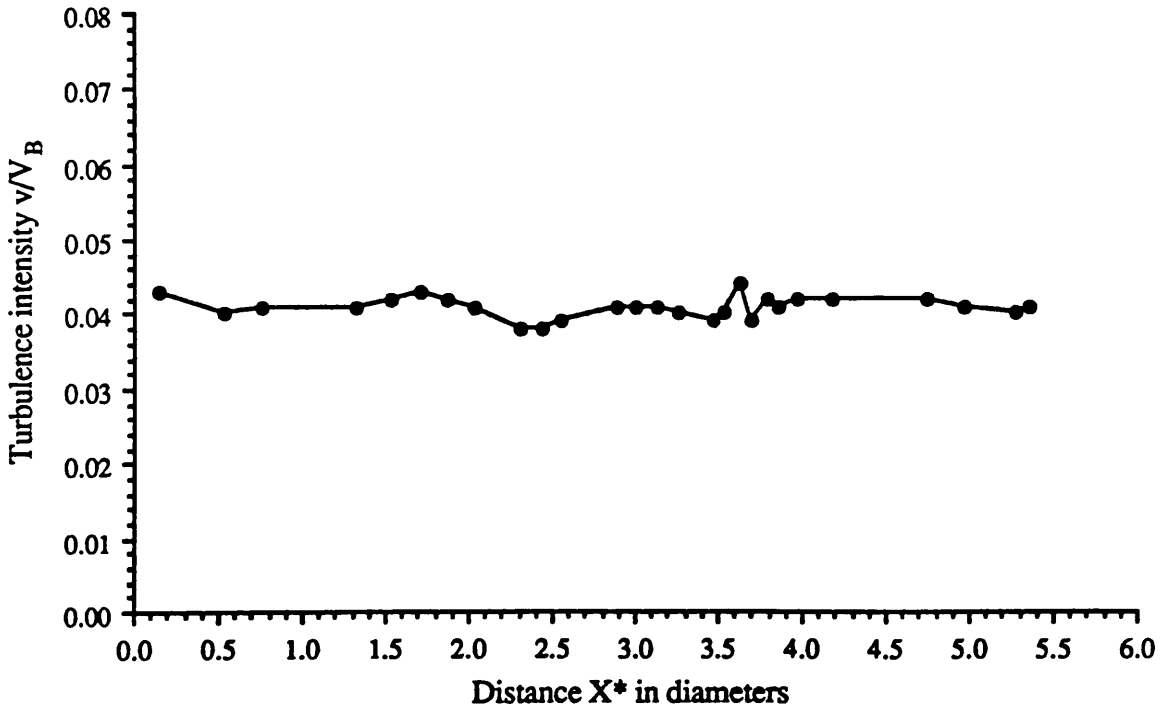


Figure 3.25 Circular diffuser: Turbulent flow, centreline variation of $\tilde{v}$ velocity.

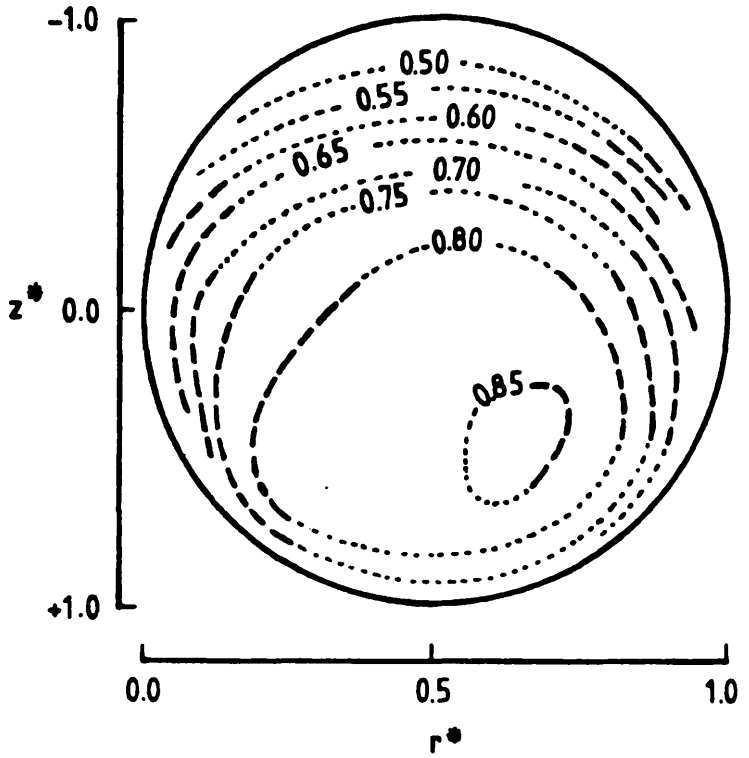


Figure 3.26 Circular diffuser: Turbulent flow, contours of U/V_B at the exit plane.

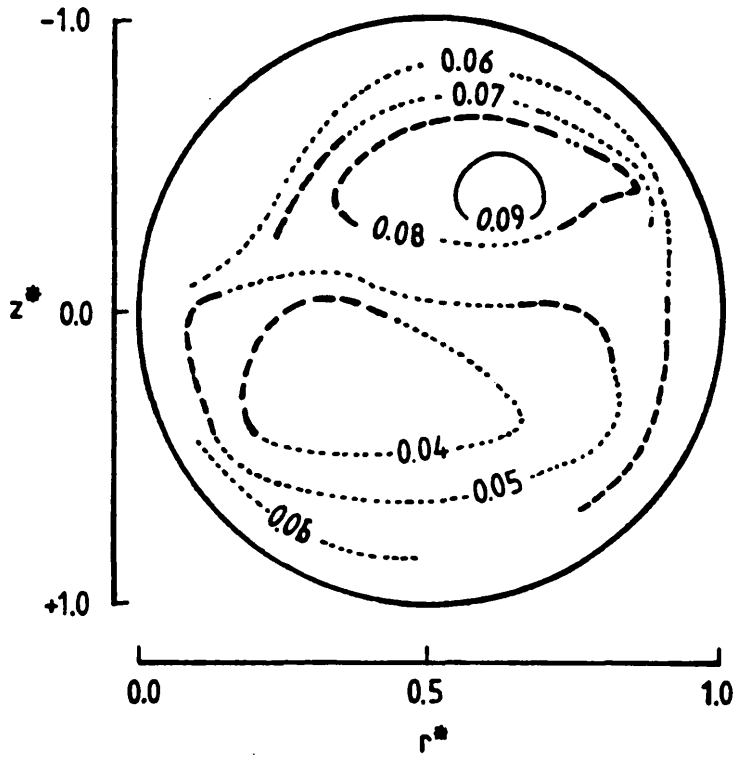


Figure 3.27 Circular diffuser: Turbulent flow, contours of $\tilde{u}/V_B$ at the exit plane.

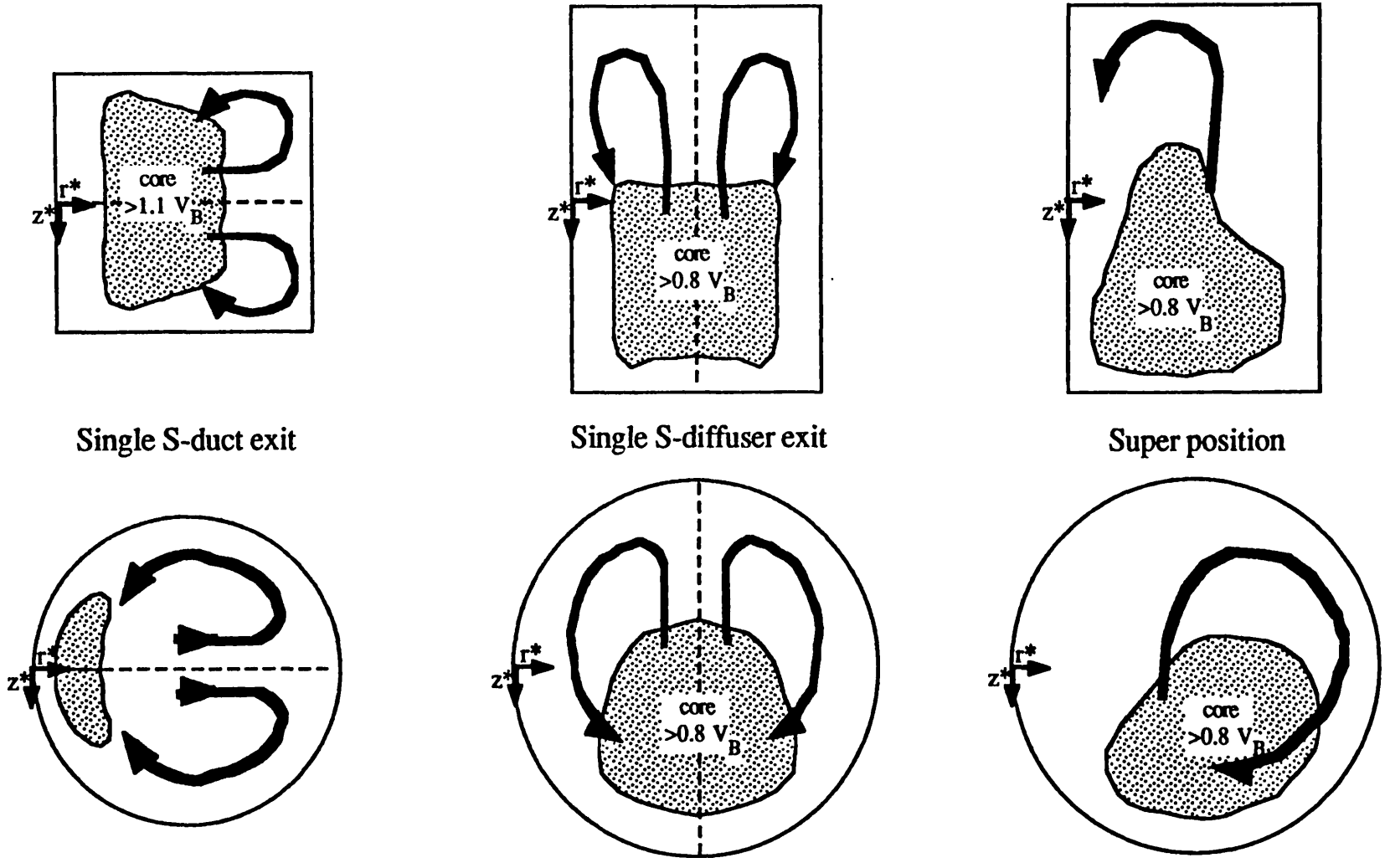


Figure 3.28 Super-position of S-duct and S-diffuser pressure driven secondary flow at the exit plane.

CHAPTER 4 LOW-SPEED GUN SIMULATOR

4.1 Introduction

This chapter is concerned with the experimental investigation of the unsteady multiphase flow in the low-speed gun simulator. The first section describes the constant-diameter and chamfered flow configurations, the mechanism which allowed the injection of the second-particle phase, the test section geometry and general operating procedures. In the subsequent results section, the measured and calculated dynamics of the projectile in the low-speed simulator are presented and followed by the measurements of the breech pressure, single- and two-phase flow velocities and heat transfer. The chapter includes a discussion of the results and their implications and ends with a summary of the more important conclusions.

4.2 Flow Configuration

As discussed in chapter 1, the real interior ballistic cycle can be modeled by the unsteady expansion of a compressible inert gas and this corresponds to the assumption that the propellant has completely burned before the projectile begins to move. The need for the characterization of the modeled gun cycle results stems from the need for better understanding of the interior ballistic cycle and for information with which to support the development of ballistic modeling codes and particularly those based on the numerical solution of the conservation equations in differential form. The experimental research at Imperial College into the area of ballistics led to the experimental apparatus of this chapter, *Khezzar (1987)* and *Bicen et al (1986b)* and has already allowed the single-phase velocity fluid to be examined with initial pressures up to 8 bar and a corresponding maximum projectile velocity of 40 m/s. In this investigation, the effects of a second phase is examined in terms of velocity and values of wall heat transfer are also reported.

Since the initial chambers of single-stage guns are generally either constant-diameter or chamfered, two interchangeable initial volumes of approximately the same capacity were used and Figure 4.1 shows the geometry of the low-speed simulator with

both initial chambers, together with the position of the measuring windows and the coordinate notation. The stationary part of the simulator comprises an initial chamber, the lock/release mechanism, the test section barrel, the muzzle and the retarder section. The initial chamber contains the gas charge in a quiescent state at the start of the cycle and this gas (nitrogen) acts as the preburned propellant for the modeled cycle. The lock/release mechanism holds the projectile by three pins resting on a cammed surface and releases the projectile when rotated. The test section barrel contains four pairs of plexiglass windows to facilitate the measurement of velocity by laser Doppler anemometry and incorporation of thin-film heat flux gauges. At the end of a cycle, the expanding gas behind the projectile was released to atmosphere through a series of holes in the muzzle section prior to the projectile entering the retarder where it was brought to rest without damage by the compression of gas in front of the projectile. The different parts of the low-speed simulator, displayed in Figure 4.1, are described in detail below.

The constant-diameter and chamfered initial chambers were machined from plexiglass and the particle injection mechanism and dimensions of the chamfered initial volume are shown in Figure 4.2. The chamfered initial chamber was used for most of the single-phase and all the two-phase velocity tests and had a total volume of 1736 cm^3 of which 230 cm^3 was occupied by the injection mechanism with 6 cm^3 occupied by solid particles in the two-phase tests of 4 % initial concentration. The injection mechanism consisted of a plate and spring arrangement which was filled with 500 μm mean diameter plexiglass beads. The second-phase injection system utilized two slightly different plates which enabled tests with concentrations of 1.3 % and 4 % of the initial volume to be conducted, and the dimensions of each are shown in the top of Figure 4.2. The 1.3 % and 4 % by volume concentrations correspond to mass loadings of about 2.3 and 6.9 respectively. The 1.3 % plate had twelve cylindrical holes of 14 mm diameter while the 4.0 % plate had twelve conical holes which contracted from 30.5 mm to 14 mm over the 13 mm plate thickness. The holes containing the particles in the injection plate were sealed on the bottom by spring-loaded cones which retracted when the projectile was released to allow the particles and gas from above the plate to flow into the breech and follow the projectile as it traverses the test section. The number of holes in the injection plate, their distribution, cone angle and the particular chamfered geometry were chosen to cause the particle distribution in the chamber to be as uniform as possible. The volume above the disk was less than 5 % of the initial volume and

assisted the particle injection with a relatively small contribution to the expansion process. Thus, the effect on initial boundary conditions was small with the initial flow assumed to be close to quiescent.

The shape of the initial volume had previously, *Khezzar (1987) Bicen et al (1986c)*, been shown to have little effect on the bulk-flow characteristics of the flow in the barrel but it can be expected to have some effect on the distribution of the particles with their high density (1180 kg/m^3) and consequent inertia. The single-phase flow experiments with the chamfered chamber were performed with the plate and spring arrangement in the initial volume but without the 500 μm particles. The nitrogen gas (zero grade) was pressurized within the initial chamber to 8 bar above atmospheric and, for the single-phase flow measurements, silicone oil droplets were added to the gas to scatter light and to represent the gas velocity.

The lock/release mechanism held the projectile in place against the initial volume o-ring seal, while the initial chamber was charged, by three pins resting on a raised cammed surface and protruding into the bore. When the initial pressure was attained and the instrumentation prepared for data acquisition, the lock/release collar was rotated and the pins dropped off the cammed surface and retracted from the barrel, allowing the projectile to move freely down the test section. The lock/release provided the mechanical trigger for the modeled cycle, similar to the ignition of the propellant in a real gun cycle, and allowed the projectile to be forced by the expanding gas and gravity to accelerate down the barrel without interference or cyclic variations as found in the case of the rack and gear mechanism of the previous simulator, *Bicen et al (1986b)*.

The test section comprised a 76.5 mm diameter smooth bore barrel of mild steel along which a 0.953 kg, 250 mm long projectile travelled approximately 1 meter. The design of the projectile, detailed in *Khezzar (1987)*, allowed the projectile position and velocity to be measured after the triggering of the cycle. A PTFE ring was fitted to each end of the projectile and prevented leakage of gas between the projectile and barrel. As the projectile accelerated down the test section, the measurement of pressure at the breech, fluid or particle velocity in the flow and barrel heat flux at one of the axial window was made behind the projectile in the expanding volume by the techniques detailed in section 2.3.

With an initial pressure of 8 bar, the projectile achieved a velocity of 40 m/s and traversing the entire test section in 33 ms, at which time it reached the muzzle region where the expanding gas charge was allowed to escape through the 1000 - 0.25 inch diameter holes. The projectile was further decelerated by the compression of air in the retarder and eventually came to a rest after rebounding several times into the test section and back into the retarder. With the aid of a sliding cover over the muzzle and a control valve fitted at the bottom of the retarder and connected to a compressed air supply, the projectile was returned to its locked starting position at the top of the barrel for a new shot. The test cycle was repeated for a sufficient number of times to obtain the required measurements to characterize the flow in the shot.

The photographs of Figure 4.3 and Figure 4.4 show the instrumentation in position around the test rig with the constant-diameter and chamfered initial geometry respectively. In the photograph of the constant-diameter arrangement, Figure 4.3, the anemometer was positioned at the third measuring window and the triggering laser situated below the lock/release trigger bar at the first window, perpendicular to the axis of the anemometer. For the chamfered geometry photograph, Figure 4.4, the anemometer was located at the first window for the detailed analysis of the boundary layer. A close-up photograph of the chamfered initial chamber is shown in Figure 4.5 with the injection plate mechanism clearly visible inside the chamber. The three hoses protruding from the top of the chamber supplied silicone oil droplet seeding, charge gas and pressure release by operating the hand valves in the lower left of the photographs of Figures 4.3 and 4.4.

As discussed in section 2.3, the 1 μm median diameter silicone-oil particles were used to allow measurement of the velocity of the gas flow and the 500 μm plexiglass particles were representative of the particle phase flow. In practice, intensive preliminary tests showed that the time-variations of pressure and projectile velocity were reproducible within the accuracy of the instrumentation so that it was necessary only to measure particle velocity traces and surface temperature changes for the heat flux measurements with intermittent checks of the breech pressure time variation.

4.3 Low-Speed Simulator Results

The results of the investigation in the low-speed gun simulator are presented in the following four subsections which quantify the dynamics of the projectile and breech pressure, single-phase velocity, two-phase velocity and transient heat flux.

4.3.1 Projectile Dynamics and Breech Pressure

The calculated and measured variations of projectile position and velocity are presented in Figure 4.6 - 4.8, for the constant-diameter and chamfered geometries. The method by which the projectile motion was calculated has been detailed by *Khezzar (1987)*, and assumes a one-dimensional unsteady isentropic expansion. In brief, the motion of the projectile can be determined by the application of Newton's law, which requires the projectile base pressure to be known. The pressure acting on the base of the projectile can be related to the breech pressure variation acting along a characteristics line if a one-dimensional unsteady isentropic expansion is assumed. The projectile motion in space can therefore be given as a function of the breech pressure record. The two resulting equations constitute a coupled set of simultaneous ordinary differential equations in the axial distance and the projectile velocity in terms of time and can be solved numerically, by a standard fourth order Runge-Kutta algorithm. If the breech pressure is assumed to vary according to the isentropic law during the expansion process, the pressure variation can be incorporated in the equations describing the projectile dynamics. The resulting equation is a first order non-linear, non-homogeneous ordinary differential equation representing an initial value problem and was solved numerically marching in space. The term for friction between the projectile and the barrel was assumed to be zero because no method to model it has been developed and the effect has been shown to be relatively small, less than 0.5 %, in previous investigations. The pressure of the gas in front of the projectile has been compensated for although the effect was negligible at the velocities prevalent in the low-speed simulator. The program employed to solve the dynamics of the projectile is listed in Appendix 4.1, and took into account the small delay in the characteristic waves resulting from the projectile motion, reflecting off the breech, moving back toward the projectile

base, with an assumed constant-diameter initial volume. For the low-speed simulator, the simple wave portion of the cycle was small and occurred while the projectile travelled approximately 12 mm or during the first 2.5 ms of the cycle.

The variations of calculated and measured projectile travel distance are displayed in Figure 4.6 in diameters from the initial position and, although the offset between the real and measured time scale was not compensated for, the calculated projectile position was with in the accuracy of the measurements, 2 %, and little different in the measurements in the chamfered and constant-diameter geometries. The projectile velocity as a function of the travel distance from the initial position, Figure 4.7, displays some differences between the calculated and measured results which occur because of the greater loading of the chamfered volume in the absence of the injection plate. With the injection plate inserted and the particles loaded in the initial volume, the chamfered arrangement produced projectile velocities almost identical to those of the constant-diameter geometry. The calculated and measured projectile velocity record, Figure 4.8, again shows the small deviation between the chamfered and constant-diameter measurements which was attributed to the slight differences in loading. The calculated velocities are in good agreement with the measurements in the constant-diameter geometry with discrepancies of less than 1 % throughout the cycle and about 0.5 % at the exit. Thus, the calculation method has provided results comparable to measurements within the accuracy of the instrumentation and the slight differences between the two initial geometries can be attributed to the small differences in volumetric loading of the cycle.

The breech pressure record for the chamfered initial geometry, Figure 4.9, shows the influence of the plate and spring mechanism and of the 4 % volume concentration of particles within the initial volume. As expected, the effect was measurable but insufficient to affect particle velocities appreciably. The change of the pressure at the breech was with in 0.5 % of that calculated with a quasi-steady isentropic expansion and supports the conclusion of *Seigel (1965,1979)* on the applicability of isentropic theory to guns.

4.3.2 Single-Phase Flow

Ensemble-average measurements of single-phase velocity on the centreline and with the constant-diameter and chamfered initial geometries are shown on Figure 4.10 and 4.11 at the first windows, 7.27 d and 4.96 d from the breech respectively. In both cases, we see the expected reduction in gas velocity with time after the passage of the projectile. The calculated centreline fluid velocity, also shown in Figure 4.10 for the constant-diameter arrangement, assumes that the velocity was linearly distributed between zero at the breech and the calculated projectile velocity at the base of the projectile at any instant in time. The agreement between calculated and measured centreline velocities is within 0.5 % and again indicates that the simplifying assumptions in the calculation method are justified for the relative low velocities in the low-speed simulator. In the chamfered initial geometry, the measured velocities of Figure 4.11 may be compared with calculated values which required an assumed virtual origin so that the ratio of the distances to the measurement location to that of the projectile base, each measured from the virtual breech, was equal to the ratio of the centreline gas velocity to the projectile velocity, by assuming a one-dimensional expansion between the virtual breech and the projectile base as in the constant-diameter case. Figure 4.11 shows two calculated centreline velocity curves, one based on a virtual origin of -0.9 d and the other of -2.6 d. The former was recommended by *Bicen et al (1986a)* and the later was calculated by assuming a constant diameter with the same initial volume. The figure shows that there is less than 0.5 % difference between the single-phase velocities measured with the 1.3 % and 4 % injection plates inserted. The measurements at the first window, X=4.96 d, are similar to the calculations with the -0.9 d origin just after the projectile passes due to the effect of the chamberage and are subsequently close to the calculations with the -2.6 d origin later in the cycle. In general the agreement between the measurements and the calculations with the virtual origin based on the initial volume are the more accurate with minor discrepancies at positions near the chamber and immediately behind the projectile.

A detailed analysis of the boundary layer at the first measuring window with the chamfered initial geometry was conducted. Ensemble-averaged radial profiles of gas-phase velocity measured at the first window, X= 4.96d, and corrected for velocity

gradient broadening near the wall, are shown in Figure 4.12 with values at r/R =1.0 in accord with those of Figure 4.11. The boundary layer thickness based on 99 % of the free-stream velocity grows from 0.116 r/R at 14.5 ms to 0.226 r/R at 26.5 ms and then decreases to 0.180 r/R at 32.5 ms. The velocity profiles of Figure 4.12 show the progression of the thickness and shape of the boundary layer after 13 ms, corresponding to 1 ms after the passage of the projectile. The corresponding rms distribution of the velocity fluctuations, Figure 4.13, exhibit an increase up to three times the centreline values near the wall, in agreement with those for a steady, turbulent boundary layer.

As the bulk-flow velocity decelerates, the radial profiles of Figure 4.12 change shape and the extent to which the boundary layer was affected can be seen in the dimensionless profiles in the boundary layer displayed in Figure 4.14. To a first approximation, the inner boundary layer profiles may be represented by power laws, *Schlichting (1979)*, with exponents from 1/7 to 1/12, as shown in Figure 4.14 The measurements comprising the four mean profiles were curve-fit with a simple logarithmic regression curve and the equations are presented for each in the legend of the figure. It seems clear, however, that the time scales of the near-wall and bulk flows are different so that the center region of the boundary layer has decelerated without the region between the measurements nearest to the wall and near r/R=0.15 being able to follow. This was particularly evident in the profile at 31-34 ms for which the rms values are also atypical of a steady state turbulent boundary layer.

The inner region of the boundary layers can be inspected in greater detail, as in Figures 4.15 and 4.16, which consider them in law-of-the-wall coordinates. The Clauser chart of Figure 4.15, shows that the wall shear-stress coefficient was large, as would be expected from the comparatively thin boundary layer and edge velocities of the order of 25 m/s. The first profile, at 14.5 ms, has a region of logarithmic variation with a value of C_f of around 0.00475. The two subsequent profiles, at 20.5 and 26.5 ms, have less well-defined regions of logarithmic variation but, bearing in mind the difficulties in measurement and the perturbed nature of the unsteady flows, they do exist and suggest values of C_f of around 0.00425. The measurements at 32.5 ms also suggest a value of C_f of 0.00425 but they deviate rather more from the law-of-the-wall. Figure 4.16 shows that all four profiles are in general accord with the standard law-of-the-wall Equation 4.1.

$$U^+ = \frac{\ln (U^+)}{\kappa} + c \qquad 4.1$$

By slightly modifying the two constants (κ= 0.41, c= 5.0) the differences between the measurements and calculated for each profile would be further reduced.

It is evident that the unsteady boundary layer, with its rapidly varying free-stream velocity, has ensemble-averaged properties which resemble those of a steady turbulent boundary layer. The free-stream decelerates by some 15 m/s in 21 ms which is similar to the deceleration of a steady boundary layer over 0.35 m in a diffuser of 6° cone angle and the results of *Kline et al (1981)* show a similar tendency for the bulk flow to catch up with the boundary layer, as indicated by the 32.5 ms velocity profile in Figure 4.12. The results are consistent with the velocity results of *Bicen et al (1986a)* which showed that the measured boundary layers were generally thinner than those calculated for steady turbulent boundary layers with zero pressure gradient, particularly in regions close to the projectile base. Even though simplifying assumptions were required, the characteristics of the unsteady boundary layer compare well to those of a steady turbulent boundary layer.

4.3.3 Two-Phase Flow

Two-phase flow in the low-speed gun simulator was of particular interest and the injection mechanism was intended to produce as uniform a particle distribution as possible in the chamber during the expansion process. *Khezzar (1987)* measured the second-phase velocity characteristics of 500 μm median diameter particles with a concentration of 1.3 % of the initial volume and these were repeated and extended during this investigation. Thus, the injection plate was modified to increase the concentration of the second-phase by a factor of 3, which corresponds to around 4 % of the initial volume.

The centreline mean velocity decays of the 500 μm median diameter solid particles with 4 % and 1.3 % initial volume loadings are shown on Figure 4.17 at the

first measuring window, X= 4.96d, together with the calculated projectile velocity and that measured for single-phase flow in the previous section. All the second-phase velocity measurements with 1.3 % volume concentration were within 1 % of the ensemble mean and 5 % of the rms values measured by *Khezzar (1987)* and had a smaller uncertainty because of the use of larger sample sizes, greater than 200. The orientation of the injection plate holes relative to the axis of the anemometer beams did not affect the second-phase velocity measurements along the centreline because of the symmetrical arrangement of the holes. Just after the projectile passed the measurement position, the trend for the particles to lag behind the single-phase was evident with similar magnitude for the two initial concentrations. The smaller initial velocities of the particles relative to those of the single-phase near the projectile base can be explained by the more rapid acceleration of the gas behind the projectile and the slower acceleration of the particles as they emerge from their annular jets. The lag between the single- and second-phase of approximately 2 m/s at 14 ms would be expected to be different if the injection mechanism design and/or position were modified. For example, if a larger fraction of the initial volume was above the plate, jets of particles at a higher relative velocity would result. At 18 ms into the cycle, the particle phase achieved the gas velocity at the centreline because the inertia of the particles ensured that their velocity dropped more slowly and this caused the gas-phase velocity to lag behind the particles for larger times. At the end of the cycle, the second-phase with the 4.0 % initial concentration led the single-phase, measured in the absence of the particle-phase, by 7 m/s, approximately 4 times greater than that with 1.3 % initial concentration.

The orientation of the holes in the injection plate, relative to the axis of the anemometer beams, could however affect the second-phase velocity measurements along a radius of the barrel because of the initial conditions and mixing of particles associated with the injection mechanism. The measurements presented in Figures 4.18 to 4.20 are based on equal numbers of individual particle velocity realizations carried out along the two symmetric planes of the injection plate, and will be discussed in detail below.

Figure 4.18 presents radial profiles of velocity for the single- and two-phase flows for the 1.3 % volume concentration at several axial positions at around the same time in the cycle. At all the locations, the lag of the particles behind the gas increased with distance from the breech and the results of Figures 4.17 and 4.18 suggest that the

particle velocities varied substantially less than the approximately linear distribution in the single-phase case. The differences displayed between the 1.3 and 4 % initial concentrations suggest that the velocity characteristics in real guns, where the second-phase loading would be much greater than 4 %, would definitely not be linearly distributed between the breech and the projectile base as measured with single-phase and small initial concentrations of particles. Extrapolation of the results to practical gun particle concentrations suggests that the particle velocities would be approximately constant at an axial station and increase slightly with axial distance, thereby agreeing with the measurements of *Klingenberg and Mach (1978)* in real guns.

Three radial profiles of velocity for the single- and two-phase flows with 1.3 % and 4 % volume concentrations at several times in the cycle are presented in Figure 4.19 and are in accord with the results of Figure 4.17. As evident in the 14.5 ms profile, the particle velocities lagged the single-phase by the same amount for the two concentrations and, in the 20.5 ms profile, the particle velocities with the higher concentrations tend to be greater than those of the lower concentration and of the single-phase flow. The particle velocities at 30.5 ms have distinctly larger magnitudes with the 4% initial concentration, particularly around the edge of the boundary layer. The noticeable lead of the second-phase above the gas velocities near the edge of the boundary layer was not evident in the previous 1.3 % initial concentration second-phase experiments and was therefore attributed to local regions of concentration greater than 4 % and resulting combined-inertia effect. The rms of the velocity fluctuations of the particles, presented in Figure 4.20 for the same time windows as those of Figure 4.19, are around twice those of the single-phase results of Figure 4.13. *Hardalupas et al (1988)* has demonstrated that a higher, non-turbulent rms of velocity fluctuations can occur in steady two-phase jet measurements due to the radial velocity gradient and the non-uniform distribution of particles. In addition to the concentration weighting of velocity measurement techniques, the variations in trajectory of the second-phase can contribute to observed fluctuations of the second-phase velocity. The initial conditions or distribution of particles in the initial volume was not homogeneous and likely to affect the subsequent second-phase flow before sufficient mixing had occurred, at location close to the initial volume. The influence of variations in the particle concentration and possibly particle trajectory effects are demonstrated in the ensemble mean and rms streamwise velocity results, particularly at the edge of the boundary layer where the

particles are shown to lead the single-phase measurements by up to 20 % more than in the rest of the flow.

Measurements of data rates, which are related to particle concentration, were made across the radius and for the two orientations of the injection mechanism arrangement shown in Figure 4.21 for the 4 % plate. The maximum data rate for all the measurements was around r/R= 0.14, the approximate boundary layer thickness. Comparison of the combined second-phase velocity realizations for the two orientations over a series of tests is displayed in Figures 4.22 and 4.23 for the 0.09 and 0.12 r/R radial positions. The results show a non-uniform distribution of data rates, related to particle concentrations, and contrasting trends for each orientation for the two plate orientations. The largest data rates for these radial positions were approximately three times those found on the centreline and occurred at the 45° orientation at 0.12 r/R and at the 0.0° orientation at 0.09 r/R. These maxima are coincident with ensemble-average velocities 9 % higher than those measured on the centreline at 30.5 ms, possibly due to the higher inertia associated with the larger concentrations of particles in this annular region. The largest data rates observed with the 0.0° orientation at 0.12 r/R and 45° orientation for 0.09 r/R were approximately twice that of the centreline, 50 % less than the other orientation for the same point, and this led to the maximum increase in velocity above that of the centreline of about 7 %. The maximum data rates were associated with a large volume fraction in the annular region near the boundary layer and indicate that the distribution of the particles was not uniform as a result of the injection mechanism, chamfered geometry and inertial effects of the particles. The difference between the single-phase velocities relative to those of the particles was more pronounced with the larger particle loading since there was a tendency for the particles to disperse slowly and their effective inertia was that of a locally high concentration of particles.

4.3.4 Heat Transfer

Measurements of wall temperature with single-phase flow in the constant-diameter geometry at five axial locations, 2.88 d, 7.27 d, 10.21 d, 13.15 d and 16.09 d from the breech, and with single and two-phase flows in the chamfered geometry at X= 4.96 d and 7.90 d, are presented on Figure 4.24 to 4.28. The location X= 2.88d corresponds to a position inside the initial chamber and the others are barrel locations which were swept by the projectile during the cycle. The locations X=4.96 d and 7.90 d of the chamfered geometry correspond to approximately the same distances from the projectile base for X=7.27 d and 10.21 d of the constant-diameter chamber. Results are presented as time-resolved measurements of temperature and of the heat flux evaluated from Equation 2.23.

In regions swept by the projectile, the sensor needed to be inset in the wall to reduce the possibility of mechanical damage due to the moving projectile. Tests were carried out to quantify the effect of radial positioning of the sensor on the wall and Figure 4.24 shows the results for three radial positions at X=2.88d in the constant-diameter chamber. The differences between the temperatures of a flush mounted sensor and that inset by 0.2 mm into the wall are, on average, less than 5 %, which was within the temperature uncertainty of the system. The differences between results with the probe flush with the wall and 0.6 mm inset in the wall increase to 25 % at later times in the cycle. For subsequent measurements at locations swept by the projectile the sensor was inset by about 0.1 mm and, according to the conclusions of Figure 4.24, was expected to measure temperatures close to those of the wall surface. To demonstrate that the slightly inset sensor will produce reliable measurements of the surface temperature change, five successive test with a flush mounted sensor are presented in Figure 4.25 and show that the cyclic variations and signal noise inherent in the measurement system was of the order of the difference between a flush and 0.2 mm inset sensor.

The variations of the surface temperature for the single-phase flow in the constant-diameter geometry are shown for the five axial locations in Figure 4.26, relative to the isentropic free-stream temperature, and in greater detail in Figure 4.27. The maximum measured surface temperature change with standard operating conditions was

always less than -7 ° C, or 5 % of the free-stream temperature difference of about -140° C at the end of the shot. At X= 2.88 d, the temperature change shows a maximum of about -5° C at around 25 ms and thereafter recovers slightly to around -4° C towards the end of the cycle. At the other four locations, the measured temperature falls rapidly as the projectile passes over the sensor due to the expansion of the gas behind the projectile and subsequently decreases at a slower rate during the rest of the cycle. The sensor temperature was initially ambient at all locations and the deviations from zero in the first few ms of each trace are within the experimental uncertainty of ±0.3° C. The temperature change at the end of the cycle reduces at locations further away from the breech with a value of around -6° C at X=7.27 d and -5° C at X= 16.09 d as seen in Figure 4.27.

The inherent noise in the sensor temperature data results in scatter in the heat flux deduced from Equation 2.23 as a consequence of the integration procedure. Polynomial curve-fits to temperature data were made at all locations to remove the scatter and three of these are presented in Figure 4.28. The resulting variations in heat flux and heat transfer coefficient for the single-phase flow in the constant-diameter geometry are shown in Figures 4.29 and 4.30 respectively, with the heat transfer coefficient,

$$h \equiv \dot{q} / \Delta T, \qquad 4.2$$

based on the temperature difference between the isentropic free-stream and the wall-surface temperature, which was assumed to be that of the sensor. In Figure 4.29 at X= 2.88 d, heat transfer from the wall to the fluid gradually increased from zero to around 1.8 x 10^4 W/m^2 at 17 ms and then reduced to 0.5 x 10^4 W/m^2 before the gas pressure was released at around 33 ms. At locations swept by the projectile (ie. X= 7.27 d, 10.21 d, 13.15 d and 16.09 d) the heat transfer increased rapidly from zero as the projectile passed over the sensor and decreased during the rest of the cycle to a value of around 1.6 x 10^4 W/m^2 for X=7.27 d and 10.21 d. At X= 13.15 d and 16.09 d, the heat flux was larger and increased after 33 ms when the gas pressure escaped through the muzzle. The convection coefficients in Figure 4.30 are consistent with those of heat flux so that, after the rapid decline, particularly at X= 7.27 d, 10.21 d and 13.15 d, the heat transfer coefficient attained values ranging from around 70 W/m^2 °K at X=2.88 d to 220 W/m^2 °K at X=16.09 d.

The heat transfer coefficients of Figure 4.30 may be compared with those obtained from a correlation of steady single-phase turbulent boundary layer data over a flat plate with zero pressure gradient starting at the breech. Figure 4.31 shows the coefficients for the five axial locations obtained from a correlation of *Incropera & DeWitt (1985)* given by:

$$Nu = 0.0308\, Re^{4/5} Pr^{1/3} \qquad 4.3$$

In applying the above correlation to the transient gun flow, a quasi-steady flow assumption was made and the Reynolds number and fluid properties were evaluated at each time step in the cycle using the corresponding projectile and centreline fluid velocity data of section 4.3. The differences between the measured and correlation results at X=7.27 d, 10.21 d, 13.15 d and 16.09 d are large immediately behind the projectile due mainly to the quasi-steady flow assumption. At X=2.88 d, the measured values in the first 3 ms of the shot are close to zero and rapidly increase over the next few ms as the flow goes through transition and becomes turbulent. The values attained are, however, higher than the correlation results by around 50 % because the correlation does not account for the favorable pressure gradient experienced by the flow, particularly in the early stages of the cycle. As the flow develops and pressure gradients reduce later in the cycle, the measured values at X= 2.88 d in Figure 4.30 approach the correlation results of Figure 4.31 and achieve values within 10 %. At locations swept by the projectile, the measured coefficients attain higher values throughout the cycle, for example up to 50 % at X = 16.09 d. These differences are thought to stem from the interaction of the projectile wake with the velocity boundary layer, in addition to the neglect of the pressure gradient in the correlation. The results are consistent with the velocity results of *Bicen et al (1986a)* which showed that the measured boundary layers were generally thinner than those calculated for steady turbulent boundary layers with zero pressure gradient, particularly in regions close to the projectile base, thereby resulting in higher heat transfer coefficients.

In Figure 4.32, heat flux measurements obtained with single-phase flow in the chamfered geometry are presented for the locations of X= 4.96 d and 7.90 d and maybe compared to those obtained with the constant-diameter geometry at the same locations

relative to the projectile base, X= 7.27 d and 10.21 d. The differences at the location nearest the breech are large during the early stages due to the slightly higher velocities and thinner boundary layer in the chamfered geometry, *Bicen et al (1986c).* Thinner boundary layers develop at the same position relative to the projectile base because they are developing from the chamfered diameter reduction and not from the breech as in the constant-diameter case. Later in the shot and at locations closer to the projectile base, the differences become smaller and became negligible at around 25 ms. The heat transfer results demonstrate that the chamfered initial geometry, relative to a constant-diameter, gives rise to a larger heat flux immediately proceeding the chamberage which decreased with distance from the breech. The location of the highest heat flux evident in the low-speed simulator also corresponded to the region where the greatest erosion in real gun occurs and its reduction to increase barrel life is of interest.

The heat flux measurements of Figures 4.33 were obtained in the chamfered geometry at X= 4.96 d and 7.90 d and quantify the effect of the 500 μm particles. The heat transfer with particles was generally higher than that without them by around 15 % at X= 4.96 d where the particle number density was expected to be relatively high. At distances further away from the breech the particles are more scarce and the effect on the wall heat transfer becomes negligible as indicated by the two identical curves at X= 7.90 d. This observation parallels that of the velocity results of the previous section and, which showed that mean and rms velocities of particles were higher at X= 4.96 d, approximately twice the magnitude of those in the absence of particles.

4.4 Concluding Remarks

The main conclusions of the experimental investigation of the low-speed gun simulator are:

1. Velocity and heat flux characteristics with the inert single- and two-phase flow of nitrogen gas and 500 μm diameter particles have been measured by laser-Doppler velocimetry and thin-film thermometry in the low-speed gun simulator.

2. The single-phase velocity characteristics of the developing transient boundary

layer compare well with those of the law-of-the-wall for steady boundary layer flows even though the free-stream velocity decreases rapidly during the process.

3. Comparisons between the velocity of 500 μm plexiglass particles with initial volume concentration of 1.3 % and 4 % and that of the fluid obtained separately and, in the absence of particles, revealed that the particles initially lagged behind the fluid because of their relatively large inertia and the lag increased with distance from the breech. Later in the cycle, the particles caught up with and led the fluid and the lead was more pronounced with the 4 % loading, with a tendency for the particle velocity to increase around the edge of the boundary layer due to the increased inertia of the higher particle concentration.

4. The rms levels of particle velocity fluctuation were higher than those of the fluid in the bulk of the flow and approximately twice the magnitude of single-phase near the wall. This observation should however be treated with caution since the fluid velocities were measured in the absence of the large particles and variations in trajectory may contribute.

5. A thin-film sensor with its surface 0.2 mm below that of the wall of the initial chamber indicated temperatures close to those of the sensor mounted flush on the wall and confirmed that measurements of heat flux at locations swept by the projectile were possible.

6. The surface temperature for the single-phase flow in the constant-diameter geometry fell rapidly as the projectile passed over the sensor due to the expansion of the gas behind the projectile. The measured temperature subsequently decreased at a slower rate during the rest of the cycle at positions near the breech and increased with axial distance consummate with the higher gas velocities. The maximum measured surface temperature change with standard operating conditions was always less than -7 ° C, or 5 % of the free-stream temperature difference.

7. Heat transfer information was obtained by curve-fit approximations to the temperature records to remove scatter in the data and showed that the wall heat flux at various locations swept by the projectile decreased in time and increased with distance

from the breech.

8. Comparison of the measured heat flux results with those obtained from a convection correlation for a turbulent boundary layer with zero pressure gradient starting at the breech showed differences at locations swept by the projectile due mainly to the effect of the projectile wake on boundary layer development and partly to the neglect of pressure gradient in the correlation method. In the initial chamber, however, the wake effect was weak and the differences, although initially large, became progressively smaller as the pressure gradient reduced later in the shot.

9. The heat flux measurements obtained with single-phase flow in the chamfered geometry were compared to those obtained with the constant-diameter geometry at the same locations relative to the projectile base and the higher heat fluxes in the chamfered geometry are due to the slightly thinner boundary layers and higher velocities in the chamfered geometry at positions near the breech.

10. The effect of 500 μm particles, with an initial loading of 4 % by volume, was to increase the wall heat flux by as much as 15 % at locations close to the breech where particle concentration were high and subsequently became insignificant with distance from the breech.

Appendix 4.1 Projectile Velocity Program Listing

"PROJVEL.FOR"

```
C     ************************************************************************
C
C     Mark C. Schmidt
C     Research Assistant
C     Fluids Section
C     Mechanical Engineering Department
C     Exhibition Road, South Kensington
C     Imperial College, London SW7 2BX,  UK
C
C                   Program Number:         #1 Projectile Velocity Calculations
C                   Program Name:           Subsonic Gun Simulator Projectile Velocity Calc.
C                   Program Language:       Fortran
C                   Program Compiler:       MicroSoft Fortran version 2.2
C                   Program Implemented on: Macintosh Plus from Apple Computers
C
C                   Program Started on:     18th February 1988
C                   Program Finished on:    20th February 1988
C                   Program Modified on:    29th March 1989
C
C     ************************************************************************
C
C                   Projectile Velocity Calculations.
C
C                   All quantities have SI units in this program.
C
C     Dependent Variables or Inputs:*************************************************
C
C     "M" is the mass of the projectile or piston in Kilograms
C     "D" is the internal diameter of the barrel in which the projectile moves.
C     "DX" is the axial integral distance in meters.
C     "XI" is the initial length of charged volume of constant diameter.
C     "XW1" is the travel distance to the first window
C     "XN" is the total length of the travel of the projectile in meters.
C     "PP" is the initial pressure of the initial volume (absolute pressure in SI units (N/m^2)).
C
C     Constants:*********************************************************************
C
C     "K" is the reflective constant for the first refractory wave to reach the projectile base.
C     "A" is the cross-sectional area of the barrel in which the projectile moves.
C     "AP" is the atmospheric pressure in SI units.
C     "AT" is the atmospheric temperature in Degrees Kelvin.
C     "AR" is the universal gas constant R for Nitrogen.
C     "Gam" is the gas constant for Nitrogen in this case.
C                   The speed of sound is sqrt(Gam*R*T)=sqrt(Gam*AR*AT)
C
C     Variables:*********************************************************************
C
C     "X" is the distance through which the projectile has moved.
C     "XPST" is the travel distance at which the first refraction wave has reflected to the projectile.
C     "T" is the temperature of the gas (***assumed for calc. speed of sound at breech***)
C     "Z" is the friction force due to the contact and air in front of the piston.
C
C     "Time" is the calculated time from the start of the cycle.
C     "Vold" is the velocity of the projectile at the previous iteration cycle.
C     "VM" is the average velocity between two successive iteration steps.
C
C     "Y1","Y2" are the values across which the integration takes place.
C     "R1","R2","R3","R4" are the variables used in the Runga Kutta algorithm.
C     "YAA" is a controlling variable in the Runge Kutta algorithm.
C     "W1" is the velocity above the first window assuming a proportional relationship.
C     "UP", "UPP","UPPP" are dummy variables used in the calculation of the projectile velocity.
C     "XM","S","S1","S3","A1","A2","AR" are function dummy variables used in the FF subroutine.
C
C     List of non-data dependent variables*******************************************
C
C     "I","II" are the Do loop counters
C     "NX" is the number of iterations in the Do Loop to cover the travel length of the projectile.
C
C     Declaration Statements*********************************************************
C
      DOUBLE PRECISION M, K, D, A, AP,AR,DX ,AT ,Gam , XI,
     *            Time,Vold,X,Z,PP,XPST,T,R1,R2,R3,R4,Y1,Y2,YAA,
     *            UPP,UPPP,VM ,XN, W1, XW1
      INTEGER I,NX
      CHARACTER OUTPUT*8,TAB*1
C
C     The following opens the input and output files for the compiler and allows tabbing to be used.
C
      OUTPUT='SPV.001'
      TAB=CHAR(9)
      OPEN (3,FILE=OUTPUT,STATUS='NEW')
C
C     Inputs for the calculations
C
      M=0.9530D0
      D=0.0765D0
      DX=0.0005D0
      XI=0.3263345D0
      XW1=0.250D0
```

```
      XN= 1.150D0
C
      Do 20 II=1,1
      PP=1.013D5+8.0D0*1.0D5
      Write (3,103) M,PP
C
C     Constants and straight forward calculations
C
      K=3.0D0
      AT=285.0D0
      AP=1.013D5
      AR=296.80D0
      Gam=1.40D0
      NX=XN/DX
      A=D**2.0D0*3.14159265D0/4.0D0
C
C     Zeroing some of the variables for the calculations to begin at origin.
C
      Y1=0.0D0
      Time=0.0D0
      Vold=0.0D0
      X=0.0D0
      Z=0.0D0
C
C     Calculations of the length at which the first characteristic wave
C                 reaches the base of the projectile therefore return to old values.
C
      XPST=K*PP*A*XI**2.0D0/(M*Gam*AR*AT)
C
C     Combination of friction and Atms. opposite force.
C
      Z=Z+2.0D0*A*AP/M
C
      T=AT
      Do 10 I=1,NX
      R1=DX*FF(X,Y1,T,Z,Gam,XI,PP,M,A,XPST,AR)
      R2=DX*FF(X+DX/2,Y1+R1/2,T,Z,Gam,XI,PP,M,A,XPST,AR)
      R3=DX*FF(X+DX/2,Y1+R2/2,T,Z,Gam,XI,PP,M,A,XPST,AR)
      R4=DX*FF(X+DX,Y1+R3,T,Z,Gam,XI,PP,M,A,XPST,AR)
      Y2=Y1+(R1+2.0D0*R2+2.0D0*R3+R4)/6.0D0
      YAA=(Gam+1.0D0)*Gam*AP*A*X/(M*Gam*287.0D0*AT)
      IF (YAA.LE.0.0000001) THEN
      UPPP=0.0D0
      UPP=Y2**0.5
      ELSE
      UPPP=((1.0D0-AP/PP)*((1.0D0-EXP(-1.0D0*YAA))/YAA))**0.5
      UPP=UPPP*Y2**0.5
      ENDIF
      VM=(Vold+UPP)/2.0D0
      Time=Time+DX/VM
      Vold=UPP
      If (X.GE.XW1) then
      W1=UPP*(XW1+XI)/(XI+X)
      Else
      W1=0.0D0
      ENDIF
      Write (3,101)TAB,UPP,TAB,X,TAB,W1,TAB,Time
9     Y1=Y2
      X=X+DX
10    CONTINUE
20    CONTINUE
      Write (3,102)TAB,UPP,TAB,X,TAB,W1,TAB,Time
C
101   Format(1X,'RUN on',A1,D13.4,A1,D13.4,A1,D13.4,A1,D13.4)
102   Format(1X,'Muzzle',A1,D13.4,A1,D13.4,A1,D13.4,A1,D13.4)
103   Format(1X,'Proj. V-Posit-CLV-Time of a Proj. Mass =',D13.4,D13.4)
      END
C
C
      Function FF(X,Y,T,Z,Gam,XI,PP,M,A,XPST,AR)
      DOUBLE PRECISION X,Y,T,Z,Gam,XI,PP,M,A,XPST,
     *  XM,S,S1,S3,A1,A2,AR
      S=Gam-1.0D0
      S1=2.0D0*Gam
      IF (X.GT.XPST) Then
      XM=X-XPST
      A1=A*2.0D0/M*PP*(XI**Gam)*((XM+XI)**(-Gam))
      S3=Gam*AR*T*(((XM+XI)/XI)**S)
      ELSE
      A1=A*2.0D0/M*PP
      S3=Gam*AR*T
      ENDIF
      A2=1.0D0-0.2D0*Y**0.5*S3**(-0.5)
      FF=A1*(A2**7)-Z
      Return
      End
```

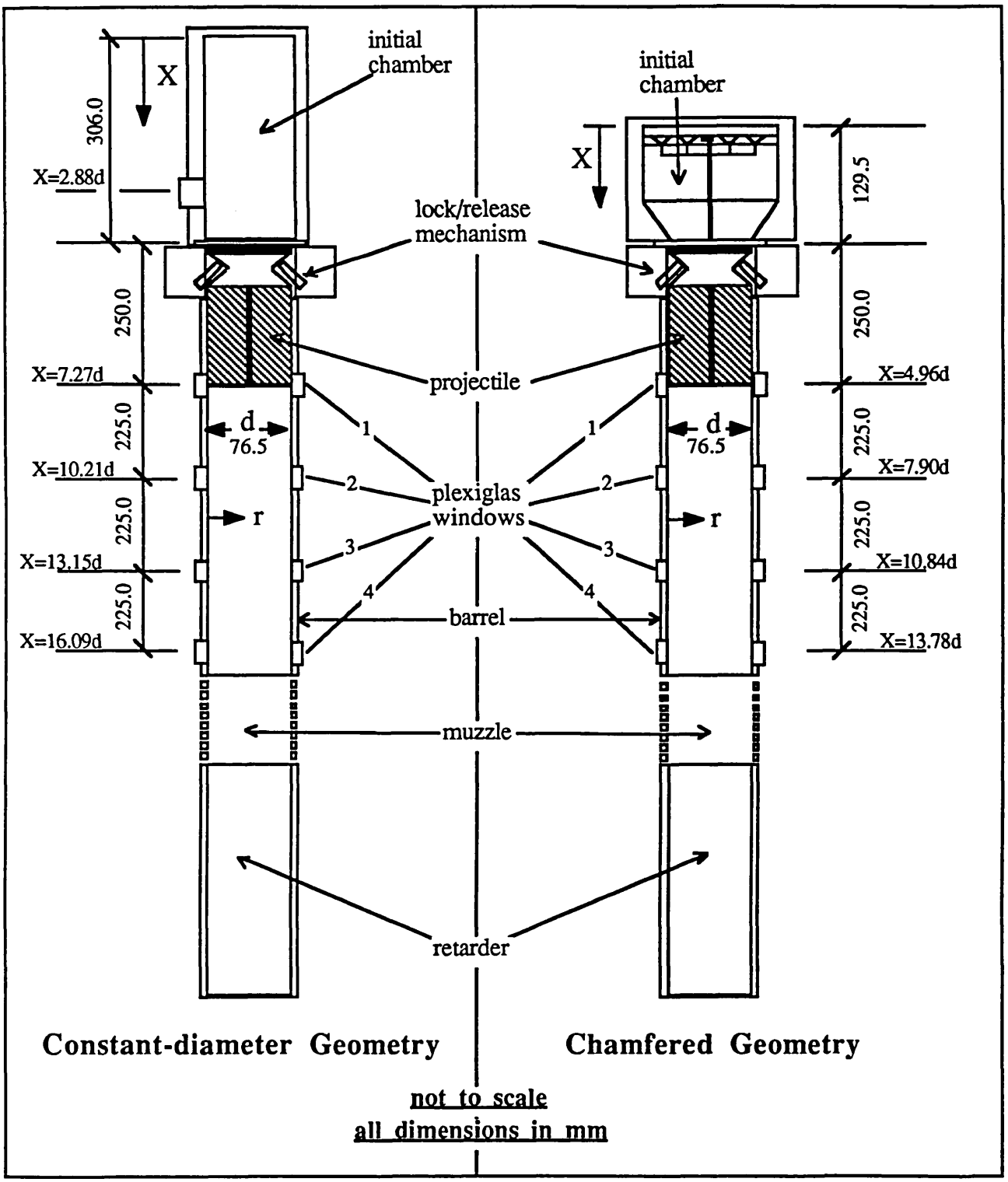


Figure 4.1 Geometry of low-speed gun simulator with constant-diameter and chamfered initial volume.

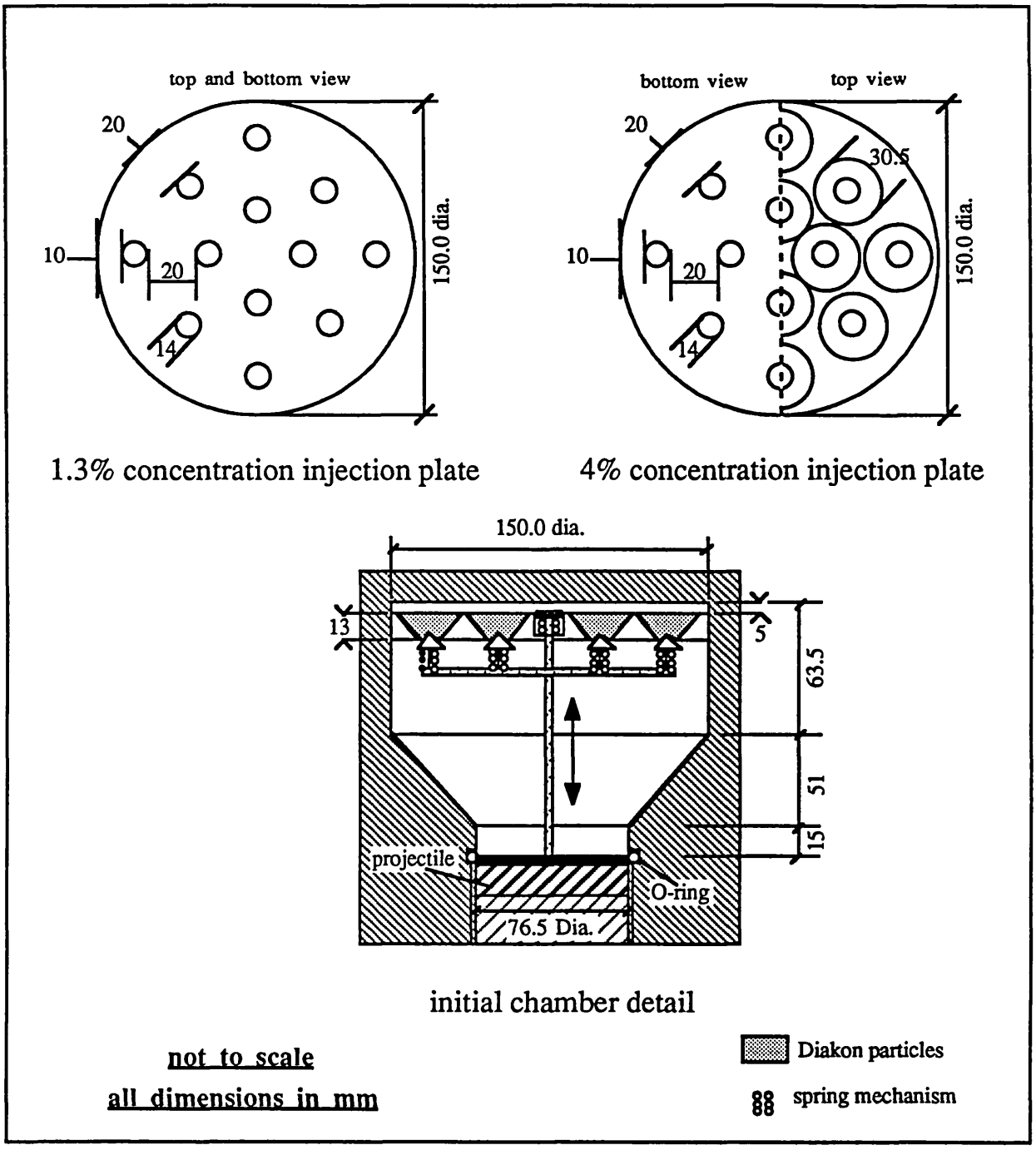


Figure 4.2 Particle injector mechanism for chamfered initial volume.

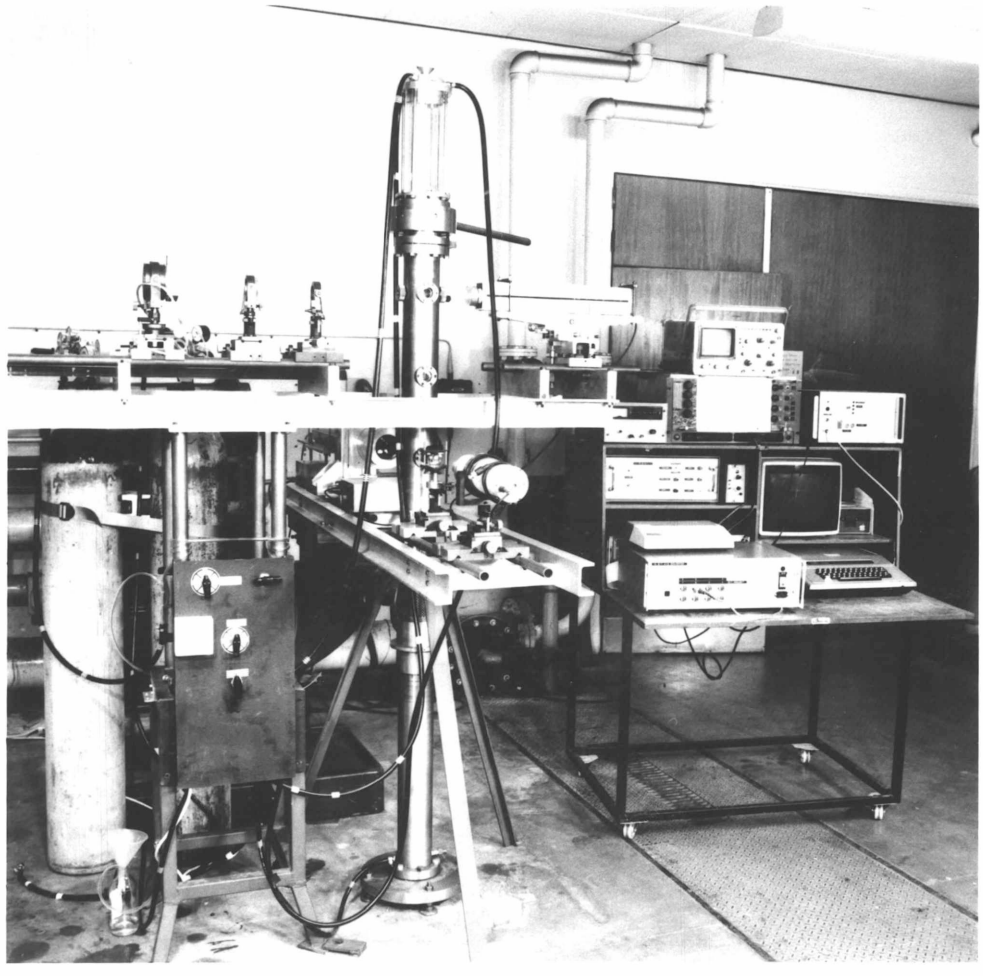


Figure 4.3 Photograph of low-speed gun simulator and instrumentation with constant-diameter initial volume.

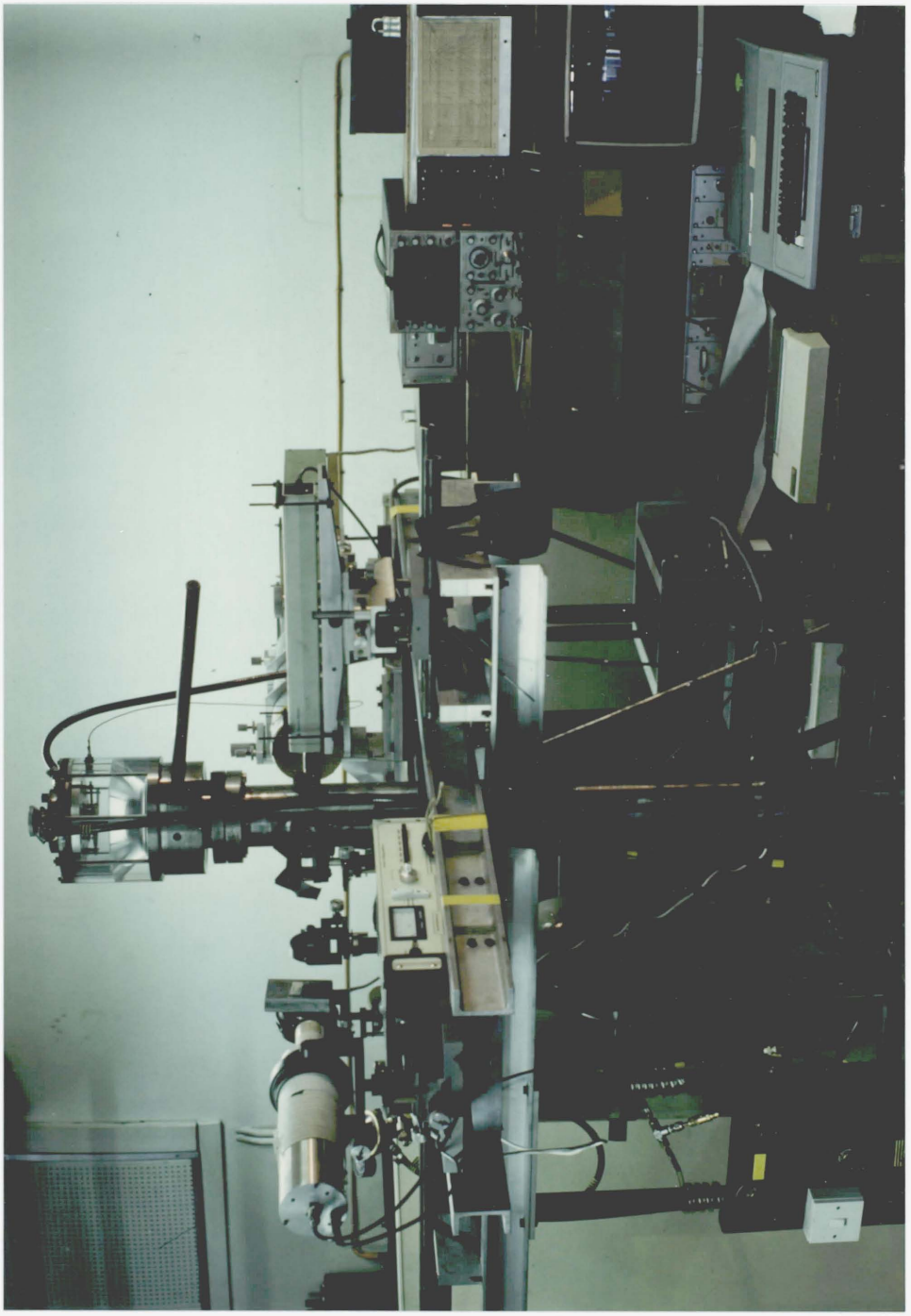


Figure 4.4 Photograph of low-speed gun simulator and instrumentation with chamfered initial volume.

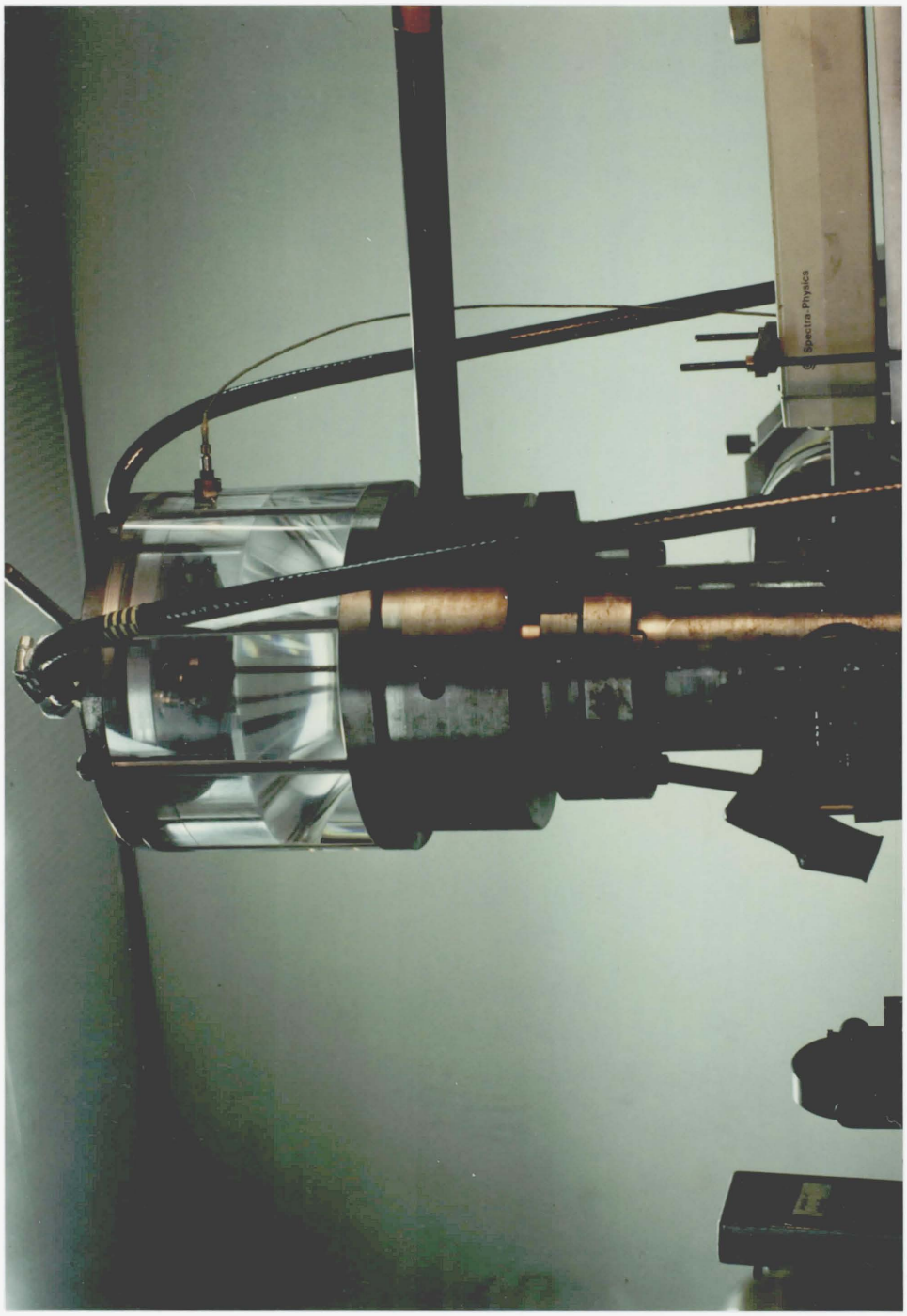


Figure 4.5 Photograph of chamfered initial volume with injector mechanism.

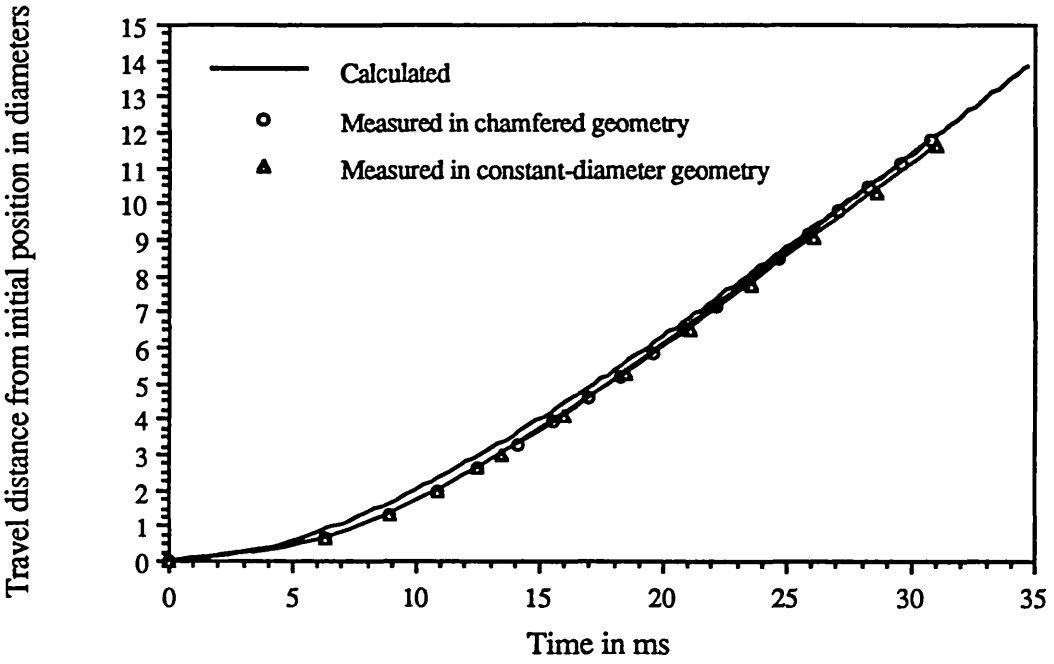


Figure 4.6 Calculated and measured projectile travel distance with time.

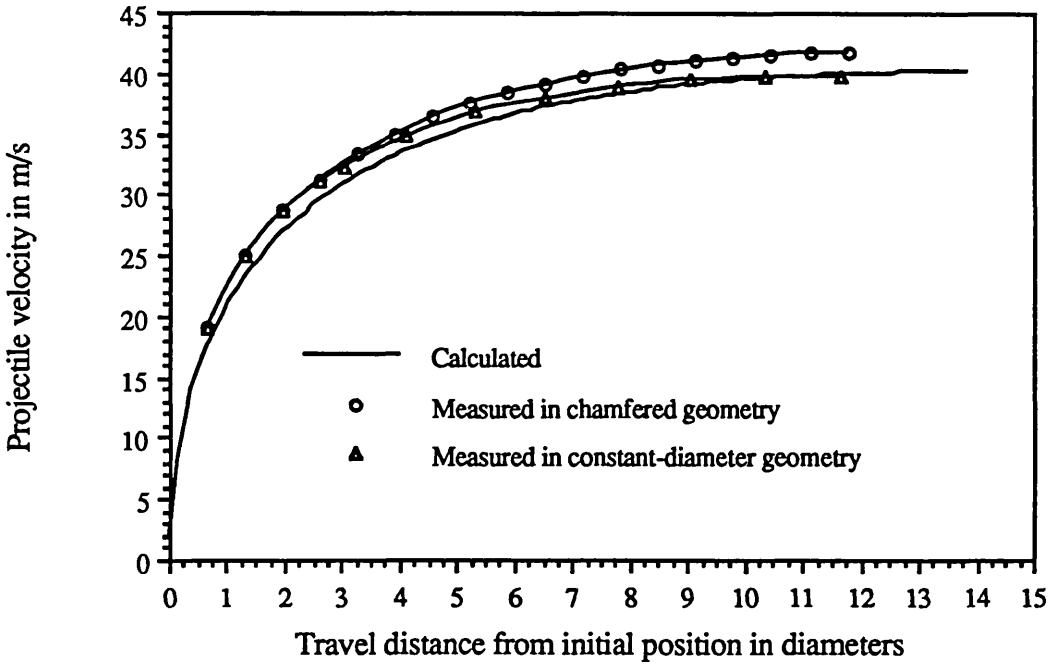


Figure 4.7 Calculated and measured projectile velocity with travel distance.

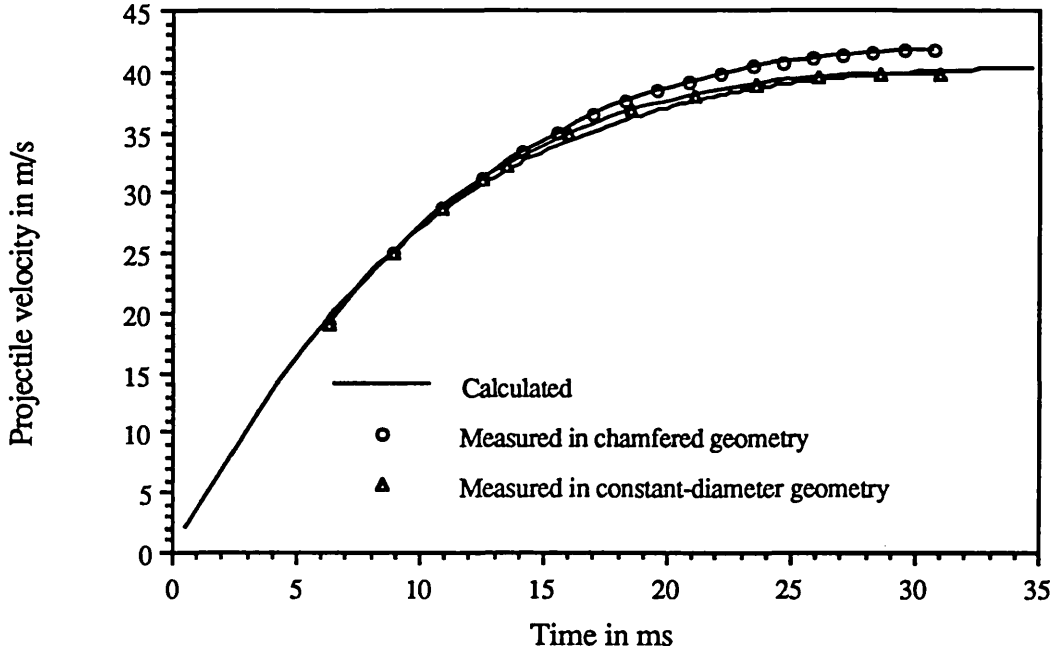


Figure 4.8 Calculated and measured projectile velocity with time.

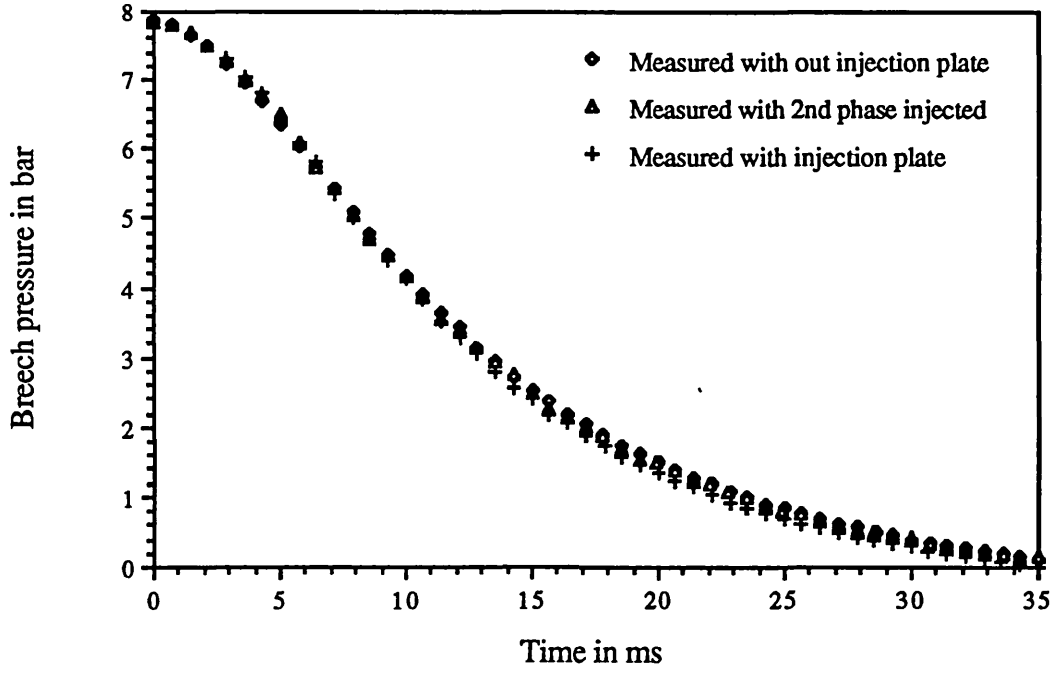


Figure 4.9 Temporal variation of measured breech pressure.

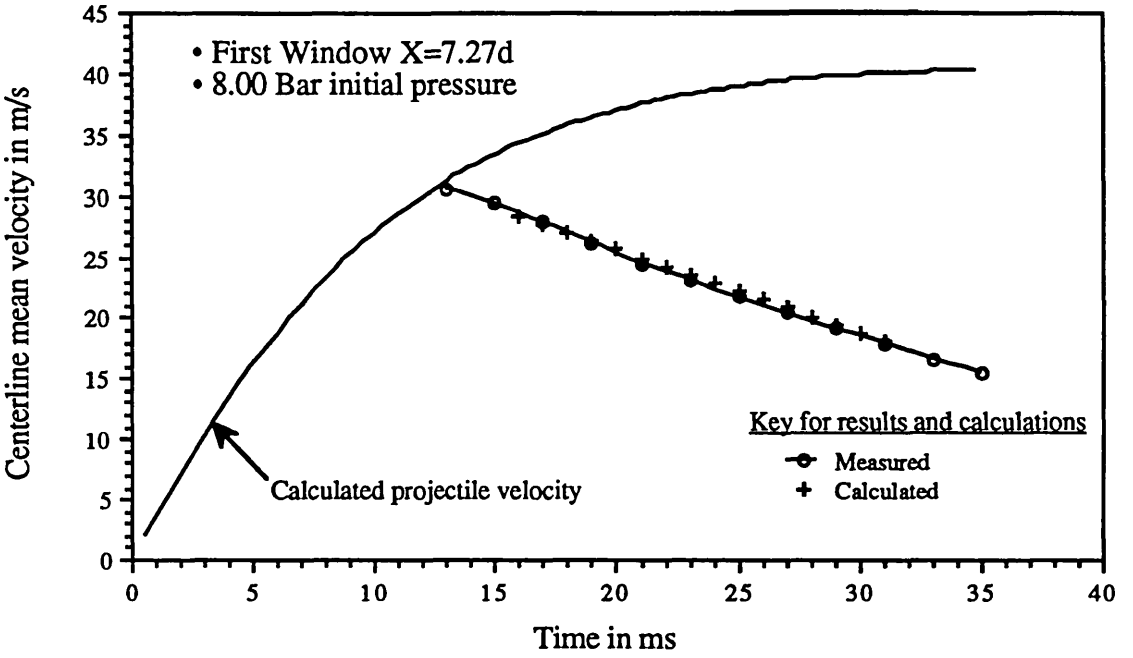


Figure 4.10 Temporal variation of measured and calculated centreline mean velocity; single-phase flow in constant-diameter geometry.

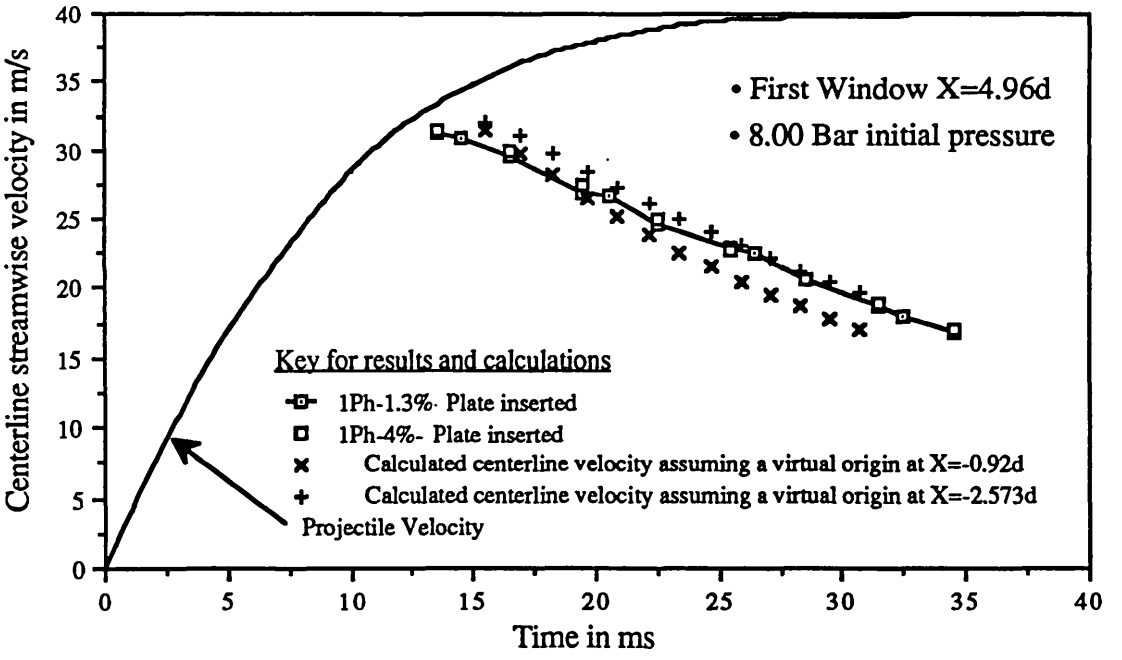


Figure 4.11 Temporal variation of measured and calculated centreline mean velocity; single-phase flow in chamfered geometry.

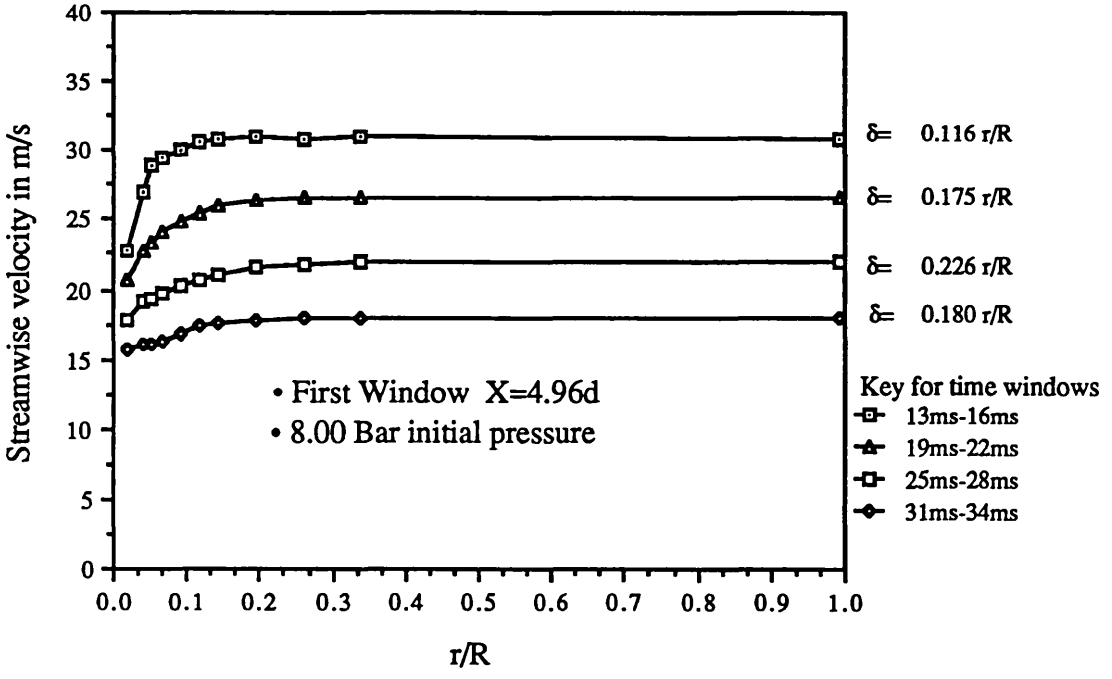


Figure 4.12 Radial variation of single-phase streamwise velocity; chamfered geometry.

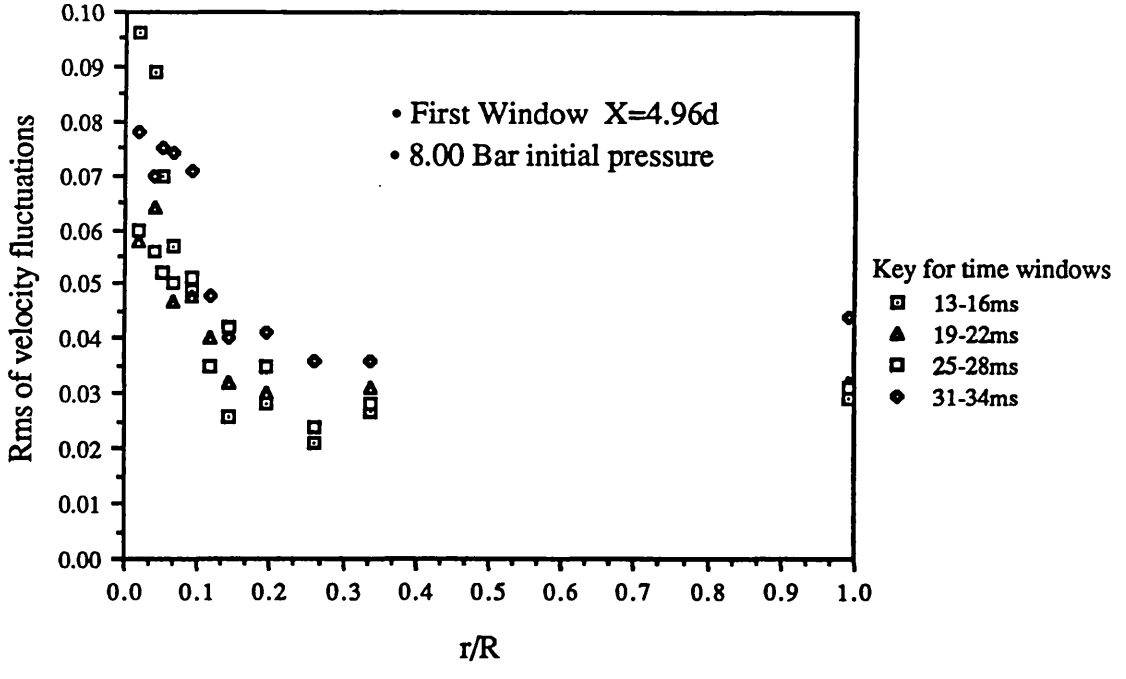


Figure 4.13 Radial variation of single-phase streamwise turbulence intensity; chamfered geometry.

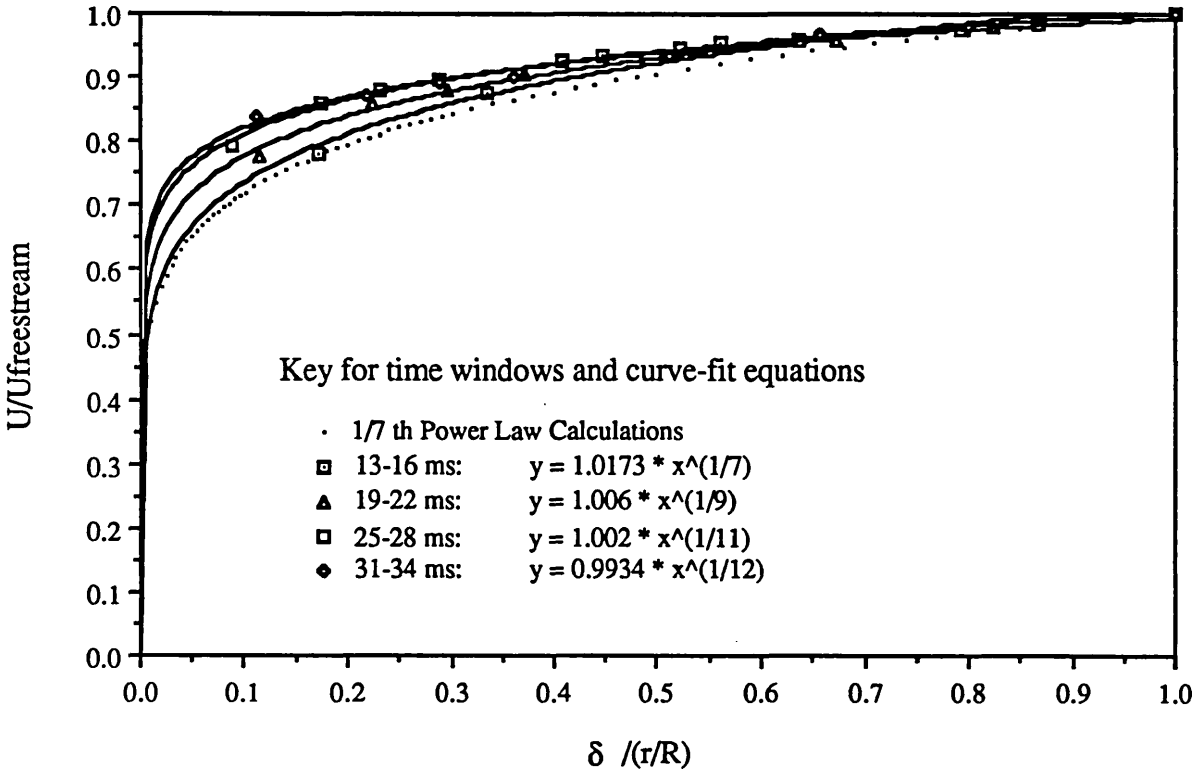


Figure 4.14 Variation of velocity profiles inside the boundary layer.

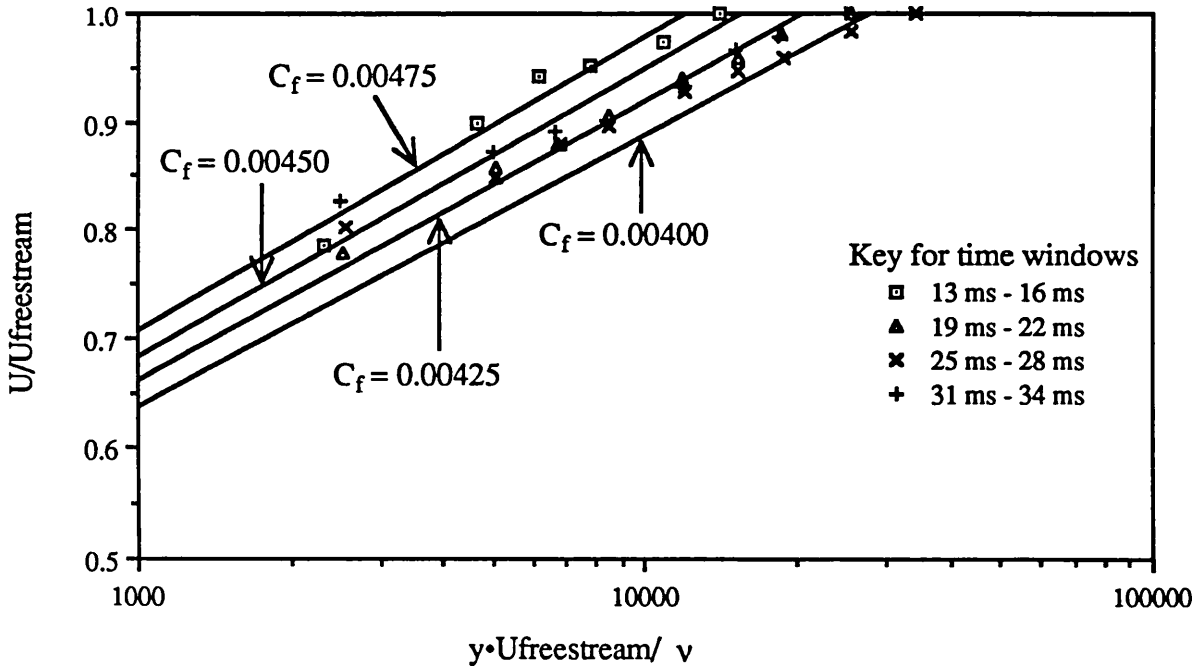


Figure 4.15 Clauser chart for the deduction of C_f.

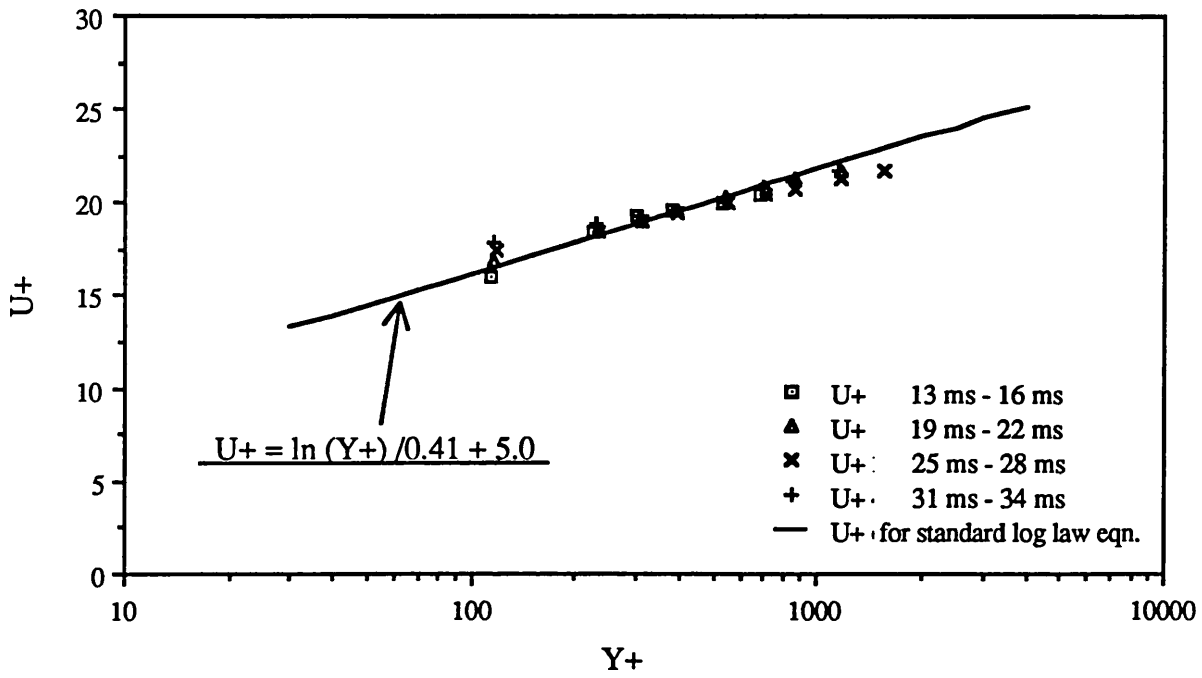


Figure 4.16 Velocity distribution displayed in standard Wall coordinates Y^+ and U^+.

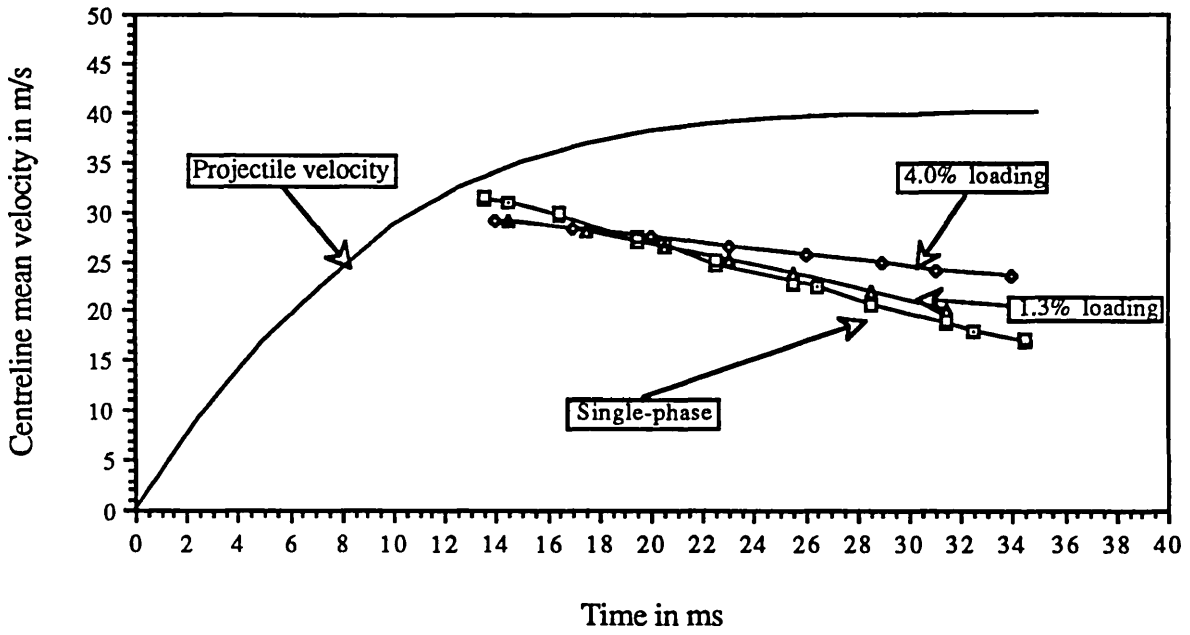


Figure 4.17 Centreline mean velocity time records at x=4.96d; single- and two-phase flows with 1.3% and 4% particle loading.

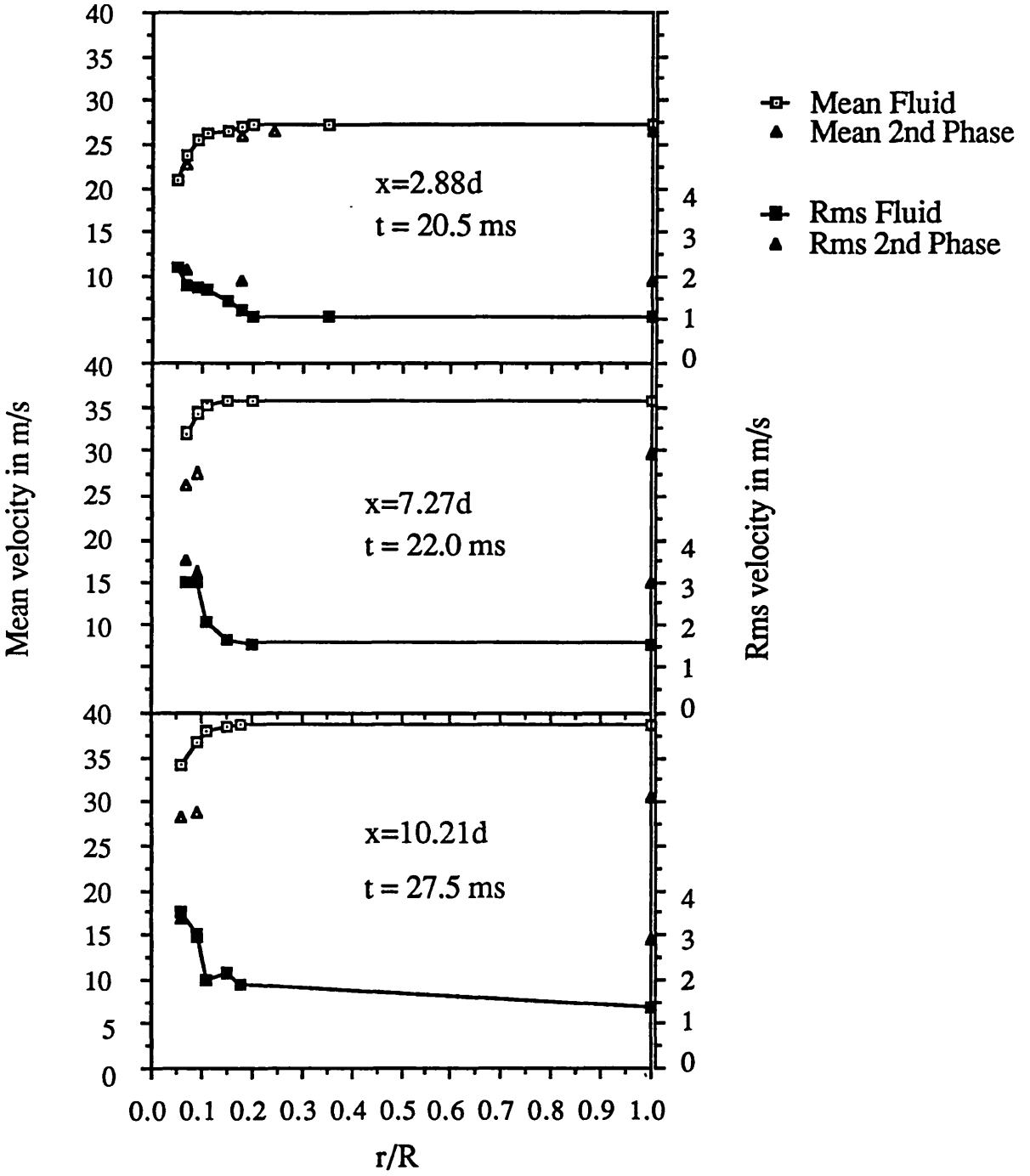


Figure 4.18 Radial profiles of mean and rms velocity at various axial locations for a time of around 24 ms in the shot; single- and two-phase flow with 1.3% particle loading.

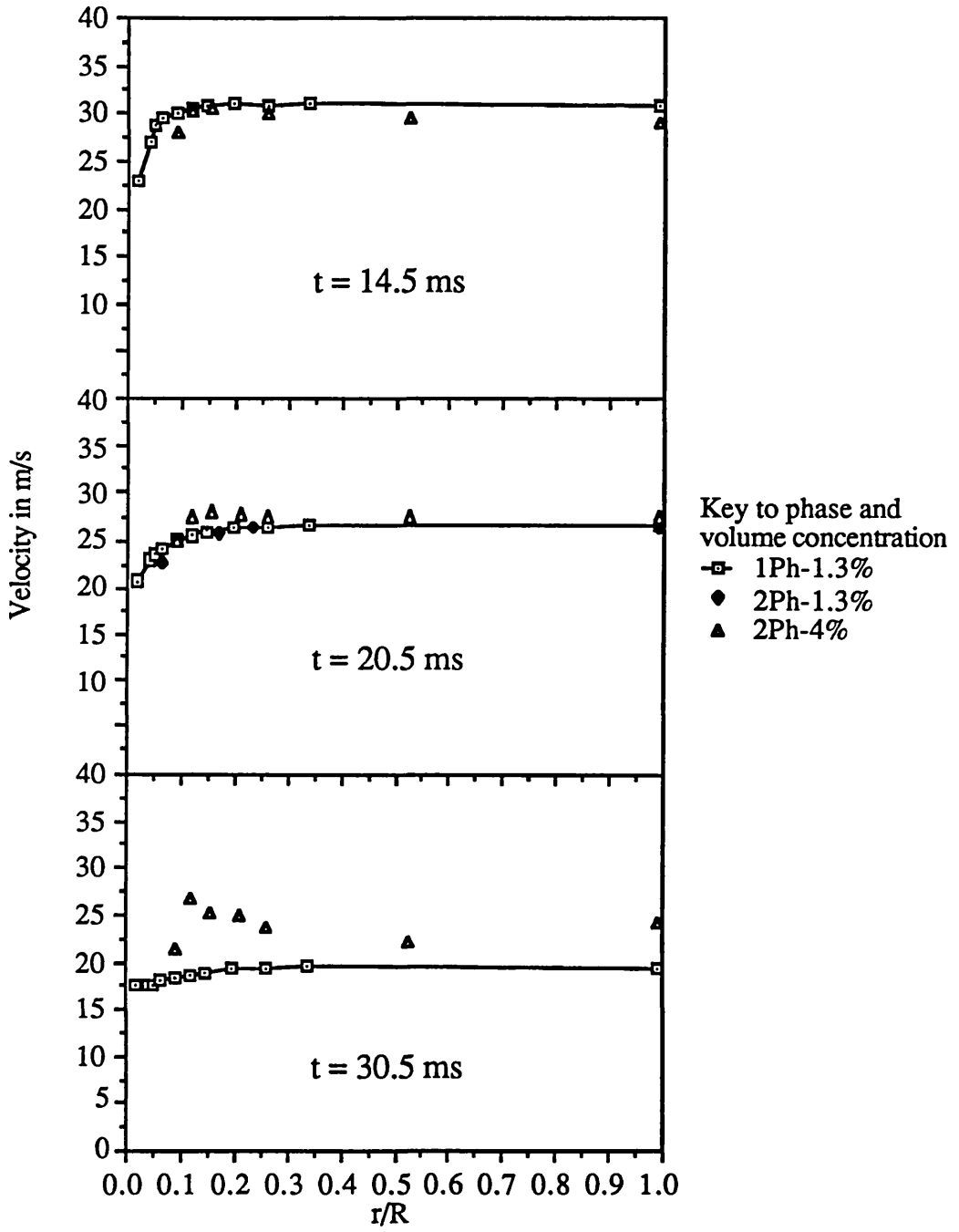


Figure 4.19 Radial profiles of mean velocity at x = 4.96d for various times in the shot; single- and two-phase flow with 1.3% and 4% particle loading.

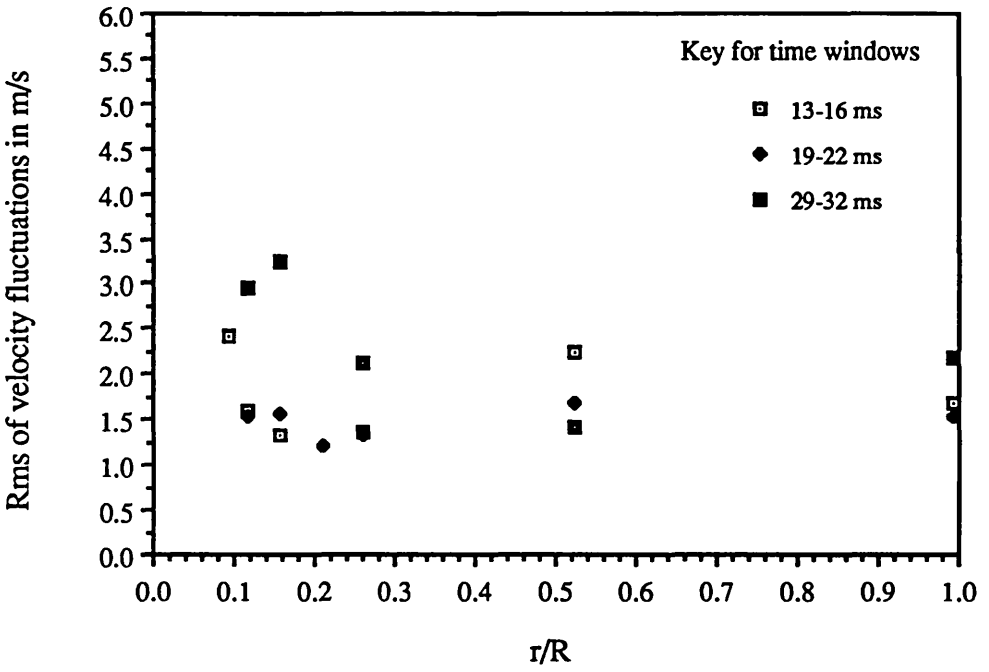


Figure 4.20 Radial profiles of rms velocity at x = 4.96d for various times in the shot; two-phase flow with 4% particle loading.

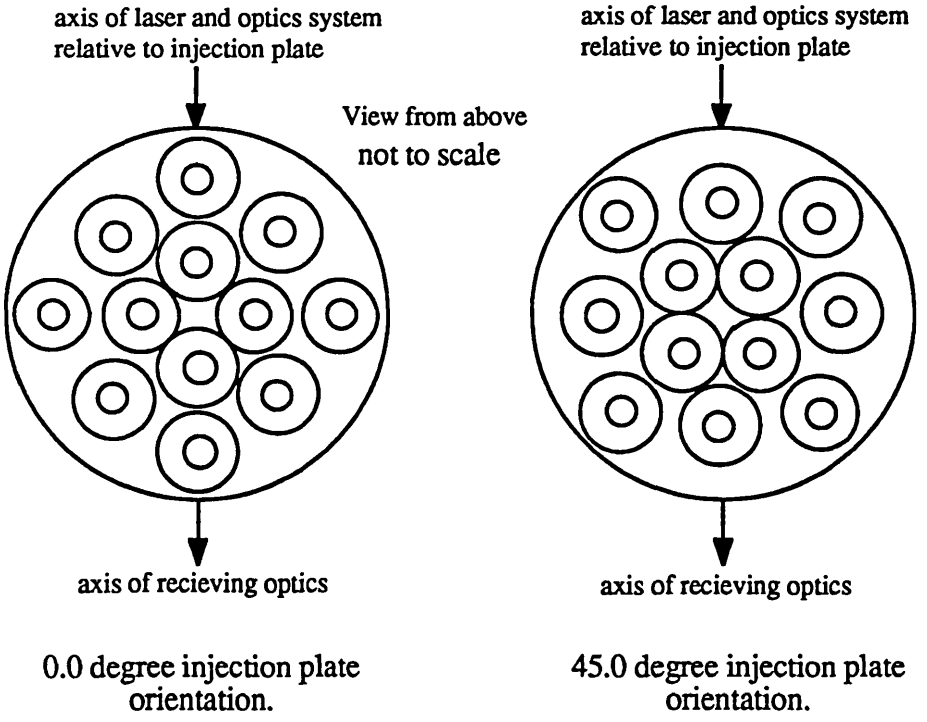


Figure 4.21 Diagram illustrating the two orientations of the injection plate.

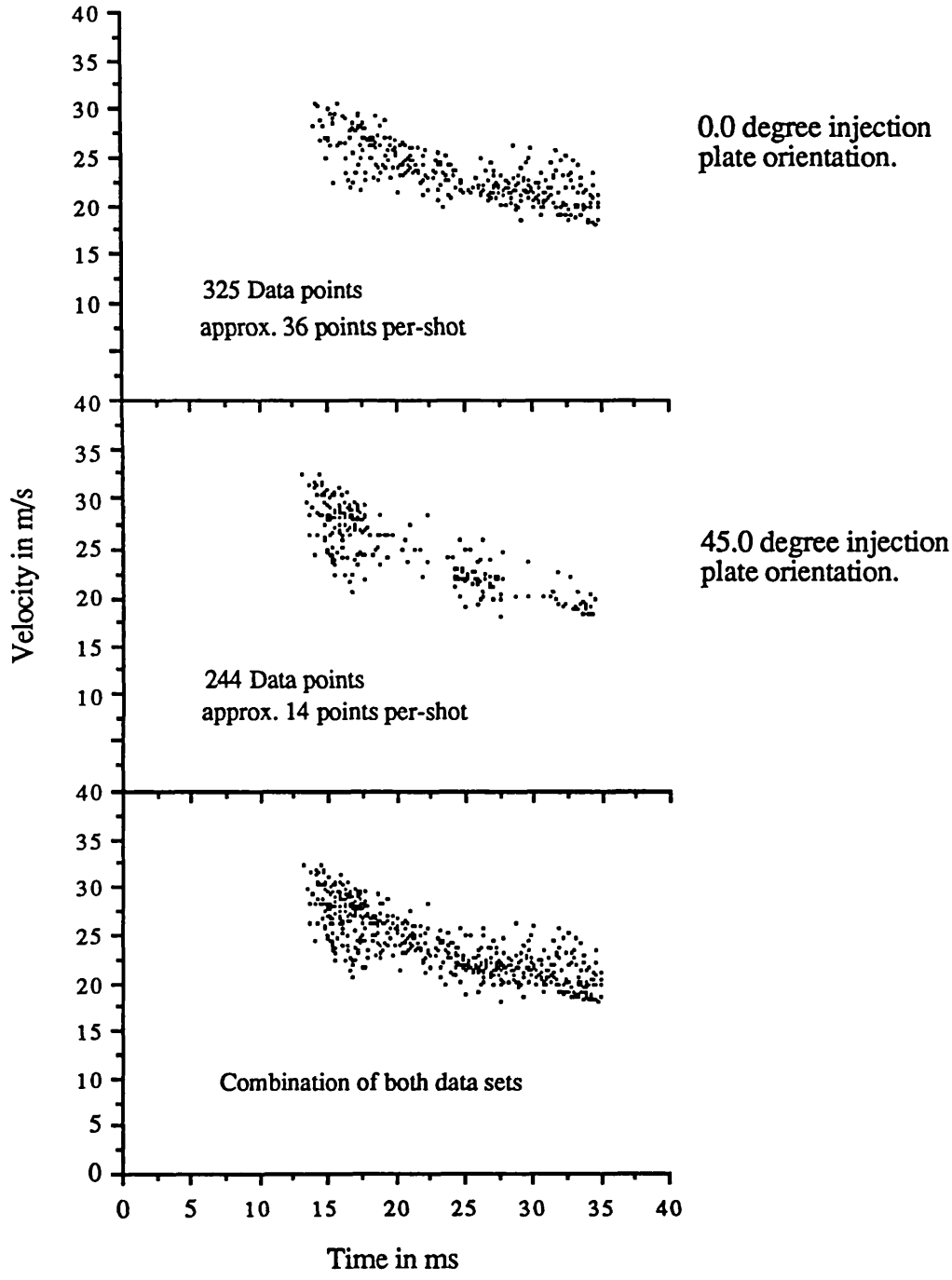


Figure 4.22 Temporal variation of two-phase data as a function of injection plate orientation; 0.09 r/R from wall.

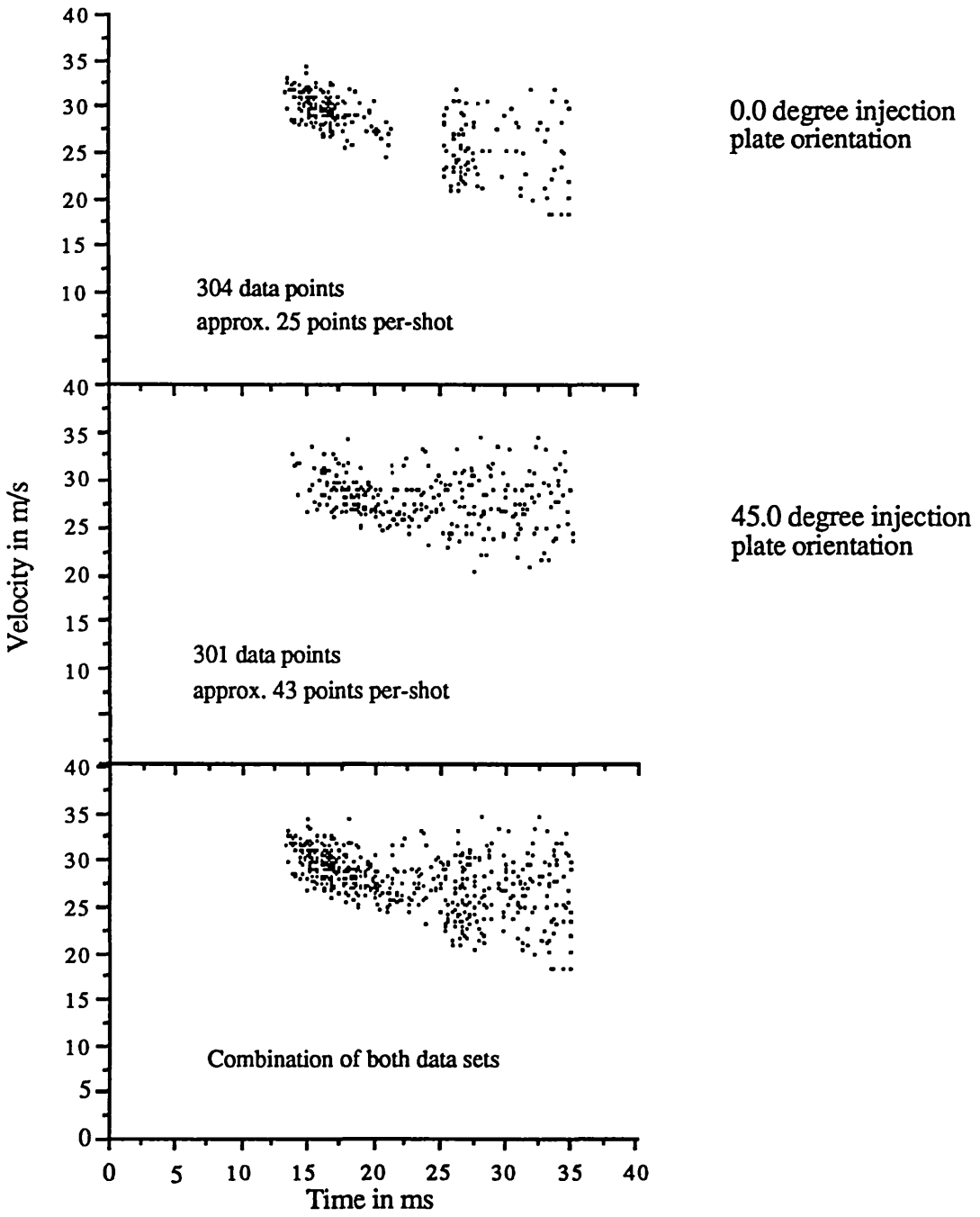


Figure 4.23 Temporal variation of two-phase data as a function of injection plate orientation; 0.12 r/R from wall.

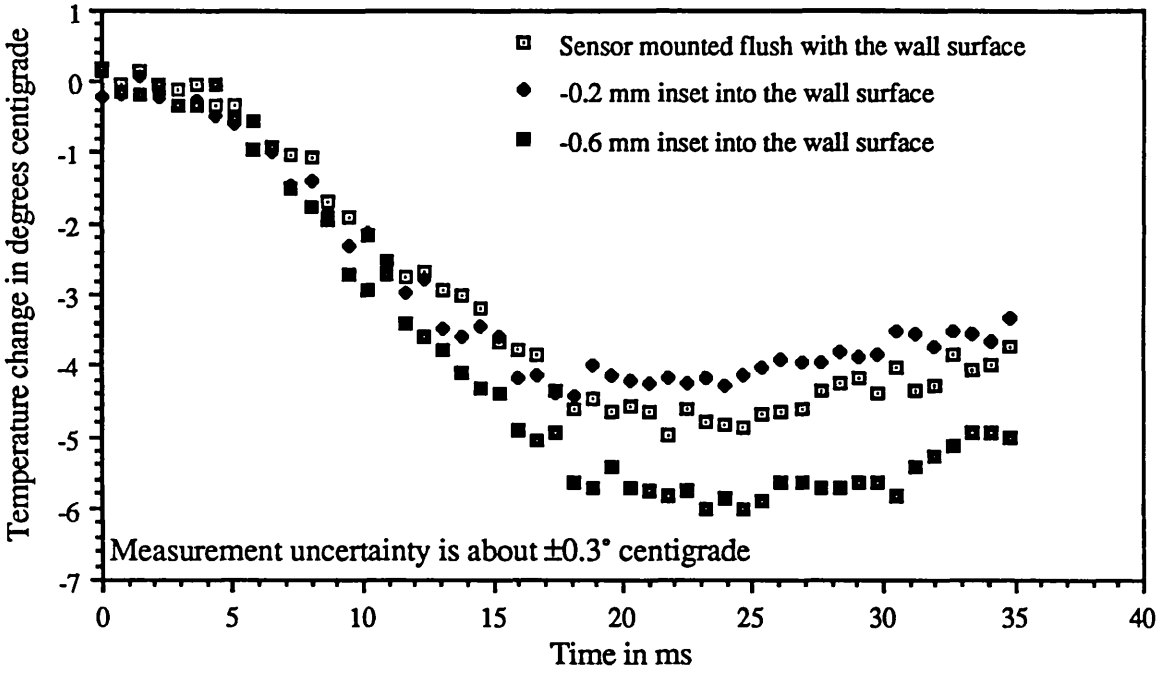


Figure 4.24 Effect of radial positioning of sensor on sensor temperature at x=2.88d; single-phase flow in constant-diameter geometry.

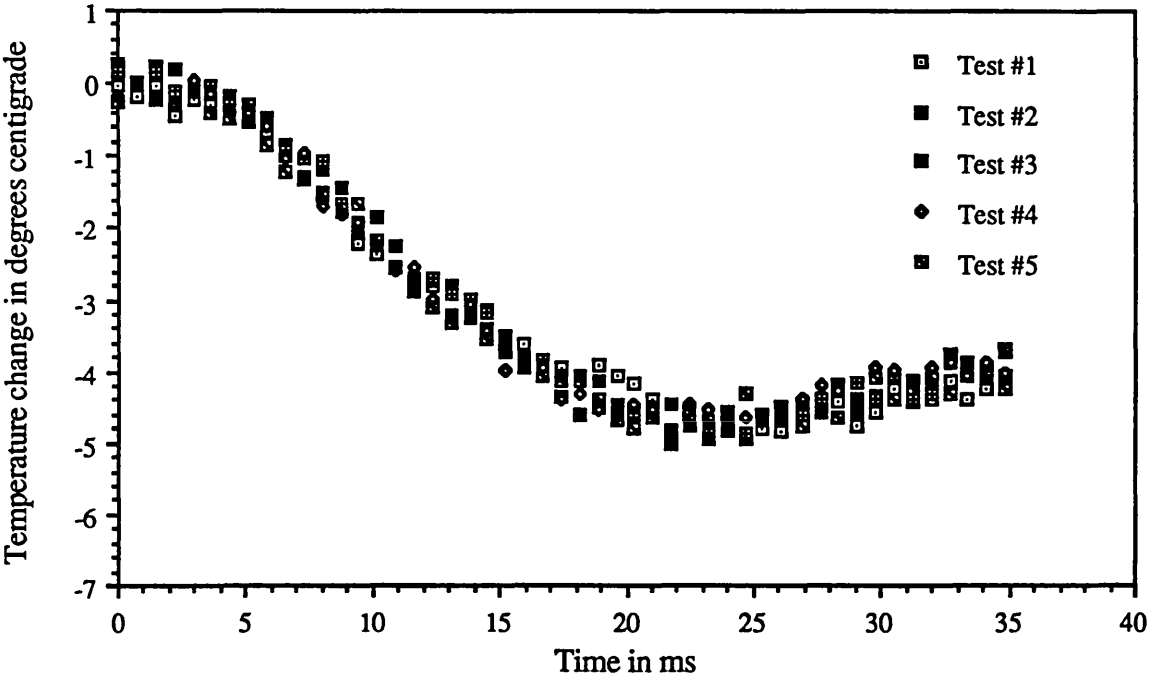


Figure 4.25 Sensor temperature variation at x=2.88d over five shots.

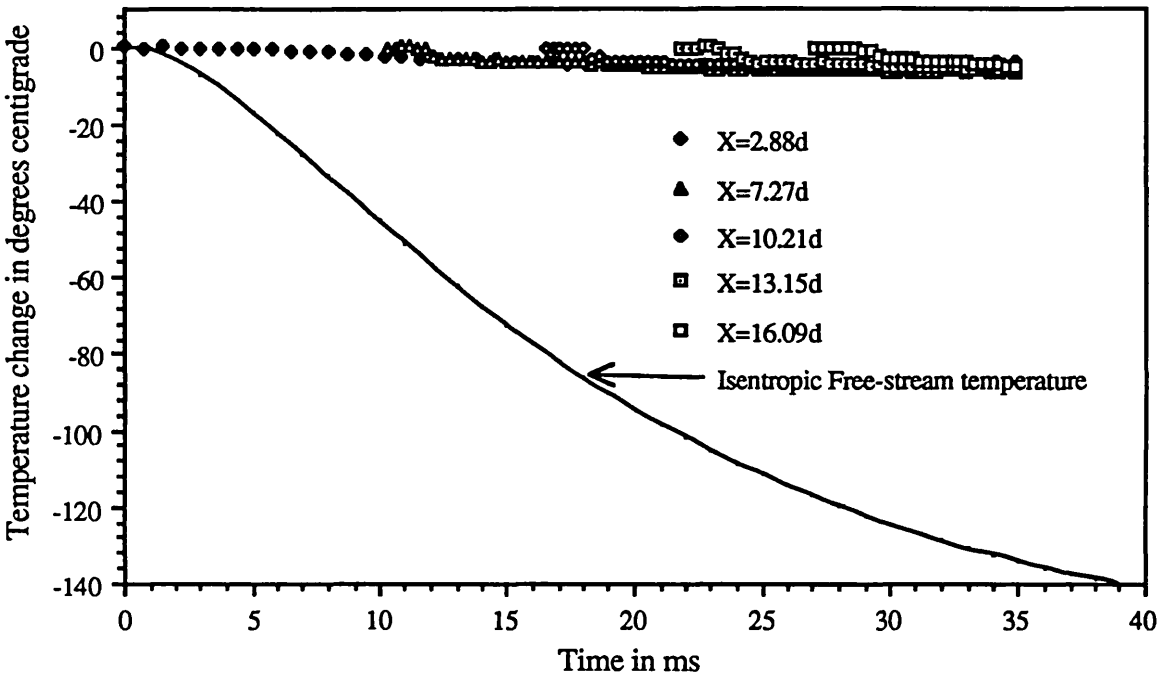


Figure 4.26 Sensor temperature time records at various axial locations relative to free-stream temperature; single-phase flow in constant-dia. geometry.

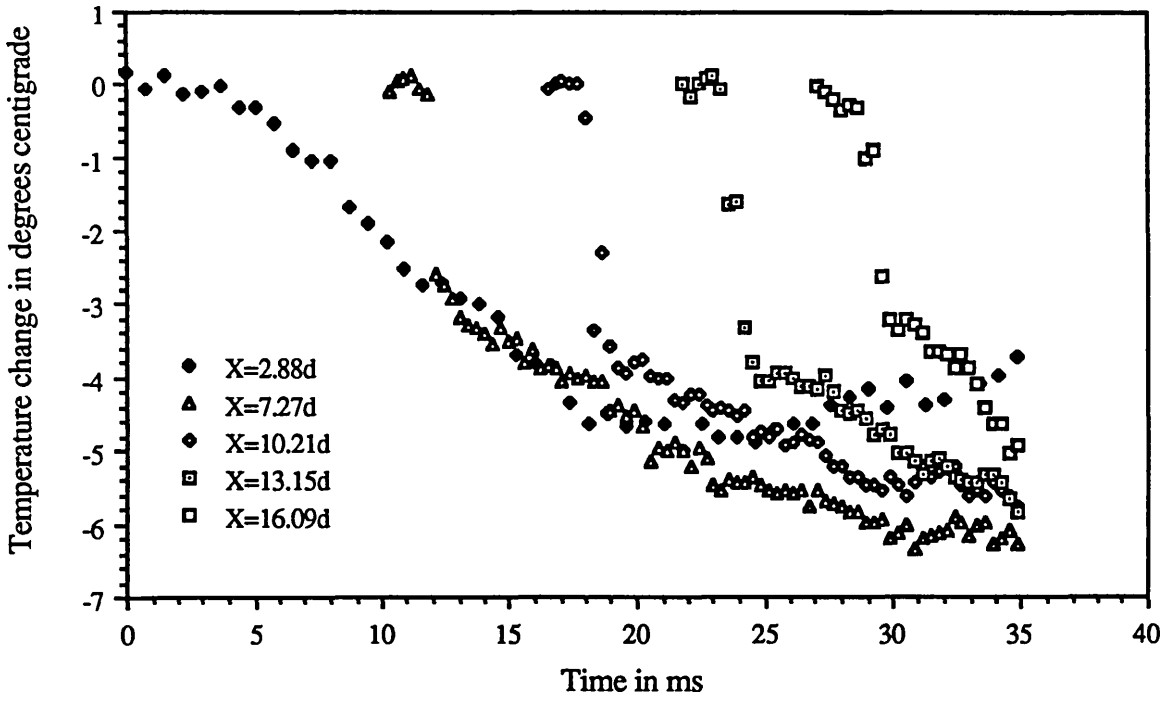


Figure 4.27 Sensor temperature time records at various axial locations; single-phase flow in constant-diameter geometry.

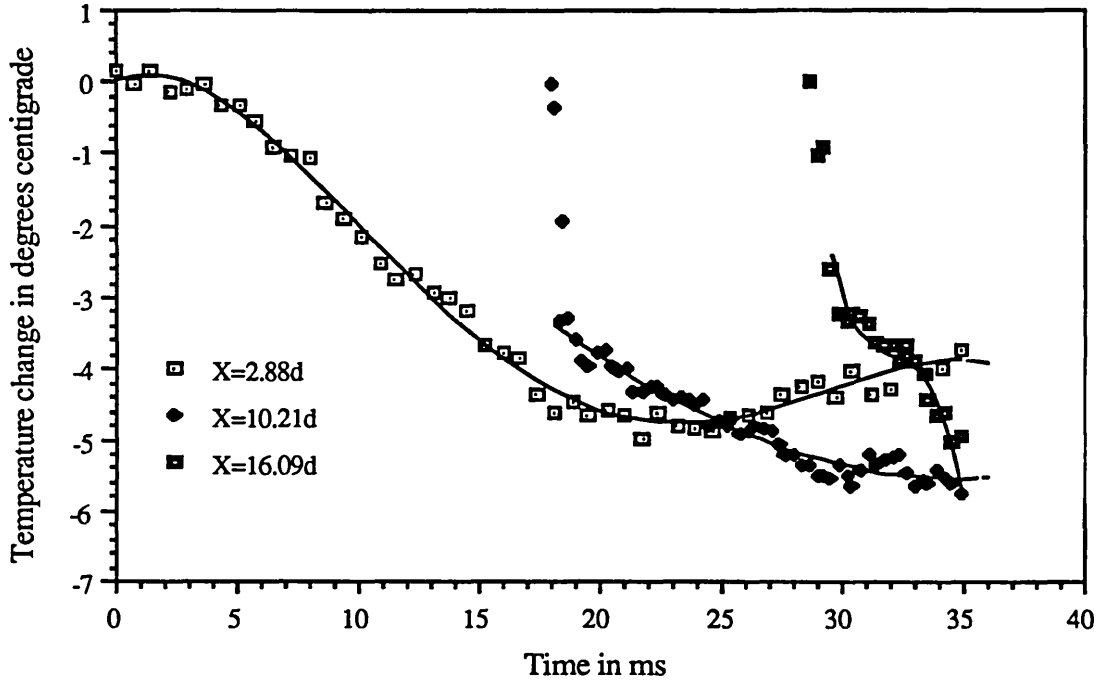


Figure 4.28 Curve-fit approximations to sensor temperature data.

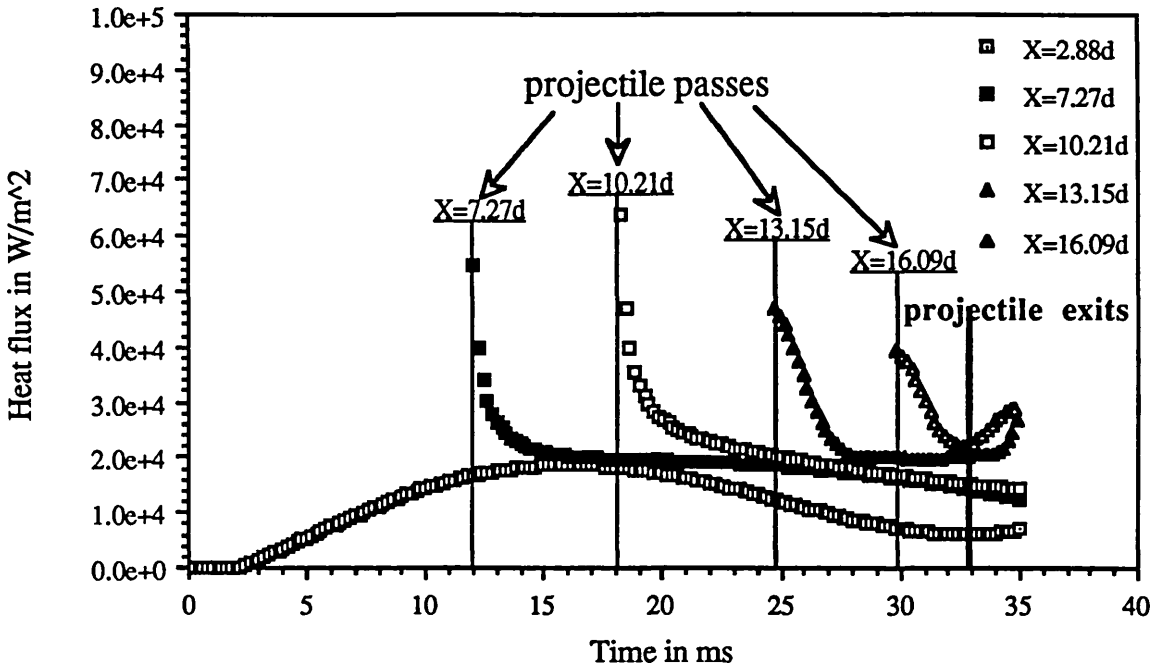


Figure 4.29 Heat flux at various axial locations; single-phase flow in constant-diameter geometry.

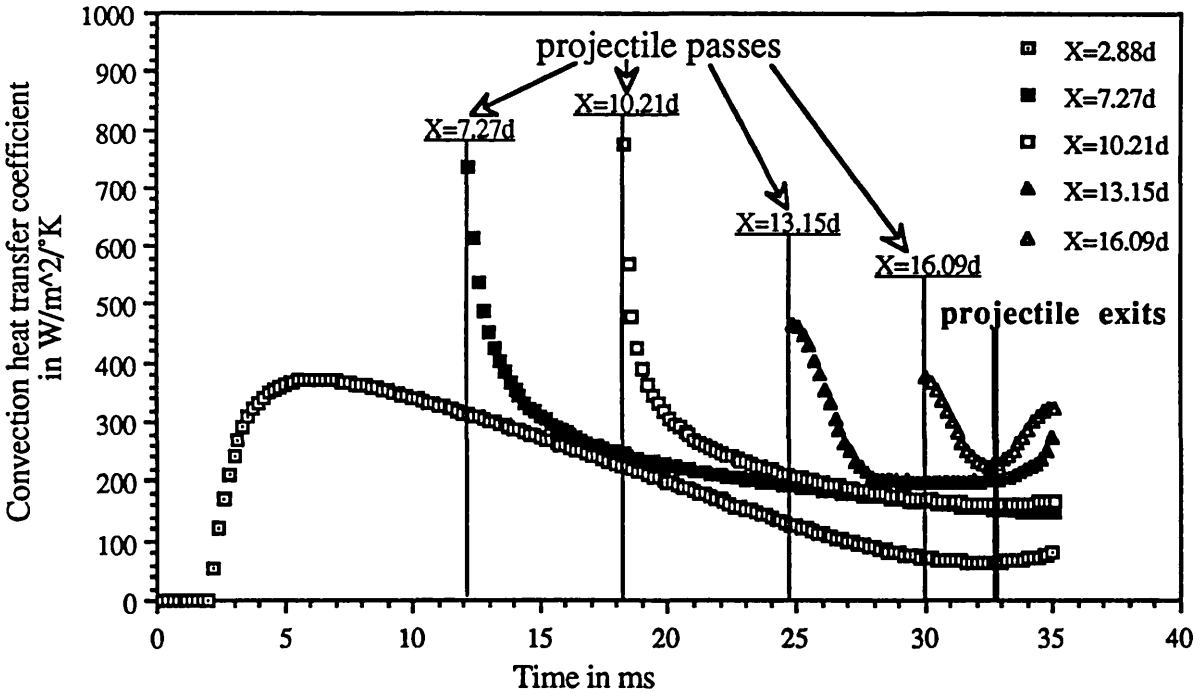


Figure 4.30 Convection coefficients at various axial locations; single-phase flow in constant-diameter geometry.

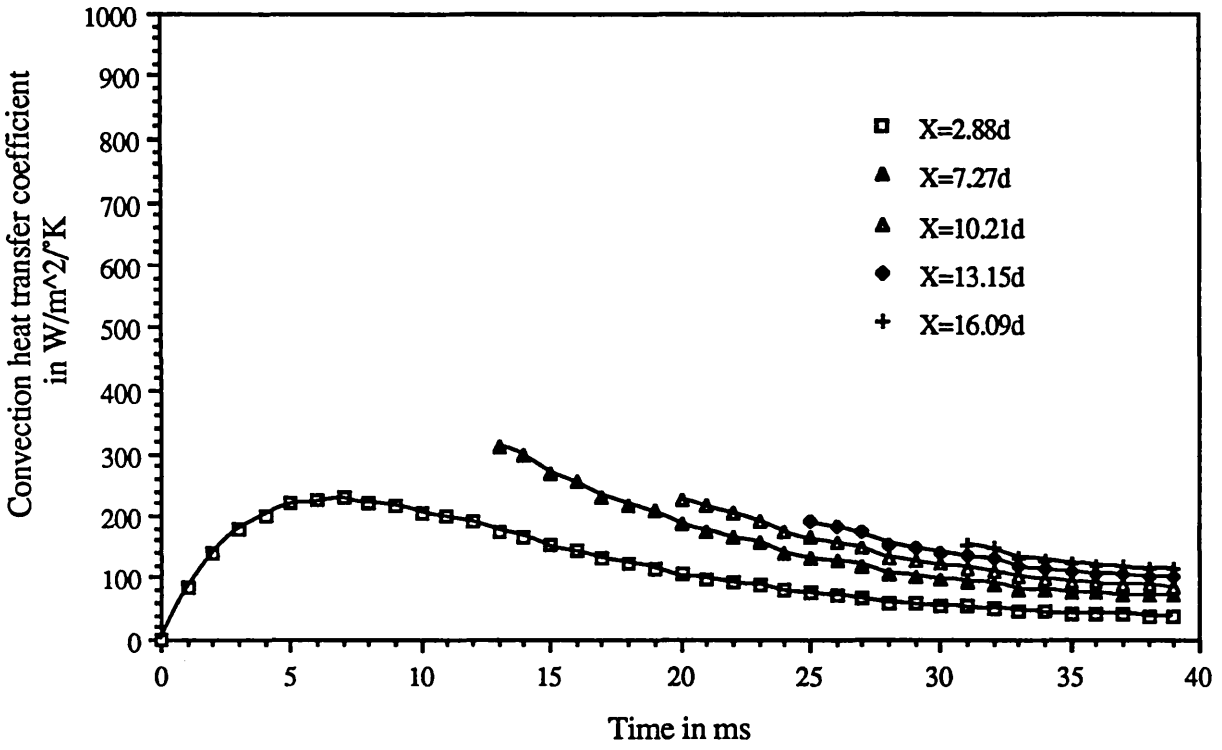


Figure 4.31 Calculated convection coefficients at various axial locations.

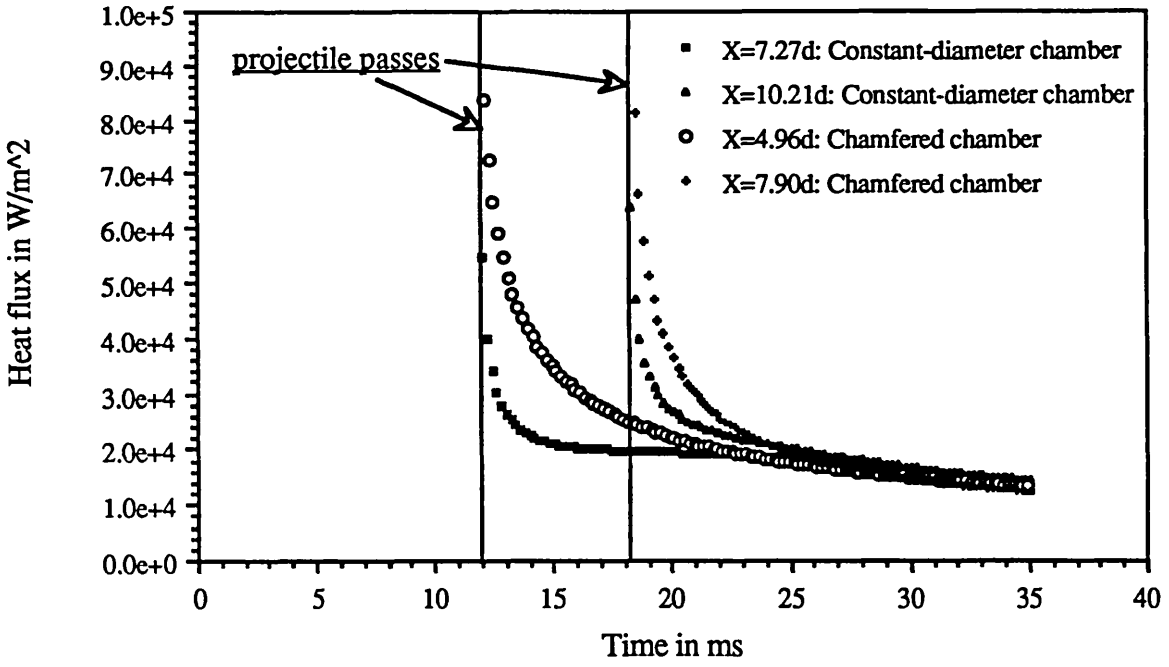


Figure 4.32 Wall heat flux at various axial locations; single-phase flow in constant-diameter and chamfered geometries.

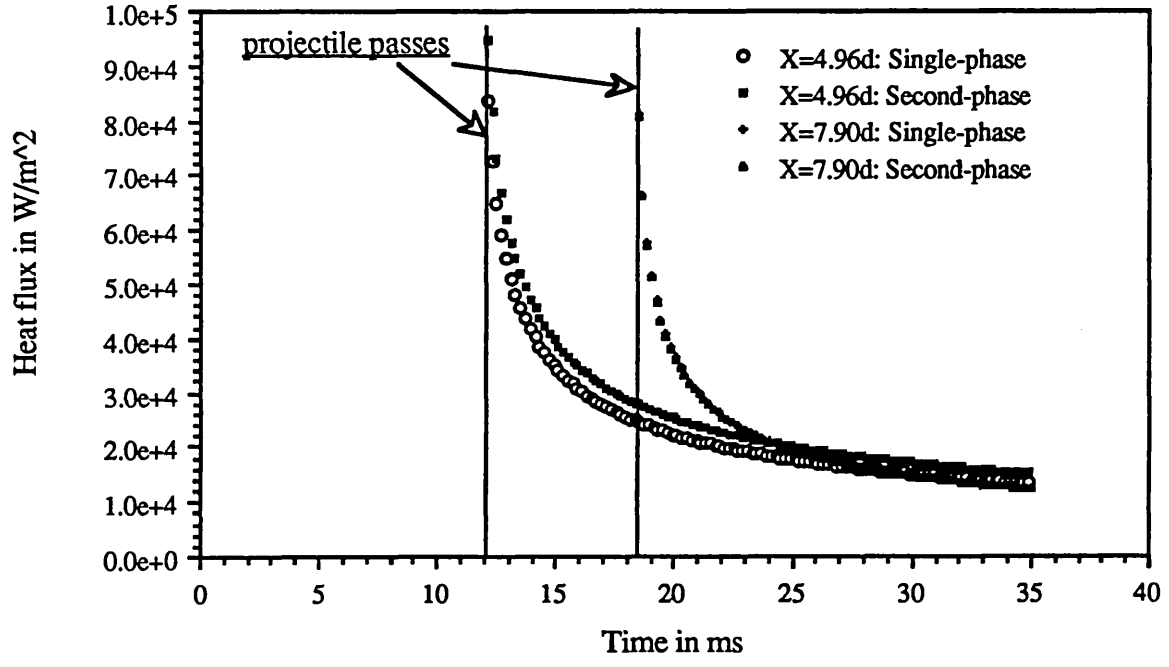


Figure 4.33 Wall heat flux at various axial locations; single-phase and two-phase flows in chamfered geometry.

CHAPTER 5 HIGH-SPEED GUN SIMULATOR

5.1 Introduction

This chapter is concerned with the experimental investigation of the unsteady single-phase flow with heat transfer in a high-speed gun simulator. The first section describes the constant-diameter flow configuration and the operating procedures. In the results section, the measured and calculated dynamics of a projectile in the high-speed simulator are presented together with the breech pressure and measurements of single-phase velocity and heat transfer are reported in subsequent subsections. The chapter ends with a discussion of the important conclusions from the high-speed simulator investigation.

5.2 Flow Configuration

The high-speed gun simulator produced substantially larger velocities than the previous low-speed simulator by increasing the initial pressure, initial volume and travel length while reducing the mass of the projectile. Thus, initial pressures of 10 and 60 bar propelled a projectile of 10.5 grams to velocities of 220 and 450 m/s at the muzzle respectively, *Schmidt (1988a,b 1989)*. Since the high-speed gun simulator produced much shorter cycle times and much greater fluid velocities than those of the low-speed rig, the high-speed instrumentation of section 2.4 was developed to allow the accurate measurement of breech pressure, heat flux and velocity characteristics during the cycle.

The high-speed simulator is shown on Figure 5.1 and operated horizontally because of its considerable overall length of 9.5 metres. It comprised an initial chamber of 22.2 mm (d) bore and 1.13 m (50.90d) length and a test section length of 2.43 m (109.46d). The seven plexiglass windows facilitated velocity and surface heat flux measurements at axial positions of 60.81d, 70.72d, 80.63d, 90.54d, 110.36d, 130.18d and 150 diameters from the breech. The projectile was captured in the retarder section which was attached to the test section via a perforated muzzle of around 20d in length. Two projectiles each of 22.15 mm diameter and 25.4 mm length were used and were

made of Acetal Plastic and Nylatron GS (Molybdenum di-sulfide Nylon 66) with corresponding weights of 13.1 and 10.5 grams. The particular designs of the projectiles and the effect of wear on the cycle repeatability are discussed in detail in the following section on projectile dynamics and breech pressure. The projectile was initially held in place against an O-ring, to prevent leakage of the initial charge gas, by three pins resting on the cammed surface of a lock/release collar mechanism similar to that utilized in the low-speed simulator. Programmable solenoid valves connected to bottled zero-grade nitrogen and air were used to; pressurize the initial volume with nitrogen, release the projectile with the lock/release mechanism activated by a pneumatic cylinder, and to return the projectile to the locked position for a new cycle with the aid of a sliding muzzle cover.

A photograph of the entire high-speed simulator, viewed from the retarder end, is presented in Figure 5.2 with the trigger laser and Doppler anemometer visible on the upper right side across from the instrumentation and the gas cylinders. A detailed photograph of the initial volume, test section and instrumentation, Figure 5.3, shows the windows situated along the barrel and the transmitting and receiving optics of the anemometer as well as the pneumatic piston used to trigger the cycle. The gas cylinders supplied charge and seeding gas to the breech end of the initial volume in the upper right, via high pressure hoses connected to solenoid valves. The computer system on the left of Figure 5.3, orchestrated the data acquisition of the breech pressure, window surface temperature and gas velocity measurements.

The operation of the high-speed gun simulator was semi-automatic and required 5 minutes per cycle compared to over 20 minutes per cycle in the low-speed simulator. The automation of the operating procedures was facilitated by the programmable switching system which controlled the solenoid valves. Starting with the projectile locked in the initial position, the first step was to set the pressure charge amplifier so that the offset voltage and drift could be compensated by the data acquisition program. This required the pressure release valves to be opened so that the initial volume was at atmospheric pressure. Secondly, the initial volume was seeded with silicone oil droplets from the blast atomizer by opening the seeding inlet at the breech and the release valve near the projectile so that the seeded nitrogen gas would flow through the entire initial volume length. Thirdly, and because the test cycle caused a loud and sudden noise, a warning bell was sounded for several seconds to warn others in the vicinity that a test

was about to occur. The initial volume was then charged to slightly above the designated pressure with nitrogen by opening the high pressure charge valve situated at the breech. The pressure of the initial volume was displayed by the instrumentation system which was readied for transient data acquisition when the pressure decreased to the pre-selected pressure by leakage past the O-ring/projectile seal. The compressed air assisted cylinder, which mechanically triggered the start of the cycle by rotating the lock/release collar mechanism, caused the pins supporting the projectile to retract during the next stage of the rig operation. The measurement cycle was started by the release of the projectile which uncovered, after its first 6 mm of movement, the laser beam focussed on the fiber-optic relay and connected to the trigger signal conditioner which initiated the pressure, temperature, and velocity instrumentation. The projectile eventually came to rest in the muzzle after rebounding into the test section and retarder several times. Compressed gas was used to return the projectile to the locked position for a new test by moving the muzzle cover into place and releasing the gas between the projectile and the breech. Finally, the projectile was locked in place by the rotation of the lock/release mechanism collar which extended the pins into the barrel against the down-stream projectile end. Of the above steps, only the covering of the muzzle and locking of the projectile in its initial place had to be completed manually.

5.3 High-Speed Simulator Results

The results of the investigation are presented in the following three subsections which quantify in turn the dynamics of the projectile and breech pressure, single-phase velocity characteristics and transient heat flux.

5.3.1 Projectile Dynamics and Breech Pressure

The projectile velocity was calculated by the program described in appendix 4.1 for the low-speed simulator, which assumed an one-dimensional unsteady isentropic expansion, given the specific initial volume, pressure, gas properties and projectile mass. The reflection off the breech of the characteristic waves generated by the projectile motion can influence the effective projectile base pressure and subsequent dynamics outside the simple-wave region and the program compensated for the reflection of

characteristics by evaluating the projectile position, $x_{p\,1st}$ at which the first wave reflected off the breech reached the projectile base as represented by;

$$x_{p\,1st}/x_0 \cong 3\,p_0 A\,x_0/M\,a_0^2 \qquad 5.1$$

where x_0 is the initial chamber length, M and A are the mass and cross-sectional area of the projectile and p_0 and a_0 are the pressure and speed of sound at the initial conditions of the gas charge. The implications of the above correction are not of major importance for the calculations of the results with the 10 bar initial pressure. In this case, the waves reach the projectile after some 11 ms and no correction is required during this time. The correction for the relatively short period between 11 and 18 ms for the 13.1 g projectile, was of the order of 3 % of the muzzle velocity at the exit of the test section. For the first projectile, with its 13.1 g mass, the variation of the projectile position with time was calculated for the seven initial pressures and the results of Figure 5.4 show that the projectile would traverse the test section in 26 ms and 8 ms for initial pressures of 5 and 60 bar gauge.

The projectile velocity was quantified by measuring the time at which a laser beam focussed across the test section was disrupted. Preliminary tests were carried out with initial pressures from 10 to 60 bar and the velocities ranged from 200 m/s to 410 m/s with the 13.1 g projectile and the results are shown in Figure 5.5 together with those calculated assuming a quasi-steady isentropic expansion. The over-prediction of projectile velocities by less than 1% at pressures below 35 bar was primarily due to the neglect of wall friction, as also suggested by *Seigel (1965, 1979)*. At initial pressures greater than approximately 20 bar, the projectile velocity at the muzzle was greater than the speed of sound (278.3 m/s) in the gas charge, assuming a quasi-steady isentropic expansion, and greater differences with the calculations are evident in the 4 % discrepancy between the calculated and measured velocities at 60 bar. *Seigel (1979)* discussed the application of isentropic theory to experimental guns and found similar differences which were attributed to the effects of friction and convective heat transfer between the walls and the gas and the projectile-barrel friction. The differences between the measured projectile velocities and those calculated with the quasi-steady isentropic expansion assumption result from the contribution of the irreversibilities in the cycle. An isentropic process, reversible and adiabatic, is one in which the effect of friction and heat

transfer are absent. Isentropicity requires that the process be infinitesimally slow and that the gradients be infinitesimally small. The expansion in the simulator was by no means slow and gradients of temperature, velocity and pressure exist. Experiments with heated propellants have, however, indicated that the extent to which the expansion is nonisentropic was small with subsonic projectile velocities and larger with transonic projectile and gas velocities, continuing to increase at higher velocities. *Seigel (1979)* showed that the increasing frictional effect at transonic velocities can reduce the projectile velocity by up to 25 % at hypersonic velocities. The velocities of the projectile in the high-speed simulator at initial pressures greater than 35 bar, with consequential transonic flow and shock waves, are represented by the isentropic expansion assumptions with discrepancies increasing to approximately 4 % at the maximum operating pressure of 60 bar.

The problem of cyclic variations resulting from projectile-barrel friction, predominantly caused by wear of the projectile in the simulator case and by wear of the barrel in practical gun situations, caused difficulties in the experimental study of the simulated interior ballistic cycle and in real guns can reduce performance and accuracy below acceptable limits. During the preliminary tests, it became clear that the projectile wore with consequential shot-to-shot variations which affected the smooth acceleration of the projectile. When the projectile was severely worn, the cycle would produce a prolonged high pitched whistling sound rather than the usual sharp crack or discharge of a test with a new or slightly worn projectile. The whistling noise was produced by the gas escaping between the barrel and the projectile as the projectile became pinched or stuck along the test section. After about 50 tests at pressures greater than 30 bar, the projectile was found to be worn by up to 0.4 mm of the radius near the front and back ends and it would not seal the initial volume satisfactorily. With the initial volume at the initial pressure prior to release, gas escaping between the projectile and the initial volume seal could be heard and the pressure would drop to below the prescribed test pressure before the mechanical triggering was initiated. The Acetal plastic projectiles (13.1 g weigh) tended to stick along the barrel at lower initial pressures with increasing wear. The effect of sticking (gitter) as it traversed the test section was clearly evident in the pressure records of which Figure 5.6, is an extreme example. Rather than the steady, almost exponential decrease from the initial pressure, a noisy, and near sinusoidal variation was evident. At initial pressures less than 10 bar, the sticking was more

pronounced, decreasing as the projectile was broken-in and increasing as the projectile became worn. As the projectile wore with each successive test, the variations in breech pressure became less repeatable and this increased with initial pressure.

To evaluate the implications of cyclic variations on the characteristics of the cycle caused by the repeated use of a projectile, many tests were conducted at initial pressures of 5, 10 and 15 bar. The centreline gas velocity and the rms of velocity fluctuations are displayed in Figures 5.7 and 5.8 for 5 and 15 bar respectively with new and used projectiles and for 10 bar with a used projectile. The variation of the mean centreline velocity between new and used projectiles at 5 bar initial pressure is clearly evident with deviations of up to 25 % immediately behind the projectile. The apparent maximum difference of 10 % in the gas velocity for tests at a 15 bar initial pressure occurred between 5 and 7 ms at which time the projectile was between 100 and 150 diameters from the measuring position. The differences in the mean centreline velocity by between 25 and 10 %, for tests from 5 to 15 bar, are considerably larger and would, for example, make comparisons with calculations difficult since a model accounting for the variation of barrel-projectile friction and wear related phenomena over the life time of each projectile would be necessary. The reason for the discrepancies at 5 and 15 bar can be attributed to the reduction of friction between the barrel and the projectile as the projectile wore, thereby causing the worn projectile to attain larger velocities, producing greater gas velocities, than with the new projectile The increase in the projectile velocity was however partially counteracted by the reduction of the effective charge due to the increase in leakage or blow-by between the projectile and the barrel from the greater tolerances. At low initial pressures, the friction between the projectile and barrel with a new projectile decreased the projectile velocity until a sufficiently large number of tests had worn the projectile so that the velocities were less than 1% different from the values calculated assuming no friction. In the 15 bar test, the larger differences later in the cycle after 5 ms were a result of the greater wear occurring at the higher velocities and subsequently lower losses due to friction and greater projectile velocities. The gas and projectile velocities in the 15 bar tests were approximately twice those produced by the 5 bar cycle and the losses due to projectile-barrel friction account for a smaller fraction at the higher initial pressure. For this reason, the cyclic variations were more evident at the lower initial pressures. The shot-to-shot changes also increased the rms of velocity

fluctuations associated not with the turbulence but with the cyclic variations. The rms of the velocity fluctuations, Figure 5.8, show differences of up to 20 % for the 5 bar tests and up to 40 % for the 15 bar tests. The 5 bar test showed no clear trend between new and used projectiles but the 15 bar test displayed s substantial reduction of the rms with the used projectile as a result of the elimination of the high-speed gitter.

To overcome the problem of variability, a harder and more resilient projectile material was found and the design modified in the area where the greatest wear was evident. By employing a more wear-resistant material, the cyclic wear was greatly reduced and variations in the projectile velocity reduced to less than 0.5 % over the life of a projectile. The sticking of the projectile was caused in part by the angle on the projectile front upon which the lock/release pins rested during the charge sequence. By replacing the forward angle with a gradual radius, the initial break-in period and the sticking problem were almost completely eliminated. The new projectile material, Nylatron GS, a Molybdenum di-sulfide Nylon 66, was the hardest and lightest plastic/nylon which could be found. The old and new projectile designs are shown in Figure 5.9 to indicate the change in shape of the radius of the forward edge of projectiles which weighed 13.1 and 10.5 grams respectively. The old and new projectiles are pictured side by side in the photograph in Figure 5.10 which shows that the new design on the right has removed the 45 ° edge from the projectile front which was prone to sticking and catching on the lip of the optical windows and between barrel sections where the tolerances maybe smaller due to the build up of worn projectile material and misalignment. This small change in the design removed the sticking phenomena completely and almost all the shot-to-shot variations. The lower density of the Nylatron GS had the advantage of reducing the projectile weight, thereby making it accelerate to slightly higher velocities.

The effect of wear on the centreline velocity for the old and new projectile designs is displayed in Figures 5.11 and 5.12, in terms of variations and repeatability over a fraction of the life of the projectiles. The results of Figure 5.12 show that the new projectile design produced repeatable results over at least 120 shots with rms fluctuations of mean centreline velocity of 1.5 m/s compared to 7.0 m/s for the old projectile design. The improved projectile did, however, need to be replaced after approximately 120 shots at a 10 bar initial pressure and doubled the operating range in which the cycle was

repeatable. Operation at higher initial pressures reduced the number of cycles for which the projectile velocity varied less that 5 % so that operation with an initial pressure of 20 bar required the projectile to be replaced after 50 tests. As a result of the reduced operating range at pressures greater than 10 bar, an initial pressure of 10 bar gauge was chosen for the detailed measurements of velocity and wall temperature.

After each projectile had been used for 120 to 140 cycles at 10 bar initial pressure, the initial volume could not be adequately sealed by the o-ring against which the projectile was held, due to the wear on the projectile base. The need to replace the projectile was readily identified by the sound of the charge gas escaping between the projectile and the barrel prior to triggering the shot and by reduction in the pressure of the gas in the initial volume between the charge and mechanical triggering sequences. With the replacement of the worn projectile, the entire test section was honed with typical shot gun cleaning tools (8 gauge) to remove any material that had worn off the projectile before a new projectile was inserted. An attempt to remove deposited projectile material from the bore with solvents, such as hydrochloric acid (HCl), was unsuccessful due to the rapid oxidation of the carbon steel barrel. Thorough cleaning and the new projectile material and design removed the sticking phenomenon and enabled tests to be conducted with variations from shot-to-shot of less than 1% of the projectile and gas velocity. The smaller mass of the newer projectile resulted in muzzle velocities which were some 10 % higher than that with the old projectile, as indicated by the comparison of calculations in Figure 5.13 for 5, 10 and 15 bar initial pressure tests with the 10.5 and 13.1 g projectiles. For tests at an initial pressure of 10 bar, the new projectile exited the test section with a velocity of approximately 220 m/s, compared to 200 m/s with the original 13.1 g projectile.

The calculated and measured projectile velocities are presented in Figures 5.14 - 5.16 for the new 10.5 g projectile with the former assuming a one-dimensional unsteady isentropic expansion as discussed in section 4.3.1. The length of the simple wave region, as calculated by Equation 5.1, occurred while the projectile travelled approximately 0.72, 1.13 and 1.90 m at 5, 10 and 15 bar initial pressures respectively.

The calculated and measured projectile travel distance records, in diameters from the initial position, are displayed in Figure 5.14. The delays between the real and

measured time scales were not compensated for in the presented results. The calculated projectile position was within 2 % of the seven measurements at the axial windows with an initial pressure of 10 bar. The projectile velocity as a function of the travel distance from the initial position, Figure 5.15, shows a slight over estimation by the calculations as would be expected because of the simplifying assumptions of the calculation method. The calculated and measured projectile velocity records of Figure 5.16 also show small differences between the calculated and measured results. The differences between the measured and calculated values are due to losses in the cycle from irreversibilities and the 6 mm delay distance before the triggering of the instrumentation which at a 10 bar initial pressure, corresponds to a inherent offset of approximately 0.6 ms for all measurements except those of Figure 5.15. The calculated projectile velocity position and time records for 10 bar initial pressures show very good agreement with the measurements as in the constant-diameter geometry of the low-speed simulator, with discrepancies of less than approximately 2 % throughout the cycle.

The measured breech pressure records, Figures 5.17 and 5.18, display typical pressure changes during a cycle at low and high initial pressures. Pressure time records for initial pressures between 1 and 8 bar (gauge) are displayed in Figure 5.17 together with the times at which the projectile left the muzzle and show that, at pressures greater than 2 bar, the projectile left the test section before the pressure at the breech decreased to atmospheric pressure. As shown between 0 and 3 ms in Figure 5.18, the measured breech pressures for initial pressures of 10, 15, 20, 25 and 30 bar did not vary because the first characteristic waves produced by the initial movement of the projectile traveling at the speed of sound in the charge gas along the initial volume, had not yet reached the breech. The signal noise at 5 ms in the cycle and, to a smaller degree at 9 and 12 ms, was due to the reflection of the mechanical shock associated with the release mechanism. The mechanical shock was identified by noting the speed of sound in the steel barrel, the length of the entire test rig and the initial volume and taking into account the delay between the actual start of the measurements and the shock associated with the mechanical triggering. The initial mechanical shock reached the breech before any measurements began and the subsequent mechanical shocks shown in Figure 5.18 are reflections of the initial shock off the end of the retarder and the breech. As in the low-speed simulator, the change of the pressure at the breech was with in 0.5 % of that calculated by assuming a quasi-steady isentropic expansion and again supports the

conclusion of *Seigel (1979)* on the applicability of isentropic theory to guns.

5.3.2 Single-Phase Flow

Cyclic variations due to projectile wear during the preliminary testing were eliminated by the new projectile design so that the projectile-velocity distribution varied by less than 2 % of the local value between the 20^{th} and 120^{th} cycles and with an initial chamber pressure of 10 bar gauge. The measurements of the mean and rms of gas-velocity fluctuations were obtained from ensemble averages over 0.5 ms and approximately 20 test cycles with statistical uncertainty of less than 1% for the mean and 10% for the rms velocity as discussed at length in section 2.4.2.

Examples of single shot realizations of measured centreline gas velocity at windows #1 and #5 for the initial pressure of 10 bar are shown in Figure 5.19 along with the calculated projectile velocity. The projectile accelerated past the first window station with a velocity of about 100 m/s (±1%) at approximately 4 ms after the projectile was released and the instrumentation triggered. The gas-velocity traces suggest acceleration immediately behind the projectile early in the cycle and the subsequent deceleration of the gas as the projectile moved towards the muzzle. The distribution of velocity data in Figure 5.19 suggests that the seeding, with silicone oil droplets to represent the gas-phase, was predominately in the gases immediately behind the projectile and not evenly distributed along the initial volume length because of the effect of charging from the breech end of the test rig. The uneven seeding of the initial volume was not sufficient to increase the measurement uncertainties or bias the statistical analysis, as was found in the second-phase seeding of the low-speed simulator, but implied small sample sizes late in the cycle, for example as can be seen on Figure 5.19 at window #1 from 8 ms to 16 ms.

The variations of single-phase velocity along the centreline at five axial positions are presented in Figure 5.20 and extend from the acceleration of the flow just behind the projectile to the deceleration at axial windows furthest from the projectile as the acceleration decreased relative to the increasing distance from the breech and window.

The centreline velocity measured during the cycle varied from about 205 m/s at window #5 to 100 m/s at window #1 while the projectile approached a velocity of about 220 m/s at the muzzle. The ensemble mean centreline velocity results for windows #1 to #5 were obtained by averaging velocity traces, such as those of Figure 5.19, over twenty cycles and may be compared in Figure 5.20 with gas velocities calculated by assuming a one-dimensional isentropic expansion between the breech and projectile base. The two centreline velocity traces in Figure 5.19 each contained approximately 750 individual realizations and over 20 shots were need for each point velocity value. The single shot traces suggest important velocity fluctuations and the core turbulence intensities were found to vary from 2.5 to 4.5 % during the cycle corresponding to the measurements presented in Figure 5.20. The maximum disagreement between the measured and calculated mean velocities in Figure 5.20 at the 1st window was approximately 10 % and about 6 % at the 2nd window. The differences occur because the viscous effects are not negligible and also because the comparatively thick boundary layers imply the importance of the two-dimensional flow. The results from the 3rd, 4th and 5th windows show similar differences following the projectile, for approximately 1 ms to 0.5 ms respectively, before approaching the calculated values. The 5th window results show excellent agreement with calculations, differing by only 2 % immediately behind the projectile and 0.5 % during the rest of the cycle. The maximum velocity was higher than the calculated value, as expected, since the boundary layer on the wall of the tube caused a favorable pressure gradient and, in general, the centreline gas-phase velocity is well represented by the one-dimensional expansion with differences mainly behind the projectile and toward the breech.

The rms of velocity fluctuations for the centreline measurements in Figure 5.20 are presented in Figure 5.21 and show a higher values immediately behind the projectile, associated with the viscous wake developing behind the projectile. The approximately constant rms of velocity fluctuations converts into a core turbulence intensity of between 4 and 4.5 % at the first window decreasing to around 2.5 % at the 4th and 5th windows. The larger centreline velocity above the 5th window produces higher rms fluctuations as seen by the marked difference in Figure 5.21.

Velocity measurements were obtained at several radial positions in each of the five axial measuring planes and are presented in Figure 5.22(a-e). They show the

variation with time and distance from the wall of the streamwise velocity and rms of velocity fluctuations at windows 1 through 5, Figures 5.22(a-e); The acceleration of the flow over the first two windows for short times, Figure 5.22(a-b), extends from the projectile's continued acceleration and subsequently became deceleration as the projectile moves further away from the measuring position and with the decrease in the projectile acceleration as the cycle progresses. Further downstream, Figure 5.22 (c-e), the flow decelerates from the passage of the projectile. The rms of velocity fluctuations normalized with local mean velocity increases to almost 10 % as the wall is approached, typical of turbulent wall boundary layers.

The radial profiles of the single-phase streamwise velocity and rms of velocity fluctuations at different times, Figure 5.23(a-e), allow analysis of the wall boundary layers as previously carried out with the results obtained in the low-speed simulator. Measurements closer than 2 mm from the wall were not possible due to the lack of seeding and high signal-to-noise ratio associated with the surface. Velocity measurements were not taken at the 6^{th} and 7^{th} windows because the projectile remained in the test section for less than 3 ms after passing the 6^{th} window. The radial distributions of mean and rms single-phase velocity at the 1^{st} window, Figure 5.23(a), show that the core occupies 83% of the diameter with a boundary layer thickness of around 3.8 mm. The boundary layer thickness in the high-speed simulator was twice as thick at that in the low-speed rig, due mainly to the increased distance from the breech, 1.35 m versus 0.556 m respectively. A notable feature of the ensemble mean velocity profile in Figure 5.23(b) for the 2^{nd} window, is the flattened profile at 6 ms, further indication of the effect of the density gradient and viscous wake on the developing wall boundary layer directly behind the projectile so that the interaction of the developing wall boundary layer and the wake region served to decrease the core velocity and increase the wall boundary layer thickness immediately behind the projectile. The mean velocity profiles at the 5^{th} window (X=110.36 l/d), Figure 5.23(e), show that the flow was almost fully developed. The rms of velocity fluctuations in all cases suggest a turbulent boundary layer as demonstrated by the increased intensity near the wall.

The variations of wall boundary layer thickness (99% of the core velocity), are displayed in Figure 5.24 with calculated results based on *Kays & Crawford's (1980)* correlation for steady turbulent boundary layers. The correlation assumes isothermal

flow with a constant freestream velocity in the streamwise direction, (no pressure gradient), a constant viscosity, a power law near-wall profile, an origin at the breech and a constant density in the streamwise direction. For the 1st window position, the correlation predicted a 5 mm (22% diameter) boundary layer, 5% more than that measured. As shown in Figure 5.24, the measured boundary layer thickness varied between 56 and 71 % of the radius at the second window and between 72 and 83 % of the radius at the fifth window. The transient characteristics of the cycle caused density and freestream velocity variations in the streamwise direction, so that only quantitative agreement between calculations and measurements were expected. Due to the scatter in the mean velocity radial profiles, the wall boundary layer thicknesses could not be resolved in Figure 5.24 better than ±0.05 r/R, increasing to ±0.08 r/R at the 5^{th} window.

The axial variations of measured and calculated boundary layer thicknesses at four different times in the cycle are shown in Figure 5.25 and confirm the increasing thickness with distance from breech, albeit with some scatter particularly for short times. The measured boundary layer thickness varied between 65 and 80 % of the radius between the 10 and 16 ms and was consistent with the results of Figure 5.24. The calculated values employed the freestream velocity obtained from the one-dimensional isentropic procedure in a correlation for boundary layer thickness based on a zero pressure gradient and distance from the breech.

The velocity profiles in the wall boundary layer are in reasonable agreement with a $1/7^{th}$ power law profile as shown in Figure 5.26(a-d). The differences from the power law in the 6 ms profile at the 2^{nd} window, Figure 5.26(a), result from the interaction of the viscous wake and the wall boundary layer immediately behind the projectile as noted above and the 5^{th} window results, Figure 5.26(d), differ from the $1/7^{th}$ power law due to the uncertainty in the wall boundary layer thicknesses. The analysis of the wall boundary layer profiles at windows 2-5 imply that the closest agreement with the $1/7^{th}$ power law occurs at successive times, ie. 11, 13, 14 and 17 ms at windows 2-5 respectively. The comparison suggests that the steady boundary layer approximation was best later in the cycle as, one would expect, rather than immediately behind the projectile.

The measured ensemble mean velocity profiles within the wall boundary layer enable the estimation of the shear-stress coefficient, via a *Clauser (1954)* analysis. The measurements at each window provide values of C_f, assuming a law-of-the-wall, (κ= 0.41, c= 5.0), as shown in in Figures 5.27(a-d). The Clauser chart of Figure 5.27 suggests wall shear-stress coefficients between 0.0034 and 0.0028 with a typical scatter of ±0.0002, within each window. The shear-stress coefficient decreases with increasing distance from the breech because the wall boundary layer develops with distance. All the Figure 5.27 profiles appear to have a region of logarithmic variation with average C_f values of 0.00315, 0.0031, 0.003, and 0.00285 at the 2nd through 5th windows respectively. The scatter corresponds to a maximum uncertainty of the shear-stress coefficient of less than ±7 %.

By assuming a constant C_f at each window, all the results can be presented in law-of-the-wall coordinates, Figure 5.28, and may be compared with wall laws with two sets of constants. All the measurements for the 2nd through 5th windows, presented in Figures 5.26 and 5.27, are shown in Figure 5.28 with emphasis on four data sets at the 2nd and 5th windows where the greatest differences are evident. Modification of the two constants for the law-of-the-wall, would reduce the discrepancies between theory and measurements further. The variation of the 5th window profile from the typical law-of-the-wall equation was a consequence of the uncertainty in the wall boundary layer thickness.

5.3.3 Heat Transfer

The experience from the heat transfer study in the low-speed gun simulator, enabled the development of the sensitive high-speed bridge circuit and interface to the data acquisition microcomputer, presented in section 2.4.3. Again, the thin-film sensor was mounted on a plexiglass window which could be interchanged with any of the plexiglass windows situated along the test section. A photograph of the thin-film sensor is shown if Figure 5.29 with the electrical connection visible on the left and the curvature of the flush mounted plexiglass window on the right. The sensor was again mounted inset into the surface to reduce the possibility of damage by the projectile traversing over

it at high velocities. The inset distance was less than 0.05 mm and made no difference in the measurements so that the thin-film was assumed to measure the surface temperature of the inside of the barrel.

The sensor temperature records presented in Figure 5.30 for four window positions show the rise in temperature of the gases in front of the projectile at all positions due to compression of the air, particularly at windows #5 & #6, and friction heating as the projectile passes the sensor position. The losses associated with the compression of the gas column in front of the projectile contribute to the differences between the measured and calculated characteristics in the previous two section. The reduction of compression heating just before the projectile passes the sensor, seen in window #6, was caused by the escape of small quantities of the gas past the projectile, often called blow-by in ballistic references. As expected, the temperature of the thin-film sensor decreased rapidly after the projectile, as the gas expanded down the barrel. Figure 5.31 displays the sensor temperature change relative to the isentropic free-stream temperature. The maximum measured surface temperature change with tests at an initial pressure of 10 bar was always less than 10 ° C, or 10 % of the free-stream temperature difference of about 100° C at the end of the shot. Figure 5.31

The temperature changes in the high-speed simulator are different from those observed in the low-speed simulator primarily because of the compression heating of the gas in front of the projectile, friction heating of the sensor as the projectile passes the measuring station and the greater velocities in the high-speed cycle. The rapid decrease in the surface temperature after the projectile swept the sensor was quantitatively similar in both simulators and less signal noise was evident in the high-speed results. The temperatures closest to the breech in both cases did not change as rapidly as those near the muzzle. Although the total sensor temperature changes in the high-speed simulator are higher, up to 10° K, than measured in the low-speed simulator, up to 6° K, similar features are evident such as the immediate decrease following the passage of the projectile and the decreased change in temperature as the cycle progresses at positions closest to the breech.

The thin-film temperature record was used to calculate the heat flux from the sensor by assuming one-dimensional heat conduction through the substrate. The

evaluation of heat flux again required a regression curve-fit of the measured surface temperature record just after the projectile passed the measuring position because the numerical method was sensitive to small changes in curvature relative to time, for example those due to signal noise. The results of Figure 5.32, indicate very high heat fluxes just after the projectile passed the measuring position, as in the low-speed simulator, and these decrease to an approximately constant value about 4 ms after the projectile passes. The peak heat flux for the tests at the initial pressure of 10 bar was about 1.2×10^6 W/m^2 at the window closest to the muzzle where the associated gas velocity and temperature difference were largest. The heat flux became constant with time at a value of about 10 % of the initial peak immediately behind the projectile. At the end of the shot, the heat flux varied from around 5.8×10^4 W/m^2 at X=60.81d to 1.35×10^5 W/m^2 at X=130.18d. Although the temperature change proceeding the passage of the projectile was similar in the two simulators, the heat flux in the high-speed simulator was twenty times greater immediately behind the projectile. Towards the end of the cycle, the heat flux in the high-speed simulator was approximately fifth times that measured in the low-speed case. The much greater heat flux as the projectile swept the measuring position in the high-speed case was due to the larger temperature difference between the wall and the fluid, as a result of the heating from friction between the projectile, and the substantially larger fluid velocities in the high-speed simulator. The muzzle velocity of the projectile was about five time that in the low-speed simulator and comparison of the relative heat flux toward the end of the cycle reflects this difference.

The convection heat transfer coefficients, Equation 4.1, presented in Figure 5.33 for the high-speed simulator, are based on the heat flux and the temperature difference between the isentropic free-stream and the wall-surface temperature, which was assumed to be that of the sensor. All locations were swept by the projectile (ie. X= 60.81d, 80.63d, 110.36d and 130.18d) and the convection coefficients are consistent with those of the heat flux. The peak convection heat transfer coefficient for the tests at the initial pressure of 10 bar was about 3.6×10^4 W/m^2 °K at X=60.81d. After the rapid decline immediately behind the projectile, the heat transfer coefficient attained values ranging from around 570 W/m^2 °K at X=60.81d to 1.33×10^3 W/m^2 °K at X=130.18d at the muzzle. The subsequent convection heat transfer coefficients measured in the high-speed simulator were ten to thirty times greater immediately behind the projectile, than those recorded in the low-speed simulator, and ranged from six to eight times larger

at the end of the cycle.

The measured convection heat transfer coefficients of Figure 5.33 may be compared with the correlation for the steady single-phase turbulent boundary layer over a flat plate with zero pressure gradient starting at the breech, which was employed in the low-speed simulator discussion. Figure 5.34 shows the coefficients for the four axial locations obtained from the correlation of *Incropera & DeWitt (1985)* given by Equation 4.3. The measured coefficients were much larger during the cycle and between 50 and 100 % underpredicted at when the projectile exits the muzzle. This correlation was used in the low-speed simulator with much better accuracy because the measuring positions were all less than 16 diameters from the breech and all the measurement positions in the high-speed simulator were greater than 60 diameters from the breech. The momentum boundary layers were also larger relative to the radius in the high-speed simulator, so that the flat plate and developing flow assumptions yielded results which are approximately half of those measured late in the cycle where the accuracy was demonstrated to be the best in the low-speed simulator.

A review of heat transfer literature provides many correlations with which to make comparisons. Many of the simpler ones, such as Equation 4.3, assume quasi-steady flow, a constant free-stream velocity with either a constant surface temperature or constant wall heat flux. *Kays and Crawford (1980)* present a turbulent boundary layer correlation for an axisymmetric body with an arbitrarily varying free-stream velocity and surface temperature, which may be written as:

$$St = 0.0287\, Pr^{-0.4}\, \mu^{0.2}\, \frac{(T_s - T_\infty)^{0.25}}{\left[\int_0^t (T_s - T_\infty)^{1.25} U_\infty^2 \rho_\infty \, dt\right]^{0.2}} \qquad 5.2$$

where St is the Stanton number (St=Nu/(Re Pr)) and all properties are evaluated at the isentropic free-stream temperature, U_∞ the bulk velocity above the sensor and T_s was the measured sensor temperature. The correlation is displayed in Figure 5.35 and shows high convection heat transfer coefficients immediately behind the projectile, as seen in the measurements, but with magnitudes of about one twentieth. The correlations gives the correct trends but wrong magnitudes because property variations are not considered

in the developing flow and mainly because the correlation is for steady flow and cannot, therefore, be expect to reproduce the results for small times. Toward the end of the cycle, the correlation yields convection heat transfer coefficients between 5 and 6 times smaller than those of the measurements. Another approach to the prediction of the convection coefficient by a standard correlation would be to assume turbulent flow in a pipe. In smooth circular tubes with fully developed velocity and temperature profiles and a Prandtl number (Pr) of approximately 1, *Incropera & DeWitt (1985)* suggest a correlation similar to Equation 4.3 and allowing for property variations;

$$Nu_d = 0.027\, Re_d^{4/5} Pr^{1/3} \left(\frac{\mu}{\mu_s}\right)^{0.14} \qquad 5.3$$

where Nu_d and Re_d are based on the diameter and local fluid properties, μ is the viscosity of the fluid at the isentropic free-stream temperature and μ_s at the surface temperature, assumed to be that of the thin-film sensor. The Reynolds number based on the diameter varies between 0.6 x 10^6 at the end of the cycle at X=60.81d and 1.65 x 10^6 at the X=130.18d measuring position, both of which are appropriate to the correlation. Toward the end of the cycle, the correlation underpredicts the measurements by less than 25 % which is reasonable particularly since the present flow was unsteady and had not achieved a fully-developed condition.

Subsequent heat flux test at higher initial pressures up to 60 bar, *Perez (1989)* in the high-speed simulator, have also shown an increase in the heat flux proportional to the rise in the projectile muzzle velocity. At initial pressures greater than 30 bar, the calculated heat flux from the sensor indicates that the finite film and substrate thickness do not allow time response appropriate to the rate of change of the sensor temperature associated with the corresponding velocities.

5.4 Concluding Remarks

The main conclusions of the experimental investigation of the high-speed gun simulator are:

1. The simulator has been shown to produce projectile and gas velocities in excess of 450 m/s with a 10.5 g projectile, which are much closer to those found in real guns than those in the low-speed simulator.

2. With initial pressures below 20 bar, the projectile did not reach supersonic velocities and the differences between those measured and calculated on the basis of a one-dimensional isentropic expansion method were less than 1 %. With transonic projectile velocities, pressures from 20 to 60 bar, the calculations over-predicted the measured projectile velocities by up to 4% at 60 bar, due to irreversibilities in the flow.

3. Cyclic variations resulting from wear of the projectile, evidenced as sticking as the projectile accelerated down the barrel, were overcome by a modified projectile design, a harder projectile material and an improved operating technique which limited the number of shots with each projectile to 120 shots.

4. Comparison of single-phase centreline gas velocity measurements, at an initial pressure of 10 bar gauge, with one-dimensional isentropic expansion calculations, indicates differences of less than 10 % caused by the thick boundary layers, with consequent two-dimensional flow.

5. The core rms turbulence intensity varied between 2.5 and 4.5% over the cycle at all the windows. Larger velocity fluctuations, immediately behind the projectile, resulted from the wake of the projectile.

6. The radial profiles allow the determination of boundary layer thickness, which varied from 17% to 43% of the bore between the 1st and 5th windows.

7. The radial distribution of the fluctuations in the mean velocity increased near the

wall, typical of those of turbulent boundary layers, to corresponding turbulence intensities of between 6.5 and 10 %.

8. Comparison of the wall boundary layer profile of the measurements at the 2nd and 5th windows with the 1/7th power law profile showed agreement except immediately behind the projectile and at positions where the uncertainty in the boundary layer thickness was larger, ie ±0.08 r/R at the 5th window.

9. The near -wall profiles corresponded to a logarithmic law of the wall and this assumption led to wall shear-stress coefficients of 0.00315, 0.0031, 0.003, and 0.00285 at the 2nd through 5th windows respectively, with a typical scatter of ±0.0002.

10. The thin-film temperature measurements showed the compression heating of the gases in front of the projectile at all positions and cooling due to the escape of small quantities of the gas past the projectile at windows near the muzzle. After the projectile swept the measuring position, the surface temperature decreased rapidly and continued to decrease at a smaller rate until the end of the cycle.

11. The peak heat flux for the tests at an initial pressure of 10 bar was about 1.2 x 10^6 W/m^2 at the window closest to the muzzle where the associated gas velocity and temperature difference were largest. The heat flux became constant with time at a value of about 10 % of the initial peak immediately behind the projectile.

12. A correlation assuming quasi-steady and fully developed turbulent flow in smooth circular tube, with the evaluation of fluid properties at the isentropic free-stream temperature, underpredicted the convection heat transfer coefficient by approximately 25 % as the projectile exits the test section. Also, a correlation based on a developing flow indicated correct trends but incorrect magnitudes due, predominately, to the unsteady and variable-property characteristics of the flow.

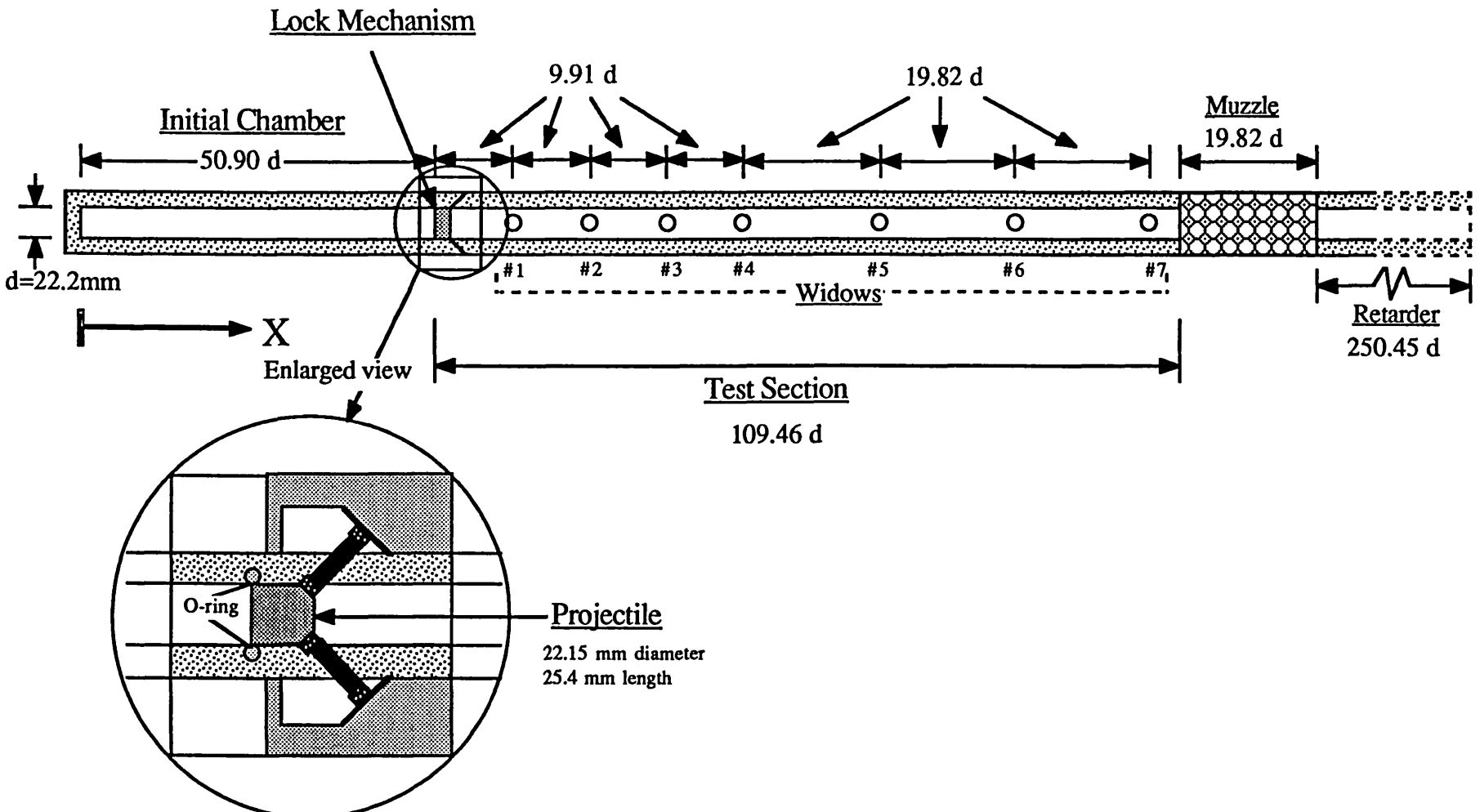


Figure 5.1. Geometry of high-speed simulator.

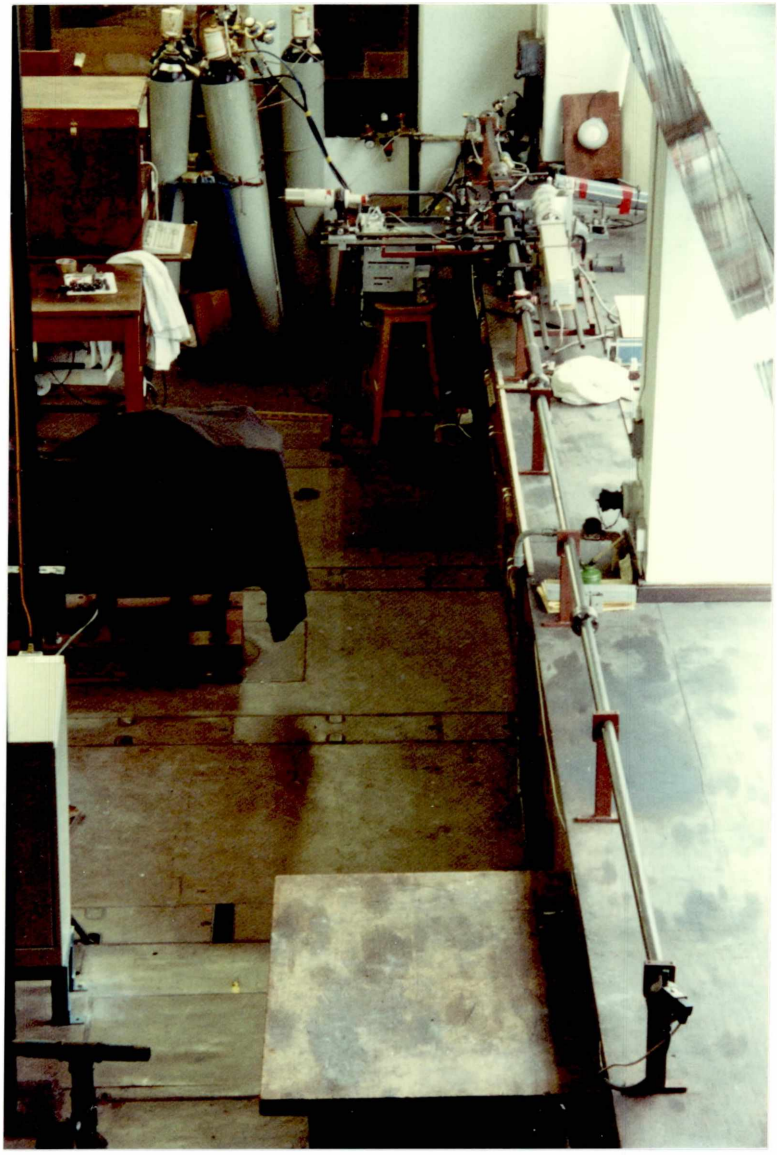


Figure 5.2 Photograph of the entire high-speed gun simulator.

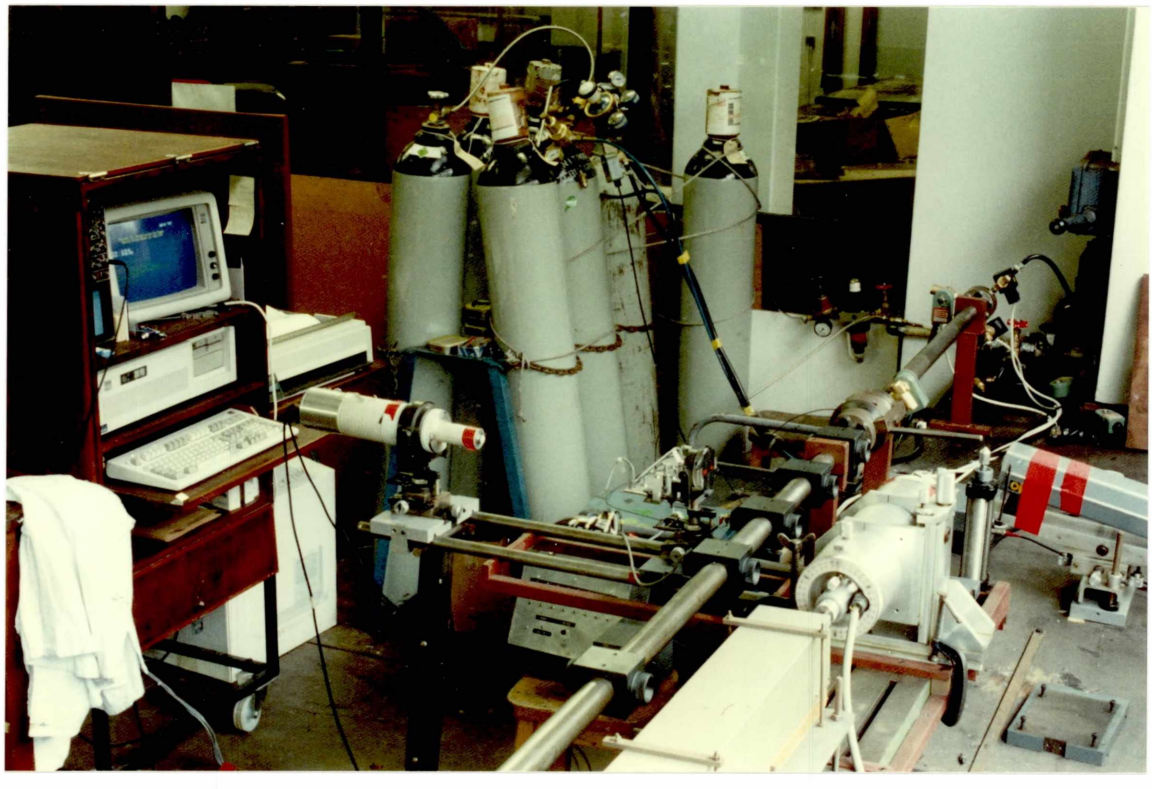


Figure 5.3 Photograph of the high-speed initial volume, test section and instrumentation.

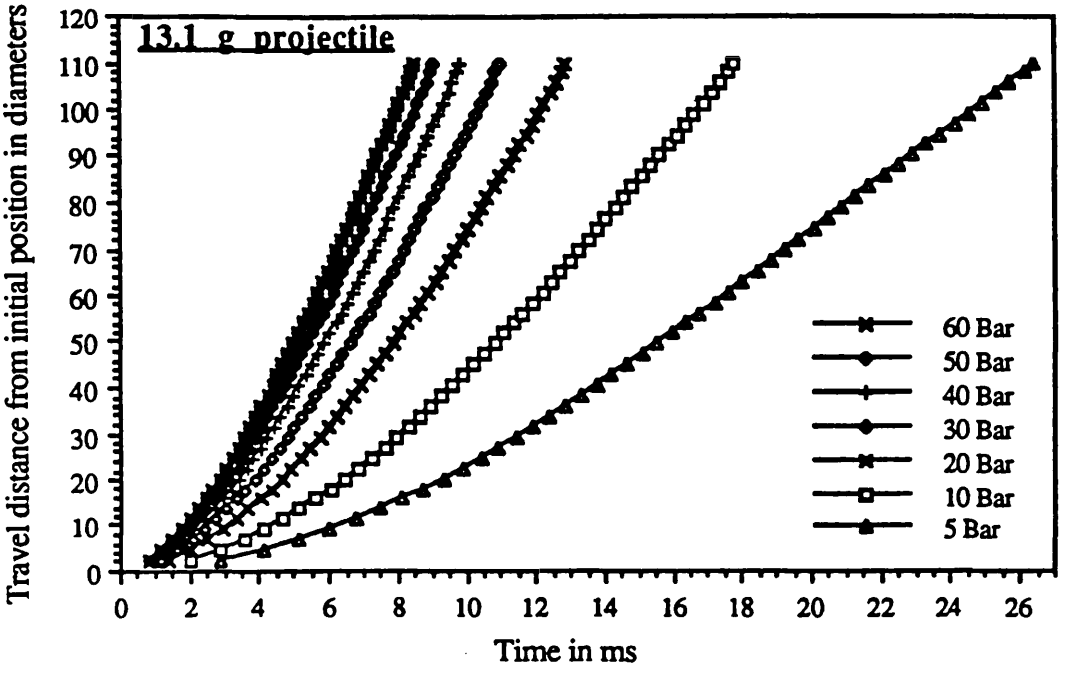


Figure 5.4 Calculated projectile travel distance with time; 13 g projectile.

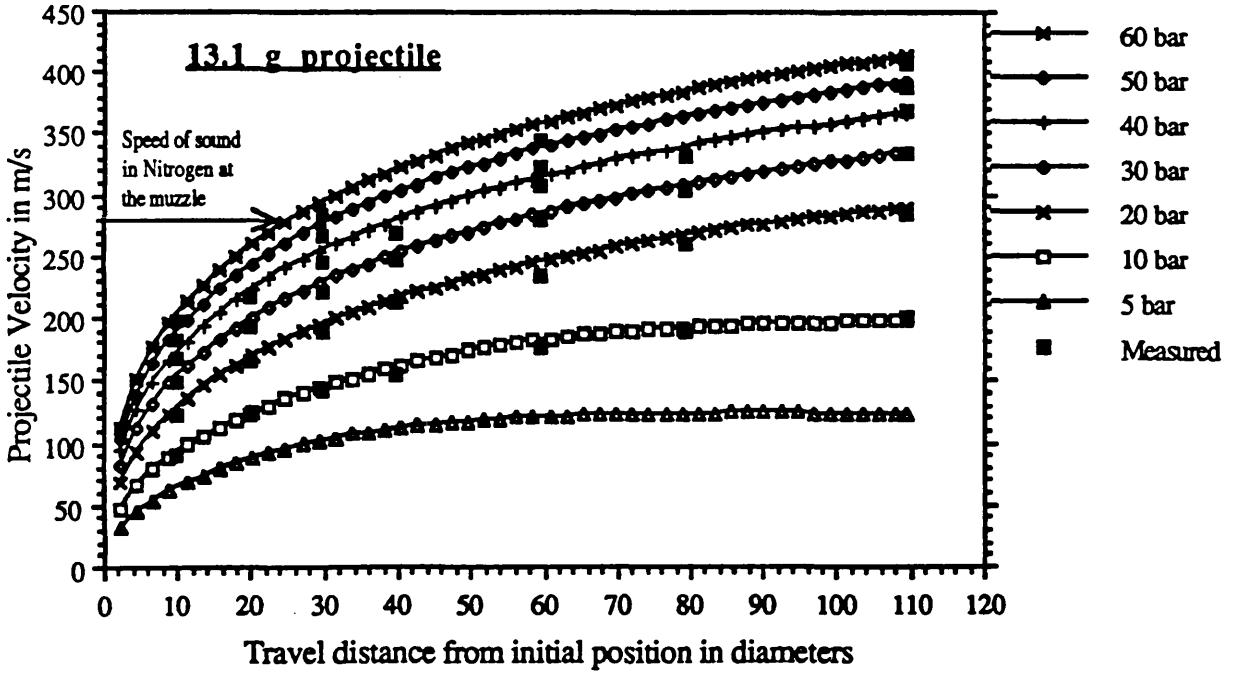


Figure 5.5 Calculated and measured projectile velocity with travel distance; 13 g projectile.

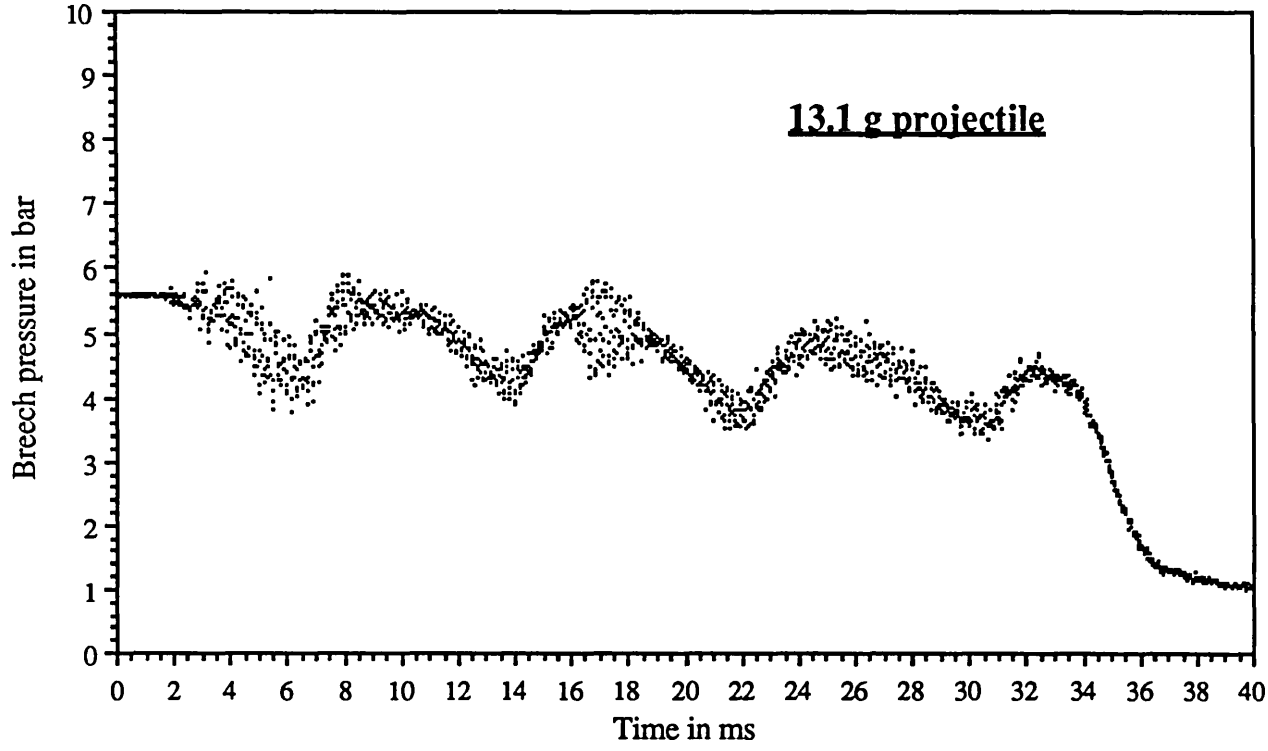


Figure 5.6 Measured breech pressure with a worn projectile.

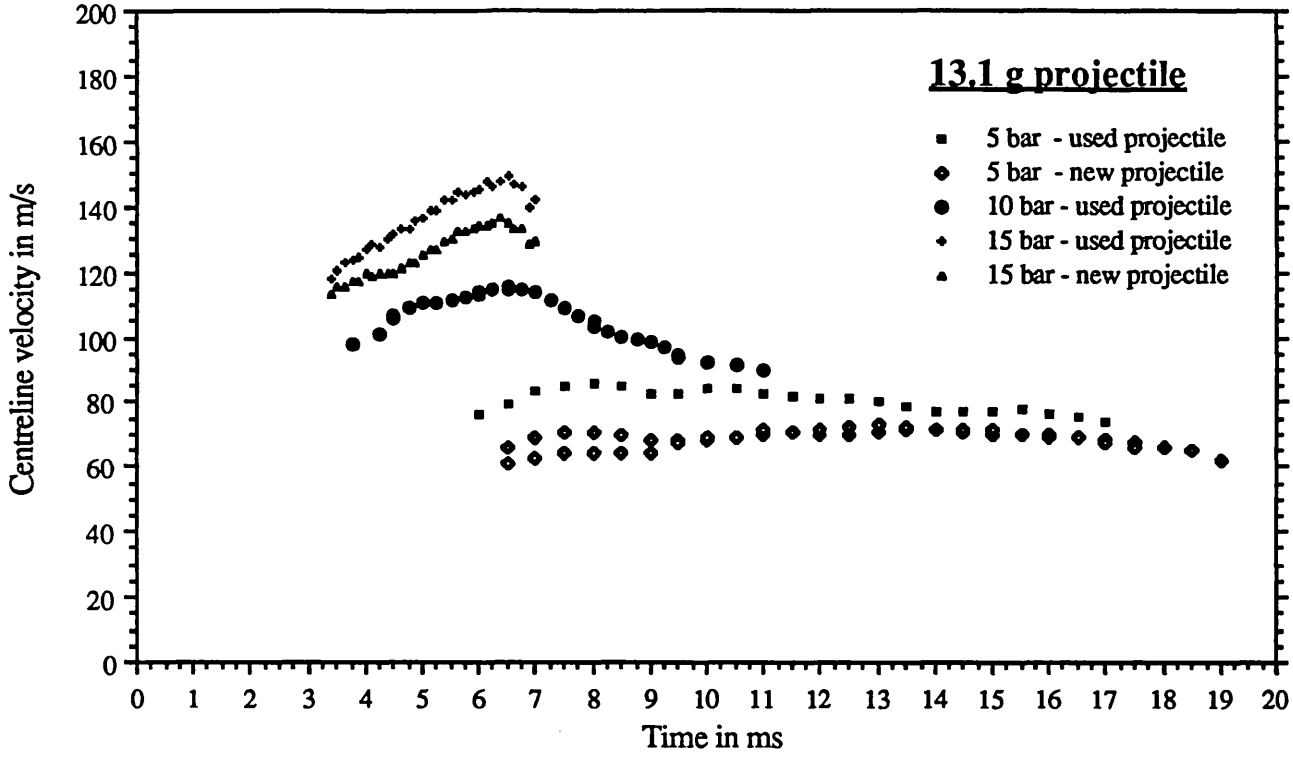


Figure 5.7 Centreline single-phase velocity at 5, 10 and 15 bar initial pressures with new and used projectiles.

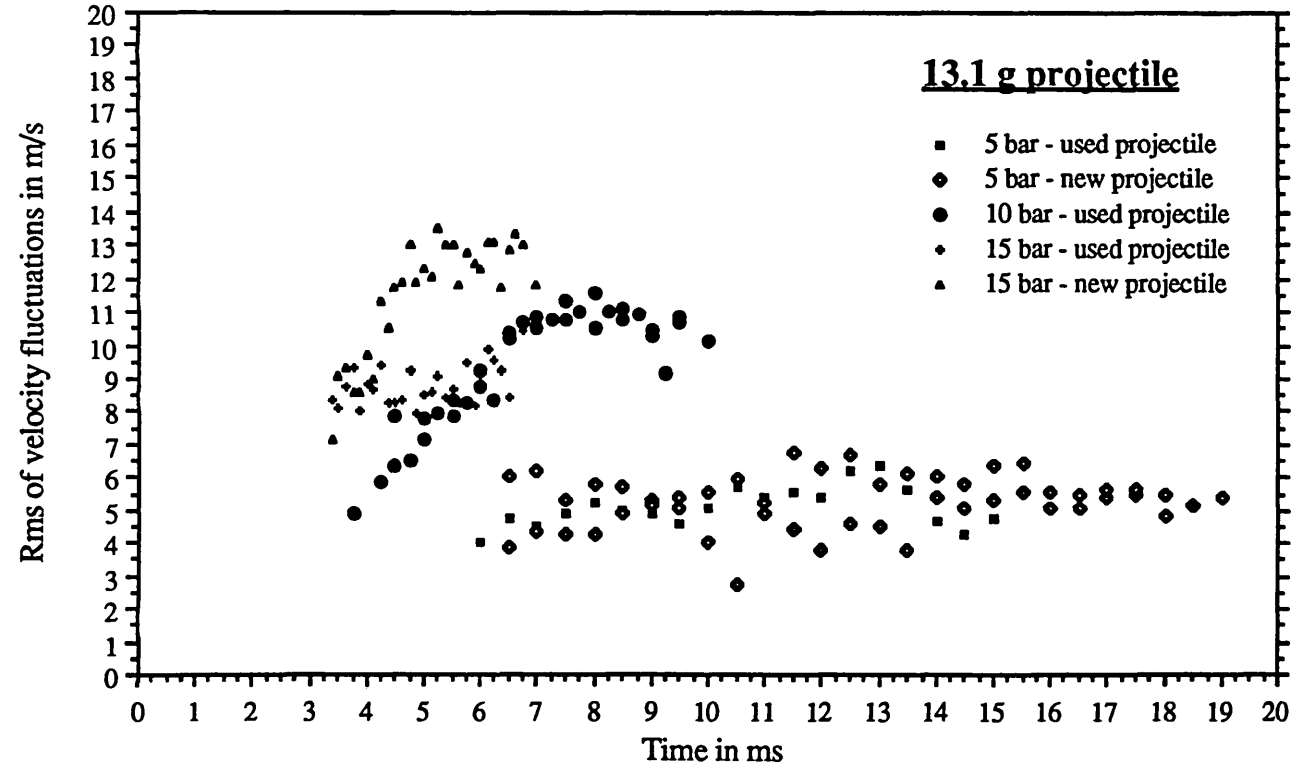


Figure 5.8 Centreline single-phase rms velocity fluctuations at 5, 10 and 15 bar initial pressures with new and used projectiles.

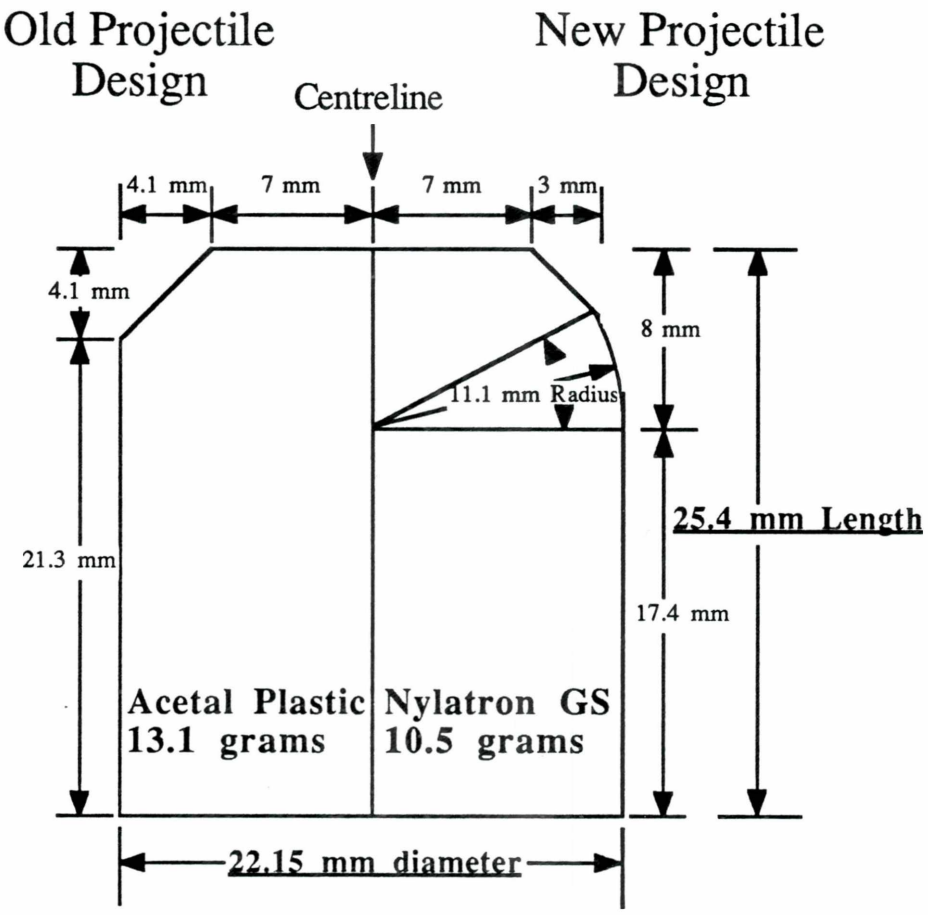


Figure 5.9 Geometry of old and new projectile designs.

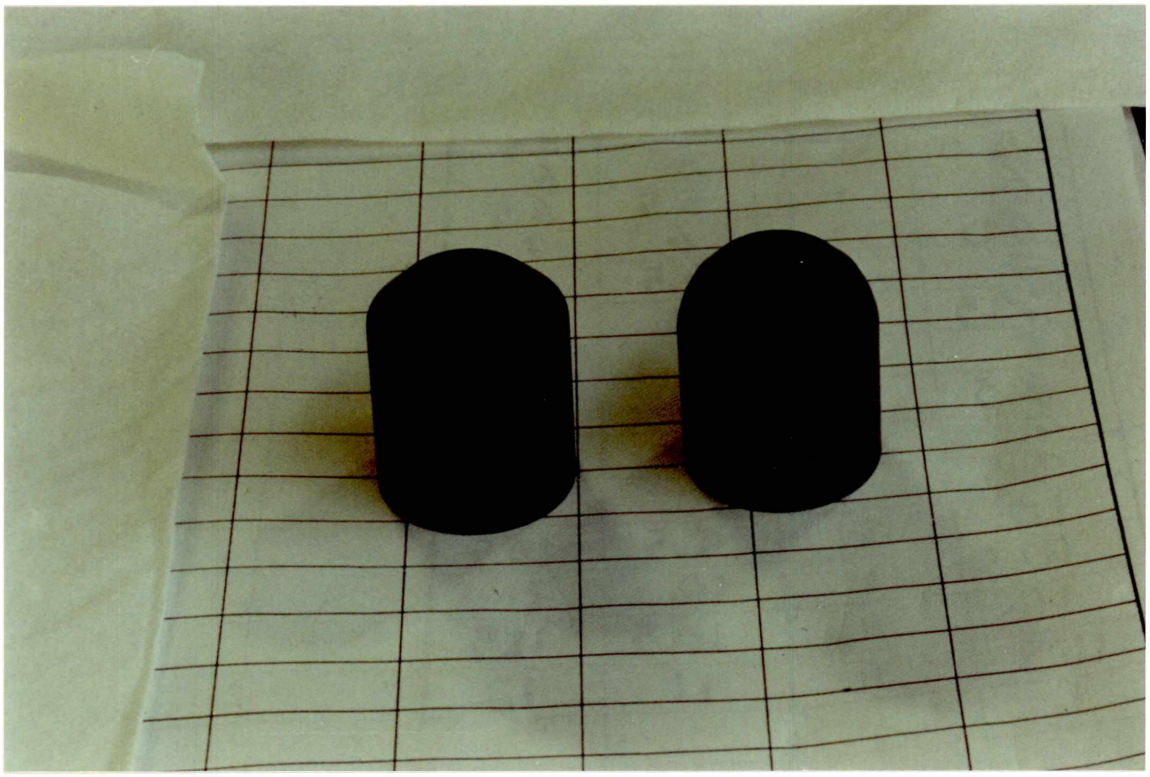


Figure 5.10 Photograph of old and new design of projectile.

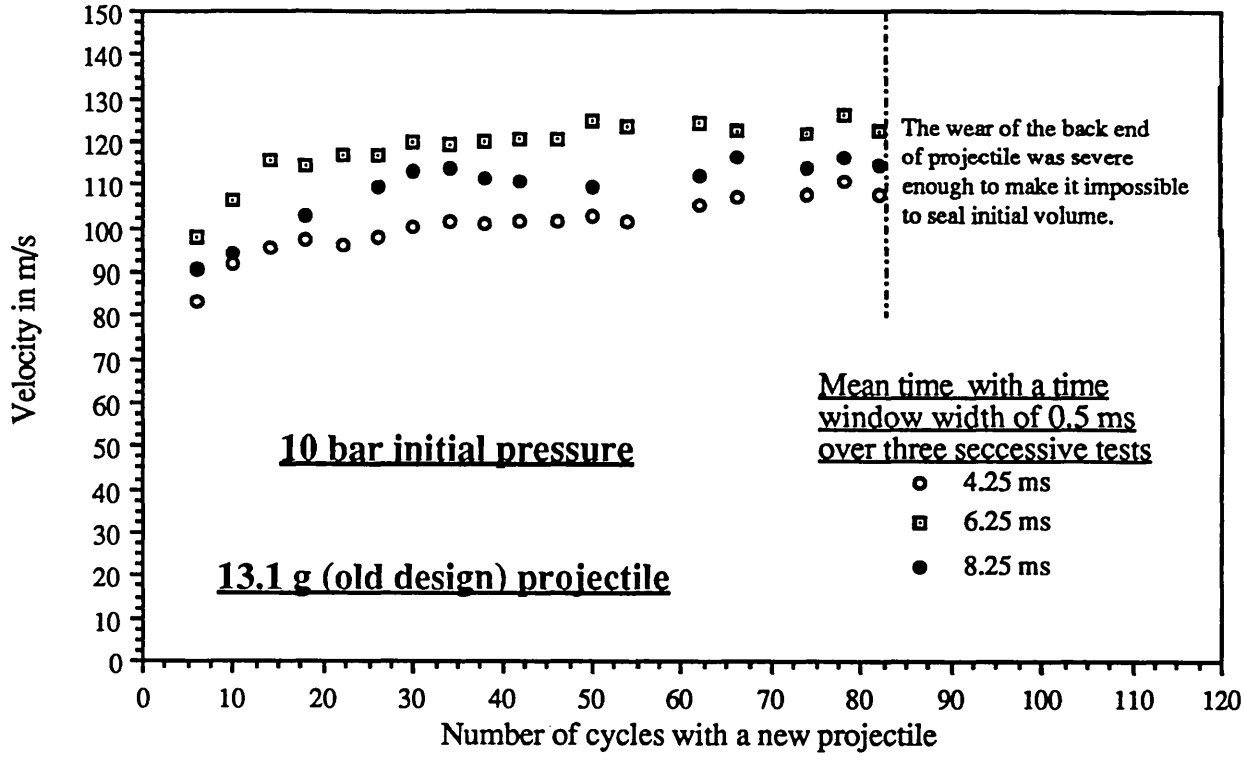


Figure 5.11 Cyclic variation of centreline single-phase velocity; 13.1 g projectile.

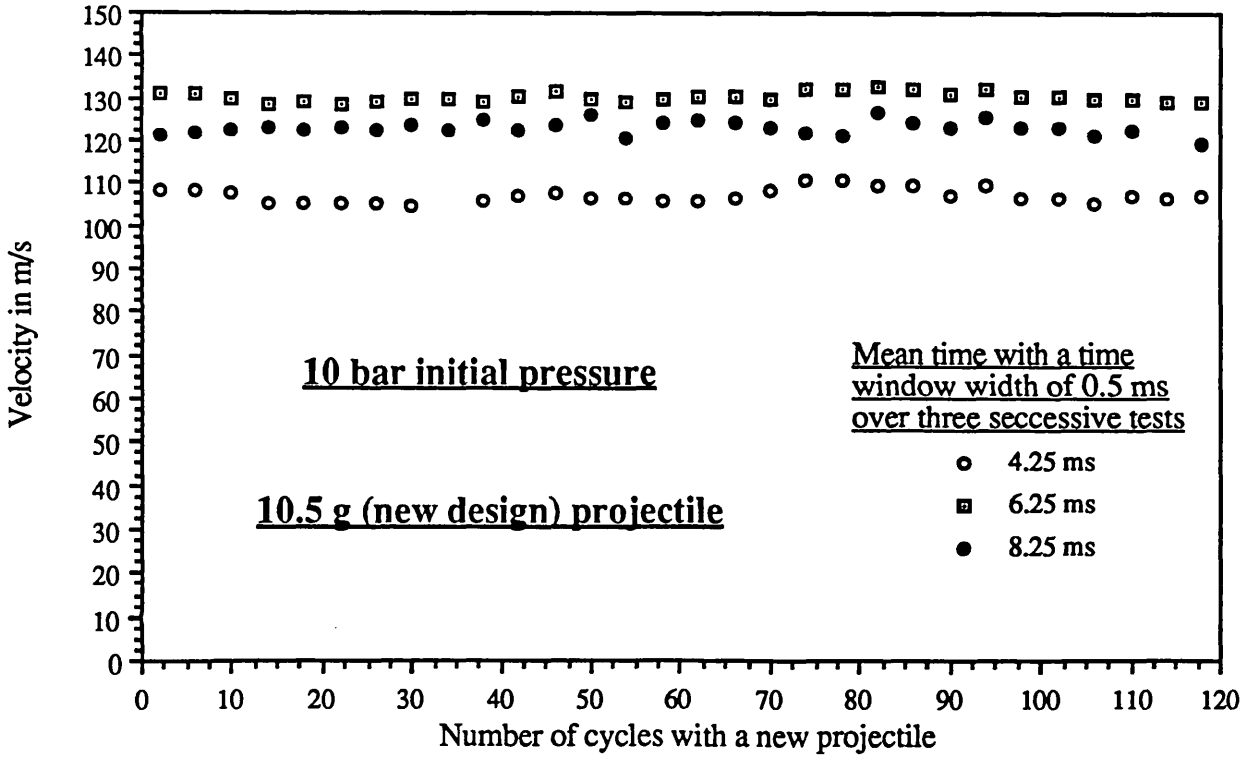


Figure 5.12 Cyclic variation of centreline single-phase velocity; 10.5 g projectile.

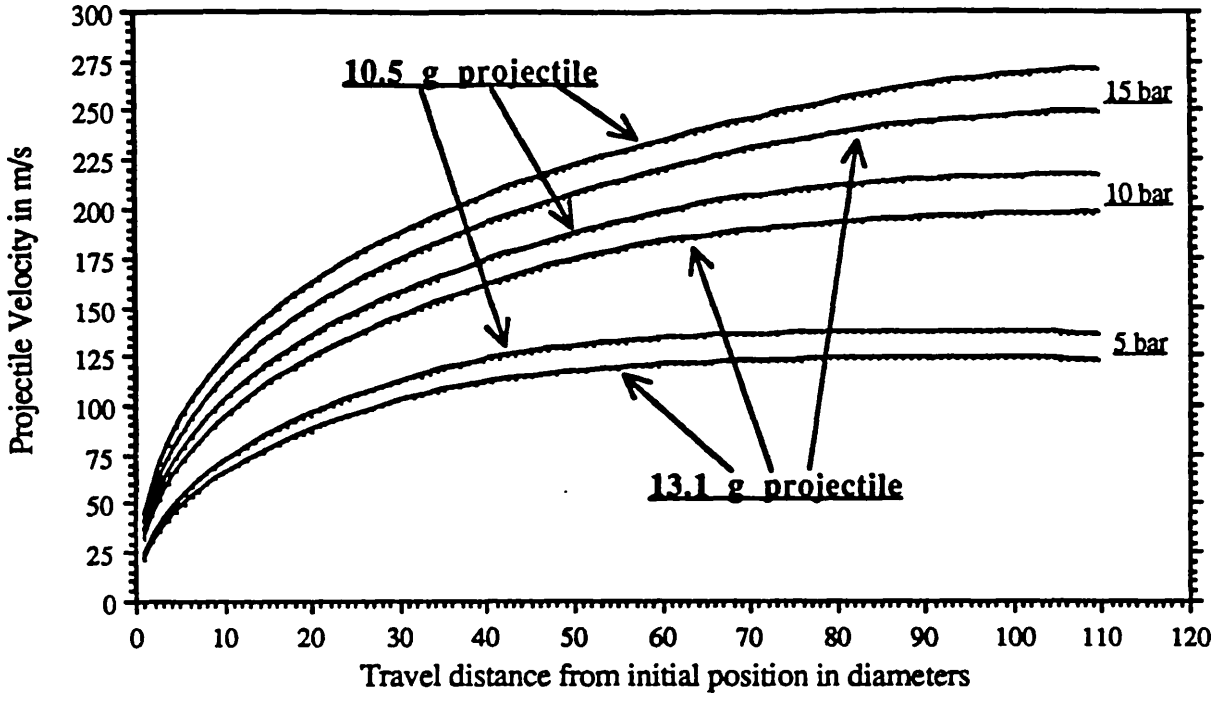


Figure 5.13 Calculated projectile velocity with travel distance for 10.5 & 13.1 g projectiles.

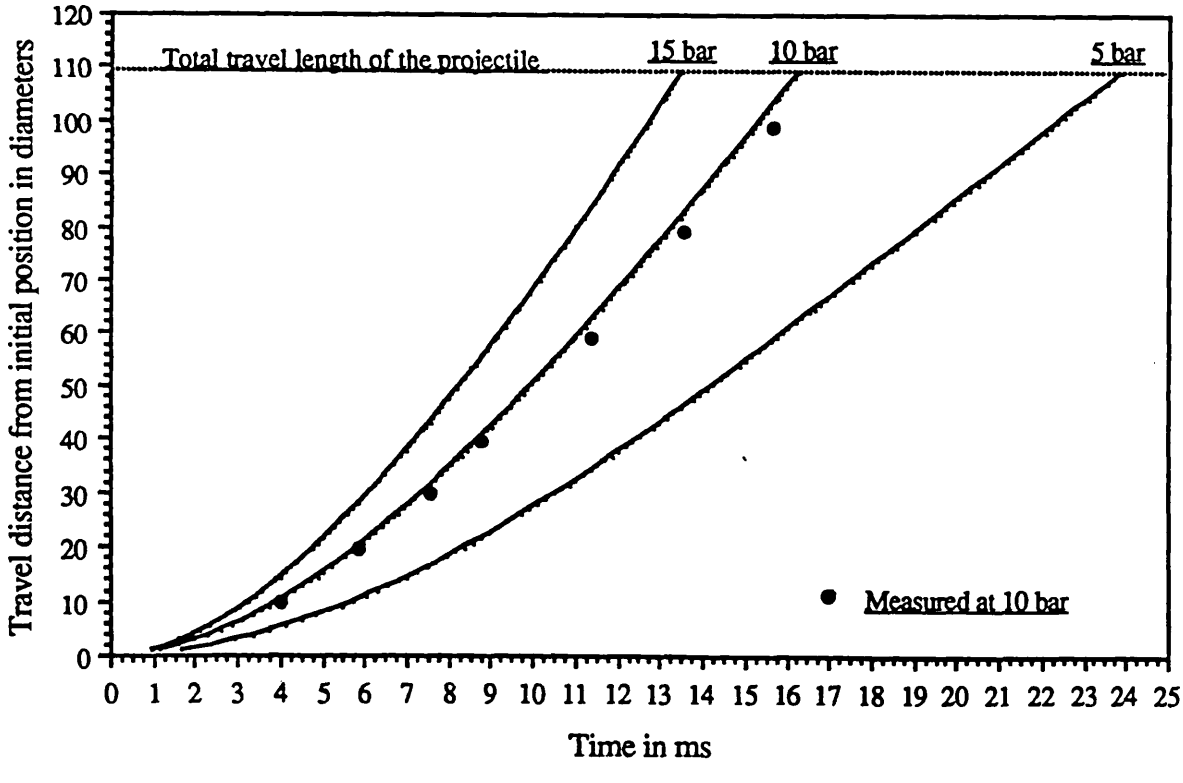


Figure 5.14 Calculated and measured projectile travel distance with time; 10.5 g projectile.

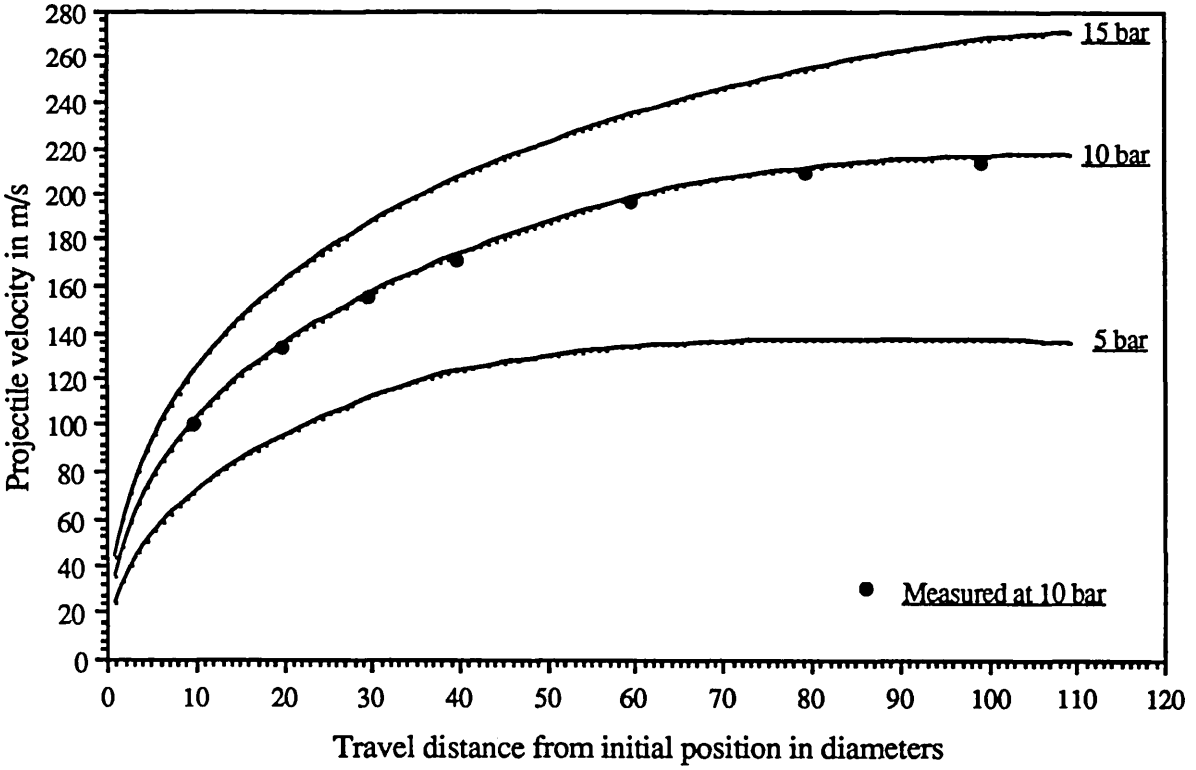


Figure 5.15 Calculated and measured projectile velocity with travel distance; 10.5 g projectile.

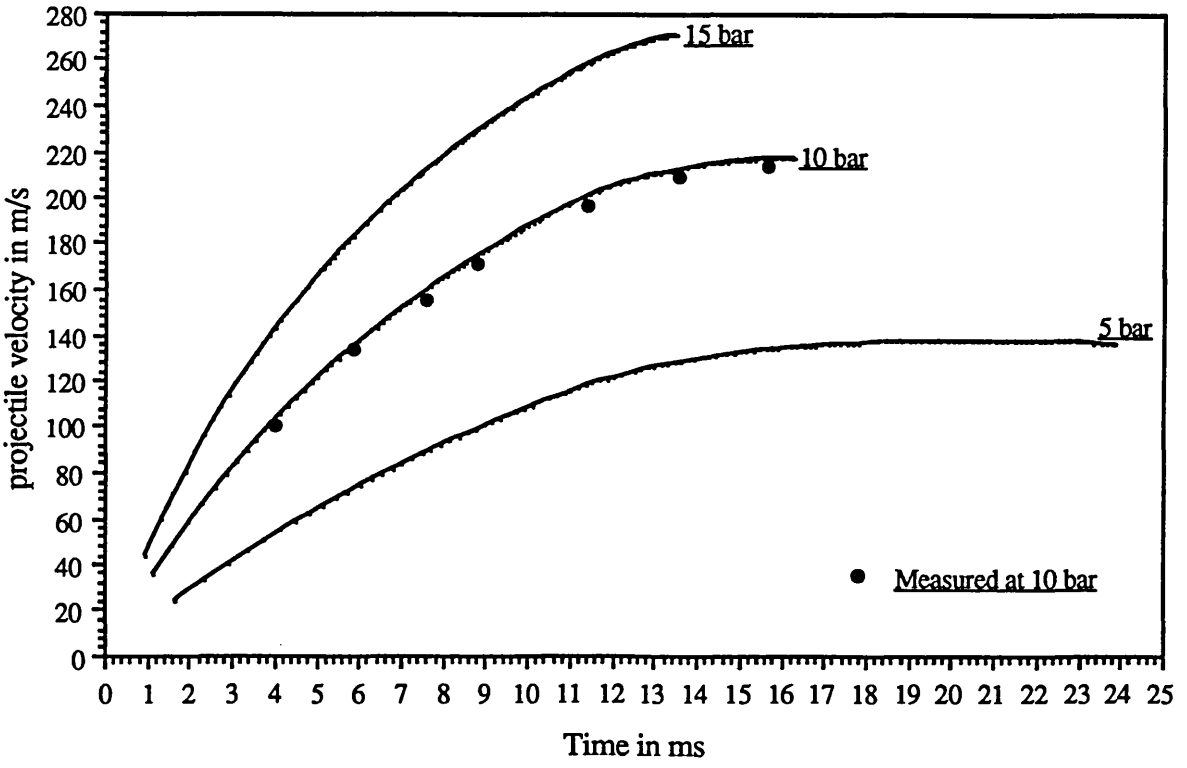


Figure 5.16 Calculated and measured projectile velocity with time; 10.5 g projectile.

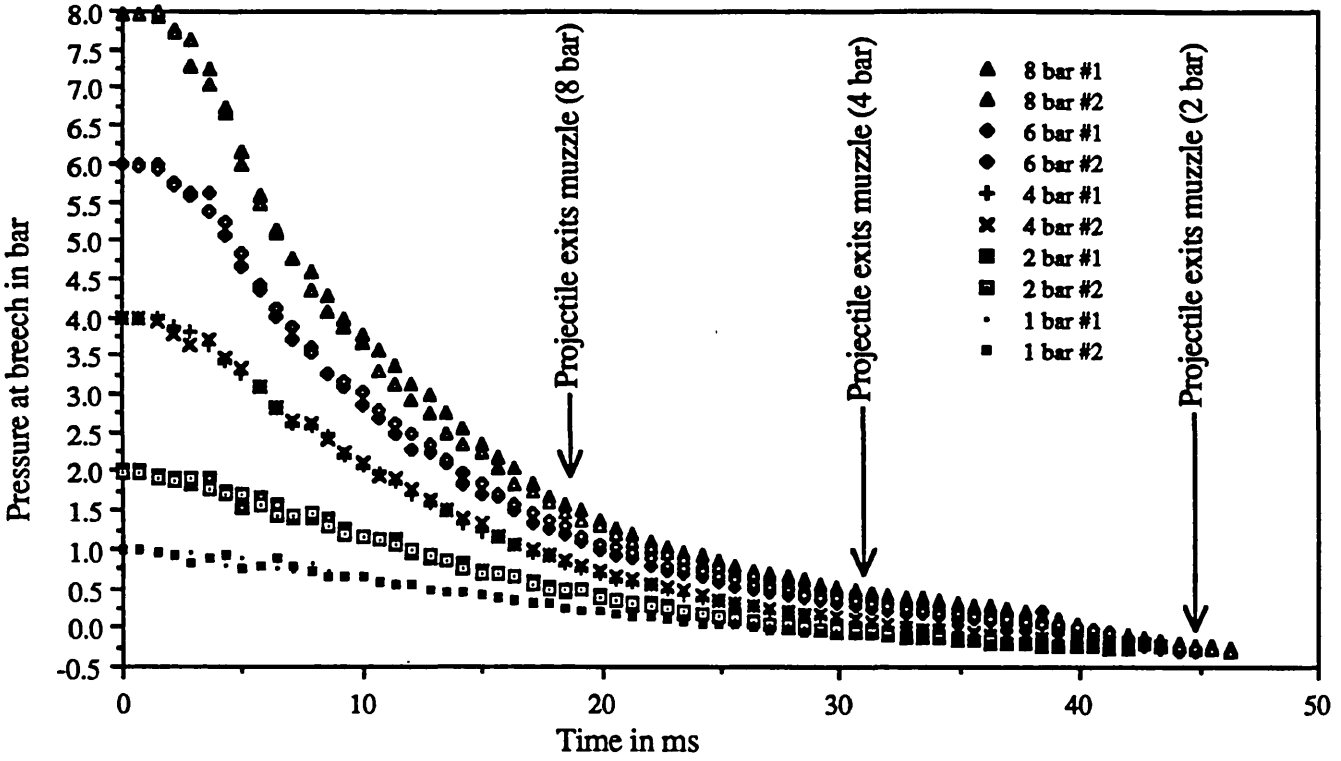


Figure 5.17 Measured breech pressure for under 8.0 bar initial pressure.

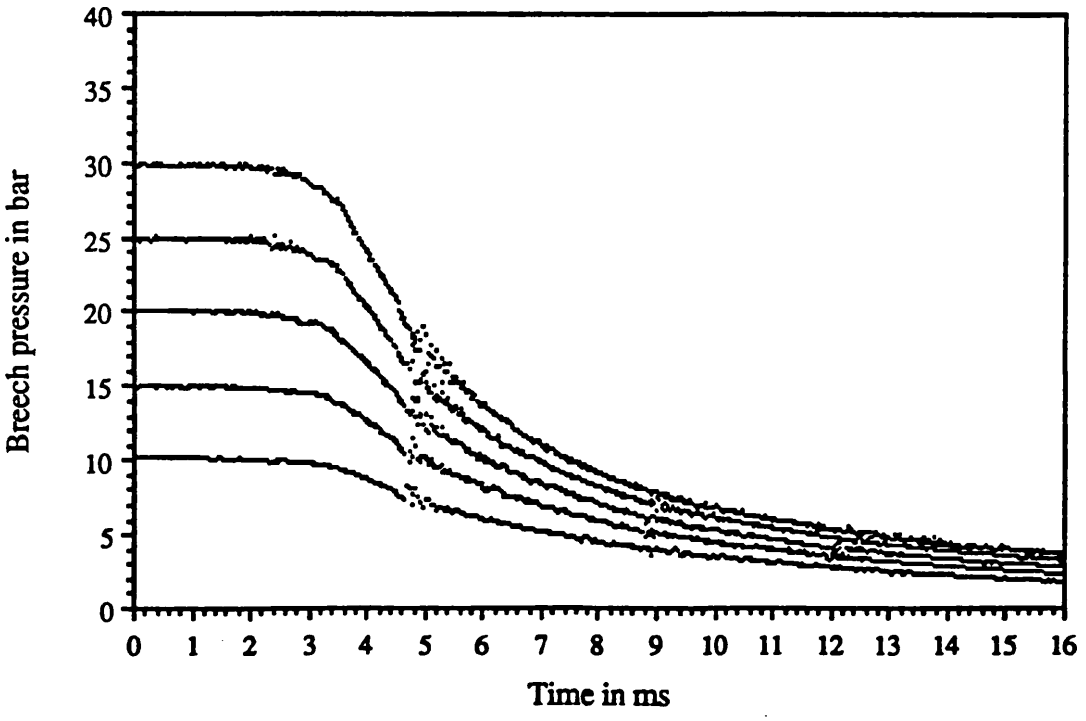


Figure 5.18 Measured breech pressure for 10, 15, 20, 25 &.30 bar initial pressure.

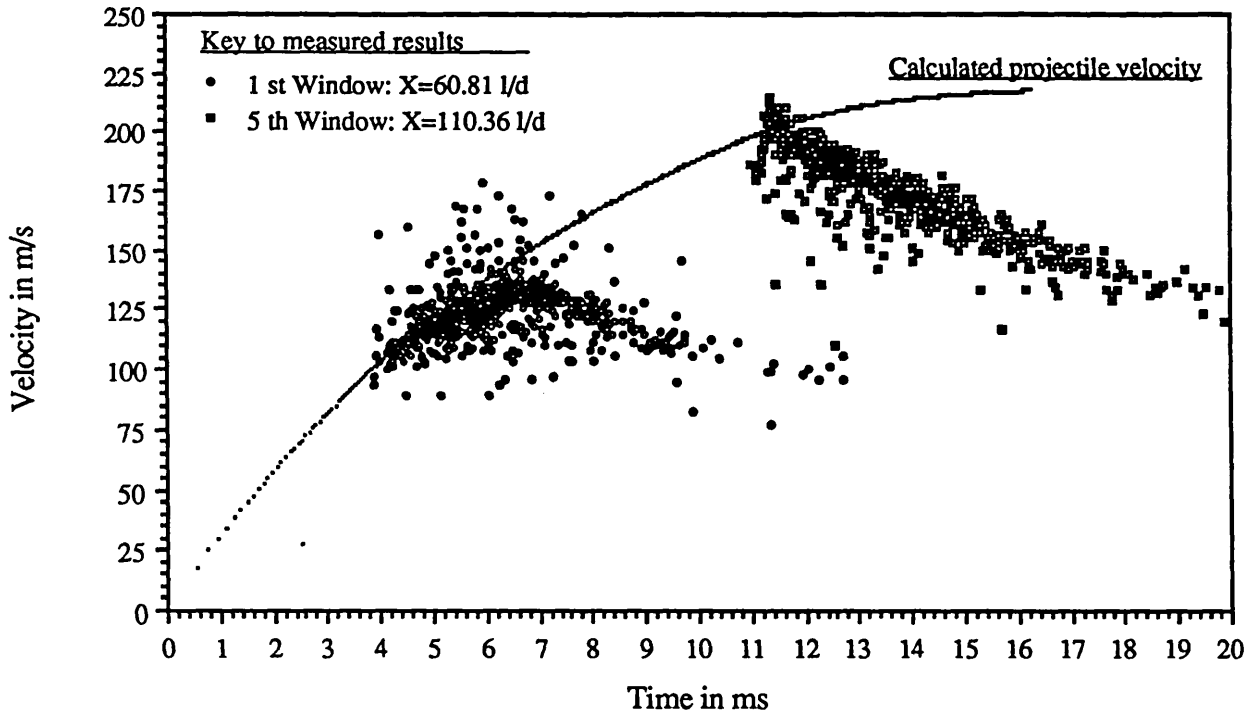


Figure 5.19 Typical velocity traces at windows #1 & #5 for an initial pressure of 10 bar.

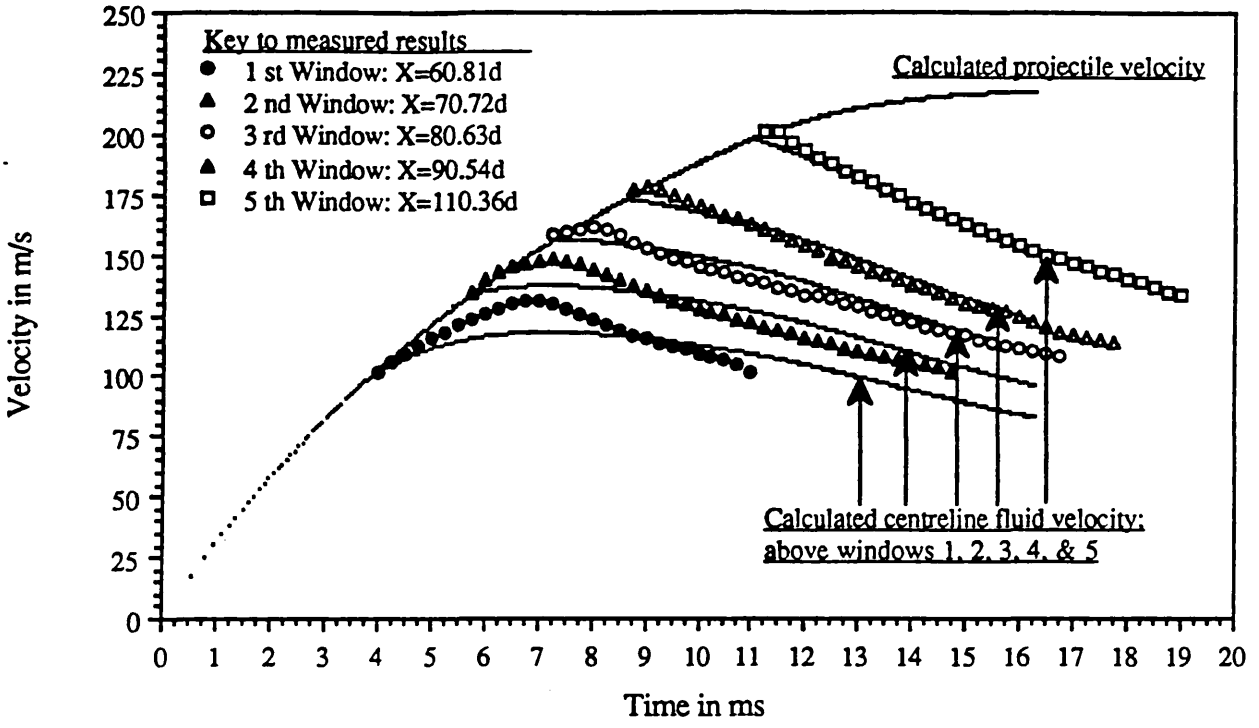


Figure 5.20 Measured and calculated centreline mean velocity for an initial pressure of 10 bar.

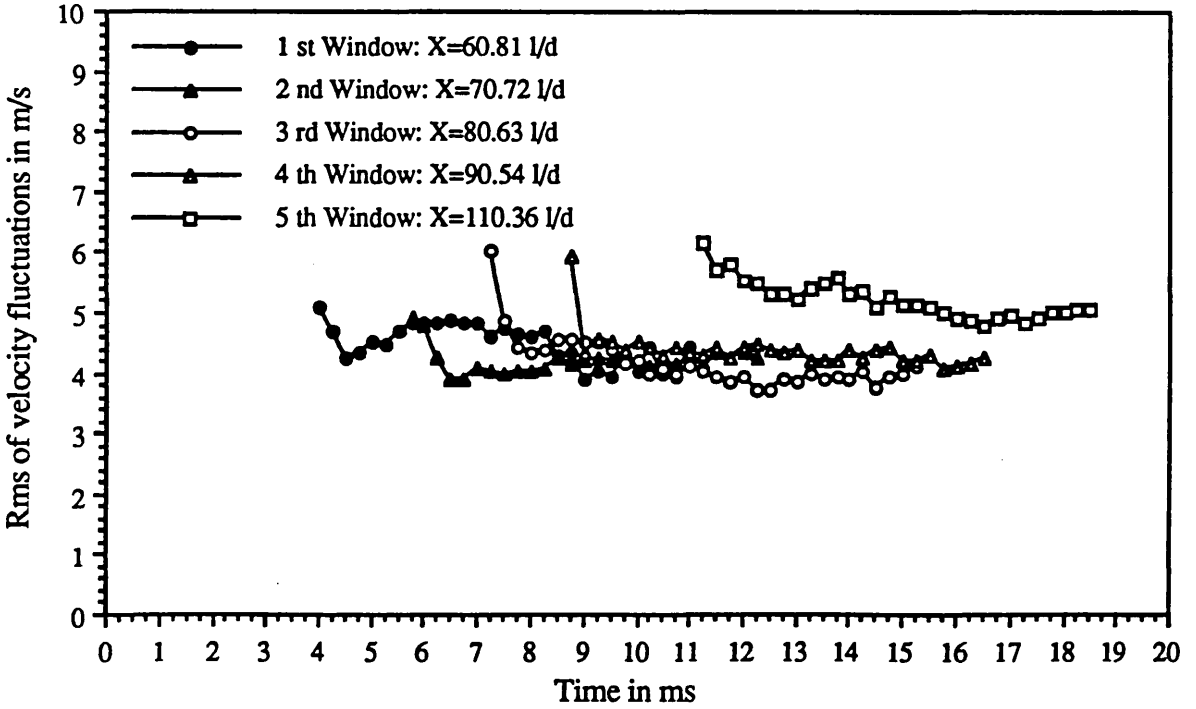


Figure 5.21 Measured and calculated centreline rms velocity fluctuations for an initial pressure of 10 bar.

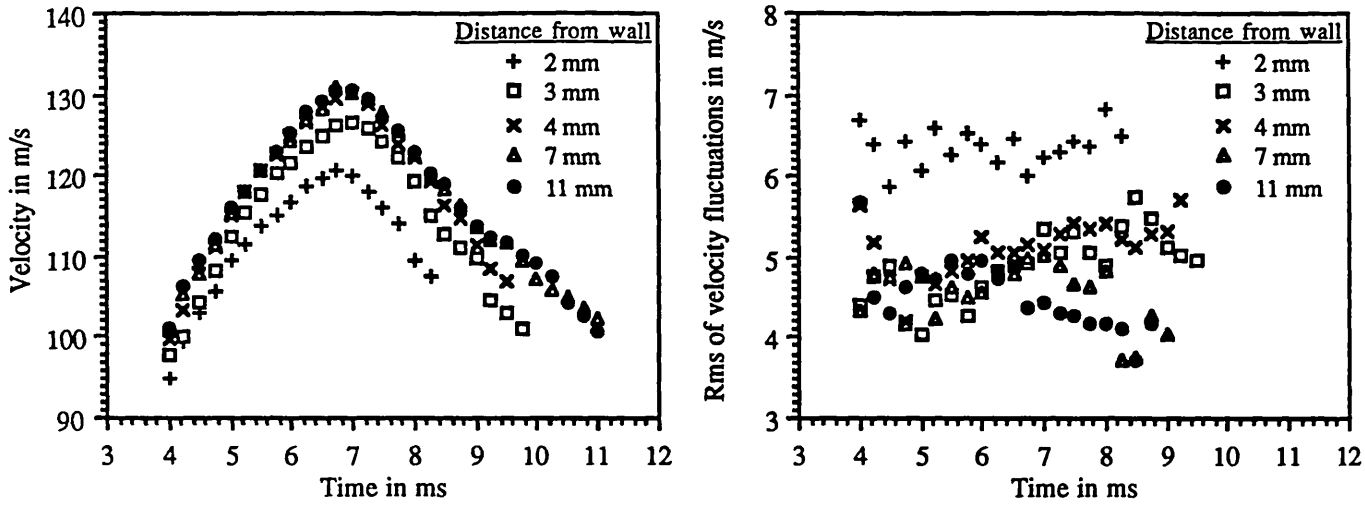


Figure 5.22 (a) Measured mean and rms velocity versus time; Window #1, X=60.81 d.

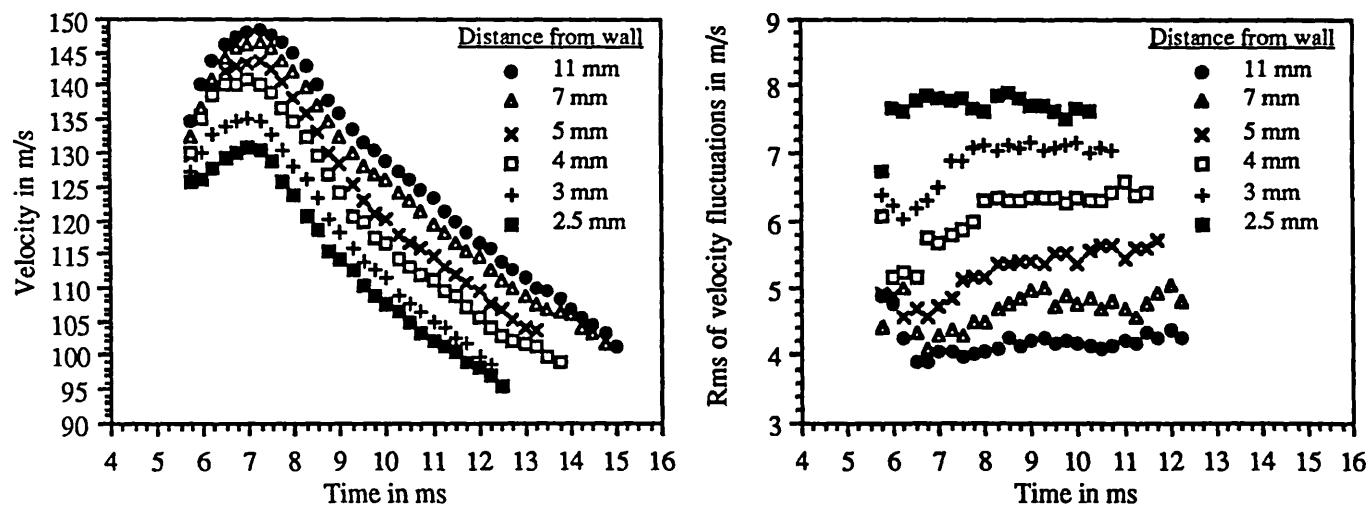


Figure 5.22 (b) Measured mean and rms velocity versus time; Window #2, X=70.72 d.

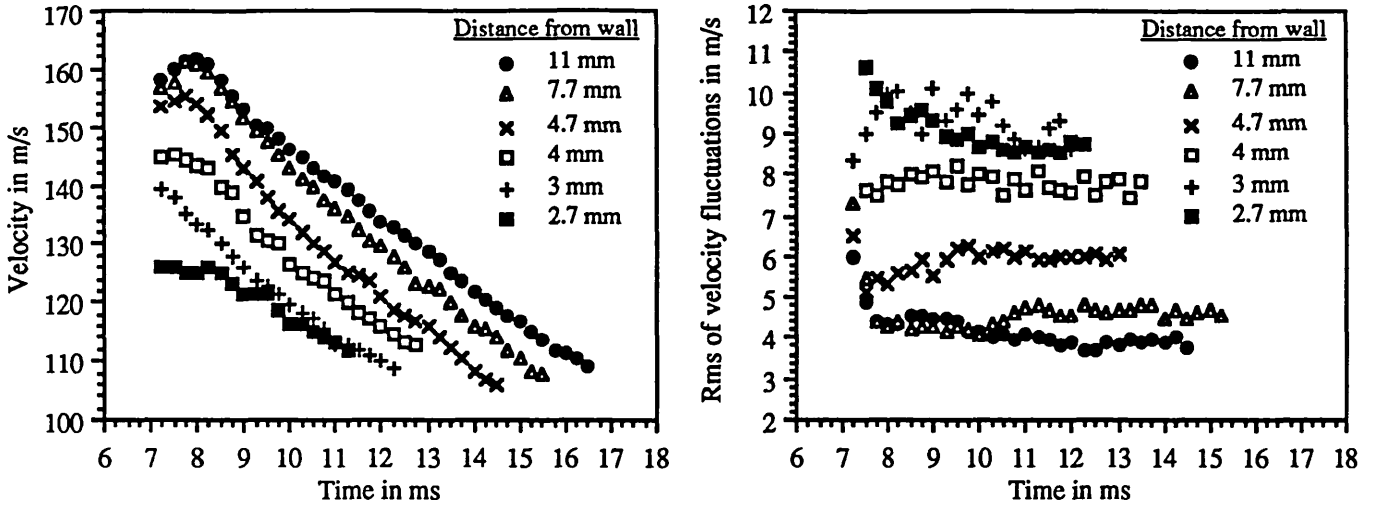


Figure 5.22 (c) Measured mean and rms velocity versus time; Window #3, X=80.63 d.

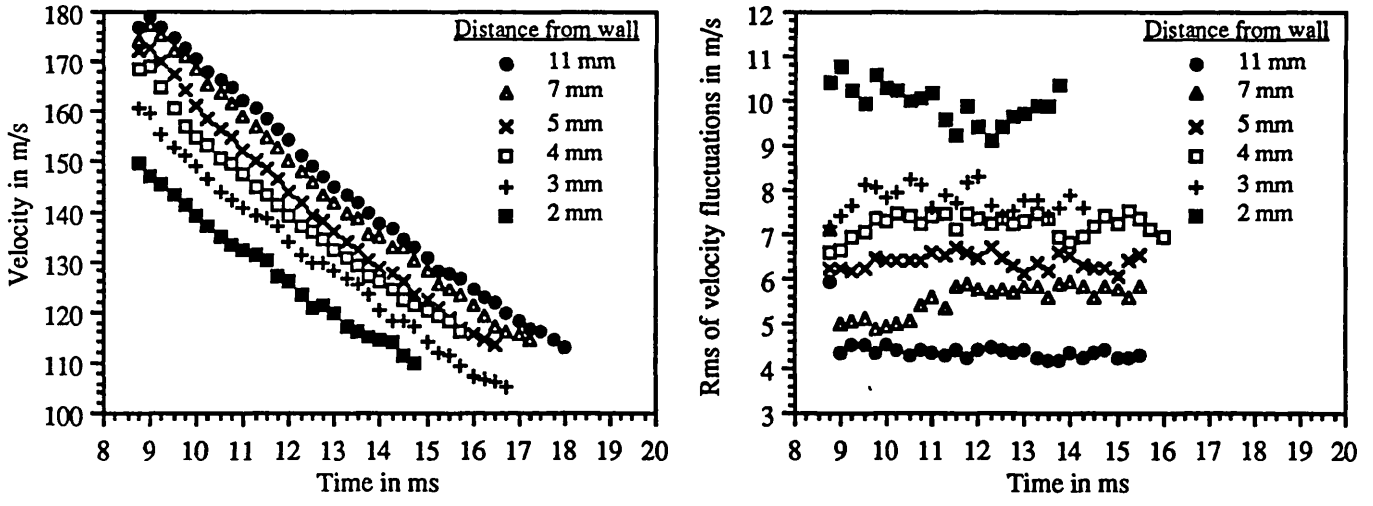


Figure 5.22 (d) Measured mean and rms velocity versus time; Window #4, X=90.54 d.

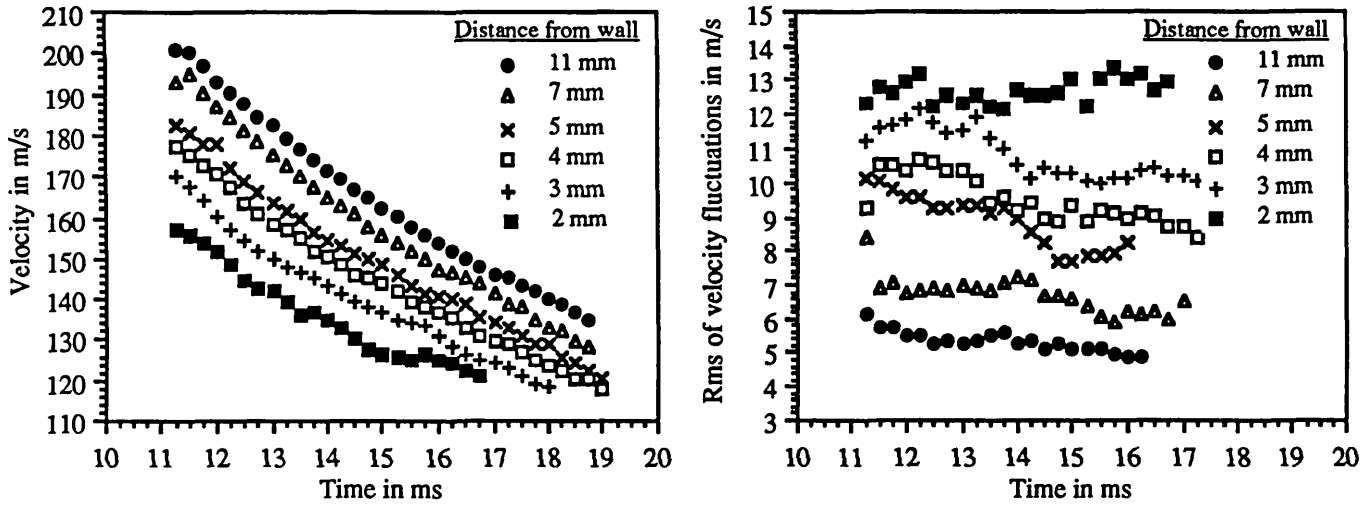


Figure 5.22 (e) Measured mean and rms velocity versus time; Window #5, X=110.36 d.

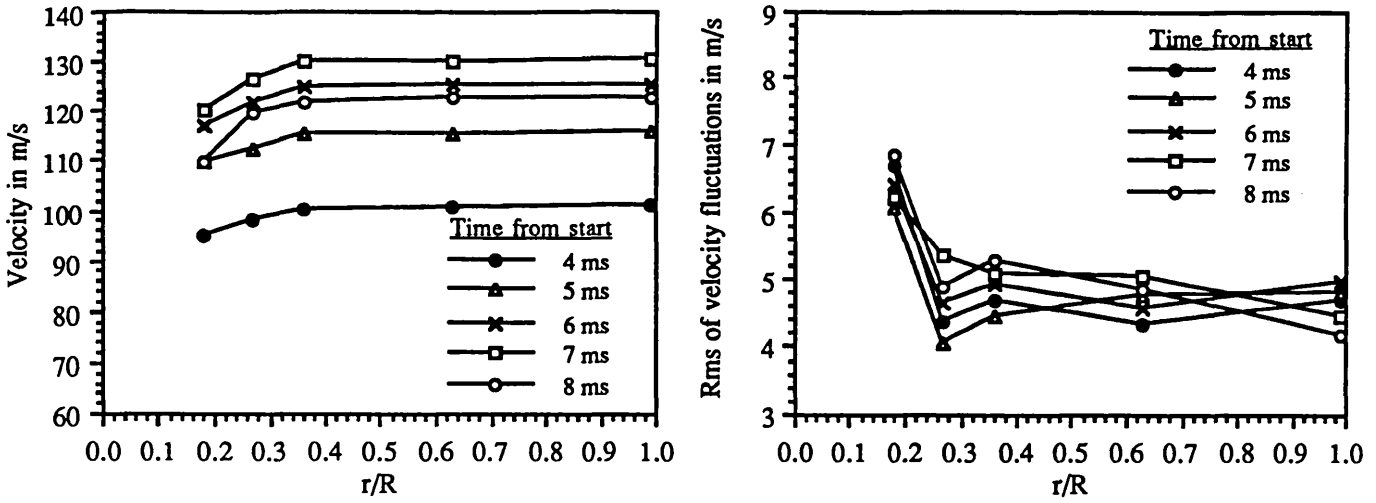


Figure 5.23 (a) Radial profiles of mean and rms velocity; Window #1, X=60.81 d.

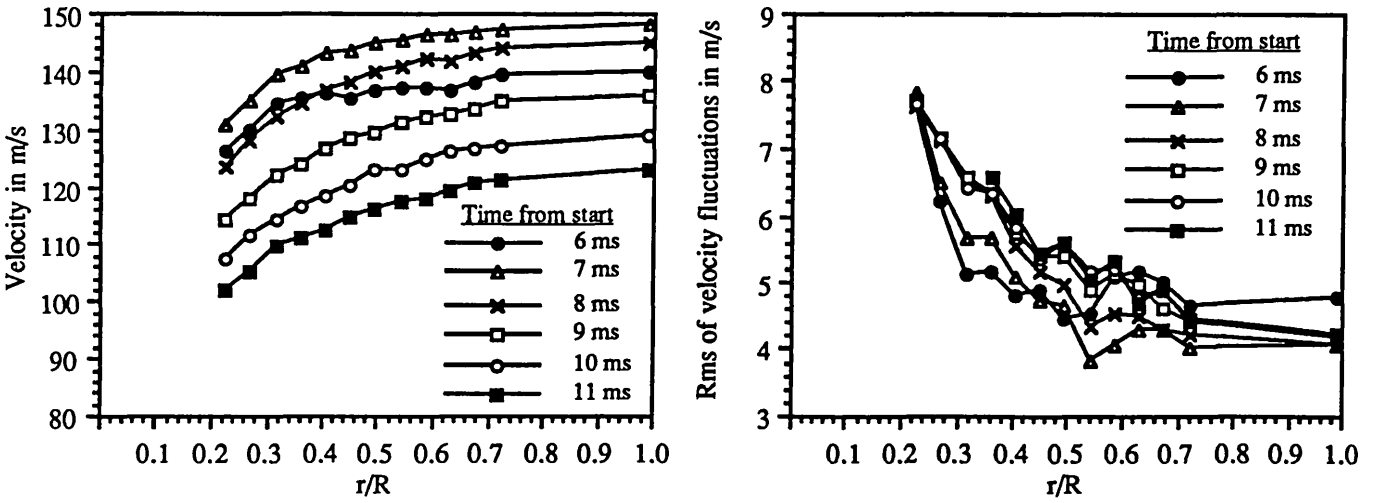


Figure 5.23 (b) Radial profiles of mean and rms velocity; Window #2, X=70.72 d.

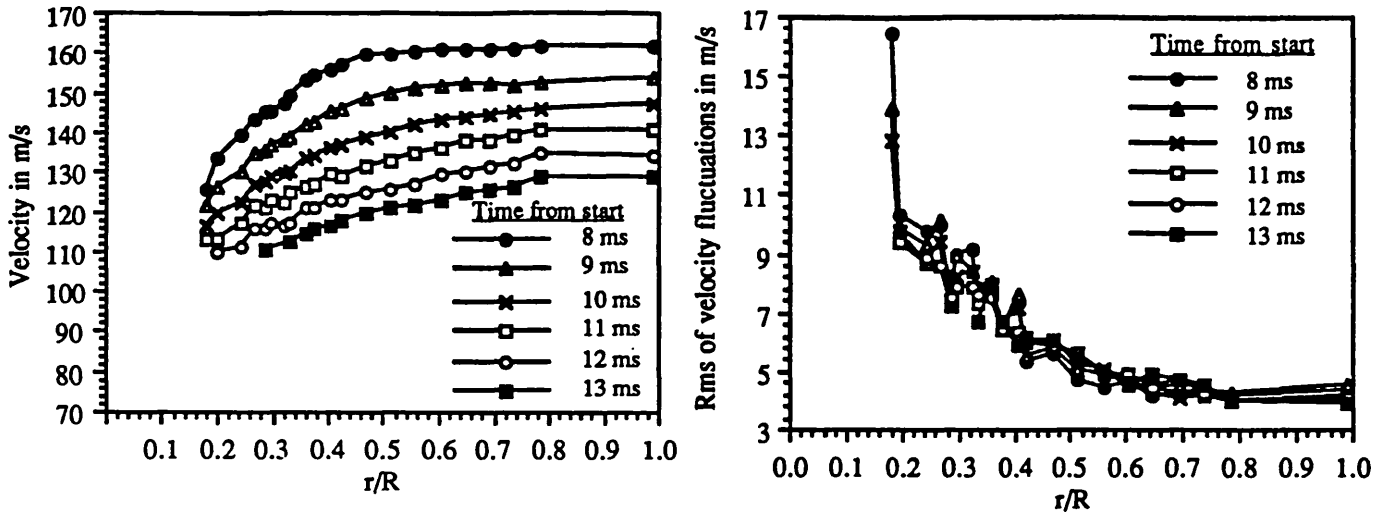


Figure 5.23 (c) Radial profiles of mean and rms velocity; Window #3, X=80.63 d.

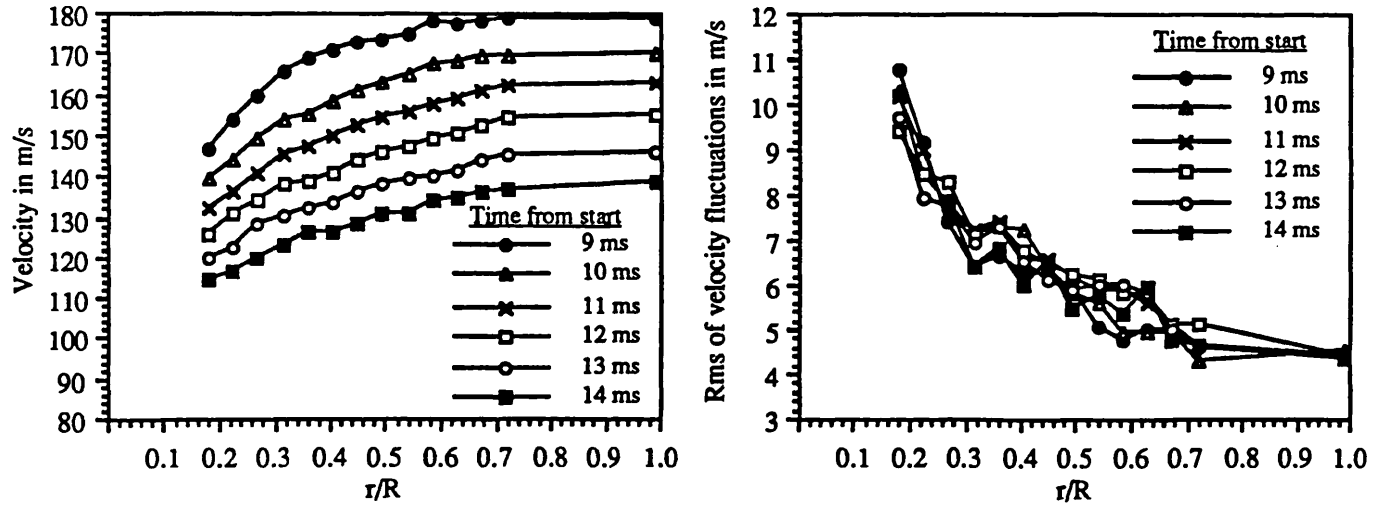


Figure 5.23 (d) Radial profiles of mean and rms velocity; Window #4, X=90.54 d.

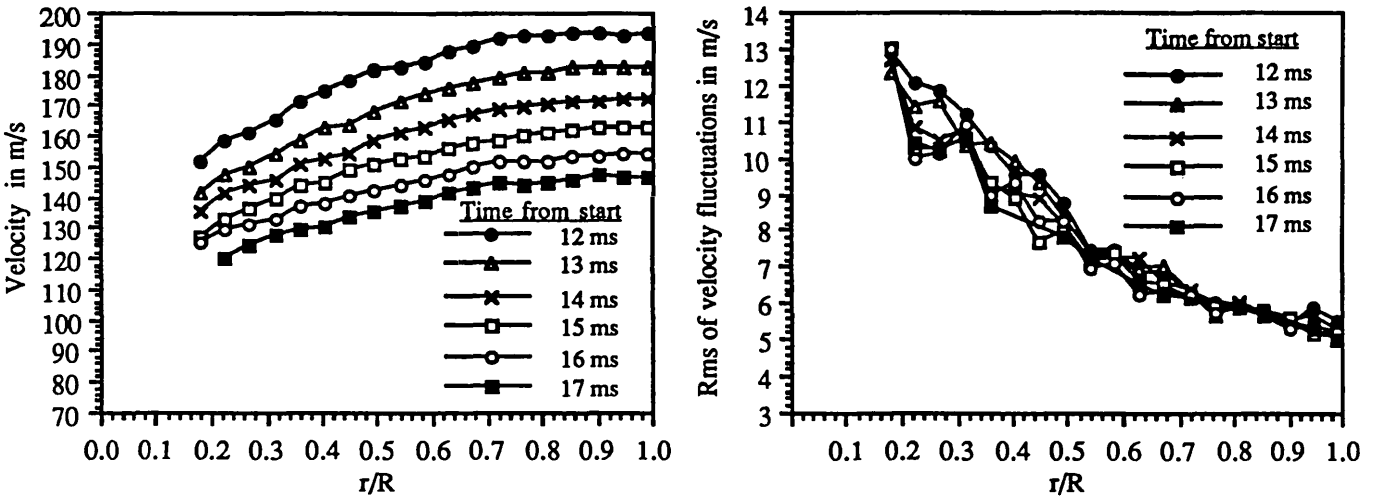


Figure 5.23 (e) Radial profiles of mean and rms velocity; Window #5, X=110.36 d.

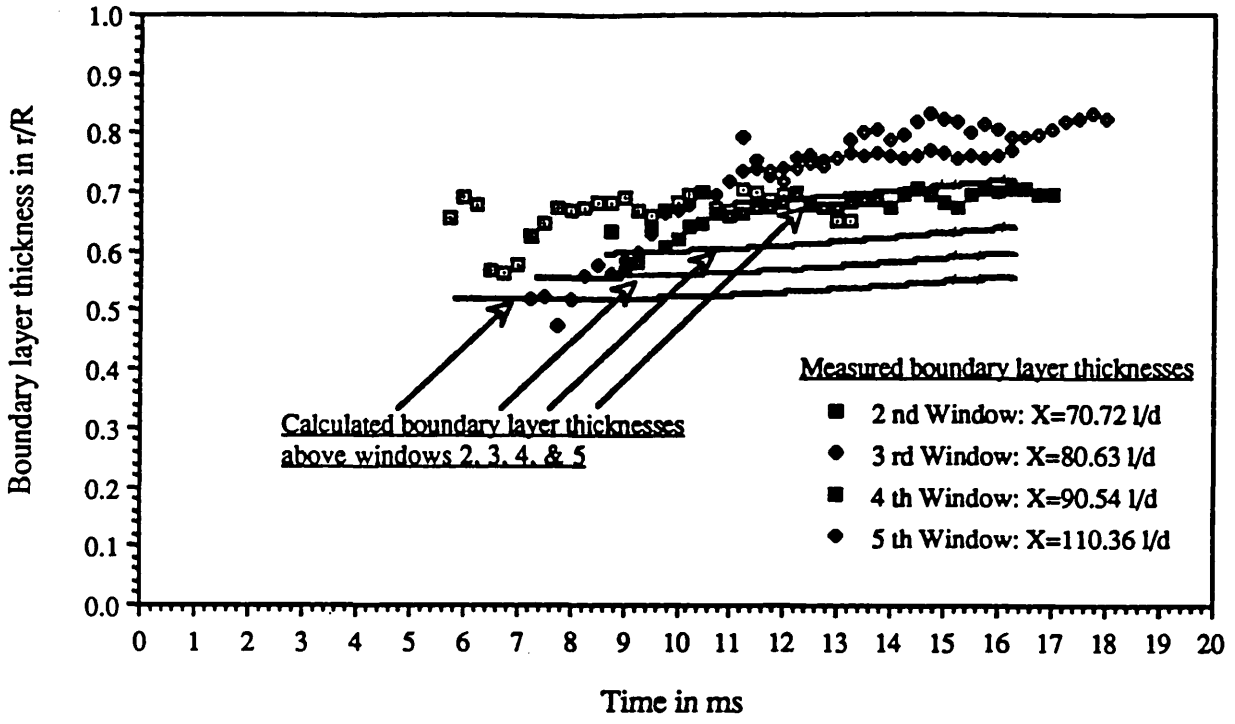


Figure 5.24 Measured and calculated boundary layer thickness variation versus time.

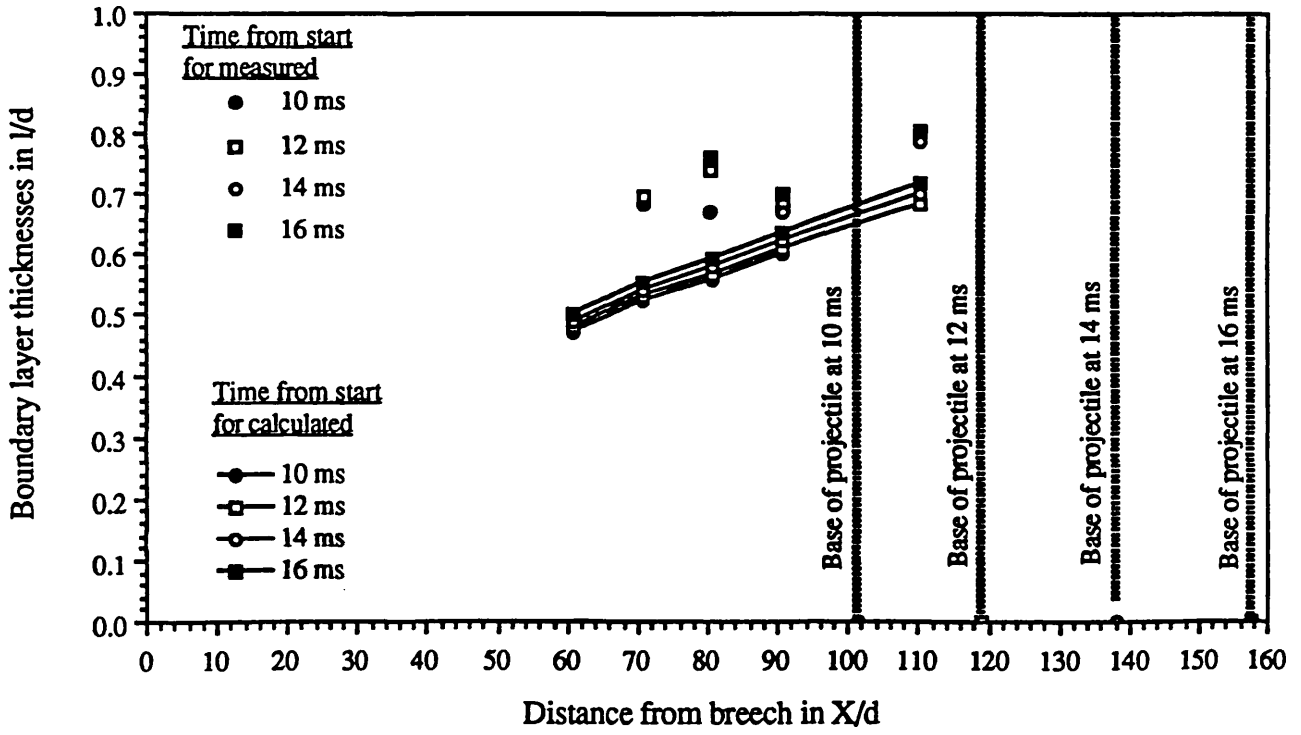


Figure 5.25 Axial variation of calculated and measured boundary layer thickness.

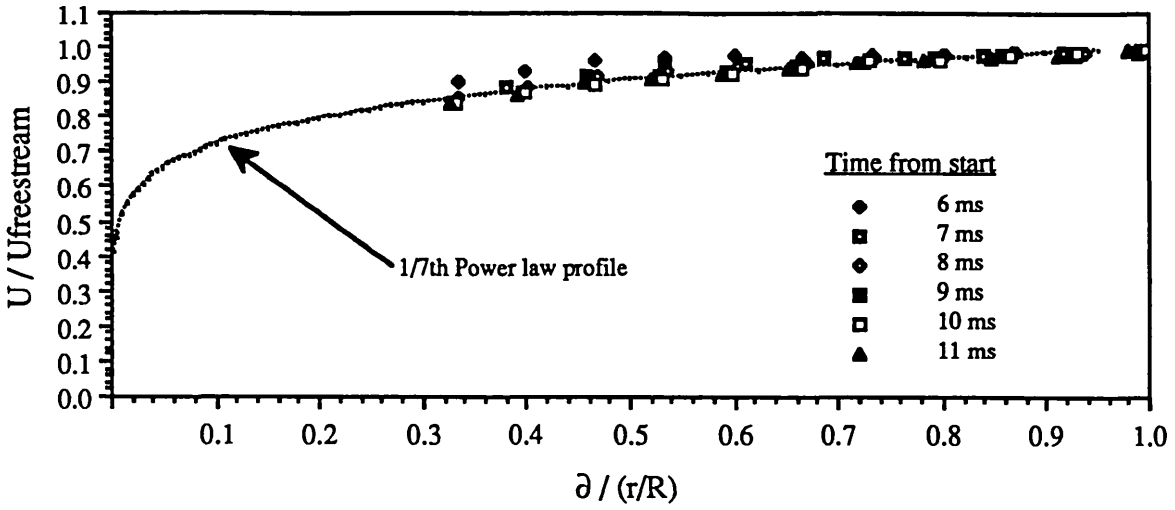


Figure 5.26(a) Boundary layer profiles; Window #2, X=70.72 d.

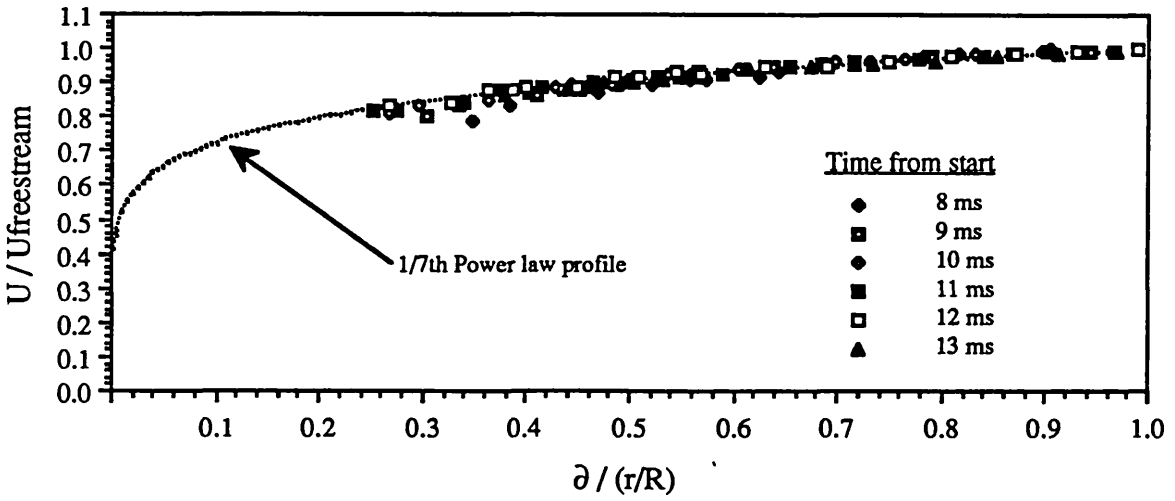


Figure 5.26(b) Boundary layer profiles; Window #3, X=80.63 d.

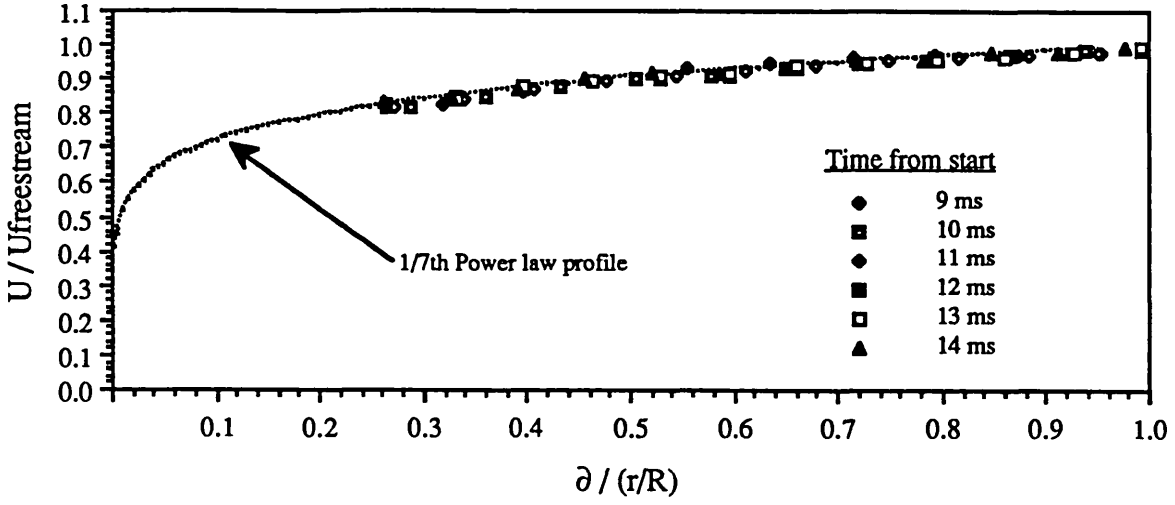


Figure 5.26(c) Boundary layer profiles; Window #4, X=90.54 d.

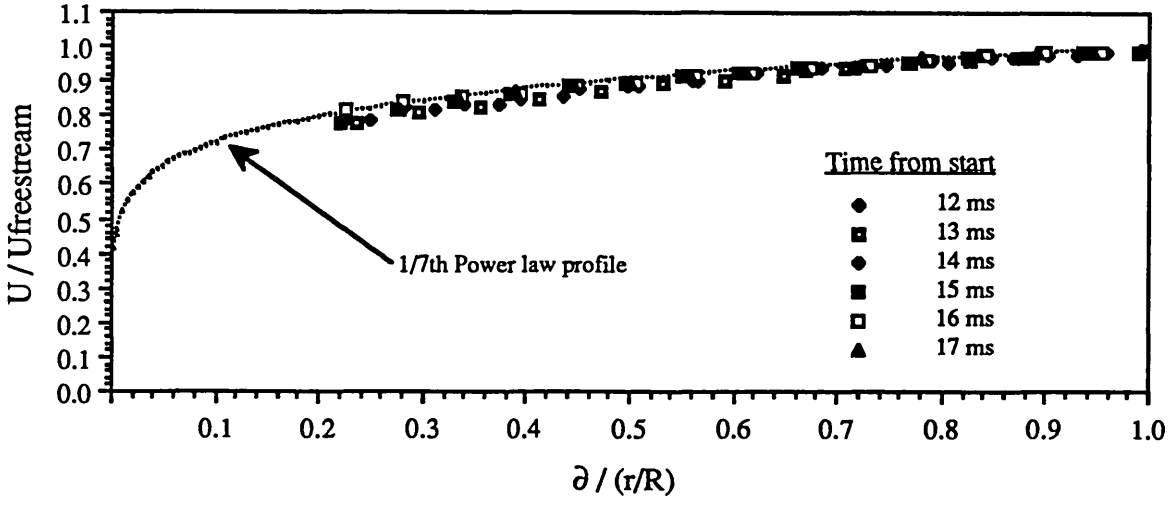


Figure 5.26(d) Boundary layer profiles; Window #5, X=110.36 d.

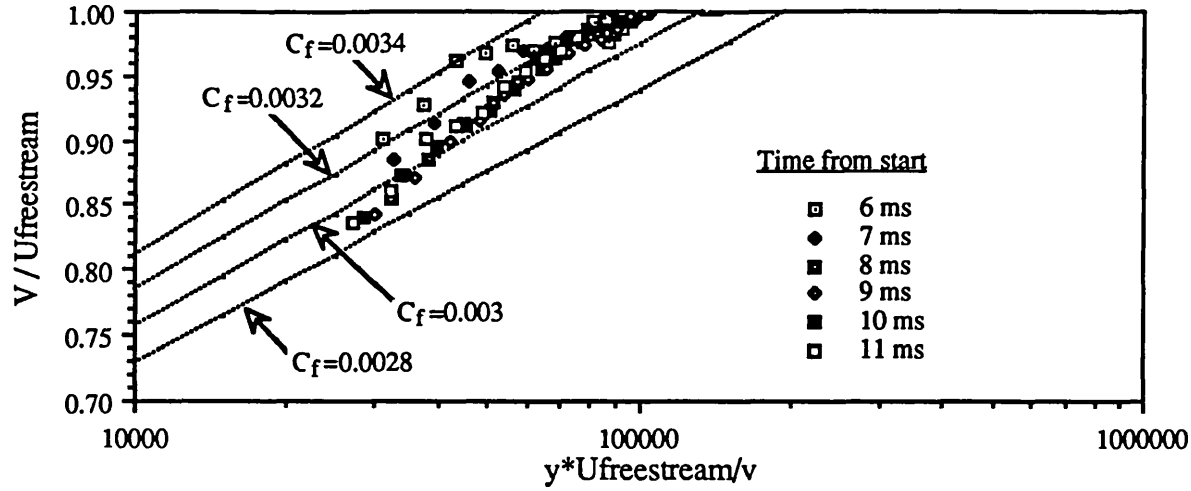


Figure 5.27(a) Clauser chart for the deduction of C_f; Window #2, X=70.72 d.

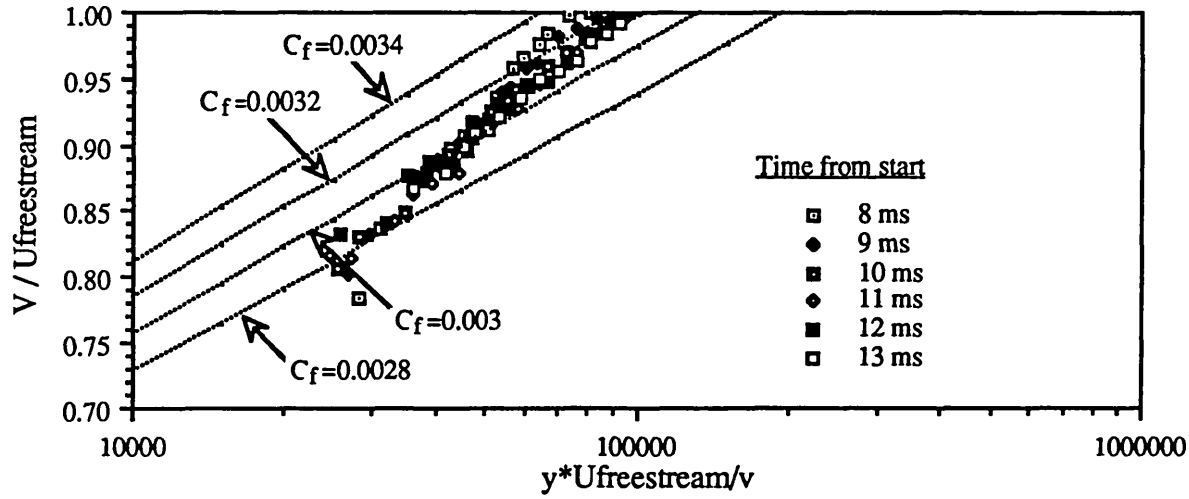


Figure 5.27(b) Clauser chart for the deduction of C_f; Window #3, X=80.63 d.

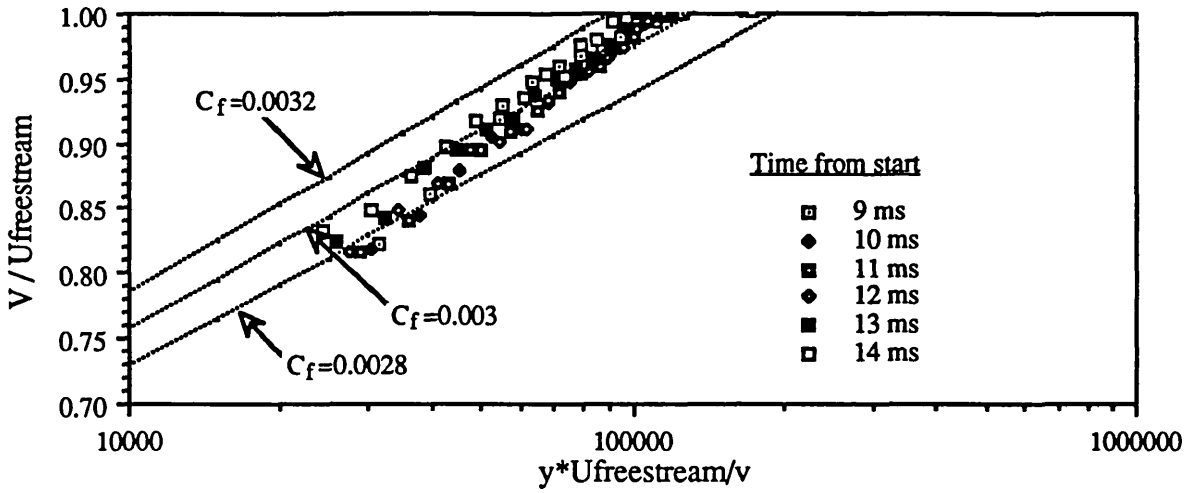


Figure 5.27(c) Clauser chart for the deduction of C_f; Window #4, X=90.54 d.

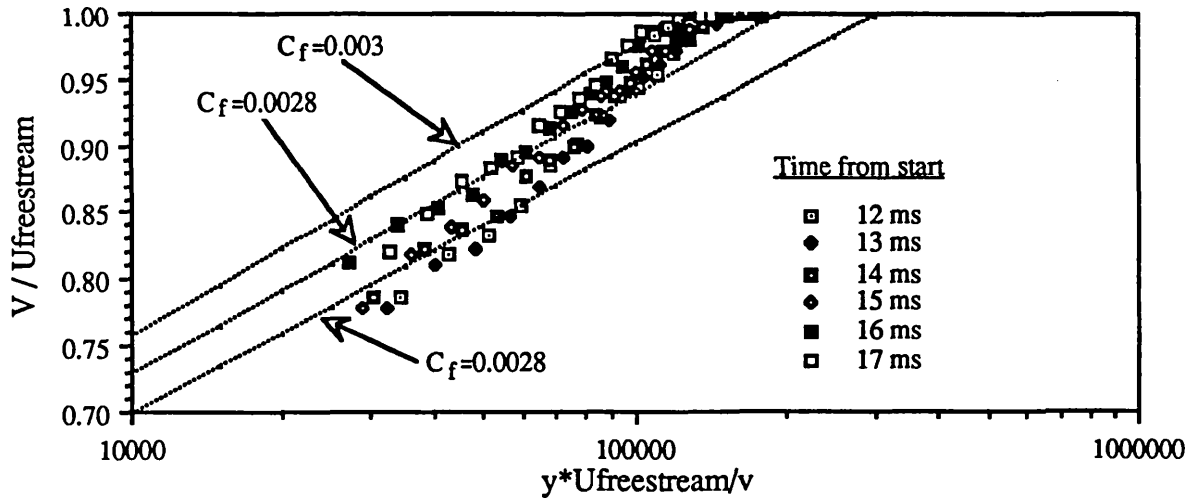


Figure 5.27(d) Clauser chart for the deduction of C_f; Window #5, X=110.36 d.

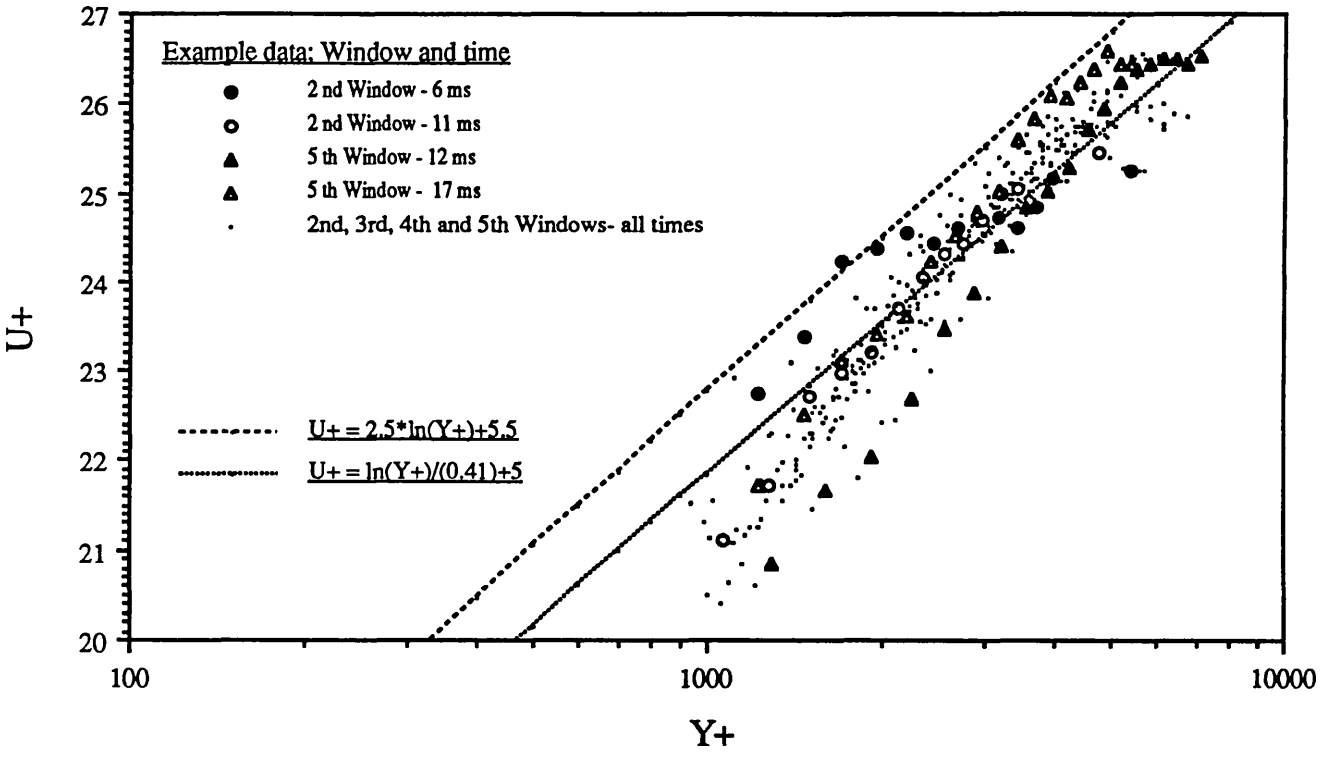


Figure 5.28 Velocity distribution displayed in standard Wall coordinates Y^+ and U^+.

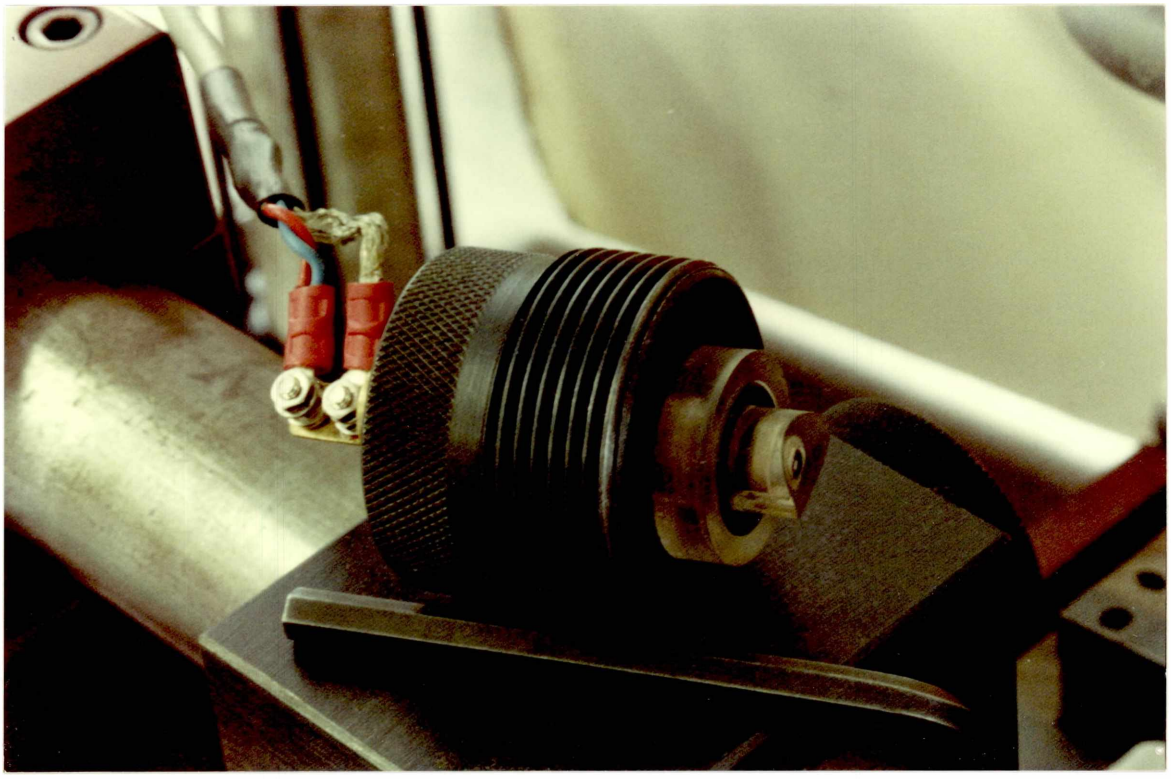


Figure 5.29 Photograph of high-speed thin-film sensor and mounting window.

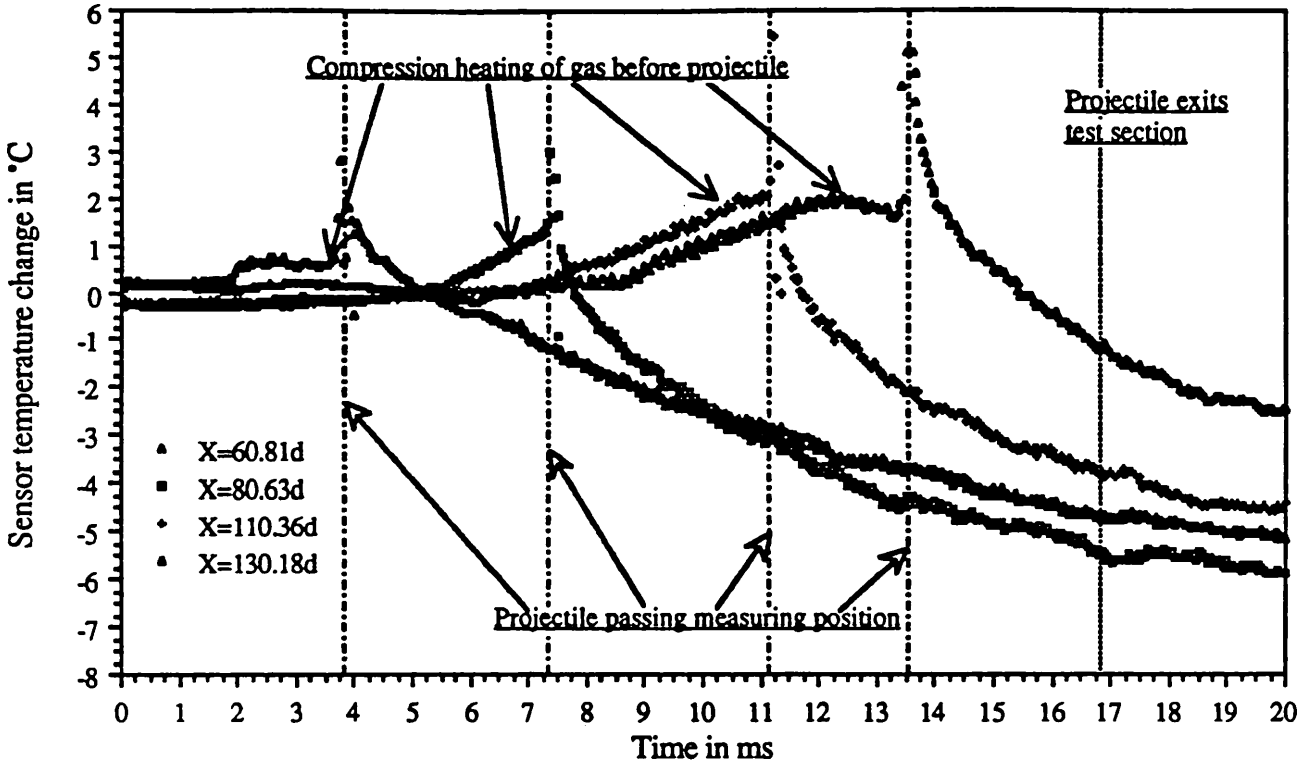


Figure 5.30 Sensor temperature record at windows #1, #3, #5 & #6 for an initial pressure of 10 bar.

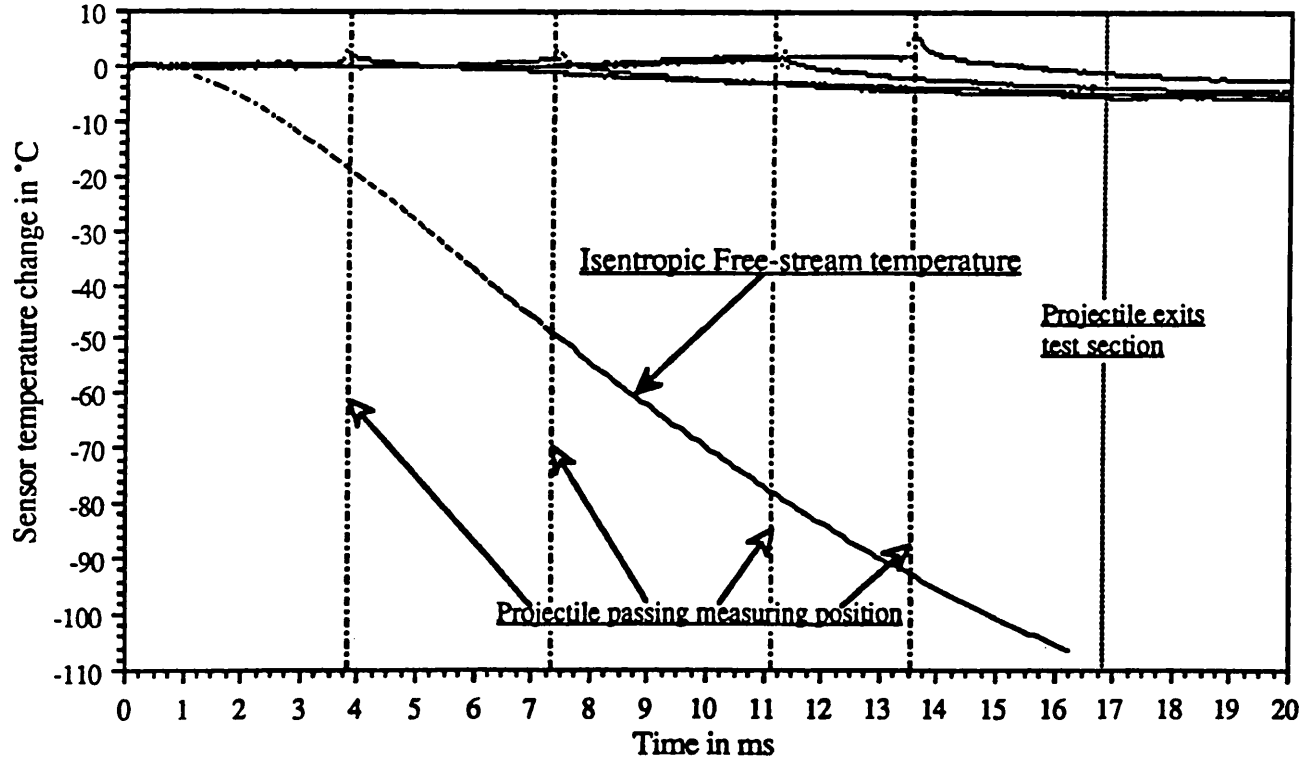


Figure 5.31 Sensor temperature records relative to free-stream temperature.

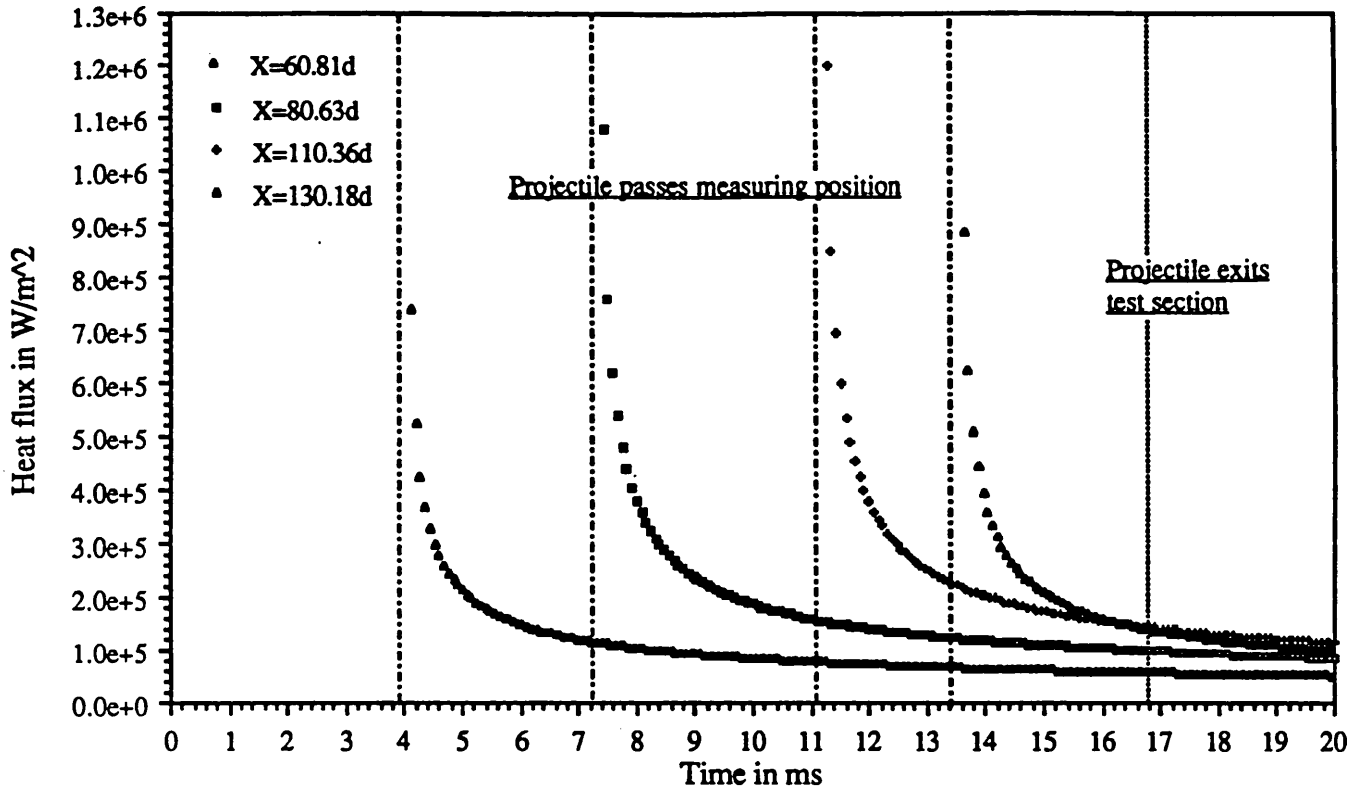


Figure 5.32 Wall heat flux at windows #1, #3, #5 & #6 for an initial pressure of 10 bar.

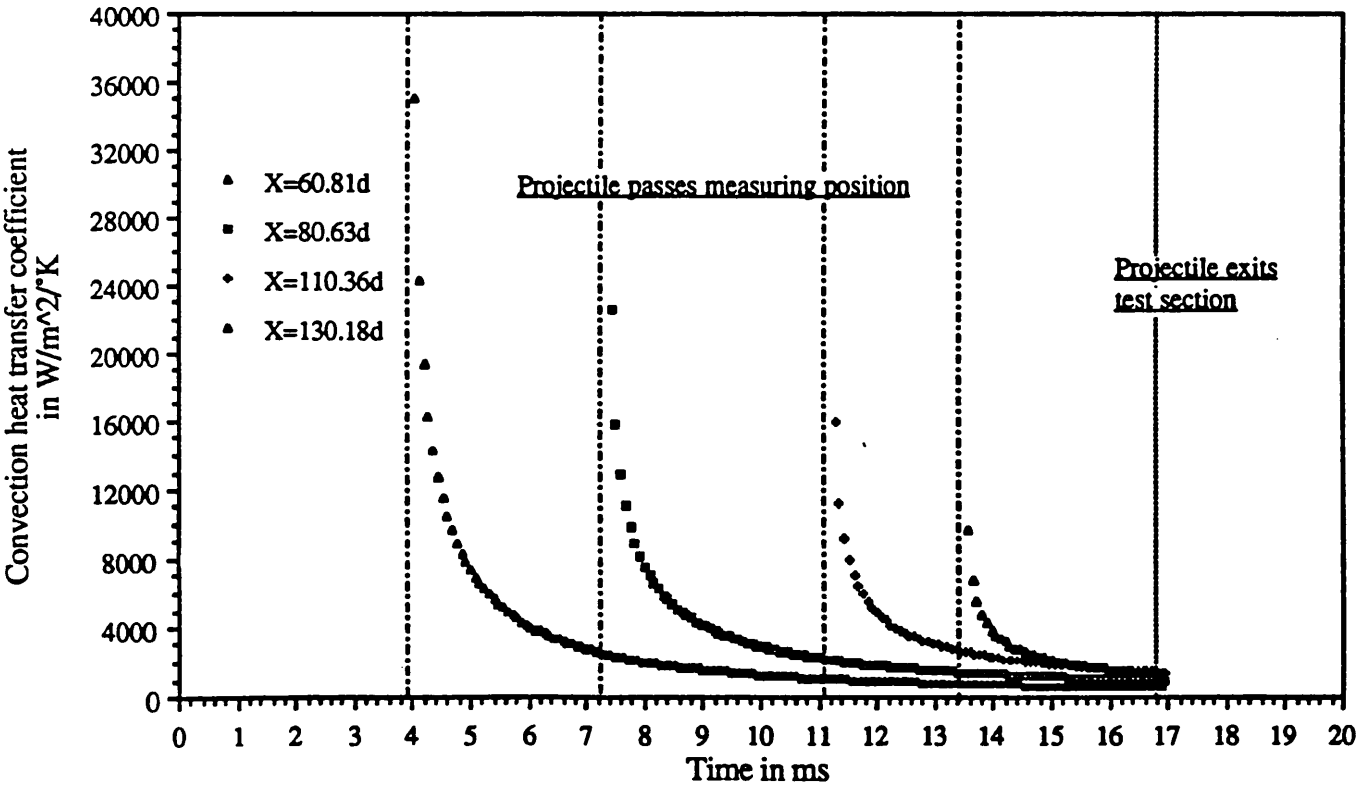


Figure 5.33 Convection coefficients at various axial locations for an initial pressure of 10 bar.

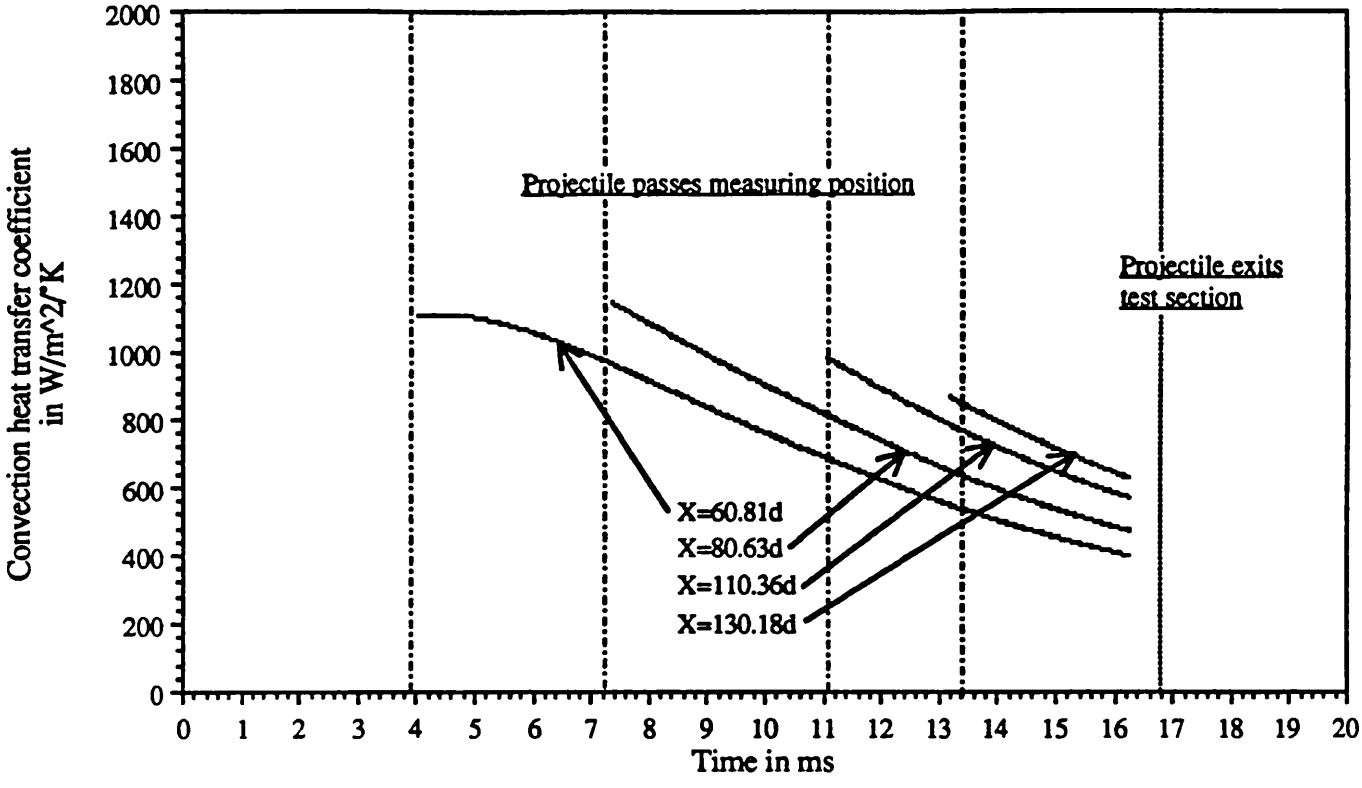


Figure 5.34 Calculated convection coefficients at various axial locations by Equation 4.3.

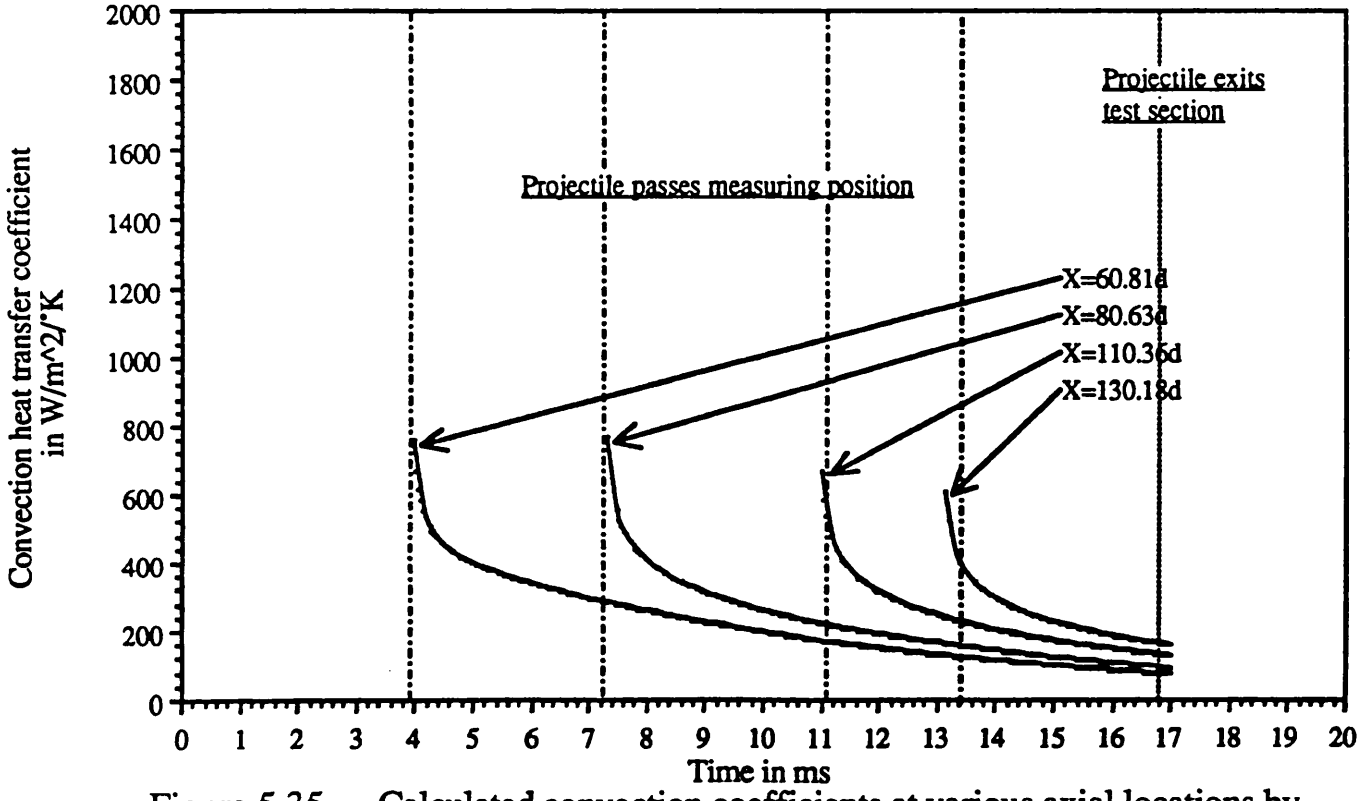


Figure 5.35 Calculated convection coefficients at various axial locations by Equation 5.2.

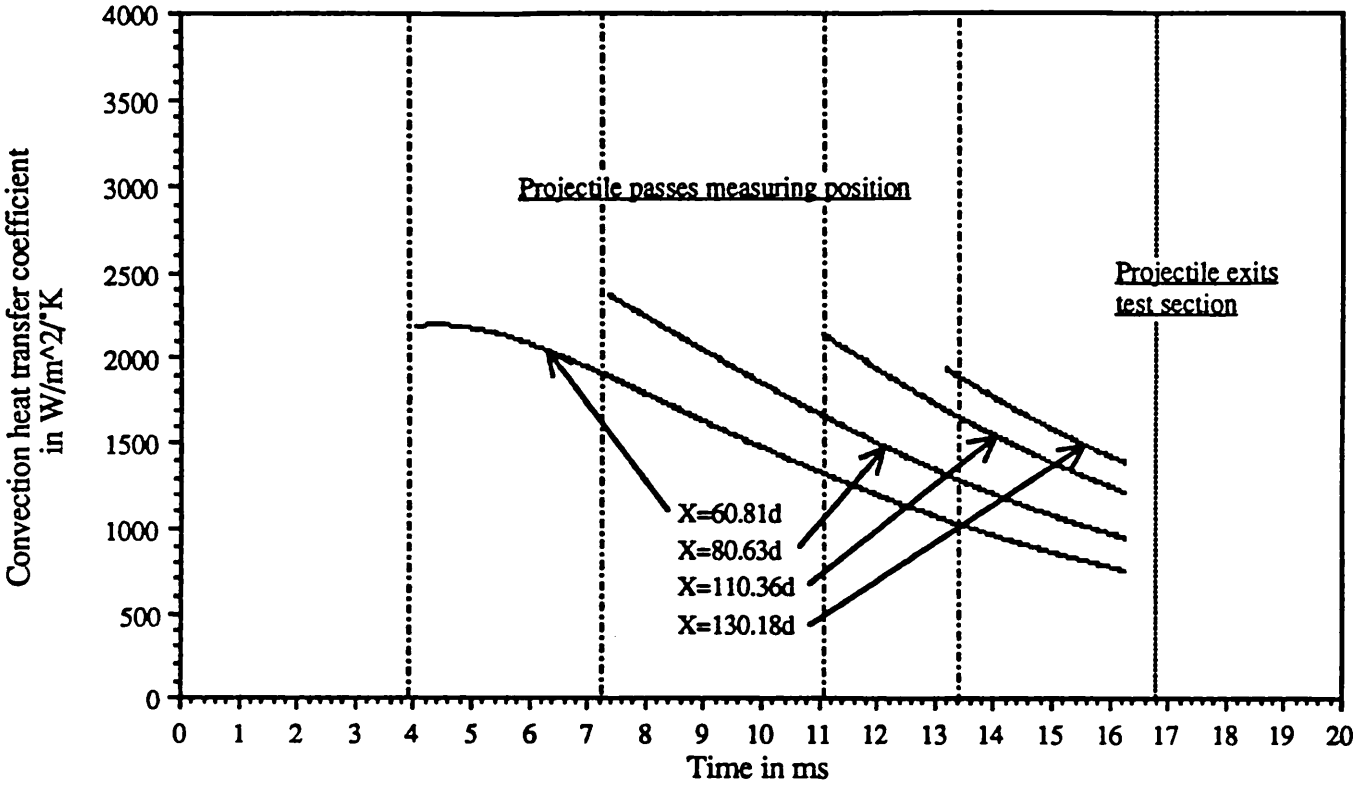


Figure 5.36 Calculated convection coefficients at various axial locations by Equation 5.3.

CHAPTER 6 CLOSURE

6.1 Conclusions

This chapter reviews the more important contributions to the development of experimental techniques, to the understanding of steady curved duct flows and to the unsteady flows in the two gun simulators. Recommendations for future research are provided in section 6.2.

6.1.1 Experimental Techniques

The bases of the measurement techniques were; manometers for the static pressure, piezoelectric transducers for the transient pressure, laser Doppler anemometers for the fluid velocity and thin-film thermometers for the wall temperature and heat flux. The application of the static pressure and anemometry techniques to the steady curved duct flows was straight forward and presented few difficulties except in the circular-duct case where the curvature of the plexiglass/water interface implied the need for geometry corrections with velocity measurements. The application of transient techniques, at moderate data rates in the low-speed simulator, also presented only minor problems which were associated with the seeding for velocity measurements and with the measurements of heat flux when the projectile passed over the sensor. The high-speed gun simulator, however, required faster time responses and higher data rates and new experimental methods were developed and evaluated. The instrumentation for the high-speed simulator represents an important contribution of this thesis by enabling the simultaneous measurement of fluid velocity, pressure, surface temperature and heat flux in the high-speed gun simulator with projectile velocities up to 450 m/s.

6.1.2 Curved Duct Flow

The investigation of steady incompressible flows in multiple curved ducts involved the measurement of velocity and static pressure in complex out-of-plane double S-bend duct diffusers. The measurements of velocity and static pressure quantified the effect of the inlet conditions and the interaction of the cross-flows generated by the

bends. The pressure distribution imposed by the geometry was shown to control the direction and magnitude of the mean velocity characteristics in the core of the flows while turbulence dictated the profiles and mixing characteristics near to the wall. The flows in the first S-bends were almost identical to those in the single S-duct cases previously studied and, together with the downstream diffuser, led to complex secondary-flow patterns with up to six vortical structures in the exit planes. The maximum secondary flow velocities at the exit of the second S-bend in laminar and turbulent flows in the rectangular S-duct and turbulent flow with a circular cross-section S-duct were 0.18, 0.11 and 0.09 V_B respectively. In all three cases, mean velocity distributions in the exit plane of the second S-bend diffuser, corresponding to the face of the compressor, were axisymmetric with maxima of 1.4, 1.0, and 0.86 V_B and with no negative velocities.

6.1.3 Low-Speed Gun Simulator

The measurements of breech pressure, wall temperature, heat transfer and single- and two-phase velocities in the low-speed simulator quantified the low-speed ballistic cycle and enabled the detailed analysis of the developing wall boundary layers. The low-speed investigation also provided guidance for the design and operation of the high-speed simulator arrangement and its high-speed instrumentation. The single-phase boundary layer was compared with the law-of-the-wall for steady flows and the agreement provided part of the evidence to conclude that the unsteady boundary layers were turbulent and similar to their steady counterparts. The velocity of a second-phase injected into the low-speed cycle with initial volume concentrations of 1.3 and 4 % was measured and the results show locally high concentrations around the edge of the boundary layer with terminal velocities associated with clusters of particles. The particle velocities measured with higher initial concentrations initially lagged behind the fluid and subsequently led the fluid and lower concentration measurements toward the end of the cycle because of their larger inertia. The measured surface temperature of a thin-film sensor mounted just below the barrel wall at positions swept by the projectile fell rapidly after the passage of the projectile due to the expansion of the flow and was used to evaluate the heat flux from the sensor and the convection coefficient. The heat flux results displayed maxima immediately behind the projectile and the convection coefficients were comparable, within 10 %, to correlations for steady turbulent boundary

layer flows toward the end of the cycle. Wall heat flux from the barrel was shown to be much larger with the chamfered initial geometry relative to the constant-diameter geometry because of the thinner boundary layers developing from the chamfered section versus from the breech and the injection of particles into the cycle increased the heat transfer by as much as 15 % at locations close to the breech.

6.1.4 High-Speed Gun Simulator

The high-speed simulator was capable of projectile and gas velocities up to 450 m/s, similar to those in practical gun systems, and measurements of breech pressure, wall temperature, heat transfer and gas-phase velocity were obtained. The measurements at a 10 bar initial pressure resulted in muzzle velocities of 220 m/s for a 10.5 g projectile and were similar to those calculated with an assumed quasi-steady ideal one-dimensional isentropic expansion and discrepancies were attributed to the developing boundary layers and the wake behind the accelerating projectile. The single-phase boundary layers occupied between 17 and 43 % of the diameter, were measured at five axial locations and compared well with the law-of-the-wall for steady turbulent flows. The measured wall temperature, heat flux and convection coefficient all displayed maxima immediately proceeding the projectile where the associated gas velocity and temperature difference were the largest. The heat flux became constant with time and a correlation assuming quasi-steady and fully developed turbulent flow in smooth circular tubes underpredicted the convection heat transfer coefficient by approximately 25 % as the projectile exits the test section. A correlation based on developing flow indicated correct trends but incorrect magnitudes due, predominately, to the unsteady and variable-property characteristics of the flow.

6.2 Recommendations For Further Work

The complex flow fields in the out-of-plane double S-bend duct experiments indicate the importance of the inlet conditions and the interaction of the secondary flows generated in each bend. No regions of flow detachment were observed throughout the experiments because of the relative large radius of bend curvature, small turning angles and small diffusing angles in the diffuser geometries. The duct geometries investigated

all tended to suppress separation along the inner curved wall at the exit where separation was most likely to occur. In root-wing intake ducts of real aircraft, the out-of-plane bends usually precede a compressor and separated flow at the compressor interface can reduce efficiency and performance. A study to quantify the effect of asymmetric inlet conditions and separated flow, in a single S-bend diffuser of the same geometry, with large perturbations in the inlet conditions, such as steps or large boundary layer trips, would contribute to understanding the development of the secondary flows and indicate how sensitive the exit plane flows would be to induced separation, similar to that caused by variations in the angles of attack, common in flight combat conditions. An investigation of S-duct diffusers with smaller radii of curvature and larger diffusing angles, which are also likely to cause separation, would benefit the design of practical intake duct geometries and closer examination of the inner region of the boundary layers would be useful, particularly to guide the development of models to calculated skin friction and heat transfer.

The extensive experiments in the low-speed simulator have quantified the gas-phase velocity, wall temperature and heat transfer characteristics in the ballistic cycle. The two-phase velocity experiments, with the higher initial loading, indicated a locally high concentration of particles in the annular region near the boundary layer thickness and this was shown to affect the second-phase velocities. An investigation of alternative methods of injecting particles and in even higher concentrations would be useful, particularly in view of the very high concentrations of the discrete phase in real guns. The simplified jet arrangement is also relevant to liquid-propellant guns so that work with sprays is desirable and feasible.

The interior ballistic simulator research has progressed through the development of the high-speed simulator and the simultaneous measurement of breech pressure, wall temperature, heat flux and velocity characteristics, made possible by the high-speed instrumentation. The breech pressure, wall temperature and heat transfer characteristics at initial pressures between 20 and 60 bars, with transonic projectile velocities, have now been measured by *Perez (1989)* as an extension to the work of this thesis but gas-phase velocities at higher initial pressures have yet to be attempted. The recommended direction for future research in gun simulators is to extend the velocity measurements to the flows with 60 bar initial pressures, to add a discrete and inert phase and subsequently

to proceed to small quantities of solid propellant in conjunction with the pressurized gas. This sequence of research will bridge the gap between the simulated and real guns and provide additional information to assist the development and validation of multi-phase numerical methods. When a reacting second-phase propellant is introduced in the high-speed simulator, a method of coupling ignition to projectile release will be necessary so that the pressure rise in the initial volume prior to the release of the projectile will not exceed the designed safe operation limit and this will probably require a rapid-acting pressure switch. The combustion of propellant will enable the investigation of erosion and, with optical access retained, particle and gas velocities along with breech pressure, wall temperatures and heat fluxes can and should be measured.

REFERENCES

Adrian R J, (1983)
'Laser velocimeter' in Fluid Mechanics Measurements
Ed. R.J. Goldstein, Springer Verlag ©1983.

Agrawal Y, Talbot L and Gong K, (1978)
Laser anemometer study of flow development in curved circular pipes, J. Fluid Mech., Vol. 85, part 3, pp. 497-518.

Arcoumanis C, Bicen A F and Whitelaw J H, (1984)
"The application of LDA to four-stroke motored model engines", Laser Anemometry in Fluid Mechanics, Published by Ladoan - Instituto Superior Técnico 1096 Lisbon Codex, Portugal, 1984.

Bansod P and Bradshaw P, (1972)
"The flow in S-shaped ducts", Aero. Quarterly, Vol. 23, pp. 131-140.

Berger S A, Talbot L and Yao L S, (1983)
"Flow in curved pipes", Annual Review of Fluid Mechanics, Vol. 15, p. 461.

Bicen A F, (1981)
"Refraction correction for LDA measurements in flows with curved optical boundaries", Mechanical Engineering Department Report FS/81/17.

Bicen A F, Khezzar L and Whitelaw J H, (1986a)
"Subsonic single-phase flow in a gun simulator", AIAA Journal, 26, 1, pp. 47-51, 1988. Also a Mechanical Engineering Department Report, FS/86/03, April 1986, Imperial College.

Bicen A F, Kliafas Y and Whitelaw J H, (1986b)
"In-bore velocity measurements in the wake of a subsonic projectile", American Institute of Aeronautics and Astronautics (AIAA) Journal Number 24, 6, 1986.

Bicen A F, Khezzar L and Whitelaw J H, (1986c)
"Subsonic single- and two-phase flow characteristics of a gun simulator", Mechanical Engineering Department Report, FS/86/43, Sept. 1986, Imperial College.

Bicen A F, Schmidt M C and Whitelaw J H, (1987)
"Preliminary measurements of heat flux in a subsonic gun simulator" Mechanical Engineering Department Report, FS/87/39, Dec. 1987, Imperial College.

Bicen A F, Khezzar L, Schmidt M C and Whitelaw J H, (1988a)
"Heat transfer and velocity characteristics of single- and two-phase flows in a subsonic model gun", Mechanical Engineering Department Report, FS/88/20, April 1988, Imperial College.

Bicen A F, Schmidt M C and Whitelaw J H, (1988b)
"Heat transfer measurement in inert single- and two-phase flows in a subsonic gun simulator", Mechanical Engineering Department Report, FS/88/22, May 1988, Imperial College.

Bicen A F, Laker J R, Schmidt M C and Whitelaw J H, (1989)
"Instrumentation for Transient Gas Velocity, Pressure and Heat Flux Measurements in a Gun Simulator", Proceedings of the 13th International Congress on Instrumentation in Aerospace Simulation Facilities, Göttingen, West Germany, September 1989.

Celmins A K R and Schmitt J A, (1984a)
"Volume Averaged Two-Phase (Gas-Solid) Interior Ballistics Equations", U.S. Army Ballistic Research Laboratory, Aberdeen Proving Ground, MD, U.S.A., Technical Report BRL-TR-2593, September 1984.

Celmins A K R and Schmitt J A, (1984b)
"Three-Dimensional Modeling of Gas-Combusting Solid Two-Phase Flows", 'Multi-Phase Flow and Heat Transfer III, Part B: Applications', Veziroglu and Bergles Eds., Elsevier Science Pub. B.V., Amsterdam, © 1984, pp. 681-698.

Clauser F H, (1954)
"Turbulent boundary layers in adverse pressure gradients", Journal of Aeronautical Science, Vol. 21, pp. 91-108, © 1954.

Clift R, Grace and Weber, (1978)
"Bubbles, Drops and Particles", Published by Academic Press, ©1978

Cook W J and Felderman E J, (1966)
"Reduction of Data from thin-film heat-transfer gages: A concise numerical technique", AIAA Journal, Vol. 4, Nº 3, pp. 561-562, 1966.

Dean W R, (1927)
"Note on the motion of fluid in a curved pipe", Philosophical Magazine, Vol. 4, p. 208.

Dean W R, (1928)
"The streamline motion of fluid in a curved pipe", Philosophical Magazine, Vol. 5, p. 673.

Drain L E, (1980),
"The laser Doppler technique", John Wiley, Chichester, ©1980.

Durst F, Melling A and Whitelaw J H, (1981)
"Principles and practice of Laser-Doppler anemometry", Academic Press, Second edition, ©1981.

Enayet M M, Gibson M M, Taylor A M K P and Yianneskis M, (1982a)
"Laser Doppler measurements of laminar and turbulent flow in a pipe bend", NASA Contractor Report 3551, and also, Int. J. Heat and Fluid Flow, Vol. 3, p. 213.

Enayet M M, Gibson M M and Yianneskis M, (1982b)
"Measurement of turbulent developing flow in a moderately curved square duct", Imperial College, Mech. Engr. Department Report FS/82/4, and also, Int. J. Heat and Fluid Flow, Vol. 3, p. 221.

Farrar C L and Lemming D W, (1983)
"Military Ballistics - A Basic Manual", Battlefield Weapons Systems and Technology Series, Volume X, © 1983, Brassey's Defense Publishers.

Founti M A and Laker J R, (1981)
"Performance characteristics of a new frequency counter to a microcomputer controlled data acquisition and processing system", Mechanical Engineering Department Report, FS/81/36, Sept. 1981, Imperial College.

Garloff J and Heiser R, (1988)
"Turbulence Modelling of One-phase interior Ballistics Flows by a Two-Equation Model", EMI Report, Expl-Nr 014; 1/88.

George W K and Lumley J L, (1973)
"The laser Doppler velocimeter and its application to the measurement of turbulence", J. Fluid Mech., Vol. 60, p. 321.

Gibeling H J, Buggeln R C and McDonald H, (1980)
"Development of a Two-Dimensional Implicit Interior Ballistics Code", U.S. Army ARRADCOM/Ballistic Research Laboratory Contractor Report ARBRL-CR-00411, Aberdeen Proving Ground, MD, January 1980.

Gibeling H J and McDonald H, (1984)
"An Implicit Numerical Analysis for Two-dimensional Turbulent Interior Ballistics Flows", U.S. Army ARRADCOM/Ballistic Research Laboratory Contractor Report ARBRL-CR-00523, Aberdeen Proving Ground, MD, February 1984.

Gibeling H J, McDonald H and Banks N E, (1983)
"An Implicit Numerical Analysis for Two-dimensional, Two-Phase Turbulent Interior Ballistics Flows", AIAA Paper No. 83-0561, 1983.

Goldstein R J and Adrian R J, (1971)
"Measurements of fluid velocity gradients using laser-Doppler techniques", Review of Scientific Instrumentation, Vol. 42, p. 1317, ©1971.

Gough P S, (1979)
"Modelling of two phase flow in guns", Page 176-196, Interior Ballistics of Guns, edited by H. Krier and M. Summerfield, Volume 66, Progress in Astronautics and Aeronautics, ©1979, Published by the American Institute of Aeronautics and Astronautics.

Gütlin E, Heiser R, Hensel D and Zimmermann G, (1987)
"Numerical and Experimental Investigation of the Ignition Process of a 105-mm Tank Gun Round", EMI Report, Expl-Nr 022; E 3/87.

Hardalupas Y, Taylor A M K P and Whitelaw J H, (1988)
"Velocity and Particle-Flux characteristics of Turbulent Particle-laden Jets", Mechanical Engineering Department Report, FS/87/14, June 1988, Imperial College.

Hawthorne W R, (1951)
"Secondary circulation in fluid flow", Proceedings of the Royal Society of Aeronautics, Vol. 206, p. 374.

Heiser R, (1987)
"Interior Ballistics Modelling of Regenerative Liquid Propellant Guns by a Gasdynamic Model", EMI Report, Expl-Nr 024; 1/87.

Heiser R, (1988)
"Gasdynamic Interior Ballistic Model for Regenerative Liquid Propulsion Systems", EMI Report, Expl-Nr 024; E 2/87.

Heiser R and Hensel D, (1988)
"Multidimensional Numerical Simulation of Large Caliber Ignition Processes", EMI Report, Expl-Nr 020; E 15/87.

Heiser R and Schmitt J A, (1985)
"Simulations of Special Interior Ballistic Phenomena with and without Heat Transfer to the Gun Tube Wall", Transactions of the Second Army Conference on Applied Mathematics and Computing, ARO Report 85-1, May 1984 pp. 405-457. Also as U.S. Army Ballistic Research Laboratory, Technical Report, BRL-TR-2732, Aberdeen Proving Ground, MD, May 1986.

Humphrey J A C, Taylor A M K P and Whitelaw J H, (1977)
Laminar Flow in a duct of strong curvature, J. Fluid Mech., Vol. 83, part 3, pp. 509-527.

Humphrey J A C, Whitelaw J H and Lee G, (1981)
Turbulent flow in a square duct of strong curvature, J. Fluid Mech. Vol. 103, pp. 443-463.

Incropera F P and DeWitt D P, (1985)
"Fundamentals of Heat and Mass Transfer", John Wiley and Sons, Second Edition, © 1985

Kays W M and Crawford M E, (1980)
"Convective Heat and Mass Transfer", McGraw-Hill, 1980.

Khezzar L, (1987)
"Experiments with steady and unsteady confined turbulent flows", Doctorate Thesis, University of London, January 1987.

Kline S J, Cantwell B J and Lilley G M, (1981)
"The 1980-81 AFOSR-HTTM-STANFORD Conference on Complex Turbulent Flows",Diffuser Flows (unseparated), Volume 1, Case #0142, evaluator: R L Simpson, pp. 262-264.

Klingenberg G and Mach H, (1978)
"In bore measurements of gas velocity and of radial gas temperature distribution", Proc. Fourth International Symp. on Ballistics, Monterey, Calf. U.S.A., October 1978.

Klingenberg G and Banks N E, (1981)
"Review on interior and transitional ballistic research: state of the art computational and experimental efforts", EMI Report, Expl-Nr 028; E 12/81.

Klingenberg G, (1985a)
"Temperature history of the interior ballistic flow of a 20-mm cannon", Journal of Ballistics, Vol. 8, No. 3, pp. 1986-2009, 1985.

Klingenberg G, (1985b)
"Invasive spectroscopic technique for measuring temperature in high pressurized combustion chambers", Optical Engineering, Vol. 24, No. 4, pp. 692-696, July/August 1985.

Klingenberg G, Schmolinske E, Mach H and Seiler F, (1985)
"Flow simulation experiments in ballistics", Journal of Ballistics, Vol. 8, No. 4, pp. 2089-2118, 1985.

Klingenberg G, Heimerl J M and Schmolinske E, (1986)
"Simulation experiments -gas gun simulator", Proc. Ninth International Symp. on Ballistics, Royal Military College of Science, Shrivenhamm U.K., April/May 1986.

Krier H and Adams M J, (1979)
"An introduction to Gun Interior Ballistics and a Simplified Ballistic Code", Page 1-36, Interior Ballistics of Guns, edited by H. Krier and M. Summerfield, Volume 66, Progress in Astronautics and Aeronautics, ©1979, Published by the American Institute of Aeronautics and Astronautics.

Krier H and Summerfield M, (1979)
"Interior Ballistics of Guns", Volume 66, Progress in Astronautics and Aeronautics, ©1979, Published by the American Institute of Aeronautics and Astronautics.

Lagrange J L, (1832)
Journal de l'Ecole Polytechnique (Paris), 21, N 13.

Lawton B, (1988)
"Heat transfer in gun barrels", Royal Military College of Science, Shrivenhamm U.K.

Levy R, McDonald H, Briley W R and Kreskovsky J P, (1980)
"A three-dimensional turbulent compressible subsonic duct flow analysis for use with constructed coordinate systems", AIAA Paper 80-1398.

Levy R, Briley W R and McDonald H, (1983)
"Viscous primary/secondary flow analysis for use with nonorthogonal coordinate systems", AIAA Paper 83-0556.

Mach H and Hensel D, (1986)
"The light gas gun- simulator for interior ballistic flows", Proc. Ninth International Symp. on Ballistics, Royal Military College of Science, Shrivenhamm U.K., April/May 1986.

McLaughlin D K and Tiederman W G, (1973)
"Biasing correction for individual realization of laser anemometer measurements in turbulent flows", Physics of Fluids, Vol. 16, Nº 12, pp. 2082-2088.

McMillian O J, (1982)
"Mean flow measurements of the flow field diffusing bend", NASA Contractor Report CR-3634, November 1982.

Melling A, (1975)
"Investigation of flow in non-circular ducts and other configurations by laser Doppler anemometry", Doctorate Thesis, University of London, 1975.

Melling A and Whitelaw J H, (1976)
Turbulent flow in a rectangular duct, J. Fluid Mech., Vol. 78, part 2, pp. 289-315.

Modarress D, (1986)
"Duct particle velocity measurement in shock tubes", Defense Nuclear Agency technical report, #DNA-TR-86-12, Government report number AD-A171 528.

Morse A, (1977)
"The effect of crank angle broadening on laser Doppler measurements in reciprocating engines", Mechanical Engineering Department Report, Listed as FS/77/18 and FS/77/26 depending upon source.

Morse A, Whitelaw J H and Yianneskis M, (1979)
"Turbulent flow measurements by laser-Doppler anemometry in motored piston-cylinder assemblies", Journal of Fluids Engineering, Transactions of the ASME, Vol. 101, pp. 208-216, June 1979.

Perez R, (1989)
"Wall Heat Transfer Measurements in a Simulation of a gun Barrel Flow", Masters Thesis, University of London, 1989.

Rask R B, (1981)
"Comparison of window, smoothed-ensemble, and cycle-by cycle data reduction techniques for laser Doppler anemometer measurements of in-cylinder velocity", Fluid Mechanics of Combustion Systems, Presented at the Fluids Engineering Conference, Boulder CO, U.S.A., June 22-23 1981, Published by ASME, pp. 11-20, 1981.

Rojas J, Whitelaw J H and Yianneskis M, (1983a)
"Developing flow in S-shaped diffusers. Part I - Square-to-rectangular cross-section diffusers", NASA Contractor Report, and Imperial College, Mech. Engr. Dept. Report FS/83/12.

Rojas J, Whitelaw J H and Yianneskis M, (1983b)
"Flow in sigmoid diffusers of moderate curvature", Proc. Fourth Symp. on Turbulent Shear Flows, Karlsruhe, Germany, September 1983, and Imperial College, Mech. Engr. Dept. Report FS/83/21.

Rojas J, Whitelaw J H and Yianneskis M, (1983c)
"Developing flow in S-shaped diffusers. Part II - Circular cross-section diffusers", NASA Contractor Report, and Imperial College, Mech. Engr. Dept. Report FS/83/28.

Rojas J, Whitelaw J H and Yianneskis M, (1984)
"Inlet condition effects on incipient separation in flow in curved diffusers", NASA Contractor Report, Mechanical Engineering Department Report FS/84/31.

Rojas-Menendez J A, (1986)
"Flow and heat transfer characteristics of diffusing curved ducts", Doctorate Thesis, University of London, 1986.

Rowe M, (1970)
"Measurements and computations of flow in pipe bends", J. Fluid Mech.,Vol. 43, part 4, pp. 771-783.

Schlichting H H, (1979)
"Boundary Layer Theory", 2nd Edition, McGraw-Hill, New York 1979.

Schmidt M C, Whitelaw J H and Yianneskis M, (1986)
"Flow in out-of-plane double S-bends", NASA Contractor Report CR-176981, Mechanical Engineering Department Report FS/86/30

Schmidt M C, (1987)
"Flow Characteristics of a Particle Loaded Gun Simulator", Mechanical Engineering Department Report, FS/87/29, Dec. 1987, Imperial College.

Schmidt M C, Whitelaw J H and Yianneskis M, (1987)
"Flow in Out-of-Plane Double S-Bends", Proceedings of the Sixth Symposium on Turbulent Shear Flows, Toulouse, France, September 1987.

Schmidt M C, (1988a)
"Preliminary Measurements in a Supersonic Gun Simulator", Mechanical Engineering Department Report, FS/88/16, April 1988, Imperial College.

Schmidt M C, (1988b)
"A Progress Report on Measurements in a High Speed Gun Simulator", Mechanical Engineering Department Report, FS/88/43, September 1988, Imperial College.

Schmidt M C, (1989)
"Single-Phase Flow in a High Speed Gun Simulator", Mechanical Engineering Department Report, FS/898/02, February 1989, Imperial College.

Schmitt J A, (1985)
A Numerical Algorithm for the Multidimensional, Multiphase, Viscous Equations of Interior Ballistics", Transactions of the Second Army Conference on Applied Mathematics and Computing, ARO Report 85-1, May 1984, pp. 649-691.

Schultz D L and Jones T V, (1973)
"Heat transfer measurements in short-duration hypersonic facilities", AGARDograph 165, AGARD-AG-165, 1973

Seigel A E, (1952)
"The rapid expansion of compressed gases behind a piston", PhD Thesis, University of Amsterdam.

Seigel A E, (1961)
"Method of Calculating Preburned Propellant Gun Performance with Special Application to Two-Stage Guns", Naval Ordnance Lab., NOLTR 61-29, June 1961.

Seigel A E, (1965)
"The theory of high speed guns", AGARDograph 91, May 1965.

Seigel A E, (1979)
"Theory of high-muzzle-velocity guns", Page 135-175, Interior Ballistics of Guns, edited by H. Krier and M. Summerfield, Volume 66, Progress in Astronautics and Aeronautics, ©1979, Published by the American Institute of Aeronautics and Astronautics.

Seiler F, (1983)
"Experimental simulation of the flow inside a gun barrel", Proc. Seventh International Symp. on Ballistics, The Hague, Netherlands, April 1983.

Shaw R, (1960)
"The influence of hole dimensions on static pressure measurements", J. Fluid Mech., Vol. 7, pp. 550-564.

Stiefel L, (1988)
"Gun Propulsion Technology", Volume 109, Progress in Astronautics and Aeronautics, ©1988, Published by the American Institute of Aeronautics and Astronautics.

Squire H B and Winter K G, (1951)
"The secondary flow in a cascade of airfoils in Nonuniform stream", Journal of the Aeronautical Sciences, Vol. 18, pp. 271-277, April 1951.

Taylor A M K P, Whitelaw J H and Yianneskis M, (1980)
"Measurements of laminar and turbulent flow in a curved duct with thin inlet boundary layers", NASA Contractor Report 3367. FS/80/29

Taylor A M K P, Whitelaw J H and Yianneskis M, (1981a)
"Curved ducts with strong secondary motion: Velocity measurements of developing laminar and turbulent flow",Transactions of the ASME, Journal of Fluids Engineering, Vol. 104, pp. 350-359, and Imperial College, Mech. Engr. Dept. Report FS/81/20.

Taylor A M K P, Whitelaw J H and Yianneskis M, (1981b)
"Developing flow in S-shaped ducts. Part I - Square cross-section duct", NASA Contractor Report CR-3550, Imperial College, Mech. Engr. Dept. Report FS/81/22.

Taylor A M K P, Whitelaw J H and Yianneskis M, (1982)
"Report on the calculation of mass flow rate from velocity profiles measured in square ducts", Imperial College, Mech. Engr. Dept. Report FS/82/13.

Taylor A M K P, Whitelaw J H and Yianneskis M, (1984)
"Developing flow in S-shaped ducts. Part II - Circular cross-section duct", NASA Contractor Report CR-3759 February 1984.

Towne C and Anderson B H, (1981)
"Numerical simulation of flows in curved diffusers with cross-sectional transitioning using a three-dimensional viscous analysis", AIAA Paper 81-0003.

Towne C, (1984)
"Computation of viscous flow in curved ducts and comparison with experimental data", AIAA Paper 84-0531.

Tsou F K and Chen S J, (1983)
"Measurement of heat transfer rates using a transient technique", ASME publication 83-HT-87.

Ward-Smith A J, (1980)
Internal fluid flow, Claredon Press, Oxford, © 1980.

Yanta W, (1973)
"Turbulence measurements with a laser-Doppler velocimeter", Naval Ordinance Laboratory Report, NOLTR 73-94, White Oak, Silver Springs MD.

Yu S C M, (1989)
"Flow behavior in an S-shaped diffuser with distorted inlet conditions: square to rectangular cross-section diffuser", Imperial College, Mech. Engr. Dept. Report FS/89/22.